Long-Term Performance of the LEGEND-200 Muon Veto: Analysis and Simulation Studies

Dissertation

der Mathematisch-Naturwissenschaftlichen Fakultät

der Eberhard Karls Universität Tübingen

zur Erlangung des Grades eines

Doktors der Naturwissenschaften

(Dr. rer. nat.)

vorgelegt von

Gina Grünauer

aus Schwäbisch Gmünd

Tübingen

2025

Gedruckt mit Genehmigung der Mathematisch-Naturwissenschaftlichen Fakultät der Eberhard Karls Universität Tübingen.

Tag der mündlichen Qualifikation:	20.11.2025
Dekan:	Prof. Dr. Thilo Stehle
1. Berichterstatter/-in:	Prof. Dr. Josef Jochum
2. Berichterstatter/-in:	Prof. Dr. Tobias Lachenmaier

Abstract

To investigate the Majorana nature of neutrinos and thereby examine the origin of their small mass beyond the Standard Model of particle physics, the Large Enriched Germanium Experiment for Neutrinoless $\beta\beta$ Decay (LEGEND) is dedicated to the search for neutrinoless $\beta\beta$-decay in enriched ^{76}Ge. The experimental phase LEGEND-200 aims to deploy 200 kg of detector mass to reach a half-life sensitivity of more than $T_{1/2}^{0\nu} = 10^{27}$ yr, corresponding to a background index below $2 \cdot 10^{-4}$ cts/(keV $\cdot$ kg $\cdot$ yr) in the region of interest (ROI). To achieve such a rare event rate, both passive and active background shielding are required. For LEGEND-200, a water Cherenkov veto serves as an active muon veto, rejecting cosmogenic muons traversing the experimental setup. The muon veto uses photomultiplier tubes (PMTs) as light detectors and a reflective foil on the inner surfaces of the water tank to increase the light yield.

In this work, nearly one year of LEGEND-200 muon veto data was analyzed, complemented by Monte Carlo simulations. To ensure stable signal performance, PMTs were calibrated once or twice per month, and additional PMTs were prepared as replacements. Detected events include muons, persistent low-multiplicity signals (the "low-multiplicity bump"), and spontaneous signals from PMTs breaks, most of which can be removed by two permanent analysis cuts, resulting in a muon rate of $r_{\text{muon}} \approx 35$ mHz. Using pulse shape discrimination and monitoring systems, different types of PMT breaks could be classified and their occurrence predicted. The total muon-induced background in the ROI was determined to be $5.46 \cdot 10^{-4}$ cts/(keV $\cdot$ kg $\cdot$ yr), in good agreement with the value measured in the GERDA experiment of $6.34 \cdot 10^{-4}$ cts/(keV $\cdot$ kg $\cdot$ yr) [1]. Monte Carlo Simulations yielded a lower limit on the muon veto detection efficiency of $\eta_{\text{sim}} \approx 99.18$ %. Contrary to previous assumptions, further simulation studies ruled out ^{60}Co β decays in the steel of the water tank as origin of the low-multiplicity bump via scintillation in the reflective foil [2, 3], but indicate a possible contribution from ^{222}Rn activity of approximately 50 mBq/kg. In addition, in the search for muon-induced neutron captures in high-purity germanium detectors, a criterion was established to classify showering muons producing secondary particles, identifying 11.02 % of muon events in simulations and 10.51 % in measured data. This classification has led to two approaches for identifying muon-induced neutron captures, which can be further validated in future work. Overall, the results of this study demonstrate the reliability of the LEGEND-200 muon veto and its contribution to achieving the background goal of the experiment.

This work was conducted within the framework of the LEGEND collaboration, with individual and collaborative contributions detailed in Appendix E.

Zusammenfassung

Zur Untersuchung der Majorana-Natur von Neutrinos und des Ursprungs ihrer kleinen Masse jenseits des Standardmodells der Teilchenphysik widmet sich das Large Enriched Germanium Experiment for Neutrinoless $\beta\beta$ Decay (LEGEND) der Suche nach dem neutrinolosen $\beta\beta$-Zerfall in angereichertem ^{76}Ge. Die Experimentphase LEGEND-200 plant den Einsatz von 200 kg Detektormasse, um eine Sensitivität auf Halbwertszeiten von über $T_{1/2}^{0\nu} = 10^{27}$ yr zu erreichen, entsprechend einem Hintergrundindex von unter $2 \cdot 10^{-4}$ cts/(keV $\cdot$ kg $\cdot$ yr) in der region of interest (ROI). Dafür werden passive und aktive Hintergrundabschirmungen eingesetzt. In LEGEND-200 dient ein Wasser-Cherenkov-Veto als aktives Myonveto zur Unterdrückung kosmogener Myonen. Das Myonveto verwendet photomultiplier tubes (PMTs) als Lichtdetektoren und eine reflektierende Folie im Inneren des Wassertanks, um die Lichtausbeute zu erhöhen.

In dieser Arbeit wurde fast ein Jahr an Daten des LEGEND-200 Myonvetos analysiert und die Analysen durch Monte Carlo Simulationen ergänzt. Für eine stabile Signalqualität wurden die PMTs ein- bis zweimal monatlich kalibriert und zusätzliche Ersatz-PMTs vorbereitet. Detektierte Ereignisse beinhalten Myonen, anhaltende Signale niedriger Multiplizität (der "low-multiplicity bump") und plötzliche PMT-Ausfälle, die größtenteils durch zwei permanente Analysekriterien herausgefiltert werden, was zu einer Myonrate von $r_{\text{muon}} \approx 35$ mHz führt. Pulsformdiskriminierung und Beobachtungssysteme ermöglichten Klassifizierung und Vorhersage von PMT-Ausfallarten. Der gesamte myoninduzierte Hintergrund in der ROI beträgt $5.46 \cdot 10^{-4}$ cts/(keV $\cdot$ kg $\cdot$ yr), in guter Übereinstimmung mit dem GERDA-Experiment $6.34 \cdot 10^{-4}$ cts/(keV $\cdot$ kg $\cdot$ yr) [1]. Monte Carlo Simulationen ergaben ein unteres Detektionseffizienzlimit des Myonvetos von $\eta_{\text{sim}} \approx 99.18$ %. Im Gegensatz zu früheren Annahmen, schlossen weitere Simulationen β-Zerfälle des ^{60}Co im Wassertankstahl, die Szintillation in der reflektierenden Folie anregen [2, 3], als Ursache des low-multiplicity bump aus, zeigen jedoch einen Beitrag von ^{222}Rn von etwa 50 mBq/kg. Außerdem wurde bei der Suche nach myoninduzierten Neutroneneinfängen in hochreinen Germaniumdetektoren ein Kriterium zur Klassifikation schauernder Myonen definiert, das 11.02 % in der Simulation und 10.51 % in den Messdaten erfasst. Damit wurden zwei Ansätze zur Identifikation myoninduzierter Neutroneneinfänge entwickelt, die in weiteren Untersuchungen validiert werden können. Die Ergebnisse zeigen die Zuverlässigkeit des LEGEND-200 Myonvetos und seinen Beitrag zum Hintergrundziel des Experiments.

Diese Arbeit entstand im Rahmen der LEGEND-Kollaboration, wobei Eigen- und Kollaborationsanteile in Anhang E aufgeschlüsselt sind.

Contents

Chapter 1

Introduction

"Omnium enim rerum principia parva sunt."

— Marcus Tullius Cicero, De finibus

The Standard Model of particle physics (SM) originally described neutrinos as massless leptons. However, experimental observations of neutrino oscillations revealed that neutrinos possess a small but non-zero mass [4, 5, 6]. One possible explanation for the small size of the neutrino mass is that neutrinos are Majorana particles. This implies that neutrinos are their own antiparticles, a hypothesis that could be confirmed by the detection of the neutrinoless double-beta ($0\nu\beta\beta$)-decay.

The Large Enriched Germanium Experiment for Neutrinoless $\beta\beta$ Decay (LEGEND) research program is dedicated to the search for $0\nu\beta\beta$-decay in enriched ^{76}Ge and is located at Laboratori Nazionali del Gran Sasso (LNGS) in Italy. By employing high-purity Germanium (HPGe) as both source and detector, the ton-scale phase LEGEND-1000 aims to achieve a half-life sensitivity of more than $T^{0\nu}_{1/2} = 1.3 \cdot 10^{28}$ yr, potentially allowing the observation of $0\nu\beta\beta$-decay. In 2023, the LEGEND-1000 demonstrator, LEGEND-200, began data taking with an aimed HPGe detector mass of 200 kg. LEGEND-200 is expected to operate for five years, reaching a half-life sensitivity of more than $T^{0\nu}_{1/2} = 10^{27}$ yr, corresponding to a background index (BI) below $2 \cdot 10^{-4}$ cts/(keV $\cdot$ kg $\cdot$ yr) in the region of interest (ROI). To achieve this sensitivity, passive and active background rejection strategies are used in the experiment, including additional detector systems to measure cosmogenic and radiogenic backgrounds. An active shielding mainly against radiogenic background near the HPGe detectors is provided by the liquid argon (LAr) instrumentation.

To suppress cosmogenic muons, which generate additional background events that could compromise the aimed BI, a water Cherenkov detector system is instrumented by LEGEND-200 as an active muon veto. The muon veto surrounds the other detector systems within a water tank and

employs photomultiplier tubes (PMTs) to detect the Cherenkov light produced by muons, while a reflective foil covering the inner tank surfaces increases the light yield [7].

This thesis focuses on the LEGEND-200 muon veto, including data processing and analysis as well as Monte Carlo simulation studies to achieve a deeper understanding of detected muon event structures. Furthermore, the detection efficiency of the operation of the muon veto system is maintained through the preparation of additional PMTs for installation.
Following this introduction, Chapter 2 presents the theoretical background of the search for $0\nu\beta\beta$-decay and serves as the motivation for the LEGEND experiment described in Chapter 3. Chapter 4 discusses the background sources and corresponding rejection mechanisms of the LEGEND experiment and includes an overview of the muon veto system and a description of its calibration procedure. Data processing and analysis of the muon veto events are examined in detail in Chapter 6. This Chapter also includes a study of PMT stability, an analysis of the waveforms and a coincidence analysis involving the other detector systems of LEGEND-200. To gain a deeper understanding of the experimental data, Chapter 7 presents the implementation of a simulation geometry and Monte Carlo simulation of the muon veto. The results of the simulations are compared with the experimental data in Chapter 8. In this chapter, different event structures are investigated, showering muons in the water tank are identified, and two approaches for the classification of muon-induced neutron captures in the HPGe detectors are proposed. Since several PMTs failed during LEGEND-200 operations, Chapter 9 provides an estimation of the muon veto efficiency development considering these failures. Furthermore, this Chapter describes the preparation of additional PMTs for a system update to maintain the detection efficiency. Finally, Chapter 10 summarizes the results and provides an outlook on the future operation of the LEGEND-200 muon veto, including potential analyses and simulation studies.

Chapter 2

Neutrino physics with respect to the neutrinoless double-beta decay

"Omnia mutantur, nihil interit."

— Ovid, Metamorphoses

One of the most remarkable achievements of modern physics is the development of the SM, which describes the known elementary particles and their interactions. Nevertheless, the present SM is unable to answer certain key questions, such as the origin of the baryon asymmetry in the universe, the composition of dark matter, and the mass of neutrinos. The SM describes neutrinos as electrically neutral leptons participating in the weak interaction and assumed to be massless. However, the discovery of neutrino oscillations provided evidence of a small non-zero neutrino mass, which requires an extension of the SM. One possible explanation would be the Majorana nature of neutrinos, which could be indicated by the measurement of the $0\nu\beta\beta$-decay, which would violate the lepton number conservation. In particular, the last possibility mentioned is of crucial relevance for this work.
The following chapter provides an overview of the SM, followed by a discussion of neutrino properties and concluding with an introduction to β decay and a description of the $0\nu\beta\beta$-decay.

2.1 Standard Model of particle physics

The SM describes all known elementary particles as fermions and the corresponding exchange particles as bosons. The fermions are classified into leptons and quarks, each forming three generations of increasing mass, while all exhibit a spin quantum number of $1/2$. Leptons do not participate in the strong interaction and possess their own quantum number, the lepton number $L = 1$ or $L = -1$ for antileptons. All known lepton interactions or decays obey the conservation of

the lepton number $\Delta L = 0$. The three generations of leptons are divided into electrons (e), muons (μ), and tauons (τ), all with a negative electric charge Q of -1, and their associated neutrino in corresponding flavors (ν_e, ν_μ and ν_τ) with $Q = 0$. Electrically charged leptons participate in both electromagnetic and weak interactions, correspondingly the neutrinos only participate in weak interactions [8]. Due to the observation of neutrino oscillations (cf. Section 2.2.1), it is now known that at least two of the three neutrino generations have a non-zero mass. This is in contradiction with the SM, which assumes neutrinos to be massless $m_\nu = 0$ [9].

Fermions that participate in the strong interaction are known as quarks q with the baryon quantum number $B = 1/3$, accordingly $B = -1/3$ for antiquarks, which is conserved in decays and interactions $\Delta B = 0$. The three quark generations consist of the up (u) and down (d), charm (c) and strange (s) and top (t) and bottom (b) flavors. The u, c and t quark exhibit a positive electric charge of $Q = 2/3$, whereas the d, s and b quark are electrically negatively charged with $Q = -1/3$. Since all quarks have a mass $m_q > 0$, they take part in all four fundamental interactions [8]. However, free quarks are not observed. They exist within bound systems called hadrons, classified into baryons and mesons. Baryons are composed of three quarks whilst mesons consist of quark-antiquark pairs. Quarks carry a quantum property called color charge, which describes the behavior of the strong interaction and comes in three types: red, green and blue. Hadrons are held together by the strong interaction, arising from the exchange of color charge of the quarks with corresponding anti-colors carried by antiquarks. The resulting hadron is always colorless, meaning it contains equal amounts of red, green and blue color charge [10].

The exchange of color charge, like all other known fundamental interactions, is mediated by bosons. They have a spin quantum number of 0 (Higgs boson) or 1 (vector or gauge bosons), depending on the particle. Vector bosons mediate the strong, electromagnetic and weak interactions. The gravitational interaction is hypothesized to be mediated by the as yet unobserved graviton with a spin of 2. This interaction is too weak to be crucial in particle physics and, therefore, not a part of the SM [11].

Gluons (g) are massless gauge bosons mediating the strong interaction via coupling to the color charge. They do not carry an electric charge, possess both color and anti-color at the same time and can interact with each other. This implies that $3 \cdot 3 = 9$ different gluons are expected, corresponding to the different combinations of color and anti-color. However, the colorless gluons $r\bar{r}$, $g\bar{g}$, $b\bar{b}$ cannot be observed. They are built from combinations, where the exchange of $(r \leftrightarrow g)$ and $(r \leftrightarrow b)$ is possible. Overall eight different gluons are contributing to the strong interaction. In the process of gluon exchange, the colors charge of the interacting quarks changes. The range of the strong interaction is about 1 fm matching the size of a nucleon. Within that range an infinite energy would be needed to divide the quarks from each other, which is called confinement. Thus, no free color charge will be observed. With increasing potential energy gluon-antigluon pairs can be built. As soon as a hadron gets sufficient energy to build quark-antiquark pairs, gluon-antigluon pairs are formed, thereby producing mesons. This mechanism ensures that only colorless particles

are produced during strong interactions [12].

The mediators of the electromagnetic interaction are photons (γ), which are massless gauge bosons. They couple to the electric charge of particles and contain no color charges. Since photons do not carry an electric charge themselves, they do not interact directly with each other in classical electrodynamics. Thus, photons have an infinite range and are described with the linear behavior of quantum electrodynamics (QED).

The weak interaction is mediated by the $W^{\pm}$ and Z^0 gauge bosons between fermions. These bosons have masses of approximately 80 GeV and 91 GeV and, correspondingly, a short range of $2 \cdot 10^{-3}$ fm. In the case of weak interaction it is necessary to distinguish between electric charged ($W^{\pm}$ with $Q = \pm 1$) and neutral (Z^0 with $Q = 0$) currents, referring to an existing or non-existing change of the electric charge. Within charged currents $W^{\pm}$ can couple to leptons of the same generation due to the conservation of the lepton number. Quark transitions between the generations are possible but suppressed [11]. This behavior is described by the Cabibbo-Kobayashi-Maskawa (CKM) mass matrix elements in Equation 2.1, where $|q'\rangle$ are the eigenstates of the down-type quarks (d, s and b) at the exchange of $W^{\pm}$

$$\begin{pmatrix} |d'\rangle \\ |s'\rangle \\ |b'\rangle \end{pmatrix} = \begin{pmatrix} V_{ud} & V_{us} & V_{ub} \\ V_{cd} & V_{cs} & V_{cb} \\ V_{td} & V_{ts} & V_{tb} \end{pmatrix} \cdot \begin{pmatrix} |d\rangle \\ |s\rangle \\ |b\rangle \end{pmatrix}. \tag{2.1}$$

The CKM matrix can be parametrized with three mixing angles θ_{12}, θ_{13} and θ_{23} and the complex phase $e^{i\delta}$ [13]. The transition probability of a quark q_i in another one q_j is proportional to $|V_{q_i q_j}|^2$. Equation 2.2 shows the approximations of the corresponding absolute values

$$\left(|V_{q_i q_j}|\right) = \begin{pmatrix} 0.974 & 0.225 & 0.004 \\ 0.225 & 0.973 & 0.041 \\ 0.009 & 0.040 & 0.999 \end{pmatrix}. \tag{2.2}$$

The diagonal values of the matrix are near to 1 according to the high transition probability within the same generation. In contrast, Equation 2.2 shows the strongly decreasing transition probability of the off-diagonal elements with an increasing distance of the generations. In neutral currents, a Z^0 boson is exchanged and the lepton number, electric charge and quark flavor are conserved. The weak interaction is responsible for radioactive decays of quarks and leptons [10].

The so far only known scalar boson in the SM, the Higgs boson (H) mediates the so called Higgs field, which is responsible for generating masses in the SM. More information about the Higgs boson and field can be found in [14].

In total all fermions, their corresponding antifermions, and bosons, the SM consists of 61 particles. However, among others these questions remain unanswered: What are dark matter and dark

energy made of? Why are there three generations of fermions? How are the masses of neutrinos generated? In order to gain a better understanding of the last question the following section provides an overview of the key properties of neutrinos.

2.2 Neutrino properties

In 1930, the neutrino was postulated by Wolfgang Pauli as a solution for the continuous spectrum and momentum conservation of β decay (cf. Section 2.3) [15]. Since in such a decay the emitted electron e^- can possess a discrete energy, there must be another particle with a continuous energy distribution carrying energy away. That was meant to be the neutrino ν_e, leading to a three-body decay

$$M(A, Z) \rightarrow D(A, Z + 1) + e^- + \bar{\nu}_e \,, \tag{2.3}$$

where $M(A, Z)$ and $D(A, Z + 1)$ are referring to the mother and corresponding daughter nuclei with atomic mass A and atomic number Z. Here, the sum of e^- and $\bar{\nu}_e$ energies is equal to the full transition energy, which is known as the Q-value [13]. Since neutrinos participate only in the weak interaction, the experimental discovery of the neutrino was made 26 years later in 1956 by Clyde Cowan and Frederick Reines. The inverse β decay was used as a detection channel for indirect evidence of antineutrinos

$$\bar{\nu}_e + p \rightarrow e^+ + n \,, \tag{2.4}$$

where the $\bar{\nu}_e$ was produced by a nuclear reactor [16]. It was assumed that there is a neutrino flavor for each lepton generation, so ν_μ and ν_τ were still to be measured. The discovery of the ν_μ succeeded in 1962 at the Brookhaven National Laboratory during the investigation of the π-decay [17]. About 38 years later, in 2000, the ν_τ was observed by the DONUT collaboration at Fermilab due to neutrino interactions in nuclear emulsion targets [18].

Since neutrinos are part of the weak interaction, a deeper understanding of this interaction is crucial for advancing the knowledge of neutrino behavior. One of the key characteristics of the weak interaction is the violation of the parity P symmetry. The parity describes the spacial symmetry transformation of particles by an inversion $\vec{x} \rightarrow -\vec{x}$ and was assumed to be conserved in all fundamental interactions. However, in 1956 Chien-Shung Wu demonstrated the violation of the parity symmetry by investigating the β decay of ^{60}Co nuclei at low temperatures in the presence of a magnetic field. The emitted electrons were mainly detected in the direction opposite to the spin of the mother nucleus [19].

The observed asymmetry is connected to the concept of helicity H. In contrast to chirality, which describes the intrinsic handedness of a particle, helicity is defined as the direction in which the

spin vector is located compared to its direction of flight:

$$H = \frac{\vec{s} \cdot \vec{p}}{|\vec{s}| \cdot |\vec{p}|}\,, \tag{2.5}$$

where $\vec{s}$ refers to the spin and $\vec{p}$ to the momentum of the particle [12]. Already in 1957, the Goldhaber experiment showed that neutrinos have a helicity of $H(\nu) = +1$ ("left-handed") and correspondingly antineutrinos of $H(\bar{\nu}) = -1$ ("right-handed") [20]. The charge conjugation C is responsible for the transition between particles and their anti-particles, through the transition of their corresponding quantum mechanical eigenstates. In the process, the sign of the electric charge changes, while mass, energy, momentum and spin (and thus helicity) remain unchanged between right- and left-handed particles and antiparticles. Considering the measurement of the Goldhaber experiment, the helicity leads to a violation of the charge conjugation C. Although the C and P are individually violated in the weak interaction, the combination of charge conjugation and parity CP is mostly conserved [13]. However, the first observed CP violation of quarks was found in the decay of neutral kaons by James Cronin and Val Fitch in 1964. They have shown that a long-lived kaon K_L^0 can decay not only into the CP-conserving state with three pions $CP = -1$ but also into the CP-violating state with two pions $CP = +1$ [21]. CP violation of quarks can be found within the complex phase of the CKM matrix (cf. Section 2.1). Given that neutrinos also participate in weak interactions, the question arises whether a comparable phase also exists in the lepton sector of the SM. The existence of such a phase would imply the need for a lepton mixing matrix and, in general, non-zero masses of neutrinos.

2.2.1 Neutrino masses

The first hint for a non-zero neutrino mass was already given in 1968 by Raymond Davis and John Bahcall during their measurements of the electron neutrino flux from the sun with the Homestake experiment. They detected only a third of the expected neutrino flux, which was called the solar neutrino problem [22]. Bruno Pontecorvo had already proposed the solution of that problem before the actual observation: the oscillation of the different neutrino flavors [23]. A prerequisite for those oscillations is the existence of neutrino mass eigenstates $|\nu_i\rangle$ with mass eigenvalues m_i ($i = 1, 2, 3$) determining the propagation of the neutrinos in vacuum. The flavor eigenstates $|\nu_\alpha\rangle$ ($\alpha = e, \mu, \tau$) of neutrinos are different from the mass eigenstates. They can be described as linear superposition of the mass eigenstates

$$|\nu_\alpha\rangle = \sum_{i=1}^{3} U_{\alpha i} |\nu_i\rangle\,, \tag{2.6}$$

where $U_{\alpha i}$ is the Pontecorvo-Maki-Nakagawa-Sakata (PMNS) matrix describing the transforma-

tion of the different neutrino flavors during their propagation. The mass eigenstates $|\nu_i\rangle$ propagate with different velocities, thus the superposition and the probability to detect a certain neutrino flavor $|\nu_\alpha\rangle$ changes periodically. The elements of the PMNS matrix describe this transformation

$$\begin{pmatrix} U_{e1} & U_{e2} & U_{e3} \\ U_{\mu 1} & U_{\mu 2} & U_{\mu 3} \\ U_{\tau 1} & U_{\tau 2} & U_{\tau 3} \end{pmatrix} = \begin{pmatrix} c_{12}c_{13} & s_{12}c_{13} & s_{13}e^{-i\delta} \\ -s_{12}c_{23} - c_{12}s_{23}s_{13}e^{i\delta} & c_{12}c_{23} - s_{12}s_{23}s_{13}e^{i\delta} & s_{23}c_{13} \\ s_{12}c_{23} - c_{12}s_{23}s_{13}e^{i\delta} & -c_{12}c_{23} - s_{12}s_{23}s_{13}e^{i\delta} & c_{23}c_{13} \end{pmatrix}, \tag{2.7}$$

where s_{ij} and c_{ij} refer to $\sin\theta_{ij}$ and $\cos\theta_{ij}$, with the mixing angle θ_{ij} and the phase δ [9]. Finally, in 2015, the Nobel Prize was awarded to Takaaki Kaijita and Arthur McDonald for the experimental evidence of neutrino oscillations and the corresponding non-zero neutrino mass [4, 5, 6]. Thus, for non-zero and non-equal mass eigenvalues m_i, the absolute eigenvalues of the PMNS matrix $|U_{\alpha i}|$ can be determined within 3σ ranges

$$|U_{\alpha i}| = \begin{pmatrix} 0.803 \sim 0.845 & 0.514 \sim 0.578 & 0.142 \sim 0.155 \\ 0.233 \sim 0.505 & 0.460 \sim 0.693 & 0.630 \sim 0.779 \\ 0.262 \sim 0.525 & 0.473 \sim 0.702 & 0.610 \sim 0.762 \end{pmatrix}, \tag{2.8}$$

with the corresponding mixing angles $\theta_{12} = 33.41^\circ\,^{+0.75^\circ}_{-0.72^\circ}$, $\theta_{23} = 49.1^\circ\,^{+1.0^\circ}_{-1.3^\circ}$ and $\theta_{13} = 8.54^\circ\,^{+0.11^\circ}_{-0.12^\circ}$ as reported in 2020 by Ivan Esteban et al. [24]. Still unsolved is the arrangement of the mass eigenvalues (mass hierarchy) and the zero or non-zero value of the phase δ (CP violation) in the PMNS matrix. Due to solar neutrino experiments it is shown that $m_2 > m_1$ but the arrangement of m_3 is still unknown. The so-called Normal Ordering (NO) $m_3 > m_2 > m_1$ would correspond to the masses of the appropriate charged lepton $m_\tau > m_\mu > m_e$, while the Inverted Ordering (IO) refers to $m_2 > m_1 > m_3$ [9]. The different possible orderings of the three neutrino mass eigenstates are shown in Figure 2.1.

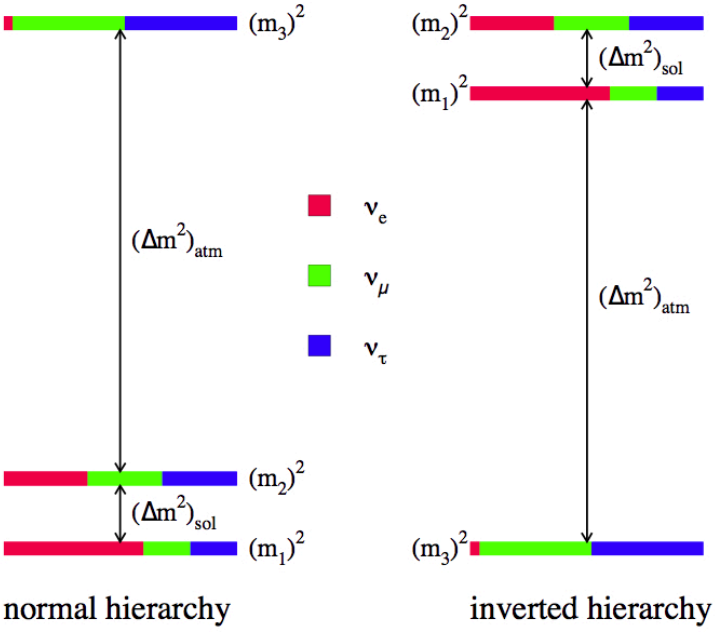

Figure 2.1.: Representation of the possible neutrino mass hierarchies. Adapted from [25].

Upcoming experiments to solve the question for the neutrino mass ordering are the Jiangmen Underground Neutrino Observatory (JUNO) in China and Hyper-Kamiokande in Japan, whereby Hyper-Kamiokande will also investigate the CP violation within the neutrino sector [26, 27]. Furthermore, it is not known yet whether neutrinos are Dirac or Majorana particles. If they are Majorana particles, additional mass terms will be introduced, as discussed in the following.

2.2.2 Dirac and Majorana neutrinos

Dirac particles are distinct from their antiparticles, whereas Majorana particles are identical to their antiparticles. In the SM, only left-handed neutrinos exist, which requires the extension of the model to accommodate a Dirac neutrino. Therefore, the investigation of the Dirac or Majorana nature of neutrinos requires an examination of their corresponding mass terms. This required considering the Lagrangian density $\mathcal{L}$, which describes the interactions and dynamics of the corresponding particles in space and time

$$\mathcal{L} = \bar{\psi}(i\gamma_\mu \frac{\partial}{\partial x_\mu} - m_D)\psi \,, \tag{2.9}$$

with the wavefunction ψ as spinor field of a free neutrino, the index $\mu = 1, 2, 3, 4$, the four-vector $x = (x_1, x_2, x_3, x_4)$, describing space and time, the Dirac matrices γ_μ, ensuring the Lorentz invariance of the Equation, and the Dirac mass m_D [13]. The spinor field ψ annihilates a lepton or creates an antilepton, while the conjugate field $\bar{\psi}$ does the opposite. The field ψ can be expressed

as a sum of the different chirality spinor fields $\psi = \psi_L + \psi_R$. Thus, the Dirac mass term $\mathcal{L}_D$ can be derived from Equation (2.9) to be

$$\mathcal{L}_D = m_D(\bar{\psi}_L\psi_R + \bar{\psi}_R\psi_L)\,. \tag{2.10}$$

Since the Dirac mass term left- and right-handed neutrinos couples left- and right-handed spinor components, it vanishes if either component is zero. Therefore, the existence of left- and right-handed neutrino components is necessary to generate a non-zero mass. To obtain the Majorana mass term $\mathcal{L}_M$, the charge-conjugated spinor field $\psi^c = C\psi C^{-1}$ removes the constraints of the pure Dirac mass term and leads to

$$\mathcal{L}_M = \frac{1}{2} m_M \bar{\psi}\psi^c + h.c.\,, \tag{2.11}$$

where m_M is the Majorana mass and $h.c.$ denotes the Hermitian conjugate. Here, the Majorana term $\bar{\psi}\psi^c$ is not invariant within global phase transitions, it violates the lepton number with $\Delta L = \pm 2$. The combination of Equation (2.10) and (2.19) leads to

$$2\mathcal{L}_{DM} = (\bar{\psi}_L\bar{\psi}_L^c)M\begin{pmatrix}\psi_R^c\\ \psi_R\end{pmatrix} + h.c.\,, \tag{2.12}$$

with the mass matrix M

$$M = \begin{pmatrix} m_L & m_D \\ m_D & m_R \end{pmatrix}. \tag{2.13}$$

In Equation (2.12) ψ_L and ψ_R^c refer to neutrinos involved in the weak interaction, with ψ_L representing left-handed neutrinos and ψ_r^c right-handed antineutrinos. However, ψ_L^c and ψ_R are not part of the SM, they are known as sterile neutrinos. The Grand Unified Theories (GUTs) provide different approaches of neutrino masses within Dirac and Majorana terms. Here, the coupling constants of strong and weak interaction are unified on the so-called GUT scale around 10^{15} GeV. In context of the GUTs, the seesaw-mechanism provides a theoretical model for understanding the relative sizes of the observed neutrinos masses. One of the simplest seesaw-type approaches gives a possible explanation for the small neutrino mass $m_L \approx 0$ in comparison to the heavy mass of the corresponding charged lepton of the same generation $m_R \approx 10^{15}$ GeV. Thus, the diagonalisation of the mass matrix M in Equation (2.13) leads to the mass eigenvalues $m_1 \approx m_R$ and $m_2 = m_\nu \approx m_D^2/m_R$. The mass eigenvalue m_1 corresponds to the heavy sterile neutrino on the GUT scale and m_2 to the relatively small neutrino mass. Since the neutrino mass term is considered to be of Majorana type within the seesaw mechanism, that approach provides further

evidence for the possible Majorana nature of neutrinos [9]. Should this hypothesis found to be correct, it could be experimentally supported by the detection of the $0\nu\beta\beta$-decay, which will be motivated and discussed in the following section.

2.3 Beta decay

In 1899, Ernest Rutherford first distinguished between α- and β-radiation, investigating their different penetration of objects and the capability of causing ionization [28]. Already one year later Henri Becquerel identified the emitted particle of the β decay to be an electron, which was found, in 1914, by James Chadwick to have a continuous energy spectrum [29, 30]. The continuity of the emission spectrum in the β decay, which occurs as three-body decay, includes the emission of a $\bar{\nu}_e$ as already shown in Equation (2.3). In this process, known as the β^--decay, a neutron transforms into a proton via the β^--decay and emits an electron and an electron antineutrino, which immediately leave the nucleus. Figure 2.2 shows the corresponding Feynman diagram.

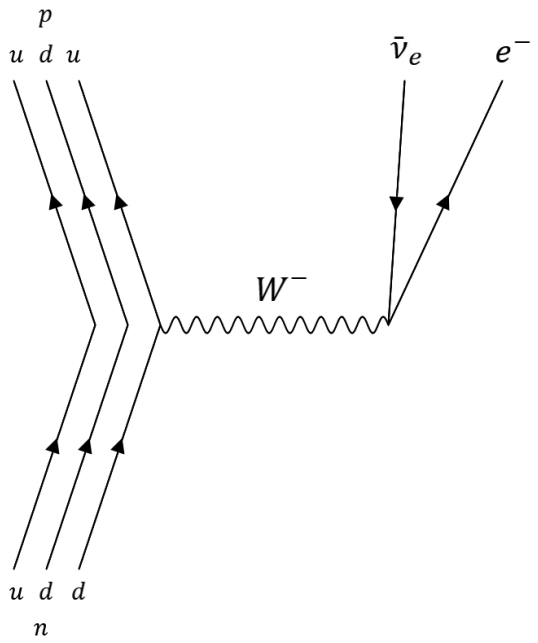

Figure 2.2.: Feynman diagram of a β^--decay, electron and electron antineutrino are mediated by a negatively charged W-boson.

In comparison during a β^+-decay a proton is converted into a neutron with the emission of a positron and an electron neutrino. A β decay is only possible if the energy of the parent nucleus exceeds the energy of the daughter nucleus produced in the decay [12]. However, there are certain isotopes, where the single β decay is energetically forbidden, but the simultaneous emission of two electrons is still allowed, known as $\beta\beta$-decays.

2.3.1 Double-beta decay

The first observed $\beta\beta$-decay (also written as $2\nu\beta\beta$-decay) was measured in 1950 at the decay from ^{130}Te into ^{130}Xe by John Reynolds [31]. It is described as a nuclear process changing the nuclear charge and therefore the atomic number Z of isobaric isotopes by two units and remaining the atomic mass number unchanged. These isotopes can be described as a function of Z using the Bethe-Weizsäcker formula

$$M(A = \text{const.}, Z) \propto c_1 + c_2 Z + c_3 Z^2 + \delta_P \,, \tag{2.14}$$

where c_1 is a constant describing the proton and neutron masses of the nucleus and the constant terms of the binding energy, c_2 and c_3 referring to the constants of the Coulomb and symmetry terms of the binding energy and δ_P to the pairing energy given to

$$\delta_P = \begin{cases} -a_P A^{-1/2} & \text{even-even nuclei} \\ 0 & \text{even-odd and odd-even nuclei} \\ +a_P A^{-1/2} & \text{odd-odd nuclei} \end{cases} \tag{2.15}$$

with the pairing term $a_P \approx 12\,\text{MeV}$ [32, 33]. This correlation can be represented in a mass parabola in which the mass of the nucleus is plotted against the atomic number. According to Equation (2.15), there is one parabola for odd A and two for even A separated by $2\delta_P$ shown in Figure 2.3. The $\beta\beta$-decay is observable, if the single β decay is energetically forbidden

$$M(Z+2, A) < M(Z, A) < M(Z+1, A) \,. \tag{2.16}$$

In the process, two β decays occur consecutively, resulting in continuous emission spectrum of the emitted electrons. These decays can be observed on both sides of the mass parabola ($\beta^-\beta^-$ on the left and $\beta^+\beta^+$ on the right side).

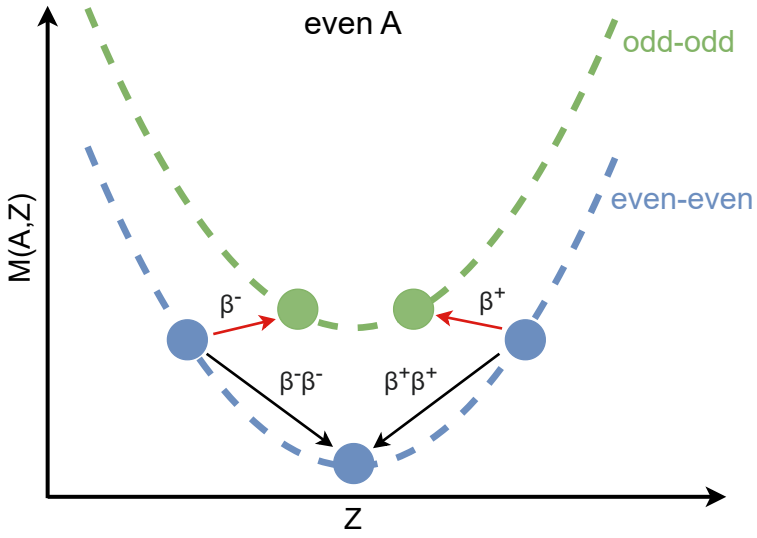

Figure 2.3.: Mass parabola as a function of the atomic number Z of an isobaric isotope participating in the $\beta\beta$-decay. The mass parabola is split into odd-odd and even-even nuclei with a distance of $2\delta_P$. The red arrows mark the energetically forbidden single β decay, whereas the black arrows show the corresponding $\beta\beta$-decays.

The $\beta^-\beta^-$-decay is part of the weak interaction of second order, where the parent nucleus decays into the daughter nucleus, two electrons and electron antineutrinos

$$M(A,Z) \rightarrow D(A,Z+2) + 2e^- + 2\bar{\nu}_e \,. \tag{2.17}$$

In the $\beta^+\beta^+$-decay, two protons are converted into two neutrons under the emission of two positrons and two electron neutrinos. The $\beta\beta$-decay conserves the lepton number and is part of the SM. Nevertheless, it occurs much less frequently than single β decay with half-lives of the order of $> 10^{19}$ yr. Up to now, 35 $\beta\beta$-decay emitters are known [13]. However, another $\beta\beta$-decay mode could be possible without the emission of any neutrinos: the $0\nu\beta\beta$-decay, which is part of current experimental efforts.

2.3.2 Neutrinoless double-beta decay

In the $0\nu\beta\beta$-decay, the mother nuclei decay into the daughter nuclei under the emission of two electrons (for $0\nu\beta^-\beta^-$) or two positrons (for $0\nu\beta^+\beta^+$) without the emission of any neutrinos

$$M(A,Z) \rightarrow D(A,Z+2) + 2e^- \,. \tag{2.18}$$

That decay mode violates the lepton number conservation and thus, is forbidden in the SM. The $0\nu\beta\beta$-decay can be understood as two subsequent decays. First, a neutron decays into a proton, emitting an electron and a right-handed electron antineutrino. That electron antineutrino is absorbed within the same nucleus (under the emission of a second electron) of a second neutron as a left-handed electron neutrino. Thus, the prerequisite for this decay mode is a Majorana nature of neutrinos. Additionally, a non-zero neutrino mass is required for a helicity matching of the emitted neutrinos. With a non-zero mass, neutrinos have a left-handed and a small right-handed component, necessary to allow the $0\nu\beta\beta$-decay. This mass is known as the effective Majorana neutrino mass $m_{\beta\beta}$, can be derived from the measured half-life and is defined as

$$m_{\beta\beta} = \left| \sum_i U_{ei}^2 m_i \right| , \tag{2.19}$$

where U_{ei}^2 are the PMNS matrix elements with the corresponding mass eigenvalues m_i (cf. Section 2.2.1) [13]. Figure 2.4 shows the Feynman diagram of a $0\nu\beta^-\beta^-$-decay, where two neutrons decay into two protons mediated by a W^--boson, emitting two electrons. The virtual Majorana neutrino emitted at the first vertex is then annihilated at the second vertex with its own antiparticle [13].

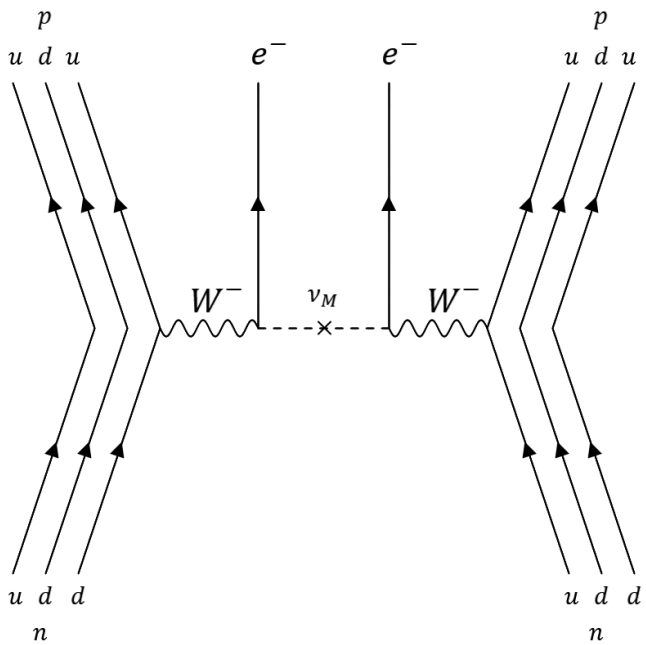

Figure 2.4.: Feynman diagram of $0\nu\beta\beta$-decay of two neutrons into protons and two electrons mediated by negatively charged W-bosons. The two Majorana-like neutrinos ν_M annihilate themselves.

The $0\nu\beta\beta$-decay has not yet been observed. A discovery of the $0\nu\beta\beta$-decay would demonstrate the Majorana nature of neutrinos. There are experimental programs searching for the $0\nu\beta\beta$-decay using different isotopes, among others ^{136}Xe, ^{128}Te or ^{76}Ge. In the case of ^{76}Ge, the isotope would decay into ^{76}Se with the emission of two electrons: $^{76}\text{Ge} \rightarrow ^{76}\text{Se} + 2e^-$. The expected endpoint energy or Q-value, as discussed in Section 2.2, would be at 2039 keV, shown by a monoenergetic line in the corresponding spectrum of the total kinetic energy (cf. Figure 2.5), since the sum of the kinetic energy of the emitted electrons is strictly defined by the difference of the masses of the nuclei before and after the decay [9].

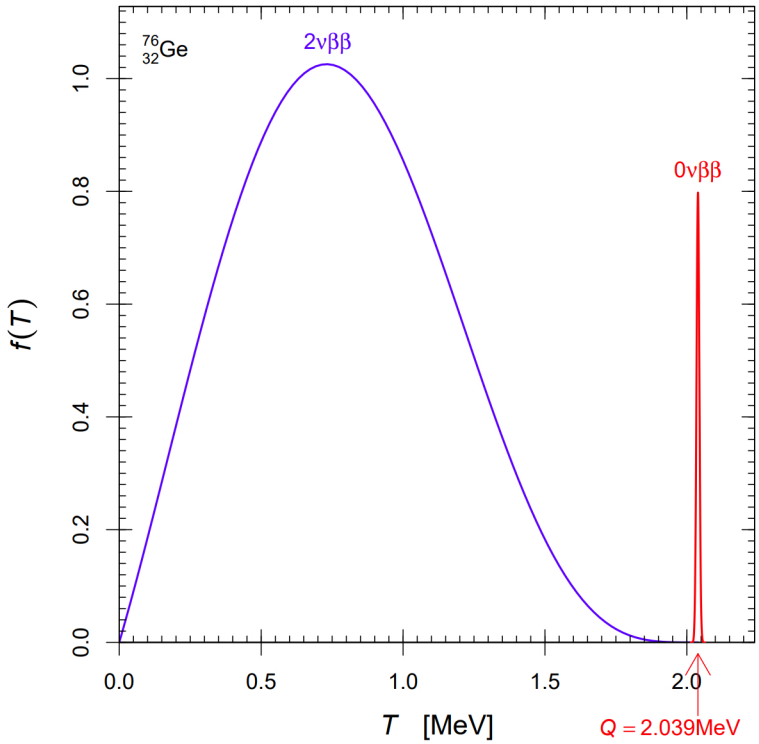

Figure 2.5.: Expected total kinetic energy spectrum of $2\nu\beta\beta$- and $0\nu\beta\beta$-decay of ^{76}Ge. Adapted from [34].

Experiments looking for the presence of this line face many challenges. Due to the extreme rarity of the $0\nu\beta\beta$-decay in ^{76}Ge, with a half-life on the order of at least 10^{28} yr, the background must be known precisely in order not to mistakenly assign a background signal to the $0\nu\beta\beta$-decay [13]. One of the experiments dedicated to the search for the $0\nu\beta\beta$-decay in ^{76}Ge is the LEGEND experiment, which will be discussed in detail in the following chapter.

Chapter 3

Overview of the LEGEND experiment

"One is always a long way from solving a problem until one actually has the answer."

— Stephen Hawking

The detection of $0\nu\beta\beta$-decay would represent a milestone in neutrino physics, as it would indicate the Majorana nature of neutrinos. The LEGEND experiment is a two-phase research program dedicated to the search for $0\nu\beta\beta$-decays in enriched ^{76}Ge. The experiment utilizes HPGe detectors, which act as both source and detector. The improvement of the full setup is crucial for a better discovery sensitivity and achieving more effective background suppression through a combination of active and passive detector systems. At the time of writing, the ongoing LEGEND-200 phase serves as a demonstrator for the future phase LEGEND-1000, which holds potential for significant discoveries.
This chapter presents an overview of the LEGEND experiment, outlining its key goals, providing an insight in the experimental setup and concluding with the description of the operating and future experimental phase.

3.1 Goal of the LEGEND experiment

LEGEND is a phased experimental program aimed at the search for the $0\nu\beta\beta$-decay of ^{76}Ge at LNGS in Italy. It comprises of two experimental phases (see Section 3.3) with different detector masses: LEGEND-200 and LEGEND-1000. In this chapter, the goals of LEGEND-1000 are treated as the final objectives of the LEGEND experiment, as they currently define the intended endpoint of the experimental program. The experiment combines the experience of the researchers of the MAJORANA and the GERmanium Detector Array (GERDA) collaborations,

using enriched Germanium as detector material. The projected discovery sensitivity (DS) corresponds to a $0\nu\beta\beta$-decay half-life of $T_{1/2}^{0\nu} = 1.3 \cdot 10^{28}$ yr at a 99.7 % confidence level (CL). In this context, the discovery sensitivity refers to the half-life at which a 3σ discovery is expected with a 50 % probability. A BI of less than $1 \cdot 10^{-5}$ cts/(keV · kg · yr) (corresponding to the background per unit exposure) or less than 0.025 cts/(FWHM · t · yr) (referring to the background within the energy resolution of the detector) is necessary to achieve this goal and to detect the $0\nu\beta\beta$-decay signal above the background signal in the ROI. Here, the ROI is an energy range around the expected Q-value equal to many multiples of the detector resolution at $Q_{\beta\beta} = 2039$ keV (cf. Section 6.4.1). Figure 3.1 shows the DS as a function of the exposure and the corresponding background levels. It demonstrates that the BI reaches the sensitivity of the minimal possible Majorana mass of neutrinos allowed in the IO [7].

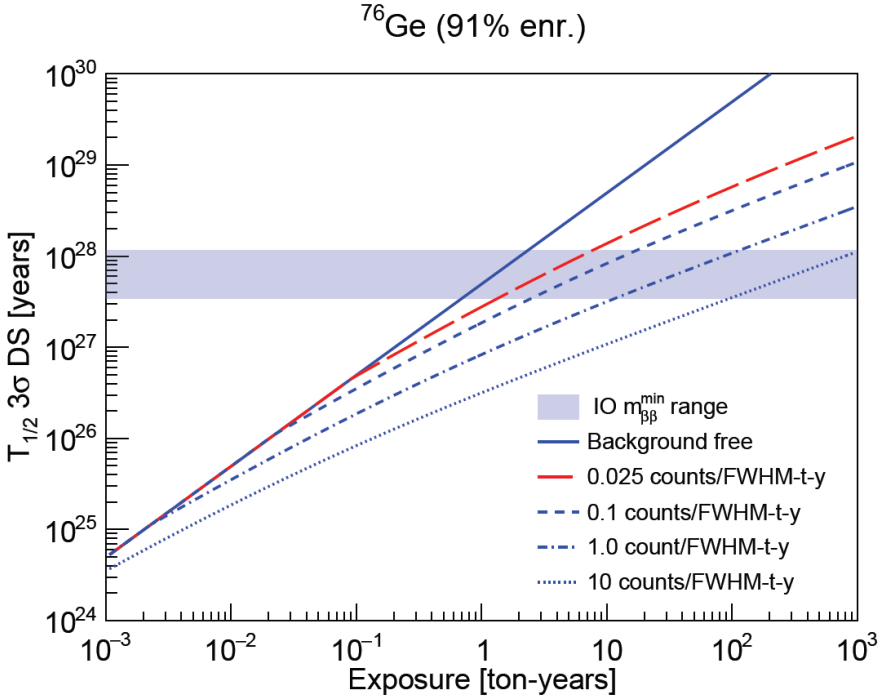

Figure 3.1.: DS to a $0\nu\beta\beta$ decay signal in ^{76}Ge as a function of exposure and BI at a 3σ CL (99.7 %). The blue lines refer to different background levels, whereas the red dashed line shows the aimed LEGEND BI. The horizontal blue range indicates the minimal possible mass value of a Majorana neutrino according to Equation (2.19) in the IO. Adapted from [7].

Achieving the aimed DS and the corresponding BI requires high detector resolution as well as both passive and active background shielding. The experimental setup intended to fulfill these requirements will be described below.

3.2 Experimental setup

The LEGEND experiment is located at the LNGS in Italy and is therefore shielded by a 3500 m water equivalent (m.w.e.) rock overburden, which reduces the flux of cosmic rays at the experiment. Figure 3.2 shows a schematic representation of the current LEGEND setup of the LEGEND-200 experimental phase. It utilizes HPGe semiconductor detectors enriched to 91 % in ^{76}Ge, which function both as decay source and detection material. The HPGe detectors are arranged in strings and surrounded by wavelength shifting (WLS) polystyrene fibers connected to Silicon Photomultiplier (SiPM) detector arrays and forming the LAr instrumentation, which provides a shielding against background sources, mainly due to the radioactivity near the HPGe array. HPGe detectors and LAr instrumentation operate within a vacuum-insulated cryostat filled with cryogenic LAr. The background sources deposit energy in the LAr, causing it to scintillate and emit 128 nm ultraviolet photons, guided by the WLS fibers to the SiPMs, where they are detected. By shifting the scintillation photons towards the visible spectrum, the WLS fibers enable more efficient detection by the SiPMs. The cryostat is embedded in a water tank including a water Cherenkov system, called the muon veto, which uses PMTs as light detectors and acts as shielding against cosmic muons.

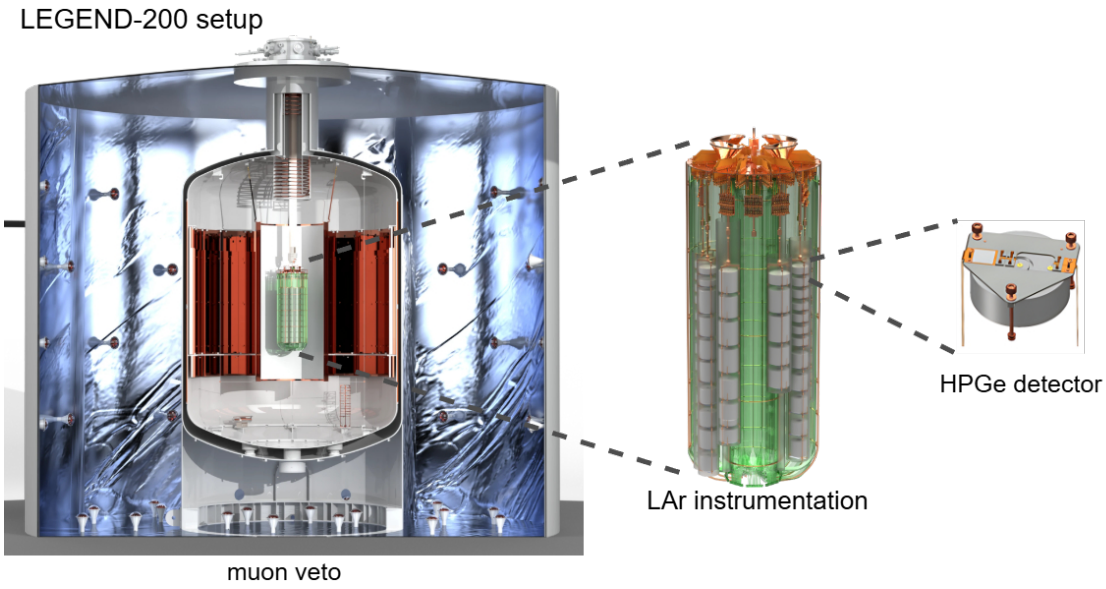

Figure 3.2.: Schematic representation of the LEGEND-200 setup, showing the whole setup including the water tank system with the muon veto on the left, the LAr instrumentation with green WLS fibers in the middle and a single HPGe detector on the right. Image courtesy of the LEGEND collaboration and adapted from [35].

In the following, the core component, the HPGe detectors, is discussed more detailed.

3.2.1 High-purity Germanium detectors

HPGe detectors are semiconductor devices made from ultrapure Germanium mono-crystals and are mainly used for gamma and X-ray spectroscopy. Semiconductors are characterized by an energy band structure with an energy gap of around 1 eV between the conduction and valence bands. If the energy gap is higher than 5 eV, the material is called an insulator, whereas with the overlap of conduction and valence band, materials are known as conductors. In the case of Germanium the width of the energy gap is given by the spacing of the lattice between the atoms of the material and is thus dependent of the pressure and temperature of the crystal and is found to be 0.665 eV [36, 37]. Incident energy can excite a valence electron of the crystal into the conduction band, leaving behind a hole, resulting together in an electron-hole pair. Thus, the conduction band is characterized by an excess of free electrons, resulting in a negative charge, whereas the valence band is defined by the absence of electrons and resulting in a positive charge. The holes can also move in the valence band with electrons jumping from their position into the hole and leaving behind another hole. This results in two possibilities of electric current carriers in semiconductors: the movement along the field lines of the free electrons in the conduction band and that of the holes in the valence band [36].
Among other sources, such as ionising radiation, thermal energy can produce electron-hole pairs, which can recombine under the emission of a photon. This direct recombination can only occur if the momentum and energy are conserved and therefore require specific electron and hole energies. However, impurities in the crystal can disturb the energy band gap by the addition of levels in between the band gap promoting the recombination. For that reason a high purity level of the semiconductor crystal and low operating temperatures are necessary to minimize the production of thermally generated electron-hole pairs and their recombination. Thus, HPGe detectors are operated at 77 K and the crystals must possess an impurity level of less than 10^{10} atoms/cm^3.
The desired signal is produced by electron-hole pairs created by excitation due to ionising radiation. Using lithium diffusion for a n^+ ohmic contact on the conduction band side and boron implantation for a p^+ ohmic contact on the valence band side, the surfaces get electrodes. Both electrodes are separated from each other by grooves or a passivation layer to avoid electrical short-circuits. With the application of an electric field, electrons and holes can travel toward the electrodes and a current can thus be measured. The Shockley-Ramo theorem can be applied to calculate the induced charge, and thus the energy of the radiation generating the observed current

$$i = q\vec{v} \cdot \vec{E}_0 \,, \tag{3.1}$$

where i refers to the instantaneous current on the electrode, q corresponds to the charge and $\vec{v}$ to the velocity of the carrier and $\vec{E}_0$ is known as the weighting field, which quantifies the contribution of the respective charge carrier to the electrode signal.

The electrical conductivity of the detector material can be increased by doping it with donor or acceptor impurities. Doping involves intentionally adding a certain type of atom to the crystal lattice of the detector material. These added atoms may have five or three valence electrons, resulting in n-type or p-type semiconductors. The fifth electron in n-type semiconductors is less strongly bound and can therefore be released from its bond with small amount of energy without creating a hole. Correspondingly, within p-type semiconductors there are unsaturated bonds and, thus holes added with the acceptor impurities. If an electron fills that hole, it is bound with less energy than in a typical bond within the detector material, since the acceptor impurity is trivalent, thereby introducing discrete energy levels within the band gap [37].
The LEGEND experiment uses p-type HPGe detectors with four different geometries, contact structures and electric field lines (cf. Figure 3.3). They can be distinguished in detectors of semi-coaxial (Coax), Broad Energy Germanium (BEGe), p-type point contact (PPC) and Inverted Coaxial Point Contact (ICPC) type.

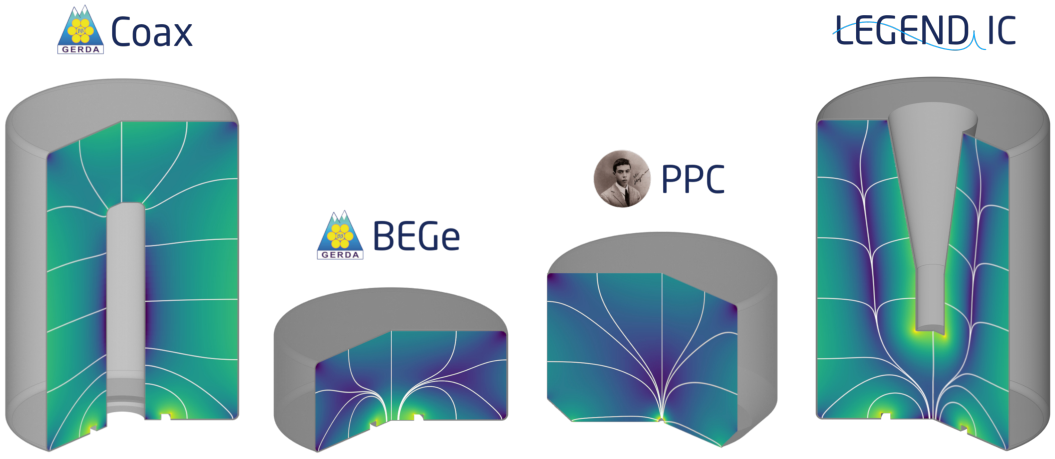

Figure 3.3.: Different geometries and field lines of the Coax, BEGe, PPC and ICPC HPGe detectors (from left to right) used by the LEGEND experiment. Image courtesy from the LEGEND collaboration.

Coax detectors The Coax detectors used in the experiment were previously used during the GERDA experiment, each with a detector mass of approximately 2 to 3 kg. Their borehole, which extends over almost the entire length of the detector, possesses the p^+ contact, whereas the n^+ contact occupies the outer surface of the detector. This geometry leads to a strong, homogeneous field in z-direction of the detector, but also shows a dependency of the pulse shape on the location of the charge generation in the detector, resulting in challenges for the energy resolution [38, 39].

BEGe and PPC detectors The BEGe (GERDA) and PPC (MAJORANA) detector design are similar to each other. Unlike the Coax detectors they only reach a detector mass of around 1 kg and have a small, in case of PPC point-like, p^+ contact. The n^+ contact covers the remaining detector surface. With the minor p^+ contact also leads to a small readout capacitance, enabling the operation with low electronic noise levels and a possible pulse-shape analysis of the detector signals, resulting in excellent energy resolution over a wide energy range [40, 41].

ICPC detectors The ICPC detectors combine the higher detector mass of the Coax detectors with the signal precision of the BEGe and PPC detectors, featuring a large borehole and a point-like p^+ contact on the opposite side. The n^+ contact covers the remaining surface, including the borehole of the detector. Since a higher detector volume leads to more inhomogeneous electric fields and a higher noise due to the higher drift time of the electrons within the detector, a detector mass from 1.5 to 4 kg is possible. The ICPC detectors enable an excellent energy resolution and pulse-shape analysis [42].

Due to tests, outages and new detector productions, the number of HPGe detectors changes in between and throughout the phases of the LEGEND experiment and there are also modifications to the whole experimental setup. The corresponding phases will be the subject of the following section.

3.3 Two-phase experiment

In order to reach a sensitivity required for the discovery of the $0\nu\beta\beta$-decay, the LEGEND experiment is structured in two phases: the current operational LEGEND-200 phase and the planned large-scale LEGEND-1000 phase. LEGEND-200 serves as an intermediate phase and demonstrator to the future LEGEND-1000.

3.3.1 Ongoing operational phase: LEGEND-200

At the time of writing, the ongoing experimental phase, LEGEND-200, aims to deploy 200 kg of HPGe detectors and builds upon the existing infrastructure of the GERDA experiment with necessary modifications, already in preparation for the requirements of LEGEND-1000. In order to reach the target detector mass 70 kg of HPGe detectors from GERDA and MAJORANA are used, and 130 kg ICPC detectors will be produced and added in LEGEND-200. The subsystems of LEGEND-200 are, except of the introduction of an additional neutron tagging system (cf. Section 3.3.2), similar to the planned systems for LEGEND-1000 and since the detector array can be lifted and lowered into the cryostat within a few days, single components can be tested and exchanged in a short time-scale in LEGEND-200.
After five years of operations a half-life sensitivity of $T^{0\nu}_{1/2} = 10^{27}$ yr with a corresponding BI

of $2 \cdot 10^{-4}$ cts/(keV · kg · yr) is planned to be reached with LEGEND-200. To achieve that goal, several improvements lowering the background level are made in LEGEND-200 with respect to GERDA and MAJORANA. The increased detector mass achievable with the ICPCs reduces the need for some additional components such as cables and holders, which would contribute to the radioactive background. Furthermore, materials with a lower level of radioimpurities and an improved, purer design for the scintillation light readout were developed [7].
LEGEND-200 started the first physics data taking period in mid-March 2023 with a total detector mass of 142 kg whereas 130 kg were operational. After one year of valid data taking, at the beginning of May 2024, data taking of LEGEND-200 was stopped to repair the 12 kg of non-usable HPGe detectors and deploy more detector mass. In mid of 2025, LEGEND-200 resumed physics data taking.

3.3.2 Future large-scale phase: LEGEND-1000

The LEGEND-1000 experiment will be constructed in Hall C at the LNGS deploying 1000 kg of detector mass using exclusively ICPC detectors. With the increase in detector mass, other components such as the LAr instrumentation, the cryostat and the muon veto system within the water tank will be scaled up. The aimed half-life sensitivity of $T_{1/2}^{0\nu} = 1.3 \cdot 10^{28}$ yr with the BI of less than $1 \cdot 10^{-5}$ cts/(keV · kg · yr) will be achieved by using improved techniques from LEGEND-200 and additional neutron tagging systems to detect muon-induced background events in the cryostat and water tank. Figure 3.4 shows the baseline design of the LEGEND-1000 detector systems.
At the time of writing, the design is still under heavy development. To lower the background level, it is planned to operate the HPGe detectors in four independent modules of 250 kg each immersed in radiopure underground liquid argon (UGLAr). Since UGLAr is sourced from a deep underground CO_2, it has a lower ^{42}K, a progeny of ^{42}Ar, level, causing additional background due to β decays. The UGLAr modules are surrounded by atmospheric-sourced LAr for additional light collection, all within a vacuum-insulated cryostat [7]. A neutron moderator is proposed to operate within both LAr volumes consisting of poly(methyl methacrylate) (PMMA) panels connected to the SiPMs of the LAr instrumentation. By neutron capture in ^{76}Ge muons can in-situ produce $^{77(m)}$Ge, which can decay with $0\nu\beta\beta$-like energies and is not covered by the detector systems of LEGEND-200. Thus, the neutron moderator system of LEGEND-1000 primarily slows down neutrons from such muon-induced interactions, reducing the production of $^{77(m)}$Ge in the HPGe detectors. Additionally, it provides a readout for scintillation light produced in the LAr volume [43]. The cryostat is embedded in a water tank including the muon veto system and additionally, a neutron tagger is integrated. The neutron tagger is designed to detect muon-induced neutrons before they reach the HPGe detectors, providing an active veto against neutron-induced backgrounds.
The design phase of the LEGEND-1000 experiment is currently heavily developed. The construc-

tion is scheduled to begin in 2026, while the first data taking phase expected to start in 2030. A total of ten years of data acquisition is anticipated. Through the start of LEGEND-1000 operations, LEGEND-200 will continue data taking.

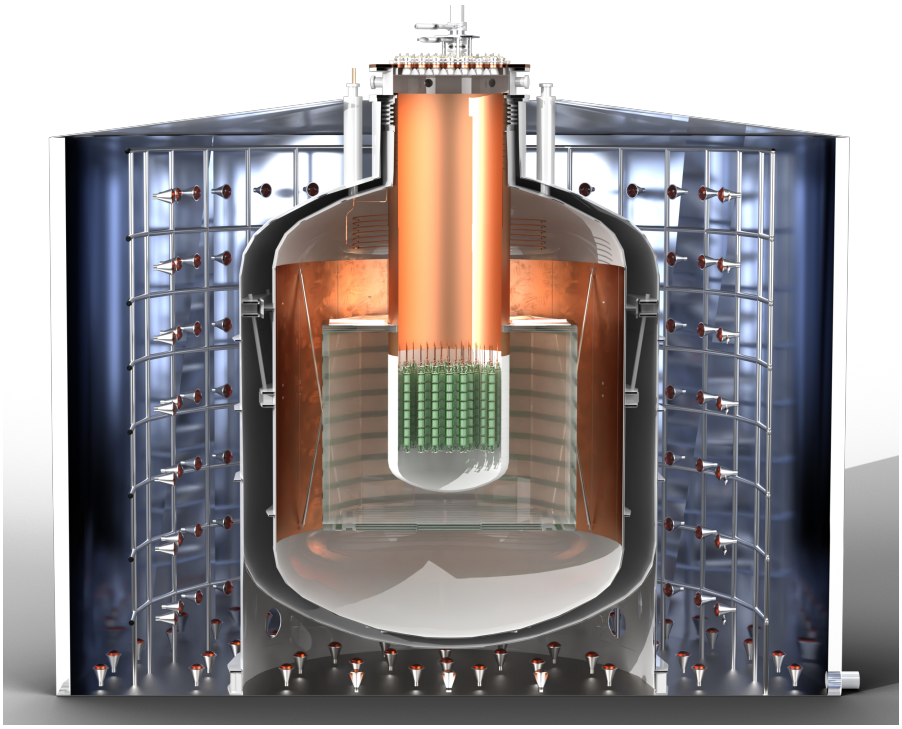

Figure 3.4.: Schematic representation of the planned baseline design for LEGEND-1000. The main components from the outermost to the innermost are the water tank including the muon veto system (PMTs on the bottom), the neutron tagger (PMTs at the scaffolding) of the water tank, the cryostat, the PMMA neutron moderator, the LAr instrumentation and HPGe detector strings. Image courtesy of the LEGEND collaboration.

In both experimental phases, the shielding systems of LEGEND are essential for achieving the desired background level. Therefore, continuous advancements are being made to the LAr instrumentation and the muon veto system. The following chapter discusses the different background sources and the rejection mechanisms and systems of the LEGEND experiment.

Chapter 4

Background sources and rejection of the LEGEND-200 experiment

"Nothing in life is to be feared. It is only to be understood."

— Marie Curie

The sensitivity of the LEGEND experiment to the half-life of $0\nu\beta\beta$-decay critically depends on the suppression of background events. Even rare interactions are able to superimpose the $0\nu\beta\beta$-decay signal, making the identification and rejection of such events essential. To achieve this, the LEGEND experiment uses a combination of analysis methods, as well as passive and active veto techniques and systems, to suppress cosmogenic and radiogenic background.
This chapter will discuss the various background sources as well as the rejection mechanisms and systems of the LEGEND-200 experiment.

4.1 Background sources

In order to achieve the target half-life sensitivity of the LEGEND-200 experiment, it is essential to understand and characterize the background. The BI must be reduced to less than $2 \cdot 10^{-4}$ cts/(keV $\cdot$ kg $\cdot$ yr) (cf. Section 3.3.1). To accomplish this, a detailed understanding of the background sources is required. For the LEGEND experiment, the primary sources can be broadly categorized into two main groups: cosmogenic and radiogenic. The cosmogenic background results from the interactions of cosmic rays with components of the atmosphere and can contribute both directly and indirectly, for instance through secondary neutron production. Radiogenic background originates from the materials used in the experiment or naturally occurring isotopes in the surrounding environment. The specific background contributions from these sources are described in more detail below.

4.1.1 Cosmogenic sources and particle showers

Cosmic radiation consists of relativistic particles traveling through space originating from the Sun, other regions of the Milky Way and from distant galaxies. The composition of the cosmic rays is dominated by protons ($\sim 90\,\%$), followed by alpha particles ($\sim 9\,\%$), with heavier nuclei making up about 1 % and electrons contributing less than 1 %. When cosmic rays interact with the Earth's atmosphere, they create secondary particles in a particle shower. Thereby, the incoming particle collides with a particle of the atmosphere, such as oxygen or nitrogen. In this process, a cascade consisting of lighter particles such as photons (electromagnetic cascade), hadrons (hadronic cascade) and mesons including pions and kaons, and consequently muons (muonic cascade), can be produced. These particles are known as secondary cosmic particles and travel towards the Earth's surface [44].

Electromagnetic cascade An electromagnetic cascade is produced mainly by two processes: pair production and bremsstrahlung. Pair production is the generation of a particle and its antiparticle from a neutral boson, which must possess an energy higher than the rest mass energy of the created particles due to energy conservation. For highly energetic photons (energies in MeV scale and higher), pair production is the dominant interaction with matter. In this process, the energy of the photon near a nucleus, which receives a recoil for momentum conservation is converted into an electron-positron pair. The high energetic electrons and positrons emit photons via bremsstrahlung, where electromagnetic radiation is produced when charged particles are decelerated in the electric field of a nucleus. In this process, the charged particle loses kinetic energy, which is emitted as photons. When a high energetic particle, such as photons, electrons or positrons, is produced within a particle shower, it can initiate an electromagnetic cascade. This shower is dominated by pair production and bremsstrahlung. The cascade continues, with particles losing energy at each step, until low-energy scattering processes dominate and the shower gradually dissolves.

Hadronic cascade Hadronic cascades involve nuclei and other highly energetic hadrons decaying or interacting with each other. At each hadronic interaction about a third of the energy goes into electromagnetic cascades. Most of the hadrons re-interact, resulting in most of the primary energy ending up in the electromagnetic component [44].

Muonic cascade Muonic cascades arise from the dominant pion or kaon decay modes within a particle shower. Thereby, more than 99 % of charged pions and over 63 % of charged kaons decay into muons with the corresponding neutrinos $\pi^{\pm} \rightarrow \mu^{\pm} + \nu_{\mu}(\bar{\nu}_{\mu})$ and $K^{\pm} \rightarrow \mu^{\pm} + \nu_{\mu}(\bar{\nu}_{\mu})$. The produced muons are relativistic and have a mean life-time of $\tau_{\mu} \approx 2.1969811 \cdot 10^{-6}$ s, resulting in travel distances to the Earth's surface and beyond [44, 45]. At sea level they are the most abundant charged particles with a flux of approximately $70\,\mathrm{m}^{-2}\mathrm{s}^{-1}\mathrm{sr}^{-1}$ for muon energies above 1 GeV. The mean energy of muons at sea level is about 4 GeV [46].

When traversing an optically transparent medium, such as water, these fast muons can emit Cherenkov radiation. This occurs when an electrically charged particle travels faster than the phase velocity of light in the medium $\beta n > 1$, where β is the ratio of the velocity of the particle in the medium v to the speed of light in vacuum c [37]. Cherenkov light is emitted via an electromagnetic shock wave with a conical wavefront at the Cherenkov angle $\cos(\theta) = 1/\beta n$, measured with respect to the particle trajectory [36].

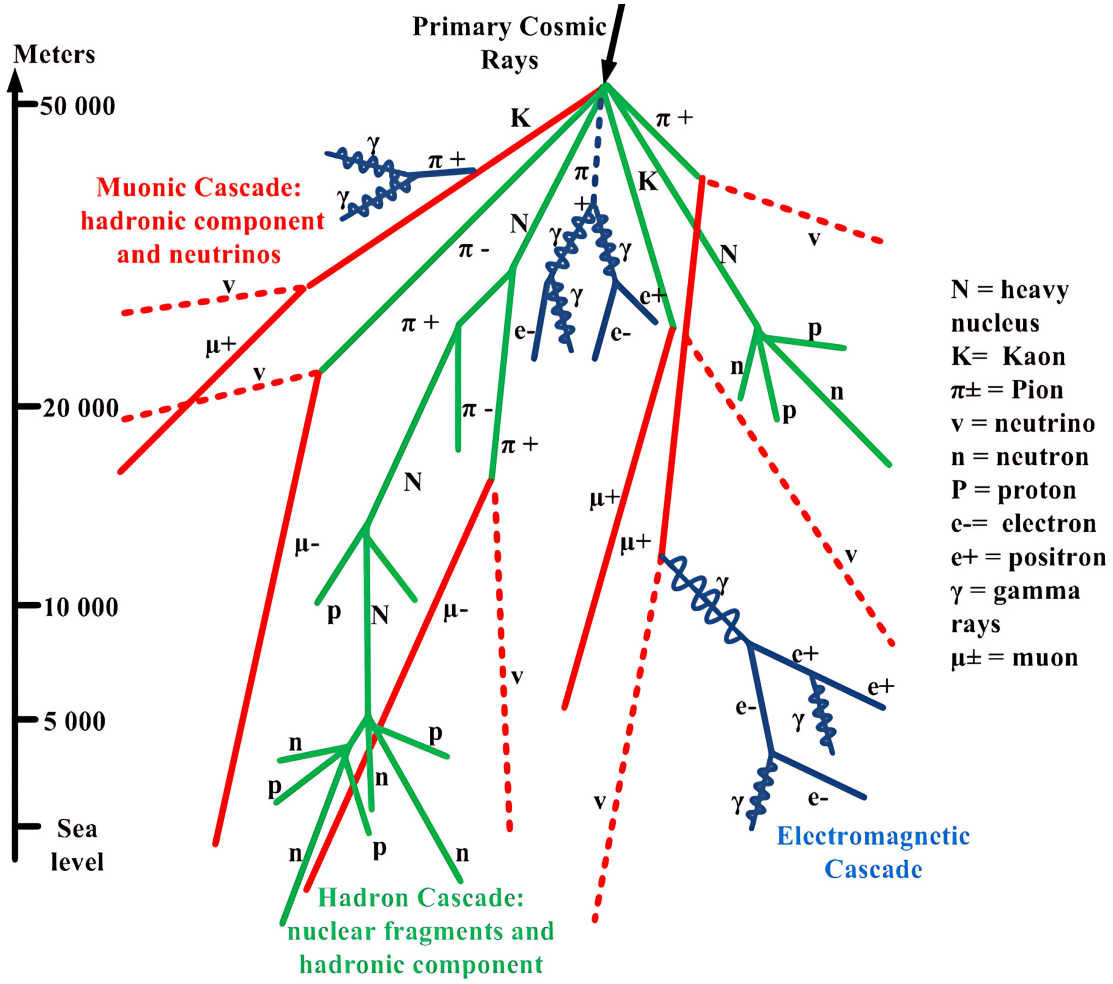

Figure 4.1.: Different types of cascades (muonic in red, hadronic in green and electromagnetic cascades in blue) produced by interactions of cosmic rays with particles in the atmosphere. Adapted from [47].

These penetrating muons, unlike electromagnetic or hadronic cascades which are mostly absorbed before reaching the LNGS, can reach the LEGEND experiment and cause both prompt and delayed backgrounds. Prompt background originates from direct interactions of muons in the detector components. Additionally, muons can produce nuclei in-situ whose decays can cause a delayed muon-induced background in the experiment. In such cases, a muon enters the experi-

ment and interacts with nuclei in the materials, such as the water or the cryostat. Particle showers can, in addition to the mechanisms discussed, be initiated by bremsstrahlung, pair production, and direct interactions of the muons with nuclei, such as spallation or inelastic scattering, which can result in pion- and kaon-production. These muon-induced particle showers can produce neutrons via spallation or photo-nuclear reactions, where the photons produced by bremsstrahlung excite a nucleus, which is then emitting a neutron [7]. These neutrons can be moderated in the surrounding materials, such as water, and subsequently captured by the ^{76}Ge of the detectors, leading to the metastable ^{77m}Ge, which has a half-life of about 53.7 s decaying into its ground state ^{77}Ge or ^{77}As [48, 49]. This process results in a background contribution in the ROI of $(1.1 \pm 0.2) \cdot 10^{-4}$cts/(keV $\cdot$ kg $\cdot$ yr) in a GERDA-like geometry. The energy of these events can lie within $\pm$100 keV of $Q_{\beta\beta}$ and thus, generate $Q_{\beta\beta}$-like signals [49]. Therefore, it is crucial for the LEGEND experiment to identify the muons and muon-induced backgrounds.
Additionally, cosmic ray exposure can lead to the production of different isotopes in the Germanium of the detectors or the atmospheric argon, for instance via spallation. During the fabrication process of the HPGe detectors, cosmic particles can induce the formation of ^{60}Co and ^{68}Ge in ^{76}Ge. The decays of both isotopes can contribute to the background of the experiment. If the two coincident γ rays at 1173 keV and 1333 keV emitted after the β decay of ^{60}Co are fully absorbed, their summed energy can contribute to the region around $Q_{\beta\beta}$. In order to minimize this background, fabricated detectors are stored underground so that short-lived isotopes, such as ^{68}Ge, can decay before deployment. In some cases the progeny ^{42}K of ^{42}Ar, produced by cosmic ray exposure of argon, can also produce $Q_{\beta\beta}$-like signals within β decays [7].

4.1.2 Radiogenic sources and environmental backgrounds

Radioactive isotopes of natural origin are present both in the construction materials of the LEGEND experiment and in the surrounding environment. The α-, β-, or γ-decays of the isotopes contribute to the measured energy spectrum of the HPGe detectors. The $2\nu\beta\beta$-decay of ^{76}Ge is the dominant background source below $Q_{\beta\beta}$. Additionally, isotopes of terrestrial origin with long half-lives such as ^{238}U, ^{232}Th and ^{40}K are expected to be present in the components due to the manufacturing process, contributing to the background up to energies of 3000 keV. This results in the decay chains of ^{238}U and ^{232}Th decaying through shorter-lived progenies up to the stable lead isotopes ^{206}Pb and ^{208}Pb. Within these decay chains, the isotopes ^{214}Bi and ^{208}Tl occur, which produce high-energy γ rays capable of Compton scattering off electrons in the ROI. The γ rays of ^{40}K do not contribute in the ROI, but have an impact on the analysis of lower energies in the spectrum and thus, on the analysis and background models of the measured energy spectrum [50]. During the fabrication and assembly of the detectors, surface impurities such as ^{210}Po and ^{210}Pb may be introduced through dust deposition or the implantation of ionized progeny from ^{222}Rn decay. These surface alphas can lead to background events above 3500 keV through the emission

of high-energy α particles with energies ranging from 3500 keV to 5300 keV. Since the α particles may deposit only a fraction of their energy within the detector volume, they can also cause signals in the ROI.
In addition, materials outside the detector array, such as the stainless steel of the cryostat and the water tank or components in the laboratory can cause background in the spectrum through γ rays or neutrons. The main contributor from the stainless steel is the 2615 keV γ ray from the ^{208}Tl decay of the ^{232}Th chain with an activity of approximately 1 mBq/kg leading to a background contribution of around $1.1 \cdot 10^{-5}$cts/(keV $\cdot$ kg $\cdot$ yr) [7, 51]. In addition, α particles occurring in the ^{238}U and ^{232}Th decay chains of the stainless steel can produce neutrons via (α, n) reactions, where an α-particle interacts with a nucleus emitting a neutron [52]. As neutrons produced by a particle shower (see Section 4.1.1), they can be captured on ^{76}Ge resulting in the metastable $^{77\mathrm{m}}$Ge, which can contribute to the ROI through its decay to the ground state ^{77}Ge with about $2 \cdot 10^{-7}$cts/(keV $\cdot$ kg $\cdot$ yr). The water tank and surrounding laboratory, including the enclosing rock, contribute γ rays, mainly via ^{208}Tl decays, since it is a daughter isotope of ^{232}Th occurring naturally in water and rock [7].
In order to tag the different background signals, various background rejection techniques have been developed in the LEGEND experiment as discussed in the following.

4.2 Passive background rejection

To reduce the background level in the HPGe detectors from external sources, LEGEND uses several passive shielding techniques. The experiment is located at the LNGS, shielded by 3500 m.w.e. of rock overburden provided by the Gran Sasso massif. Therefore, the muon flux is reduced by a factor of $\sim 10^6$, resulting in a residual rate of $\sim 3.4 \cdot 10^{-4}$ /(s m^2) with a mean muon energy of $\langle E_\mu \rangle = 270$ GeV [53].
Further shielding is provided by the water volume of the muon veto and the LAr inside the cryostat, which both attenuate external γ rays and moderate neutrons originating from the surrounding rock and structural materials, such as stainless steel. The moderation reduces the number of fast neutrons capable of activating detector materials and lower the reach of these neutrons.
The use of radiopure materials, especially in components located near the HPGe detectors, further reduces the background contribution. For this purpose, the HPGe detectors are cleaned and installed in an ^{222}Rn controlled atmosphere to prevent surface alpha contamination. In addition, low-radioactivity front-end electronics and construction materials, such as stainless steel, are used for the cryostat and water tank [7, 51].

4.3 Active background rejection

The active background suppression techniques used in the LEGEND experiment are composed of various analysis methods (cf. Section 4.3.1) and anti-coincidence cuts using the active background detection systems: the LAr instrumentation (cf. Section 4.3.2) and the muon veto (cf. Section 4.3.3).

The result after applying the active background rejection methods of the first LEGEND-200 data set is shown in Figure 4.2. It presents the energy spectrum after quality, muon veto anti-coincidence and multiplicity cuts in white, and additional LAr instrumentation anti-coincidence and pulse shape discrimination (PSD) cuts in red.

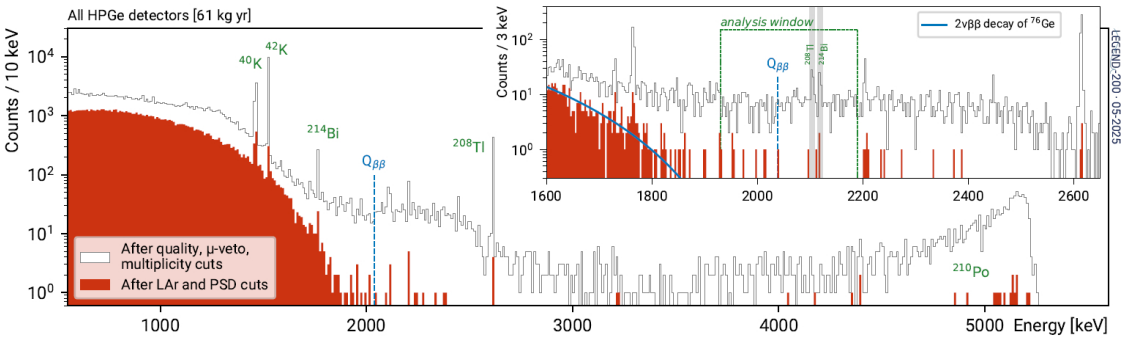

Figure 4.2.: Energy spectrum of the first LEGEND-200 data with 61 kg · yr Germanium exposure above the β decay energy of ^{39}Ar of $Q_\beta = 565$ keV after active background rejection cuts. The white histogram shows the energy spectrum after quality, muon veto and multiplicity cuts. The red histogram corresponds to the energy spectrum after additional LAr instrumentation and PSD cuts. The main radioactive contributors are marked with green, where $Q_{\beta\beta} = 2039$ keV is shown in blue. The inset presents a close-up from 1600 keV up to 2650 keV with finer binning. The gray marked bars are exclusion regions due to the ^{208}Tl and ^{214}Bi γ lines. Taken from [50].

4.3.1 HPGe analysis criteria

By applying quality cuts based on detector performance and additional analysis criteria for instance based on the shapes of the signals, several types of background events can be suppressed. A $0\nu\beta\beta$-decay event is expected to appear as a single-site event (SSE) in a Germanium detector, since the two emitted electrons deposit their energy within a small localized region, corresponding to the total energy of $Q_{\beta\beta} = 2039$ keV (cf. Figure 4.3d). Events in which more than one HPGe detector registers a signal thus can be rejected using a multiplicity cut. Here, multiplicity refers to the number of detectors that simultaneously record an event. In addition, the signal shape is considered by a PSD. For detectors with a small p^+ electrode, two classifiers can be found in the rising edge of the signal [50]. The ratio of the maximum current amplitude (A) to the charge amplitude (E) defines the A/E classifier. It is used to reject multiple-site event (MSE) occurring

for instance after Compton scattering of natural γ rays within the detectors. Since MSEs deposit smaller, separated charge bunches, these events have lower A/E values than SSEs (cf. Figure 4.3c) [54].

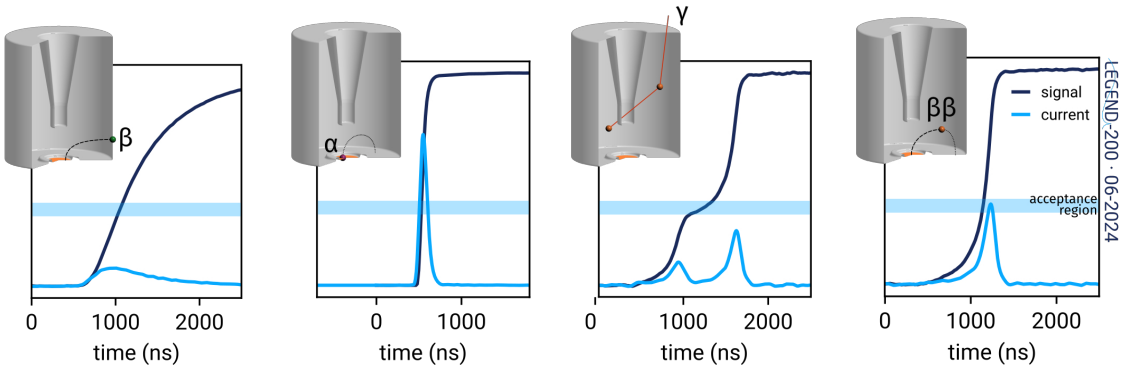

Figure 4.3.: Illustrated pulse shapes showing typical signals from a n^+ surface event from a β particle (a), a p^+ surface event from an α particle (b), a MSE (c), and a SSE from $0\nu\beta\beta$-decay (d). Image courtesy of the LEGEND collaboration.

The late-charge (LQ) classifier is based on the area over the last 20 % of the charge signal [55]. With that classifier, p^+ surface events caused by incident α or β particles can be rejected [50]. Events near the n^+ electrode, mainly caused by β particles, have a small rise time due to their energy deposition in the so-called dead layer, which is the region near the surface where the electric field is zero and thus the current can not be measured. Energy deposited in that region results therefore in a small charge amplitude and a slow pulse rise time, since charge can only be transported via diffusion. This results in a low A/E and high LQ value for n^+ surface events (cf. Figure 4.3a). The main source for p^+ surface events are α particles. They have a small penetration depth and thus are shielded by the n^+ surface, but can penetrate at the thinner p^+ electrode. Since they deposit energy directly at the p^+ contact, which has a strong electric field, they have a small rise time and high current amplitude and with that a high A/E and small LQ value (cf. Figure 4.3b) [7].

Since the Coax detectors have a large p^+ surface, they exhibit different pulse shape characteristics from the other HPGe detector types and therefore Coax detectors cannot use the same PSD classifiers. Here, an artificial neural network is applied for the MSE cut combined with a rise time cut to reject events near the p^+ surface. More detailed information about this cut can be found in [54].

However, background events can result in a $Q_{\beta\beta}$ signal-like pulse shape, which cannot be identified by the analysis cuts described above. Thus, anti-coincidence cuts using the LAr instrumentation and muon veto, described below, are necessary.

4.3.2 Liquid argon instrumentation

The LAr instrumentation of LEGEND-200 is designed to detect scintillation light produced in the LAr volume surrounding the HPGe detectors. The scintillation light, emitted at a wavelength of 128 nm, is generated by energy depositions from background sources such as cosmic muons and natural radioactivity in the LAr. WLS fibers absorb the ultraviolet light and re-emit it at longer wavelengths, guiding the light to the SiPMs, where it is detected. Coincidences between signals in the LAr instrumentation and the HPGe detectors within a time window of $[-1, +5]$ μs around the HPGe trigger allow for effective discrimination between potential $0\nu\beta\beta$-decay signals and background events [7]. The veto condition of the LAr instrumentation requires a total number of at least 4 photoelectrons (p.e.) per detected event and at least 4 triggered SiPM channels as discussed in [56].
Under these conditions, the LAr instrumentation provides a suppression factor of approximately 1.81 for energies below 1700 keV, primarily due to the rejection of the Compton continuum below the γ lines of ^{40}K and ^{42}K. Because ^{40}K decays via electron capture and deposits low or no energy in the LAr, it produces minimal scintillation light and is therefore not efficiently vetoed by the LAr instrumentation. In contrast, the γ rays from ^{42}K deposit significant energy in the LAr, resulting in a suppression factor of about 5. In the ROI around the $0\nu\beta\beta$-decay signal, the anti-coincidence cut with the LAr instrumentation yields a suppression factor of approximately 4.8, would lead to a BI of $8.25 \cdot 10^{-3}$ cts/(keV $\cdot$ kg $\cdot$ yr) in the ROI [57].

4.3.3 Water Cherenkov muon veto

To identify cosmogenic muons traversing the experimental setup, LEGEND-200 uses a water Cherenkov detector system as an active muon veto. Given the high average energy of the incoming muons, $\langle E_\mu \rangle = 270$ GeV, these muons emit approximately 270 Cherenkov photons per centimeter of track length in water via the Cherenkov effect described in Section 4.1.1 [2].
If a muon passes the water tank of the LEGEND experiment, Cherenkov photons are produced and can be detected by the PMTs mounted within the muon veto system. Additionally, muons can induce electromagnetic showers within the tank via bremsstrahlung or pair production, or interact with nuclei in the water, leading to further secondary particles and signals. Without active muon rejection, the muon-induced background contribution in LEGEND-200 corresponds to $5.46 \cdot 10^{-4}$ cts/(keV $\cdot$ kg $\cdot$ yr) in the ROI (cf. Section 6.4.1). The muon veto suppresses the BI significantly. As the muon veto of LEGEND-200 constitutes the core focus of this work, its operational principles and background reduction capabilities are discussed in detail in the following chapters.

Chapter 5

Muon veto system of the LEGEND-200 experiment

"Was wir beobachten, ist nicht die Natur selbst, sondern die Natur, die unserer Fragestellung ausgesetzt ist."

— Werner Heisenberg

To reduce the background induced by cosmogenic muons in LEGEND-200, the muon veto system serves as active muon shielding. It consists of a water Cherenkov veto surrounding the cryostat and detects the Cherenkov radiation produced by incoming muons via PMTs mounted on the inner surface of the water tank.
This chapter provides a detailed overview of the muon veto system, starting with the setup and components, including the geometry, reflective foil and PMT configuration. It continues with a description of the data acquisition system and the trigger conditions and concludes with the calibration procedure, which ensures stable data taking.

5.1 Setup and components

The water tank of LEGEND-200 serves as the outermost background shielding system, surrounding the cryostat and including a water Cherenkov muon veto. Adapted from the GERDA experiment, the tank has a diameter of 10 m and a height of 9.4 m, corresponding to a total water volume of 590 t [53]. It is filled with demineralized water supplied by the water purification system of the XENONnT experiment, which is located at Hall B in the LNGS [58].
To detect the Cherenkov light produced in the water tank, the muon veto instrumentation inside the water tank, schematically shown in Figure 5.1a, contains a reflective foil covering the inner tank surfaces to increase the light yield (cf. Section 5.1.1) and a total of 53 PMTs for the photon

detection (cf. Section 5.1.2). The PMTs are distributed across three different areas within the water tank: the wall, the floor and the pillbox (referring to the area directly beneath the cryostat) marked in red in Figure 5.1b.

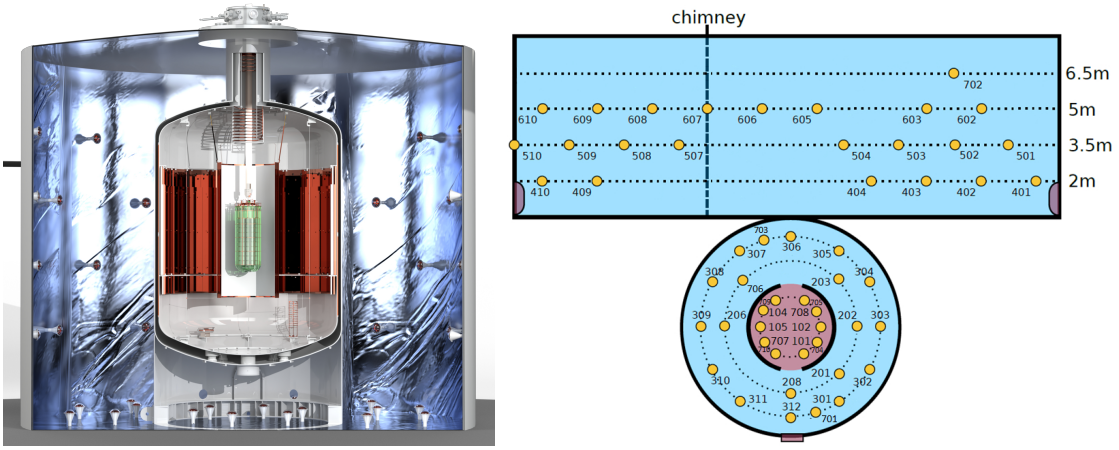

(a) (b)

Figure 5.1.: (a) Schematic representation of the LEGEND-200 setup showing the water tank instrumentation surrounding the cryostat. Image courtesy of the LEGEND collaboration. (b) PMT distribution across the wall (blue rectangle, 23 PMTs), floor (blue circle, 20 PMTs) and the pillbox (red circle, 10 PMTs) of the LEGEND-200 muon veto at the beginning of data taking in March 2023. The red semicircles on the wall refer to the manhole through which the water tank can be accessed. Adapted from [2].

Since the muons traveling vertically through the neck of the cryostat are more likely to deposit high energies in the HPGe detectors, the pillbox is an important area to detect these muons. For this purpose, the PMT density in the pillbox is higher than in the other areas, whereas 4 additional PMTs were moved from the upper wall row at 6.5 m down to the pillbox during the transition from GERDA to LEGEND-200 [59].

5.1.1 Reflective foil

LEGEND-200 uses the reflective foil 'Daylighting Film DF2000MA' manufactured by 3M and better known as 'VM2000', to increase the detection probability for optical photons in the water tank by a factor of two to three. This improvement is primarily due to the foil's reflectivity exceeding 99 % in the visible wavelength range [60]. Additionally, the foil features WLS properties, converting ultra-violet (UV) photons into the optical region around 400 nm. Optical response measurements of the VM2000 foil by Geis et al. found that approximately 3−7.5 % of the incoming light in the 250−370 nm range is wavelength-shifted [61].
During GERDA operations, VM2000 was also found to exhibit scintillation [3]. The VM2000

foil mounted in the LEGEND-200 water tank has a thickness of 66 μm. The ingredients of the VM2000 foil are a manufacturers secret. Based on the patent which most likely corresponds to the VM2000 foil, approximately 40 μm of the foil consist of polyethylene naphthalate (PEN) layers. The remaining foil layers are made of PMMA [62]. PEN is a plastic scintillator and thus, responsible for the scintillation properties of VM2000. For standard PEN, Manzanillas et al. measured the light emission to be in between 400 nm and 600 nm with a peak at approximately 440 nm when excited by electrons emitted from a ^{207}Bi source. The time response was found to be about 25.3 ns with approximately 5440 produced photons per MeV electrons [63].
The effect of VM2000 foil scintillation within the muon veto is discussed in detail in Chapter 8.1.2.

5.1.2 Photomultiplier tubes

For the detection of the Cherenkov photons, the muon veto of LEGEND-200 employs 8" PMTs of the types 9350KB and 9354KB manufactured by ET Enterprises Limited (ETL) [3]. The PMTs consist of an evacuated ultra-low background borosilicate glass bulb containing a blue-green sensitive bialkali photocathode with an active area of 430 cm^2 [64]. If a photon hits the photocathode, a photoelectron is released via the photoelectric effect, which refers to the absorption of a photon by a material resulting in the emission of an electron (cf. Figure 5.2) [37].

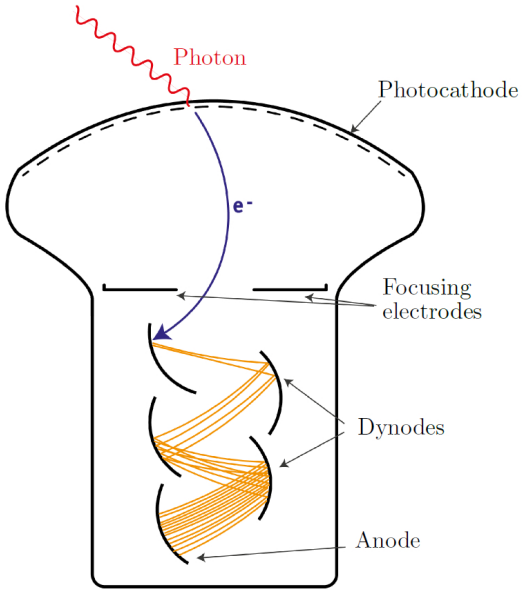

Figure 5.2.: Schematic representation of the photodetection principle of a PMT. The incoming photon (red) releases via the photoelectric effect a photoelectron in the photocathode. The photoelectron is then multiplied by the linear-focused dynode structure, resulting in an electrical signal at the anode. Adapted from [65].

An acceleration voltage is applied to the PMT, which accelerates the photoelectron towards

12 electrodes within the glass bulb, called (linear-focused) dynodes. At the dynodes, the incoming photoelectron releases two to five secondary electrons, creating an electron avalanche. If the electron avalanche reaches the anode, it is multiplied up to 10^6 to 10^7 times, known as gain of the PMT. The incoming electrons are converted into a current output at the anode, which creates the readout signal. This signal is amplified by the base of the PMT, which refers to the electronics located at the socket of the PMT. The base is sealed with epoxy against leaks and connects to the high voltage (HV) and signal cable and distributes the voltage across the dynode stages [2]. Even in the absence of incident light, PMTs produce small spontaneous pulses caused by thermionic emission from the photocathode. These pulses are known as dark counts and define the noise threshold for photon detection [66].

When a photon hits the photocathode of a PMT, several effects are to be considered for the detection of the photon through the PMT. First, the photon detection efficiency (PDE) gives the probability for the photon to be detected. It is the product from the so-called quantum efficiency (QE) and the collection efficiency (CE).

The QE describes the wavelength dependent probability for an incoming photon to emit a photoelectron from the photocathode [66]. For the used ETL PMTs in the LEGEND-200 muon veto, Figure 5.3 shows that the QE has its maximum at approximately 400 nm, which also corresponds to the region to which the VM2000 shifts UV photons to (cf. Section 5.1.1) [64].

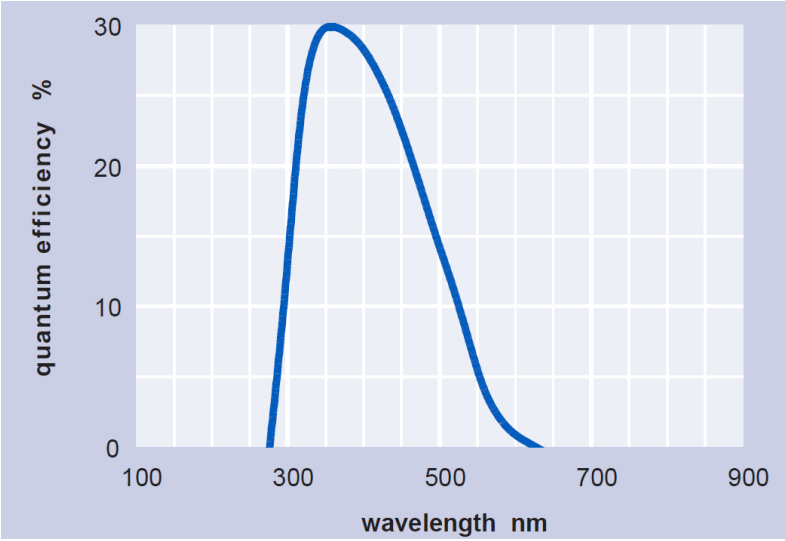

Figure 5.3.: Exemplary response curve of an ETL 9354KB PMT showing the QE as a function of the wavelength. The QEs of ETL PMTs of type 9354KB and 9350KB are similar, since they only differ in the radioactivity of their glass bulb [53]. Taken from [64].

The CE describes the number of emitted photoelectrons at the photocathode divided by the number of incoming photoelectrons at the first dynode. If electrons differ from their favorable trajectory to the first dynode in the PMT or produced secondary electrons do not contribute to the

multiplication because they miss the effective area of a dynode stage, some photoelectrons are not detected [66]. A CE of 85 % is assumed for the muon veto PMTs of LEGEND-200.
Additionally, timing properties of PMTs have an impact on the output signal. The transit time (TT) of a PMT describes the time for the output signal to increase to 90 % of the total pulse height. This time has a fluctuation which is called the transit time spread (TTS) and indicates the time resolution of the PMTs [66]. For ETL PMTs of type 9350KB and 9354KB, the TTS is given to be 2.7 ns at FWHM [64].
Since the muon veto PMTs operate in water, the electronics need a waterproof housing. For this purpose, the steel encapsulations used in GERDA also protect the LEGEND-200 muon veto PMTs against water [3]. They consist of a steel cone attached to a cylinder, which is mounted on a bottom plate. In between the encapsulation and the PMT a μ-metal cone is placed to protect the dynode structure of the PMT against the magnetic field of the Earth [2]. Due to environmental reasons, the spectroscopic oil, which was filled in between the PMT and the encapsulation to smoothen the transition of the refractive index between water and the borosilicate glass of the PMT, was removed during the shift from GERDA to LEGEND-200. Furthermore, the polyethylene terephthalate (PET) cap used in GERDA to offer a window for the photons to the photocathode, was replaced with a thicker acrylic cap to protect the PMT after the oil removal against the pressure of the water. These modifications also led to a reduction in the number of photons reaching the photocathode by approximately a factor of 3 [59, 67].

5.2 Data acquisition system

When a PMT detects light, the output signal is transmitted via the same cable that supplies the HV. A high-pass filter, referred to as the splitter box (cf. Figure A.1), decouples the signal from the HV line before being forwarded to a FlashCam digitizer (cf. Figure 5.4). The readout electronics of this digitizer is based on Field Programmable Gate Arrays (FPGAs) and converts the analog to a digital signal via analog-to-digital converters (ADCs) of type AD9634 by Analog Devices. More detailed information on the operating principle of the FlashCams can be found in [68]. Three FlashCam ADC cards, each providing 24 channels with 12-bit resolution at a sampling rate of 250 MHz, are connected to the muon veto PMTs, with one card assigned to each PMT distribution area and to the calibration control unit (see Section 5.3) [69]. The configuration of the FlashCams is done via the control framework Object-orientated Real time Control and Acquisition (ORCA), which additionally provides a real-time monitoring of the output data [59, 70]. The assignment between the board and channel stored in ORCA and the corresponding PMT identification (ID) can be found Table A.1 in the Appendix. The taken signals are stored in waveforms containing 220 samples, resulting in a total 880 ns trace lengths per taken event.

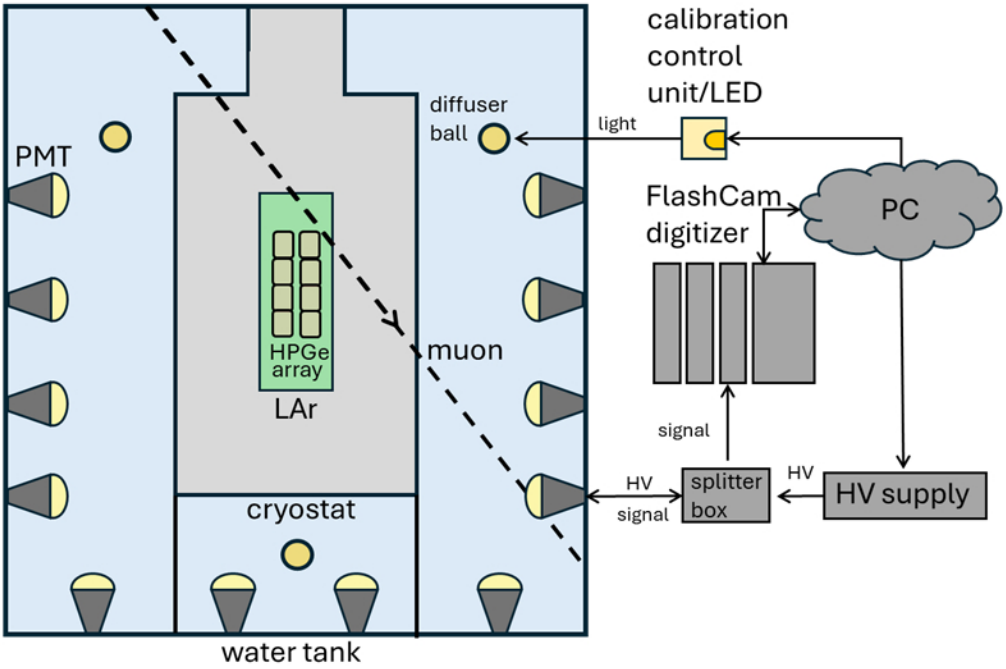

Figure 5.4.: Schematic representation of the muon veto data acquisition (DAQ) chain of LEGEND-200, illustrating the PMTs distributed in the water tank. The PMTs are connected via the splitter box to the HV power supply and the FlashCams. During calibrations, a signal is sent to the calibration control unit vie the PC, which additionally controls the DAQ system.

An event is recorded as soon as the trigger conditions of the muon veto system are met, which include both light intensity and a multiplicity requirement. The light intensity trigger threshold was set to 0.5 p.e. per contributing PMT, corresponding to 15 ADC channels, as described in Section 5.3. The multiplicity trigger thresholds vary by PMT distribution area:

- pillbox: 6 PMTs
- floor: 4 PMTs
- wall: 4 PMTs

The muon veto triggers when the multiplicity condition is met in at least one of these areas, provided that all contributing PMTs also meet the light trigger criterion. To perform a baseline correction, approximately the first 320 ns of the recorded waveform represent the baseline preceding the event. The remaining waveform contains the PMT signals following the trigger.
In addition, the FlashCam digitizers are connected to the DAQ Personal Computer (PC), controlling the power supply, which provides the HV for the PMTs as shown in Figure 5.4. Furthermore, the PC sends a signal during calibration to the calibration control unit, which was developed in [67]. This control unit pulses UV light-emitting diodes (LEDs), whose light is guided via

optical fibers to five diffuser balls shown in Figure 5.5 inside the muon veto. The diffuser balls provide an isotropic light distribution throughout the water tank [3].

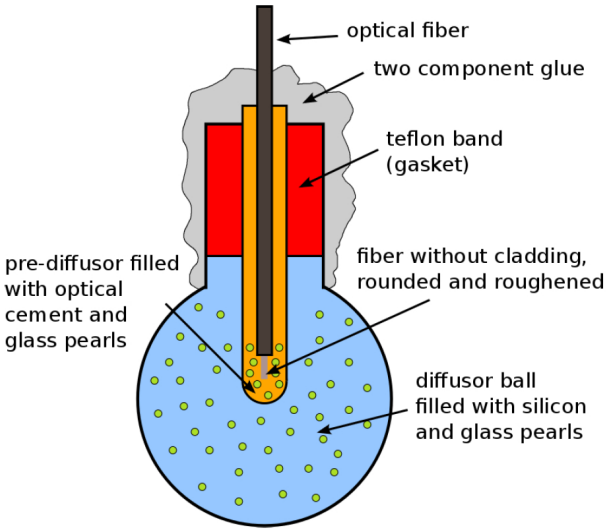

Figure 5.5.: Schematic representation of a diffuser ball used for the PMT calibration of the LEGEND-200 muon veto. Taken from [2].

5.3 Calibration of the PMTs

In this work, the calibration procedure for the LEGEND-200 muon veto was based on and further developed from the methods described in previous works [59, 67]. According to Section 4.3.3, the mean muon passing the water tank generates 270 Cherenkov photons per centimeter. Assuming a vertical track through the water tank of approximately 9 m, this results in 243000 produced photons. With the PMT coverage of approximately 0.5 % [3] and 53 PMTs in the muon veto, an average of $\approx$ 22 photons reaching each PMT can be assumed. To ensure the detection of these and more energetic muons, the PMTs were calibrated to cover a dynamic range of at least 100 p.e.
At the beginning of physics data taking in March 2023, the baseline of the muon veto's ADCs were set to 300 ADC channels to get a wider dynamic range. In August 2023, the baseline was increased to 1000 ADC channels to allow a more detailed analysis of signal undershoots aiming for a further improvement of the dynamic range (cf. Section 6.3.2). Since the used FlashCam ADCs provide a 12-bit resolution, the ADC channels range from 0 to $2^{12} = 4096$. With the baseline set to 1000 ADC channels, 3096 ADC channels remain available for signal amplitude. Thus, to reach a range of at least 100 p.e., the PMTs are calibrated such that one p.e. corresponds to approximately 30 ADC channels.
Therefore, during the calibration of the muon veto the UV LEDs are pulsed with an intensity to obtain a single p.e. charge from the PMTs. This refers to a supplied voltage of 10.6 V for the wall and floor and 10.3 V for the pillbox LEDs. The charge Q_{PMT} of a PMT signal can be approximated

with a Gaussian distribution and calculated using the distribution of the signal height in ADC channels via

$$Q_{\mathrm{PMT}} = \mathrm{m}_{\mathrm{Gauss}} \cdot 0.1953125\,\mathrm{mV} \cdot 4\,\mathrm{ns} \cdot \frac{1}{50\,\Omega}\,. \tag{5.1}$$

In Equation (5.1) $\mathrm{m}_{\mathrm{Gauss}}$ represents the mean of the single photoelectron peak (SPP) of the charge histogram. The voltage corresponding to 1 ADC channel with a voltage full-scale input range of 800 mV is given by $0.1953125\,\mathrm{mV} = 800\,\mathrm{mV}/4096$. The time per ADC sample are $4\,\mathrm{ns} = 1/250\,\mathrm{MHz}$ and $50\,\Omega$ refers to the used termination resistor. The charge of the PMT signal is related to the gain g of the PMT via

$$g = \frac{Q}{q}\,, \tag{5.2}$$

with the elementary charge $q \approx 1.602 \cdot 10^{-19}\,\mathrm{C}$. This results in a target gain for the PMTs is $g_{\mathrm{target}} \approx 2.9 \cdot 10^{6}$. To reach this gain, the supplied voltage of each PMT is adapted according to

$$V_{\mathrm{target}} = V \left(\frac{g_{\mathrm{target}}}{g} \right)^{\frac{1}{kn}}\,, \tag{5.3}$$

where $n = 12$ is the amount of dynodes, V is the supplied voltage at the moment of the calibration and k a dynode material specific constant between 0.7 and 0.8 [66, 71].
During calibration, the PMTs are set to the corresponding calculated voltage. An example of the charge spectrum of a PMT is shown as black line in Figure 5.6. The leftmost peak, shown in blue and fitted with a Gaussian, represents the pedestal. It corresponds to waveforms without photon signals and reflects baseline fluctuations caused by noise. The SPP is also fitted with a Gaussian distribution, shown in gray, whereas in green the double p.e. peak is indicated. The measured double p.e. peak indicates a too high light intensity for the corresponding PMT. Since five LEDs are pulsed to calibrate 53 PMTs the light intensity has to be adapted in that way, that all PMTs detect the single p.e. peak. That can cause a double p.e. peak in PMT which are for instance near to the LED. The combined fit is shown in red with the resulting mean value, which is marked through the yellow line.

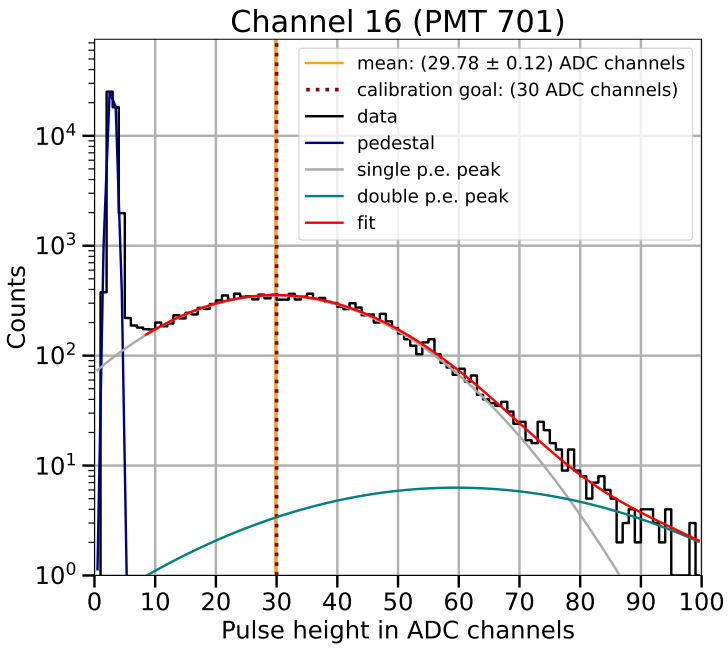

Figure 5.6.: Example of a charge histogram showing the SPP of a floor PMT 701. The data is shown in black, where the fit of the pedestal rising from the electronics noise is represented in blue and the combined fit of single (gray) and double (green) p.e. peak is displayed in red. The yellow line shows the calculated mean of this fit, where the dashed red line shows the calibration goal set to 30 ADC channels.

If the mean value of the SPP differs from the calibration goal resulting in a voltage difference of more than 1 V according to Equation (5.3), the PMT voltage is adjusted. After the adjustment of all muon veto PMTs another set of calibration data is taking to cross-check the results. To ensure stable signal performance, the muon veto system of LEGEND-200 is calibrated once or twice per month during the operation of the experiment.

Chapter 6

Muon veto analysis

"Das Unerwartete und das Unerhörte gehören in diese Welt. Nur dann ist das Leben ganz."

— Carl Gustav Jung

The analysis of data from the muon veto PMTs is essential for identifying muon events and applying the anti-coincidence cut to the HPGe detector array data. This requires precise event assignment as well as the development of data-cleaning criteria, based on investigations of PMT waveforms and artifacts in the event parameters. Given the data acquisition period of nearly one year, PMT malfunctions and failures, which can lead to erroneous signals, must also be considered. After applying the necessary cuts to clean the dataset, the remaining muon events can be included in the data processing chain of all detector systems. This enables the estimation of the muon-induced background, which would contribute to the BI in the ROI of LEGEND-200 without an active muon suppression.
The following chapter describes the analysis of the muon veto data, which was mainly developed in the context of this thesis. It begins with an overview of the general LEGEND-200 processing chain and outlines the preparation and synchronization of the muon veto data. This is followed by a study of PMT stability over the data acquisition period, which is succeeded by the development of additional cuts based on investigations of the waveforms. Ultimately, a coincidence analysis involving the data of the LAr instrumentation and the HPGe detector events is performed.

6.1 Processing chain and muon veto events

The muon veto system contributes to both calibration (cal) and physics (phy) data acquisition in LEGEND-200. The phy data is analyzed for $0\nu\beta\beta$-decay events and calibrated using the preceding cal data. Data acquisition is organized into time periods consisting of multiple runs. Each period comprises runs with the same hardware configuration, and each run typically covers around one

week of phy data with the corresponding previous cal data. The data are stored in LEGEND HDF5 (LH5) format, a LEGEND specification based on Hierarchical Data Format 5 (HDF5).
In this work, nearly one year of phy data is analyzed in relation to the muon veto system as shown in Table A.3. In total, 55 runs are considered, beginning with period p03 run r000 taken in March 2023, marking the first phy data of LEGEND-200 used for $0\nu\beta\beta$-decay analysis following the commissioning of the experiment, and ending with p11 r004 in May 2024. After this period, a new HPGe detector deployment began, interrupting phy data acquisition.
ORCA stores the data as binary files in the first analysis stage-tier-0/DAQ-tier. To decode data and store various analysis parameters, the LEGEND-200 processing chain includes five additional-tiers (cf. Figure 6.1).

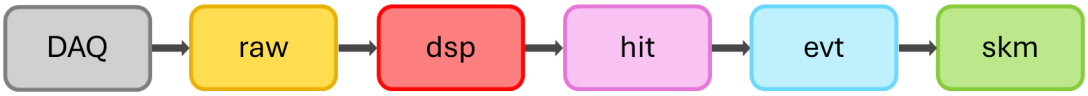

Figure 6.1.: Flow chart of the LEGEND-200 processing chain going from DAQ- over raw-, digital signal processing (dsp)-, hit- and event (evt)- to the skimmed (skm)-tier.

Tier-1, the raw-tier, contains event waveforms stored in LH5 format. The following dsp-tier includes uncalibrated parameters, which are then calibrated in the hit-tier. Therefore, the m_{Gauss} (cf. Section 5.3) values obtained from the calibration fits are stored in yet another markup language (YAML) files and read during the hit-tier processing. At the evt-tier, multiple detectors and detector systems are combined and cropped in the skm-tier, which includes data cleaning to exclude malfunctioning detectors, retaining only the data relevant for the final $0\nu\beta\beta$-decay search. The muon veto data is present in all analysis-tiers and provides a muon flag generated in the evt and stored in the skm-tier.

6.1.1 Muon flag

The primary purpose of the muon veto system is to detect muons passing through the experiment (cf. Section 4.3.3). When the Cherenkov light produced by a muon exceeds the trigger threshold of the muon veto (see Section 5.2), the signals of all PMTs are recorded as waveforms in the DAQ and then processed to the raw-tier. An example waveform of all PMTs signals during a muon event is shown in Figure 6.2. It can be identified by its flat baseline, followed by the simultaneous signal increase in ADC channels of various PMTs to their maximum of this event. Finally, the signal amplitudes are decreasing (cf. Section 6.3.1). All events are saved with their recording time as a timestamp in UNIX format, which counts the number of seconds since January 1st, 1970.
In addition to muons, other sources e.g., malfunctioning PMTs, can generate light inside the water tank, which is also detected by the PMTs. These sources are discussed in more detail in Section 6.3 and Chapter 8.

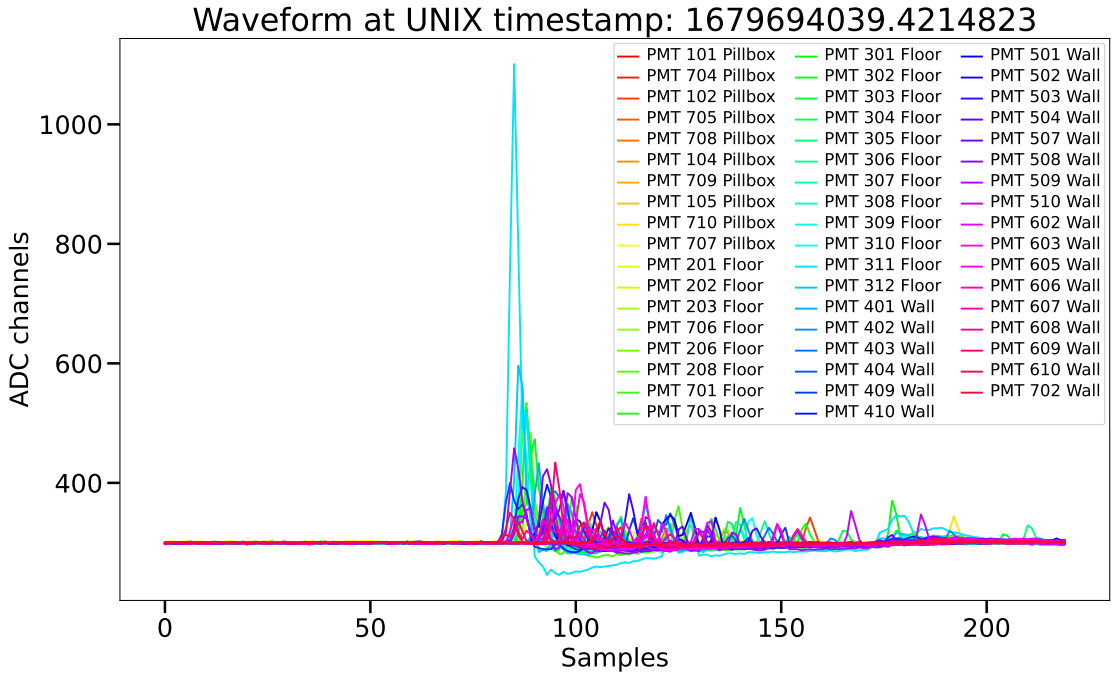

Figure 6.2.: Example of waveforms of all PMTs (represented in different colors) in ADC channels as a function of the samples, each lasting for 4 ns. The legend shows the PMT ID with the corresponding PMT distribution area within the muon veto. The muon event was recorded at UNIX timestamp 1679694039.4214823 (seconds since January 1st, 1970).

To identify muon-induced events among all triggered events of the muon veto, selection criteria based on the PMTs waveforms are applied, resulting in the creation of a muon flag. Therefore, the maximum pulse height of each waveform in an event is evaluated, and the channels of all triggered PMTs are stored in the dsp-tier. Additionally a linear upsampler is applied to achieve 1 ns binning of the waveform. The maximum pulse height (cf. Figure 6.2) is used to approximate the charge of a PMT pulse as discussed in more detail in [72]. To convert the pulse heights to p.e., the values are normalized using the fitted m_{Gauss} from the previous calibration (see Section 5.3) in the hit-tier.

The muon flag is generated in the evt-tier. Therefore, the total light in p.e. is summed up (referred to as integral light) and presented as a function of the number of triggered PMTs (multiplicity) per event within a two dimensional histogram as shown in Figure 6.3. Two cuts, one for the so-called low-multiplicity bump and one for flashing PMTs, are represented in red within that Figure marking events, which are not caused by muons. Accordingly, the events outside these cuts are flagged as muon events.

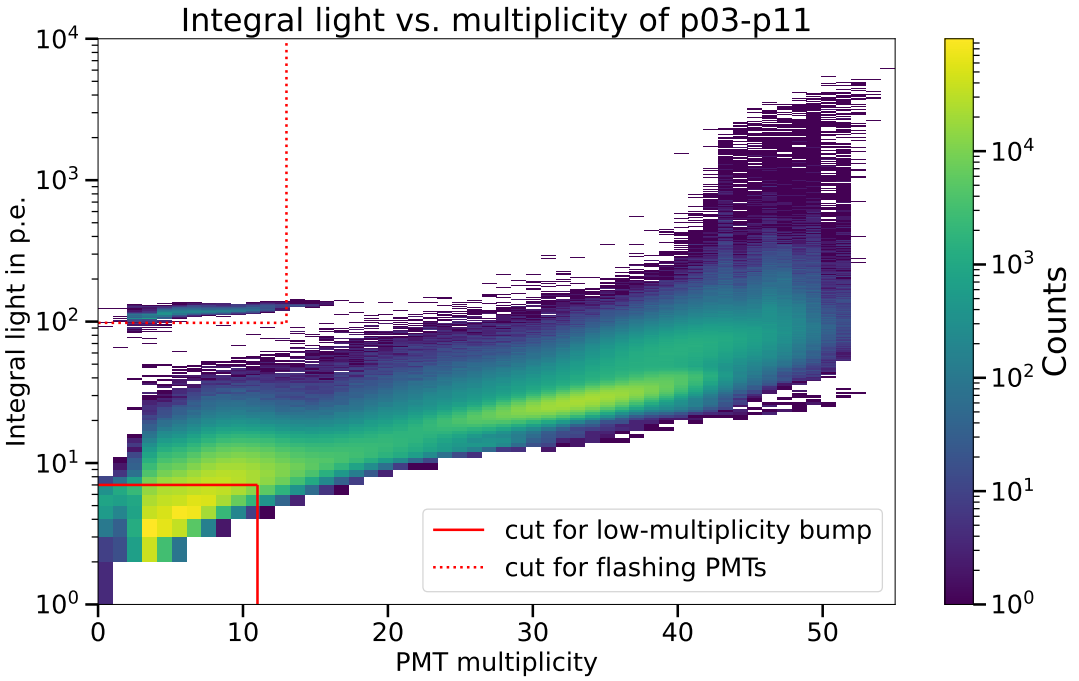

Figure 6.3.: Two dimensional histogram of the integral light in p.e. as a function of the PMT multiplicity per event for p03 to p11. The red solid line marks the cut for the low-multiplicity bump data. The red dotted line shows the cut for flashing PMTs. Events outside both cuts are flagged as muon-induced events.

Cut for low-multiplicity bump The low-multiplicity bump marks the region of low-multiplicity and integral light in Figure 6.3. The data in this region is probably caused by scintillation of the VM2000 foil as discussed in more detail in Section 8.1.2. Additionally, low-energy muon events or muons passing only an edge of the water tank can create events in the low-multiplicity bump region (cf. Section 8.1.1). Thus, the cut is defined using a normal distribution fitted to both the integral light and the multiplicity distribution of the bump in the data, as shown in Figure 6.4. In order to consider only the muon branch without signals of malfunctioning PMTs, as discussed in Section 6.2, the histograms of PMT multiplicity (see Figure 6.4a) and integral light (see Figure 6.4b) between p03 and p11 are considered after data cleaning using PSD cuts (cf. Section 6.3.3). The gaussian fit results in a mean value of 6.18 ± 0.25 with a standard deviation $\sigma = 1.73 \pm 0.25$ for the PMT multiplicity. A CL of 99.865 % is considered, using the mean value plus three times the standard deviation. The mean value minus three standard deviations falls below the trigger threshold and can therefore be considered negligible. This results in an approximate multiplicity of 11.37, which is conservatively rounded down to 11 to minimize the exclusion of low-energy muon events. For the integral light, with a mean value of (4.33 ± 0.04) p.e. and a standard deviation $\sigma = (1.03 \pm 0.04)$ p.e., the cut is approximated to 7.42 p.e. and, thus conservatively rounded down to 7 p.e. Finally, the cut for the low-multiplicity bump results in multiplicity ≤ 11 and p.e. ≤ 7.

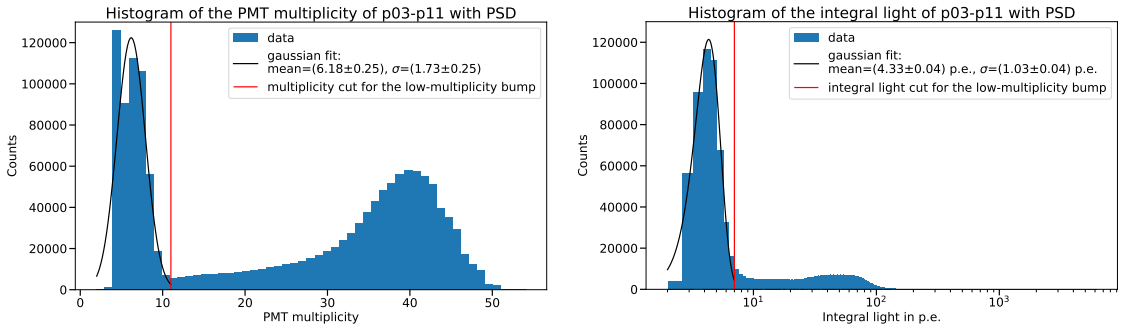

(a) (b)

Figure 6.4.: Histograms of the muon brach between p03 and p11 after all PSD cuts (cf. Section 6.3.3). (a) PMT multiplicity histogram with gaussian fit of the first peak (black) gives a mean multiplicity of 6.18 ± 0.25 with a standard deviation $\sigma = 1.73 \pm 0.25$. The gap between a multiplicity of 4 and of 6 PMTs is a result of the pillbox and floor/wall multiplicity trigger threshold. Using a CL of 99.865 % by considering the mean value plus three times the standard deviation, the multiplicity cut for the low-multiplicity bump is resulting at a multiplicity of 11 (red). (b) Integral light histogram with gaussian fit of the first peak (black) gives a mean integral light of (4.33 ± 0.04) p.e. with $\sigma = (1.03 \pm 0.04)$ p.e., leading to the integral light cut for the low-multiplicity bump 7 p.e. (with a CL of 99.865 %) in red.

Cut for flashing PMTs Figure 6.3 shows one island of data points at a multiplicity below approximately 20 PMTs and an integral light above approximately 80 p.e. with a visible gap to the muon branch. This island is attributed to flashing PMTs (cf. Section 6.2.2), meaning that the data is not induced by muon events. These events are discussed in more detail in Section 6.3. As for the low-multiplicity bump, the cut is defined using a fit of a normal distribution to the data (cf. Figure 6.5). The gaussian fit results in a mean value of 6.03 ± 0.31 with a standard deviation $\sigma = 2.5 \pm 0.33$ for the PMT multiplicity (cf. Figure 6.5a). A CL of 99.865 % is considered resulting a cut value of 13.53 and conservatively rounded down to a multiplicity cut of 13. For the integral light, with a mean value of (116.61 ± 0.38) p.e. and a standard deviation $\sigma = (6.22 \pm 0.38)$ p.e., the cut is approximated to 97.95 p.e. and, thus conservatively rounded down to 98 p.e.. In total, the cut for flashing PMTs is defined by a multiplicity of ≤ 13 and a p.e. of ≥ 98, as indicated by the red dotted line in Figure 6.3.

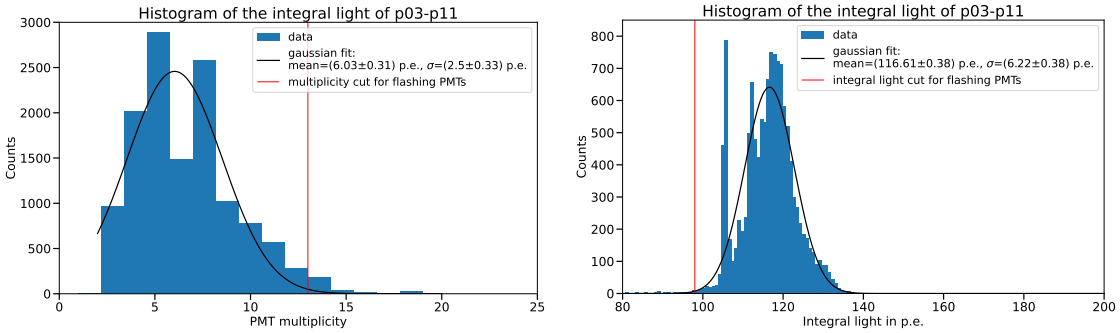

(a) (b)

Figure 6.5.: Histograms of the data at a multiplicity below approximately 20 PMTs and an integral light above approximately 80 p.e. between p03 and p11 after all PSD cuts (cf. Section 6.3.3). (a) PMT multiplicity histogram with gaussian fit of the first peak (black) gives a mean multiplicity of 6.03 ± 0.31 with a standard deviation $\sigma = 2.5 \pm 0.33$. The gap between a multiplicity of 4 and of 6 PMTs is a result of the pillbox and floor/wall multiplicity trigger threshold. Using a CL of 99.865 % by considering the mean value plus three times the standard deviation, the multiplicity cut for the low-multiplicity bump is resulting at a multiplicity of 13 (red). (b) Integral light histogram with gaussian fit of the first peak (black) gives a mean integral light of (116.61 ± 0.38) p.e. with $\sigma = (6.22 \pm 0.38)$ p.e., leading to the integral light cut for the low-multiplicity bump 98 p.e. (with a CL of 99.865 %) in red.

The resulting muon flag is assigned to simultaneously recorded HPGe detectors events as discussed in Section 6.1.2. Finally, the muon flag is propagated to the skm-tier and there contributing with an anti-coincidence cut.

Figure 6.6 shows the resulting muon rate with standard deviation from p03 to p11, averaging to $r_{\text{muon}} \approx 35\,\text{mHz}$, which is in good agreement to the value of the commissioning data determined in [59] and the muon rate measured in the GERDA experiment [2]. The gray boxes mark the different data taking periods. Since tests involving different HPGe voltages were performed during p05, this period is excluded from further analysis. The muon rates in periods p03, p07, p08 and p10 exhibit several outliers, corresponding to the events responsible for the bright spots and islands seen in Figure 6.3, which are discussed in more detail in Section 6.3.

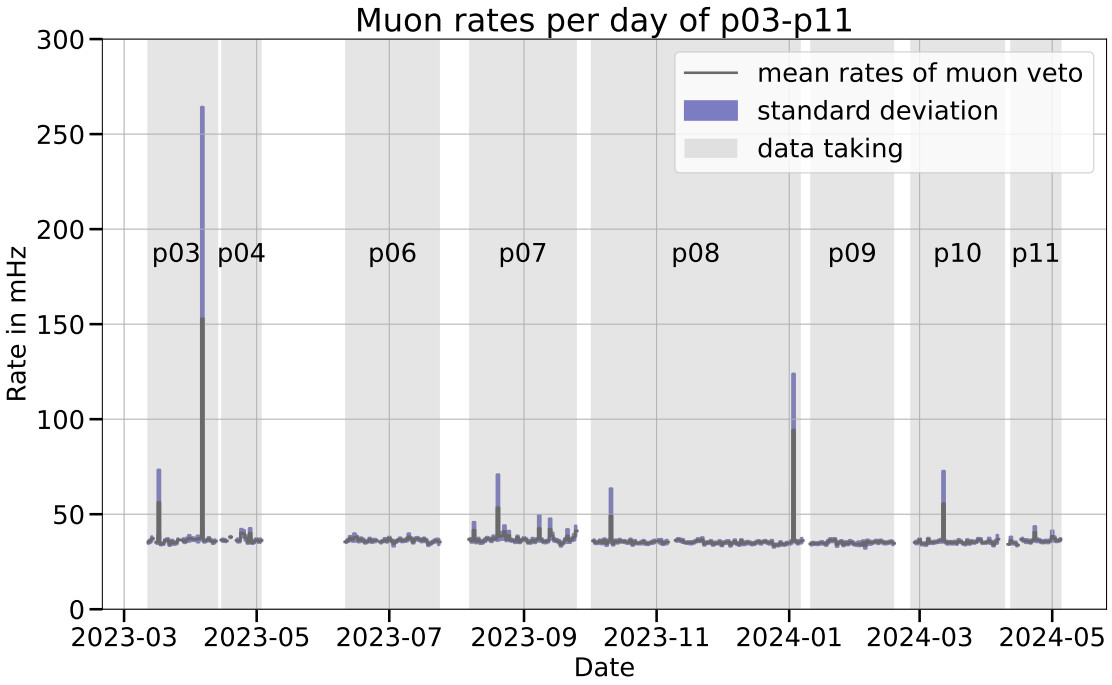

Figure 6.6.: Muon rate from p03 to p11 (the gray boxes represent the single data taking periods), averaged per day (dark gray) with corresponding standard deviation (dark blue).

6.1.2 Event matching between muon veto and HPGe DAQ systems

For the identification of muon-induced HPGe detector events, simultaneously occurring muon veto and HPGe events must be assigned to each other in the analysis. Since the HPGe detectors are connected to a different DAQ system than the PMTs of the muon veto, the events of both systems are synchronized using a Global Positioning System (GPS) clock [50]. Event timestamps are stored in UNIX format and may differ between the two DAQ systems due to post-trigger settings, even for simultaneous events. This leads to a time offset between the UNIX timestamps stored by the two systems.

To correlate the timestamps of the associated events during analysis, the timestamps of the so-called MUON AUX channel and the muon veto were empirically compared. The MUON AUX channel forwards the trigger signal of the muon veto directly to the HPGe DAQ system and therefore has timestamps in the HPGe DAQ format. The muon veto trigger timestamps stored in the MUON AUX channel in the HPGe DAQ can be compared with those from the muon veto DAQ. Figure 6.7 shows the offset between the timestamps of the two DAQ systems, as assigned via the MUON AUX channel trigger, exemplarily on period p07.

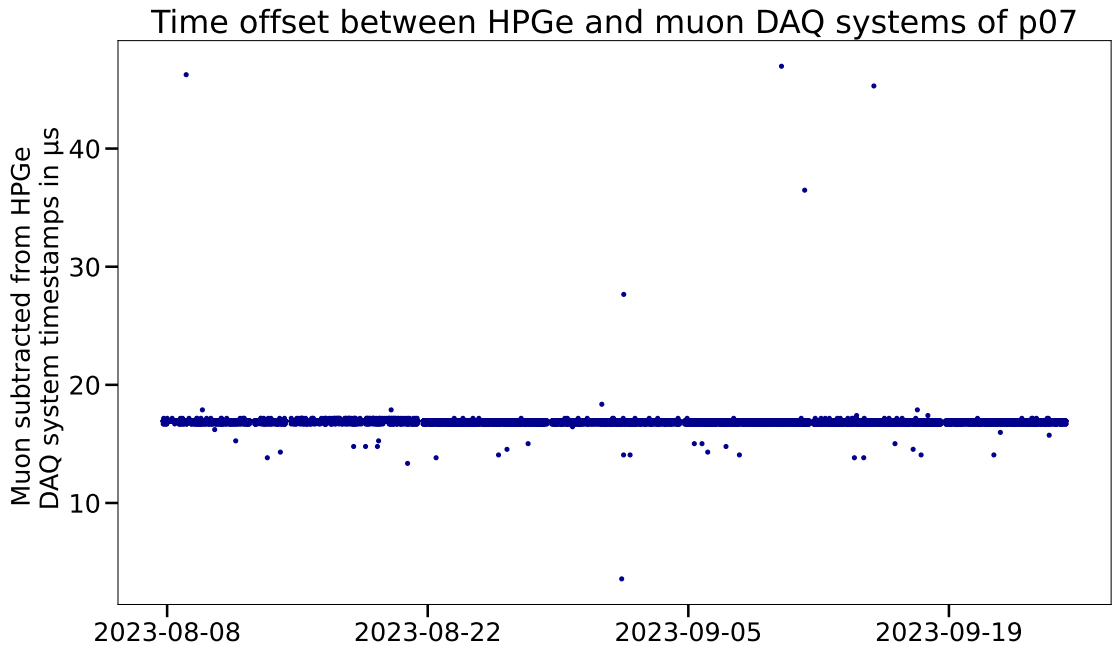

Figure 6.7.: Offset between HPGe and muon DAQ systems as a function of the date exemplarily shown for p07. Most of the events are shown at a timestamp delay of approximately $16.928 \cdot 10^{-6}$ s with variations in multiples of $1/2^{22}$ s, which is the value of the timestamp resolution. The outliers above that value can be explained by delayed coincidences due to neutron captures for instance (cf. Section 4.1.1). The outliers below can be caused by PMT afterpulses or flashers (cf. Section 6.3.3).

According to Figure 6.7, the timestamp delay is approximately $16.928 \cdot 10^{-6}$ s with variations in multiples of $1/2^{22}$ s, corresponding to the timestamp resolution. The outliers above the line at $16.928 \cdot 10^{-6}$ s can be explained by delayed coincidences for instance due to neutron captures in the water (cf. Section 4.1.1), while the outliers below the line can primarily be explained with afterpulse triggers or flashing PMTs (cf. Section 6.3.3) [73]. To correctly assign all events, muon veto timestamps are matched to HPGe timestamps if their delay falls within $1 - 238$ multiples of $1/2^{22}$ s (from $0\,\mu$s up to approximately $56.5\,\mu$s), a criterion empirically derived from the comparison of the MUON AUX and muon veto triggers. This assignment is performed in the evt-tier after the muon flag is generated, resulting in a boolean muon flag for the muon veto DAQ system and another boolean muon flag for the HPGe DAQ system.

6.1.3 Muon veto monitoring

The monitoring of the muon veto data stream is provided by three platforms: the DAQ monitoring, the SlowControl monitoring and the LEGEND-200 monitoring dashboard. For the DAQ monitoring a Grafana monitoring page [74] is directly connected to the ORCA DAQ system and shows the live status of the PMT baseline and the trigger rate. The SlowControl monitoring presents the

live values of the supplied PMT voltages and the corresponding current.
In the scope of this work, the plots and data preparation for the LEGEND-200 monitoring dashboard were developed, which provide a semi-live monitoring of analysis plots. Data acquired by LEGEND-200 is directly stored and processed at the computing environment of the LNGS. The LEGEND-200 monitoring dashboard synchronizes cal and phy data every 6 hours via rsync [75]. For cal data of the muon veto, the SPPs of each PMT as well as the difference of the fitted m_{Gauss} relative to the previous calibration and the distribution of m_{Gauss} (cf. Section 5.3) with the corresponding standard deviation σ are presented (cf. Figures Figs. B.1 to B.3). Due to the variety of the m_{Gauss} distribution and the standard deviation, these plots provide information about the performance of the calibration and PMTs. Since the muon veto is calibrated manually once or twice a month, the calibration data is updated by hand after each calibration.
In order to provide monitoring for phy data of the muon veto, several phy data plots were integrated and updated every 6 hours via a daemon. The muon veto events (cf. Figure 6.3) and rates (cf. Figure 6.6) are updated for the current run and displayed on the LEGEND-200 monitoring dashboard (cf. Figures Figs. B.4 to B.6). If outliers occur in these plots, the corresponding PMTs are investigated further for potential malfunctions (cf. Section 6.2).

6.2 PMT stability during operation

Between p03 and p11, several outliers in the amount of integral light as a function of multiplicity (cf. Figure 6.3) and muon rate (cf. Figure 6.6) can be found. Each outlier can be attributed to instabilities or breaks of individual PMTs. These breaks manifest differently in the data, suggesting various causes. Monitoring systems allow the early detection of the decreasing signal quality of some PMTs, which can then be investigated further and, in case of a malfunction of the PMT, deactivated to prevent faux signals in the muon veto. However, some PMTs may break without prior indication.
During phy data acquisition for LEGEND-200 between p03 and p11, nine PMTs were removed from operation. They showed either a decreasing signal quality (often correlated with a decreasing gain) or failure (cf. Table A.3). These can be categorized into three types of PMT breaks based on their evolution of their signals prior to failure, which are described in more detail in the following sections.

6.2.1 Aging PMTs

PMTs are known to show signs of aging and gradual loss of data quality over time (e.g., a decreasing gain), primarily due to aging of the photocathode. Aging results in reduced signal quality, observable through decreasing gain at a supplied voltage, increasing anode current, and lowering rate of the PMT as shown in studies such as [76, 77, 78]. Between p03 and p11, two PMTs

of the LEGEND-200 muon veto showed this behavior, where PMT 704 serves as a representative example in the following.
PMT 704 was deactivated during p03 r003 on April 5th, 2023, following an increase in current over the previous days (cf. Figure 6.8a), while the supplied voltage remained constant (cf. Figure 6.8b). The current increase correlated with a rising dark count rate, indicating a malfunction of the PMT for instance due to enhanced thermionic emission from the photocathode (cf. Section 5.1.2).

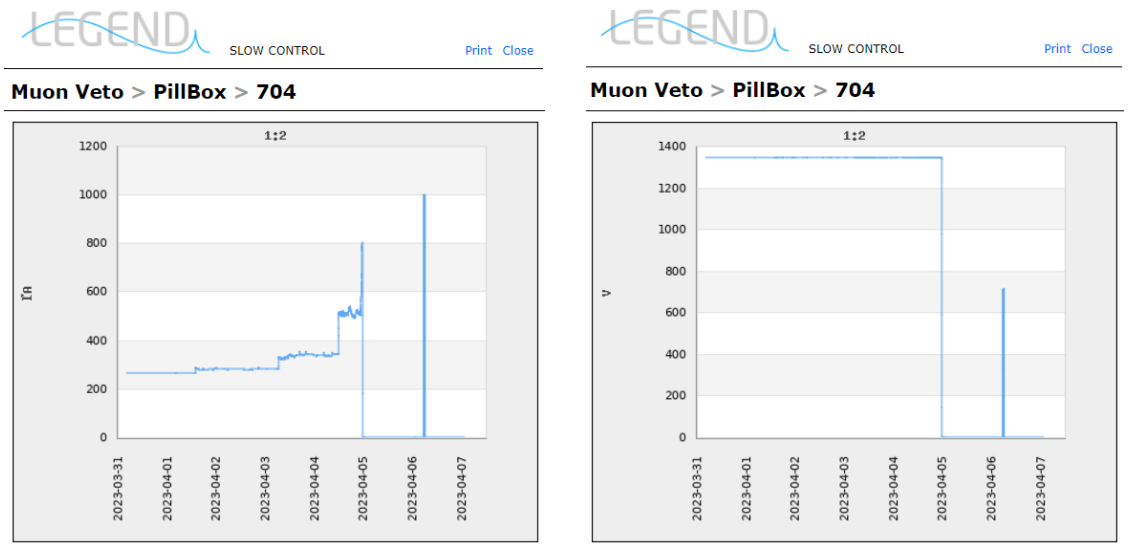

(a) (b)

Figure 6.8.: (a) Screenshot of the SlowControl monitoring displaying the increasing current of PMT 704 between March 31st, 2023 and April 7th, 2023. The PMT was shut down at reaching the in the SlowControl set overcurrent threshold of 600 μA to prevent the PMT from flashing. The increase of the current is correlated to a increasing dark count rate of the PMT and thus indicating a malfunction. The narrow peak on April 6th, 2023 was caused by a test during a calibration. (b) Screenshot of the SlowControl monitoring showing the supplied voltage of PMT 704 between March 31st, 2023 and April 7th, 2023, remaining constant during the increase of the current. The narrow peak on April 6th, 2023 was caused by a test during a calibration.

The PMT was deactivated from the overcurrent protection of the SlowControl on April 5th, 2023, after the current exceeded 600 μA. During a calibration on April 6th, 2023 a reactivation was attempted to confirm the persistence of the current increase and to rule out other causes. As the current immediately rose to 1000 μA and with that exceeding again 600 μA (cf. Figure 6.8a), it was decided to deactivate the PMT permanently and remove it from the DAQ.
The muon rates averaged over 6 hours of the single PMTs in p03 r003 are presented in Figure 6.9. The rate of PMT 704 starts to decrease on April 1st, 2023, simultaneously with the first increase of the PMT current (cf. Figure 6.8a). The rate increases during a spike at April 4st, 2023 and decreases again afterwards resulting in a rate around 0.1 mHz indicating background noise.

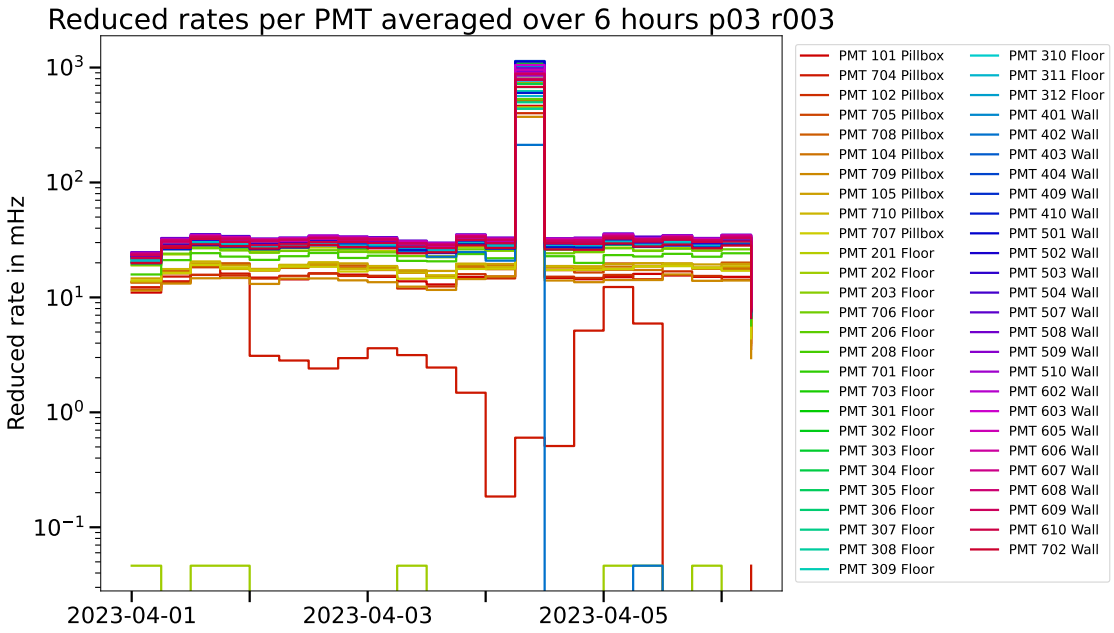

Figure 6.9.: PMT rate of events flagged as muon in p03 r003. PMT 202 (light green) and PMT 502 (dark blue) show a rate below 1 mHz, were turned off due to flashing (cf. Section 6.2.2) but not yet excluded from the DAQ at p03 r003. Due to electronic noise they were still able to generate a small rate during that time. PMT 402 (mid blue) shows a spontaneous outage after a spike in the rate (cf. Section 6.2.3). The rate of PMT 704 (red) decreases during the period, indicating aging properties.

Given the increasing current (cf. Figure 6.8a) and simultaneously decreasing rate (cf. Figure 6.9), PMT 704 and, with a comparable behavior, PMT 701 during p09 r000 are categorized as breaking due to aging. Since this type of PMT breaking does not cause any light signals in advance that can be detected by other PMTs, only faux events are generated during the failure. With that the data acquisition of the muon veto system is only affected with additional events at that time. Since the evolution of current and rate occurs gradually, it is possible to early detect aging PMTs and deactivate them as soon as this trend is observed in the LEGEND-200 monitoring dashboard and the SlowControl monitoring.

6.2.2 Flashing PMTs

Another type of broken PMTs in the LEGEND-200 muon veto system are flashing PMTs, a well-known phenomenon observed in other experiments [79, 80]. These PMTs exhibit spontaneous and unpredictable light emission, often caused by electrical discharges within the PMT or its voltage divider [81]. Because the emitted light is mainly detected by neighboring PMTs in the muon veto, the trigger conditions (cf. Section 5.2) may be fulfilled, causing the flash to be falsely identified as a muon event.

A flashing PMT typically causes spontaneous, recurring spikes in the muon rate as measured during p07 r001 (see Figure 6.10). For instance, a spike that affected all PMTs occurred on August 9th, 2023. Thereafter, the rate of PMT 311 dropped, followed by another spike a few hours later.

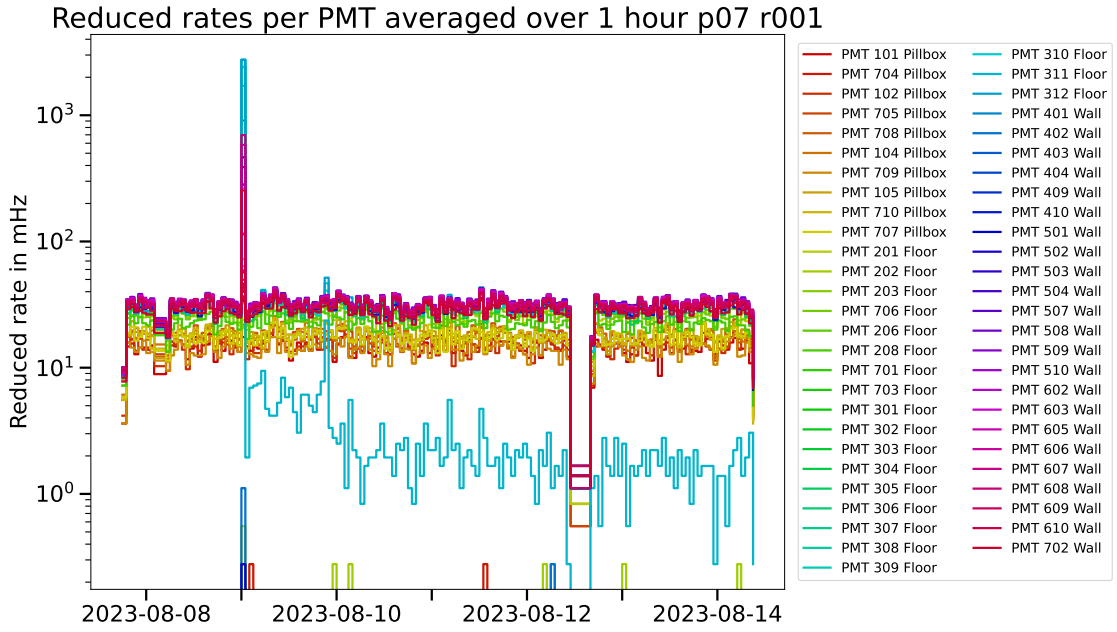

Figure 6.10.: Hourly PMT rate of p07 r001. After a spike on August 9th, 2023, the rate of PMT 311 decreased. The gap on August 12th, 2023, was due to a temporary outage of the ORCA DAQ system. Rates below 1 mHz indicate PMTs, which are turned off but not yet excluded from the DAQ. Due to electronic noise they were still able to generate a small rate during that time.

Flashing PMTs can also be identified by investigating the spatial light distribution among the muon veto PMTs as shown in Figure 6.11. This muon veto map shows the mean detected light in p.e. for each PMT, averaged over all events. During p07 r001, PMT 311 detects approximately one order of magnitude more events than the other PMTs, which confirms its flashing behavior. The directly adjacent PMTs 310 and 312 detect approximately twice as much light as the other PMTs due to the flashing of PMT 311.

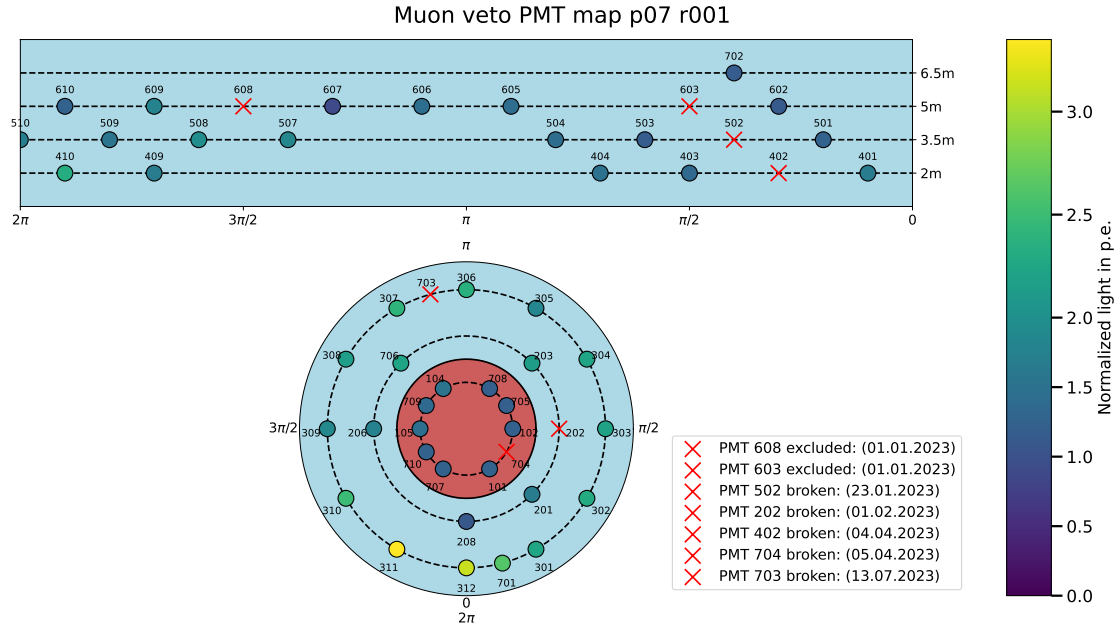

Figure 6.11.: PMT map showing the mean of the maximum pulse heights across all detected events for each PMT during p07 r001. For a better readability, the color bar was set to a maximum value of 3.3 p.e. The flashing PMT 311 has a maximum value of approximately 72.09 p.e. Two PMTs, marked as excluded, were turned off but not yet excluded from the DAQ. Five additional PMTs broke in later periods. PMT 311 shows one order of magnitude more light than the other PMTs. One of the directly neighboring PMT (312) shows events approximately twice as bright as the remaining PMTs.

Because the same PMT is repeatedly responsible for light production in case of flashing, the light is observed with similar intensity by the surrounding PMTs. This results in a narrow p.e. distribution with low-multiplicity in the two dimensional histogram of the integral light as a function of the multiplicity (cf. Figure 6.12). If the flash is sufficiently bright to exceed the p.e. range associated by low-energy muons, a cut on multiplicity and p.e. can be applied. Events generated by bright flashing PMTs can be rejected by conservatively using: multiplicity ≤ 13 and p.e. ≥ 98, as shown in Section 6.1.1.

A current indicative of flashing PMTs, as observed in aging PMTs and described in the previous Section, was not detected. The supplied current and voltage of flashing PMTs remain the same in the SlowControl monitoring during flashing. Once a flashing PMT has been identified, it is deactivated and excluded from the DAQ to prevent artificial dead time in the muon veto data acquisition. In between p03 and p11 four PMTs were identified as flashers in the muon veto and subsequently deactivated.

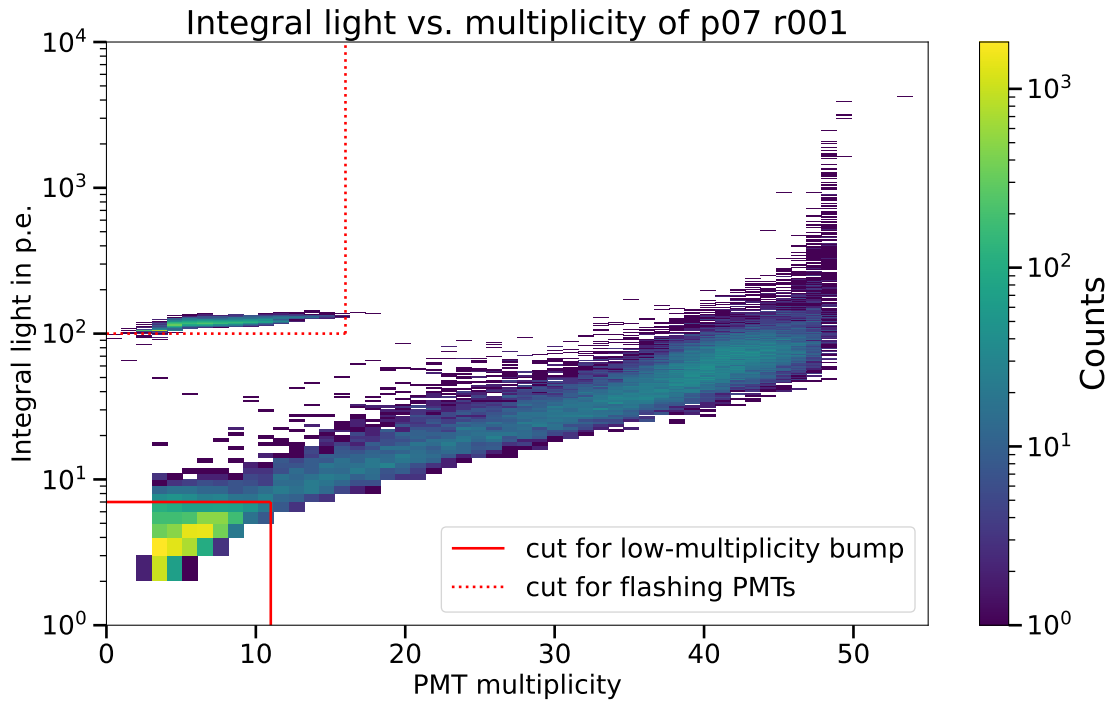

Figure 6.12.: Two-dimensional histogram of the integral light in p.e. as a function of the PMT multiplicity for p07 r001. The red solid line marks the cut for the low-multiplicity bump data. The red dotted line corresponds to the cut applied to flashes from PMT 311.

6.2.3 Spontaneously breaking PMTs

In addition to the previously discussed PMT malfunctions, a third type was observed in three PMTs between p03 and p11. This malfunction is characterized by a single spike in the rate of all PMTs in the muon veto, followed by a PMT no longer detecting any events (cf. rate PMT 402 (mid blue) Figure 6.9). This failure is not preceded by a previous change over several days in the muon veto monitoring systems and is thus classified as spontaneous PMT break. At the moment of the spike, the current rises sharply and the PMT is shut down by the overcurrent protection of the SlowControl on April 4th, 2023 (cf. Figure 6.13). The PMT was tested again during a calibration on April 6th, 2023 and immediately enters an overcurrent state as soon as voltage was supplied and thus, was excluded afterwards from the DAQ.

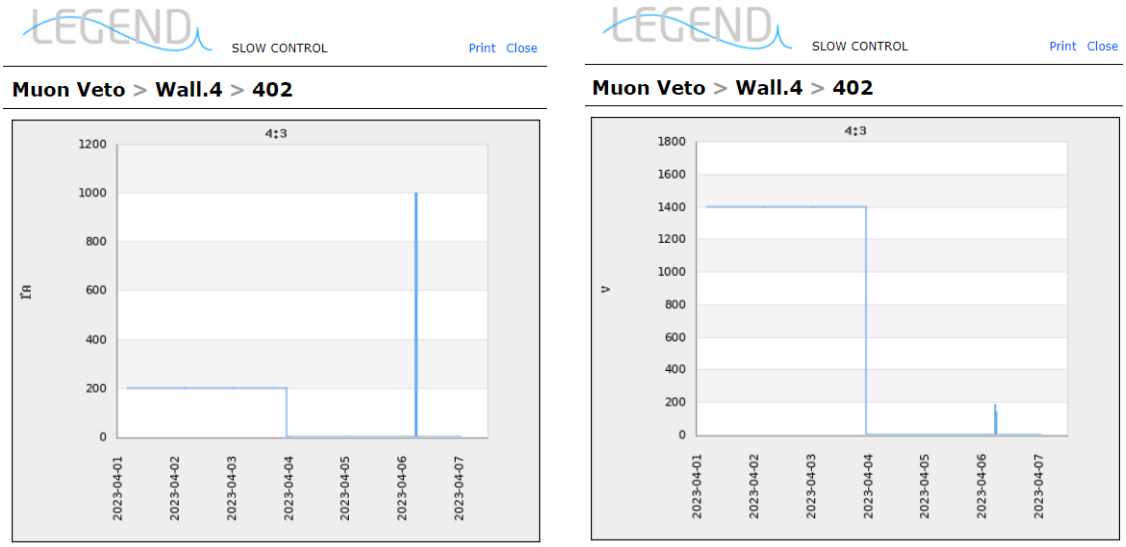

(a) (b)

Figure 6.13.: (a) Screenshot of the SlowControl monitoring showing the constant current of PMT 402 between April 1st, 2023 and April 7th, 2023. It suddenly turned off marking the random PMT break on April 4th, 2023. The narrow peak on April 6th, 2023 was caused by a test during a calibration. (b) Screenshot of the SlowControl monitoring showing the constant supplied voltage of PMT 402 between April 1st, 2023 and April 7th, 2023. The supplied voltage suddenly turned off showing the random PMT break on April 4th, 2023. The narrow peak on April 6th, 2023 was caused by a test during a calibration.

Unlike aging PMTs (cf. Section 6.2.1), the monitoring systems cannot predict spontaneous PMT failures in advance. However, a change in the waveform baseline was observed before all four spontaneous PMT breaks between p03 and p11. A few hours before a spontaneous PMT break, the baseline of the breaking PMT starts to increase overall, as shown in Figure 6.14. Shortly before the break, the baseline may rise repeatedly up to the saturation limit of the ADC. This produces light of varying intensity, which may be related to varying intensity of sparking in the PMT base and can be detected by the other PMTs, as shown by the spike in the rates at break.
One possible explanation for the baseline offset is the failure of the dielectric of a capacitor in the PMT base. This causes a high current to flow through the capacitor, which can lead to a short circuit, followed by a spark in the base, which is detected by the other PMTs via spiking in the rate. To confirm this hypothesis, the affected PMTs should be examined outside of phy data taking periods in the experiment. That could be done as soon as the water of the muon veto system is drained next time for instance to repair or replace PMTs (cf. Section 9.4).

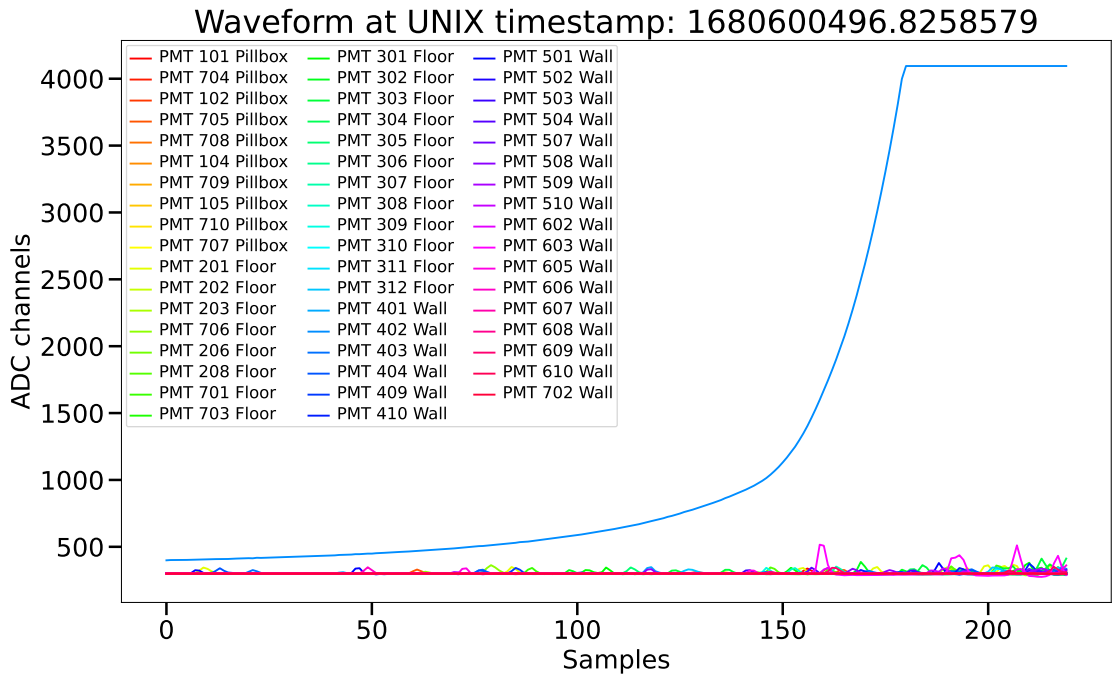

Figure 6.14.: Example of waveforms of all PMTs recorded a few hours before the break of PMT 402 on April 4th, 2023. The baseline of PMT 402 increases, probably due to a high current a the capacitor of the PMT base, and saturates at 4095 ADC channels.

6.3 Waveform based analysis

The investigation of the PMT waveforms allows for the classification of muon events as shown in Section 6.1.1 and the detection of spontaneously breaking PMTs (cf. Section 6.2.3). By analyzing the shape, baseline position and saturation of the waveforms between p03 and p11, additional waveform classes can be identified, as described in the following. That enables both the identification of further malfunctions of the PMTs and a PSD, which is used in the further analysis (cf. Section 6.3.3).

6.3.1 Waveform classes

The waveforms of the PMTs can be divided in four classes in total: muon-like, baseline offset, noisy and saturated, which are described in detail below.

Muon-like A PMT waveform is classified as muon-like, indicated by a short light event in the water tank, if during approximately 80 samples (320 ns) the trigger conditions are not met (cf. Section 5.2), and this is immediately followed by a rise in pulse height in several PMTs to a maximum. These maxima are followed by subsequent decreases in the peak amplitudes of the triggered PMTs in that waveform (cf. Figure 6.2). A minimum below the baseline (undershoot)

may follow a peak above the baseline due to the discharge of the capacitors in the base (cf. Figure 6.2 light blue waveform). The depth of the undershoot increases with the amplitude of the preceding peak [37]. Since the light produced by the muon via the Cherenkov effect reaches the PMTs within nanoseconds, such a waveform indicates a muon event. The maximum values of the waveforms depend on the energy of the muon and its path through the water tank.

Baseline offset A baseline offset in a PMT waveform, as illustrated in Figure 6.14, may indicate issues with the base, such as defective capacitors (cf. Section 6.2.3). Thus, waveforms where at least one PMT shows an offset from the baseline throughout the entire waveform are classified as baseline offset and indicate a malfunctioning PMT.

Noisy Figure 6.15 shows an example of a PMT waveform classified as noisy, exhibiting strong baseline fluctuations likely caused by electronic noise. It is empirically defined by the absence of peak amplitudes exceeding the other peaks in the waveform of the corresponding PMTs by a factor of seven. A lower threshold would risk misclassifying low-energy muons as noisy, as their maximum signal amplitude might not clearly stand out from the baseline. Additionally, the deviations from the baseline are nearly symmetric for maxima and minima.

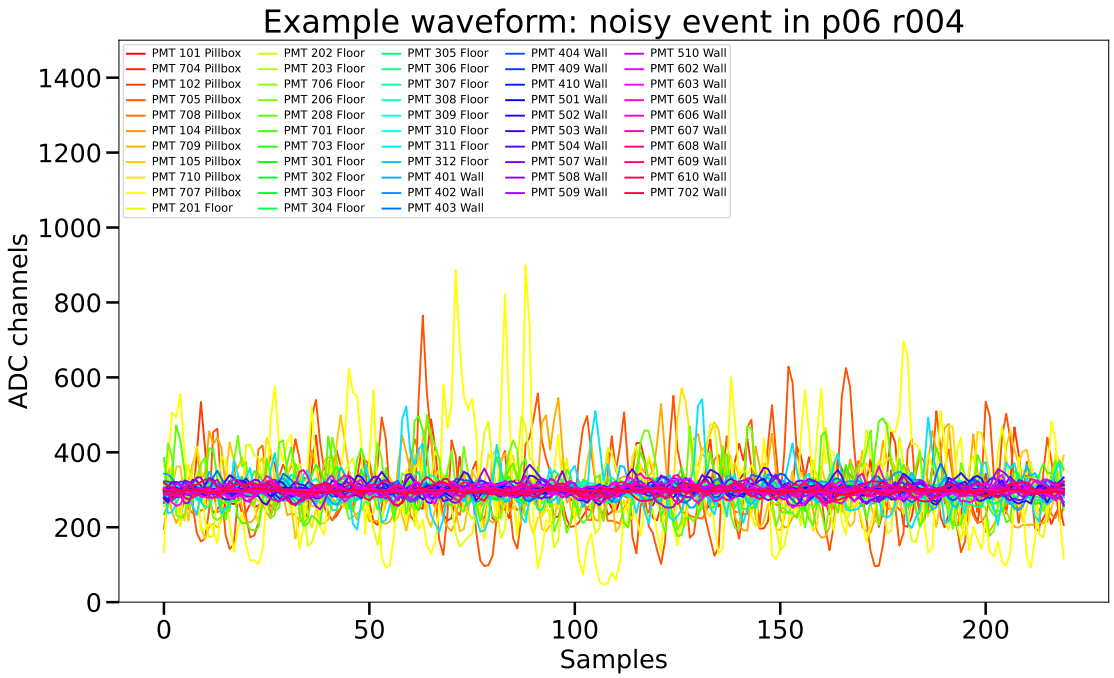

Figure 6.15.: Example of a waveform classified as noisy, showing no outstanding peak amplitudes and similar deviation from the baseline of maxima and minima within the waveform.

Saturated Saturated waveforms are classified by reaching at least one ADC channel limit as shown in Figure 6.16. Once the saturation occurs, the precise determination of the p.e. of the

corresponding PMT is not possible anymore. To improve that, the baseline was set higher to 1000 ADC channels in August 2023 as motivated in Section 5.3. This increases the number of waveforms saturated at the upper end, but reduces those saturated in the undershoot region. Since the undershoot amplitude is always smaller than the signal pulse amplitude, but increases proportionally with it due to the coupling capacitor charge in the base, the undershoot depth can be used to reconstruct the preceding signal height [82]. However, the peak reconstruction only led to a shift in the integral light in p.e. as a function of the PMT multiplicity histogram and did not allow for further classification as discussed in more detail in Section 6.3.2.
Saturated waveforms indicate bright, i.e., high-energy muon events. However, if only one PMT shows a saturated waveform and all other PMTs measure only a few p.e., there are two possibilities: a flashing PMT producing additional secondary electrons within the PMT with little or no light detectable by the other PMTs or a muon directly hitting the base of a PMT. Figure 6.17 presents an example of a waveform of a flashing PMT. In Section 6.3.3, the distinction of saturated events caused by muons and by flashing PMTs is made.

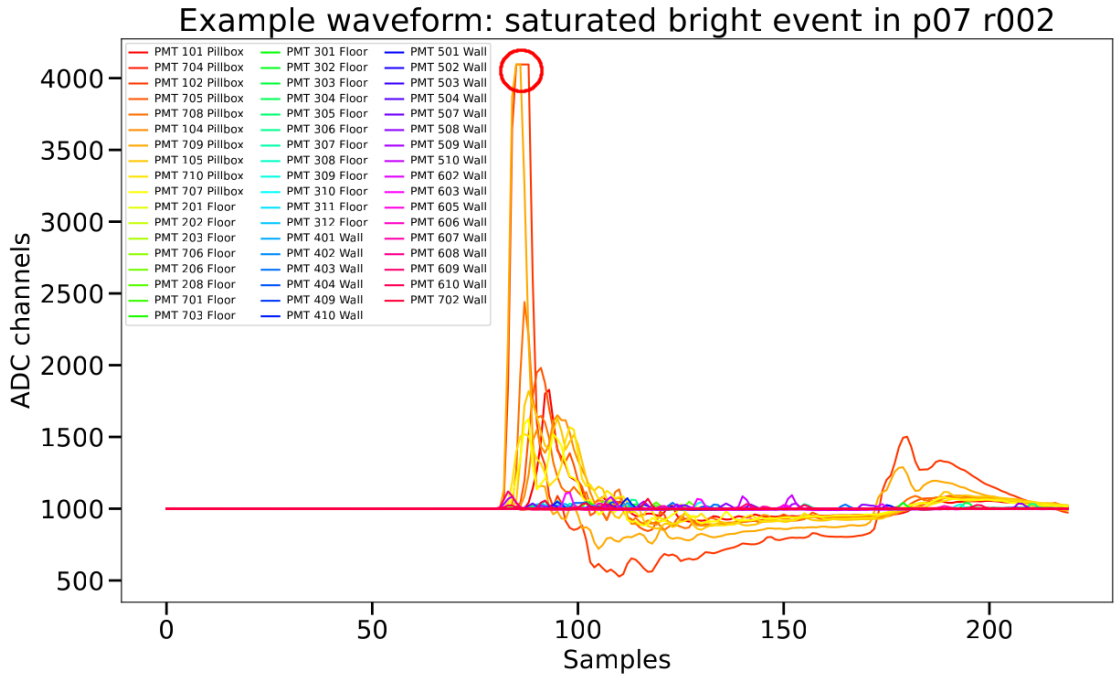

Figure 6.16.: Example of a saturated waveform, where one PMT show saturation in the upper ADC channel edge (marked with the red circle) inhibit the precise determination of the p.e. amount of the current event.

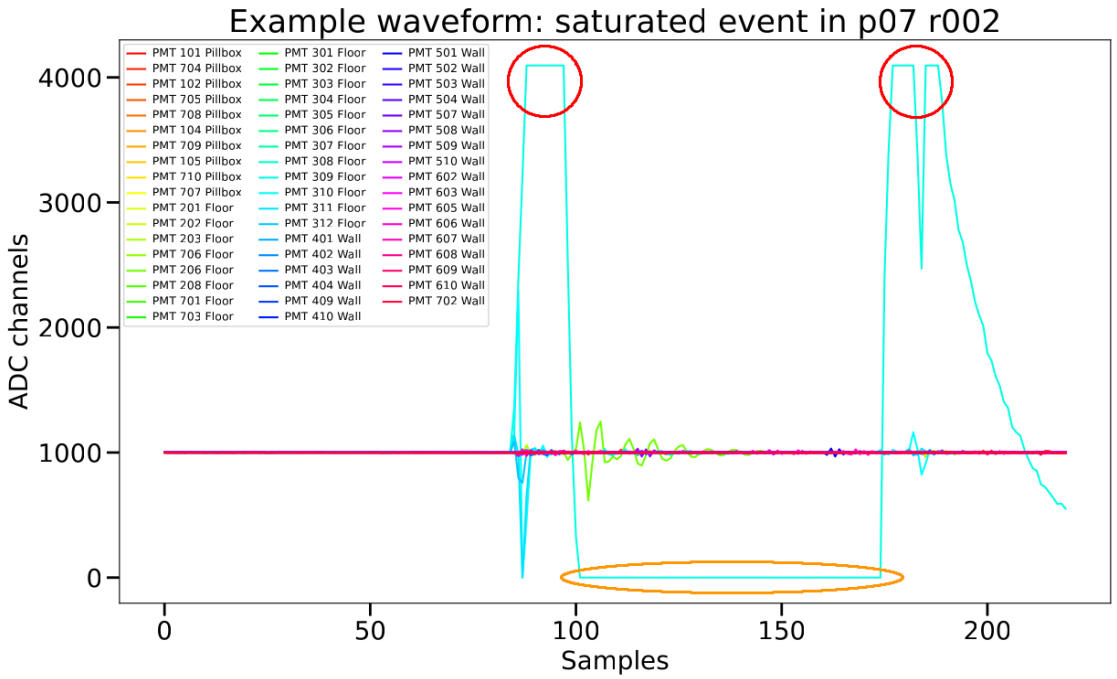

Figure 6.17.: Example of a saturated waveform, where PMT 309 shows three saturated regions, two in the upper edge (marked in red) and one lasting for more than 40 samples in the lower edge (marked in orange). The other PMTs remain unsaturated.

6.3.2 Undershoot analysis

The analysis of the undershoots was motivated by their potential to reveal new structures in the integral light in p.e. as a function of the PMT multiplicity histogram. This is should be enabled through the reconstruction of signal maxima saturated by the ADC limit. Although this limit is generally accepted, since the purpose of the muon veto is to provide a binary muon flag rather than an interaction classification of the muon, this study investigated whether further classification of the detected muons is feasible. Specifically, the possibility of the identification of showering muons is investigated, under the hypothesis that particle showers within the water tank would deviate from the typical Cherenkov light pattern due to the enhanced light production from additional pair production and bremsstrahlung processes (cf. Section 4.1.1). To obtain the proportionality constant between the signal and undershoot amplitudes, the slope between them can be determined for each PMT. In order to determine the signal amplitudes, the full minimum of the undershoot must be captured in the waveform. Therefore, the baseline of the PMTs was set to 1000 ADC channels in August 2023 in order to maintain the resolution up to 100 p.e. and to enable further reconstruction of the signal maximum via undershoots. Figure 6.18a represents the pulse minima as a function of the maxima and the corresponding linear fit and residuals of an example PMT channel in p07 r002. However, the data points exhibit increasing residuals from

approximately 1800 ADC channels signal height. This deviation is expected due to saturation at 3095 ADC channels, indicating a non-linear relationship between maxima and minima. Hence, the reconstruction of signal heights based on proportionality with the minima is not feasible.
As an alternative approach to determine the signal heights of saturated peaks, they were approximated using a Gaussian function fitted to the peak outside the saturation region, as illustrated in Figure 6.18b. The resulting Gaussian peak is taken as the reconstructed signal amplitude.

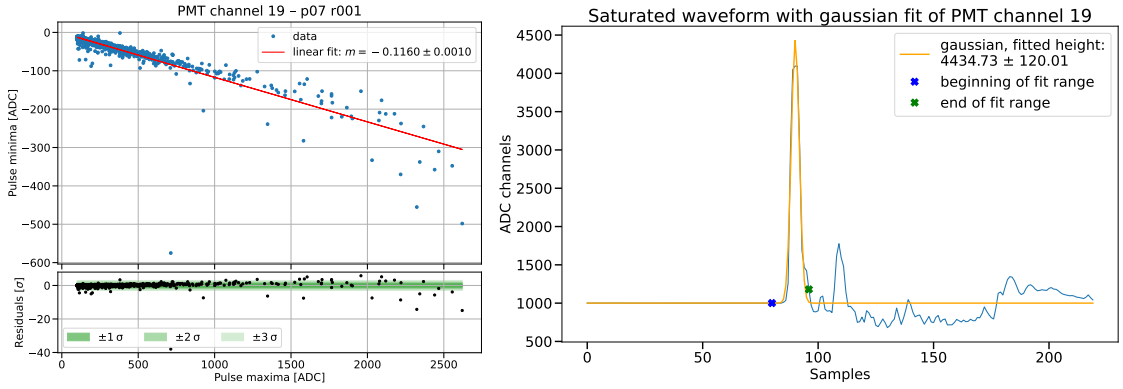

(a) (b)

Figure 6.18.: (a) Pulse minima as a function of the pulse maxima in ADC channels of PMT channel 19 of p07 r002 in blue. The red line indicates the linear fit. The residuals, with $\pm 2\sigma$, and $\pm 3\sigma$ bands shown in varying shades of, are displayed below. (b) Example of a saturated waveform of PMT channel 19 of p07 r002 in blue with fitted Gaussian distribution in orange. The blue and green crosses mark the beginning and end of the fitting range.

The reconstruction of the signal amplitude leads to an average increase of approximately 11.63 % in the integral light (in p.e.) per event with saturated waveforms, rising from 904.10 ± 2.48 p.e. to $1009.22^{+124.14}_{-86.09}$ p.e. Here, the symmetric uncertainty represents three times the standard deviation (3σ), corresponding to a 99.7 % CL of the baseline variation across events, while the asymmetric uncertainties reflect the fit errors. Figure 6.19 shows the PSD filtered (cf. Section 6.3.3) integral light in p.e. as a function of the PMT multiplicity for p03 to p11 without peak reconstruction and additional with new p.e. values after peak reconstruction of saturated waveforms. The reconstructed peak heights can not be distinguished from the saturated ones in that representation and with that no improvement of the classification is possible here.

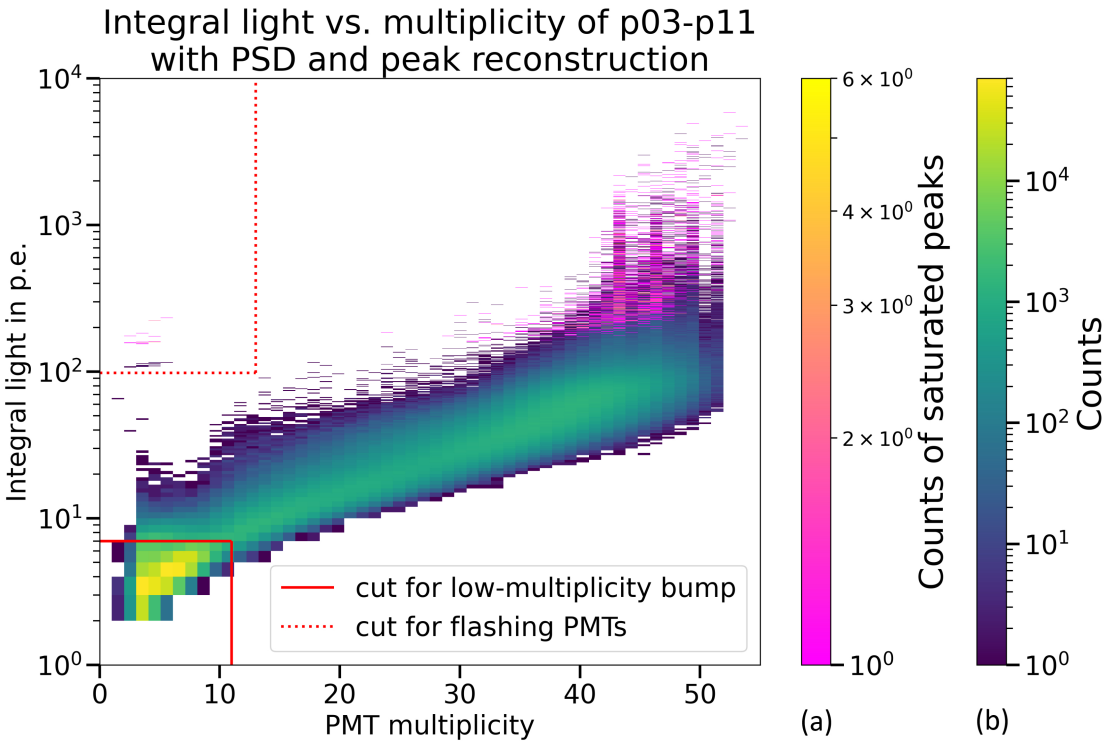

Figure 6.19.: Integral light in p.e. as a function of the PMT multiplicity, including PSD filtering (cf. Section 6.3.3), shown both and with (a) and without (b) reconstructed values for saturated waveforms for periods p03 to p11.

For a closer investigation the reconstructed peak heights are displayed as a function of the saturated peak heights in Figure 6.20. Only data after baseline increase in August 2023 is used to provide a clearer illustration of the peak reconstruction without the additional effect of the baseline shift. Two different branches can be distinguished in Figure 6.20, labeled as (a) and (b). Branch (a) shows flashing PMTs not filtered by the PSD, while branch (b) show bright events. All branches show a growing difference between reconstructed and saturated peaks with increasing p.e. number. This is to be expected, since the saturated peaks are limited in height, unlike the reconstructed ones. In summary, no new structure can be identified above the peak reconstruction. For this reason, the reconstructed peaks are not taken into account in the following analyses; instead, the saturated peaks are used.

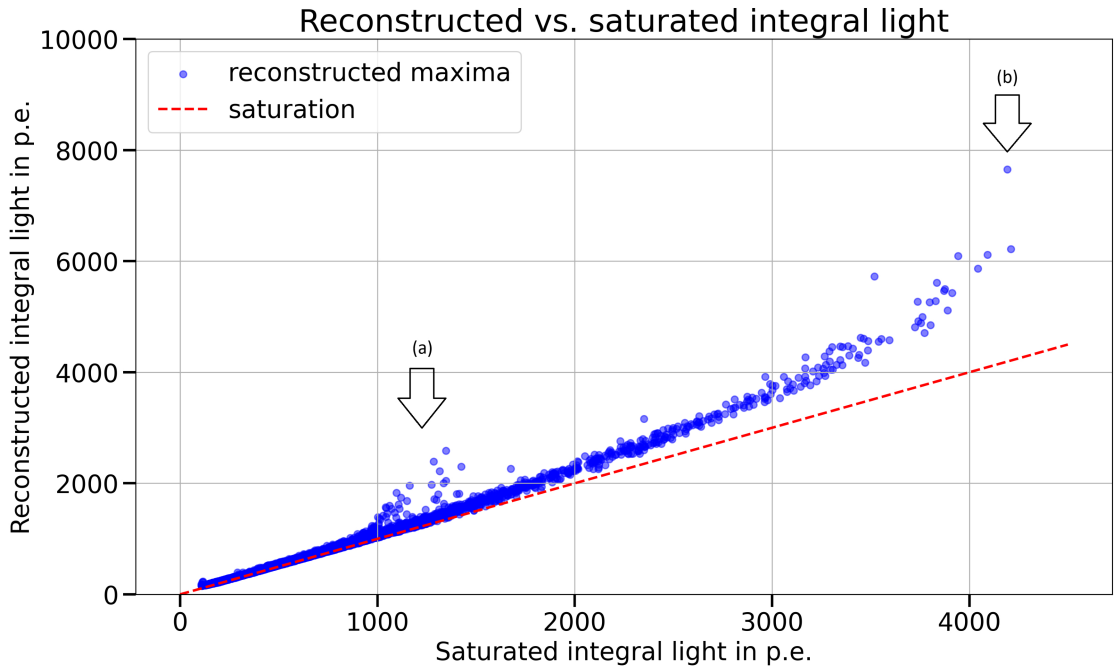

Figure 6.20.: Reconstructed integral light as a function of the saturated integral light in p.e. (blue dots) after the baseline increase in August 2023. Two different branches can be identified. Branch (a) is caused by flashing PMTs, while (b) is the result of bright (muon) events. The red dashed line marks the height of the saturated integral light. The difference on the y-axis between the reconstructed maxima and the red line shows the total amount of reconstructed light in the corresponding event. No unexpected structures are shown in this plot.

6.3.3 Pulse shape discrimination

To perform a PSD and filter malfunctioning PMT events based on their waveforms, the waveform classes introduced in Section 6.3.1 are used. Empirically, four different PSD cuts can be defined:

- Broken PMT base: waveforms that do not touch the baseline (cf. Figure 6.14), indicating a malfunctioning PMT base.
- Noisy: waveforms without a dominant peak. A dominant peak is defined as a maximum exceeding seven times the mean of the amplitude peaks of that waveform (cf. Figure 6.15), likely caused by electronic noise or PMT afterpulsing.
- Non-physical noisy: noisy waveforms whose maximum amplitude is below 1 p.e., likely due to electronic noise. The term "non-physical" refers to the lack of a real light-induced signal capable of passing the trigger threshold.
- Flashing PMT: a single saturated PMT with two upper-edge and one lower-edge peaks that persist for at least 40 samples (cf. Figure 6.17), caused by a flashing PMT.

The different PSD cuts are presented in Figure 6.21, showing the events filtered by each cut in the integral light in p.e. as a function of the PMT multiplicity histogram for period p03 to p11. Additional time-selection cuts are applied to time intervals with flashing PMTs that are not clearly identified by the PSD cuts. In total, four time intervals are excluded, summing to 6718 s as shown in Table 6.1.

Table 6.1.: Time-selection cuts of the muon veto in between p03 and p11. The PMT channel refers to the malfunctioning PMT causing the signals.

PMT Channel	Period	Run	Start time [UNIX]	End time [UNIX]	Duration [s]
31	p03	r003	1680600496	1680600499	3
17	p06	r004	1689230497	1689230512	15
40	p08	r014	1704250000	1704253200	3200
40	p08	r014	1704285000	1704288500	3500

Since events with low light production in the water tank or very bright signals that saturate PMTs and ADCs can also fall into most of the PSD cuts, these are only used for muon veto internal analyses and are excluded from the data processing chain to avoid faux event rejection. However, the non-physical noisy cut is included in the data processing chain, as it only affects events that do not exceed the trigger threshold and are thus considered non-physical, indicating electronic noise. The remaining events after applying all the cuts are subsequently classified as muon events or, for multiplicity ≤ 11 and p.e. ≤ 7 (cf. Section 6.1.1), as low-multiplicity bump events, which form the basis for further analyses.

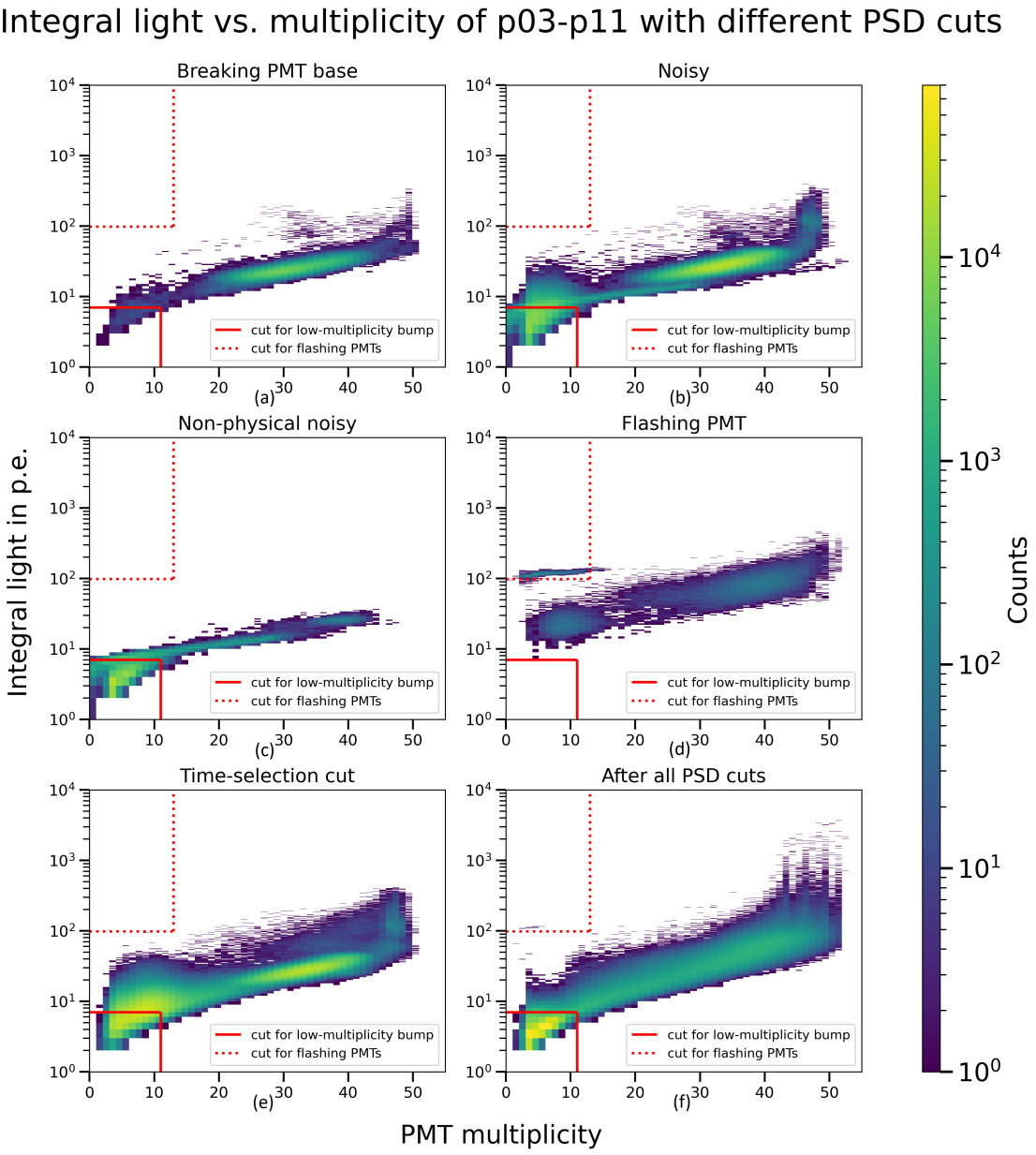

Figure 6.21.: Integral light in p.e. as a function of the PMT multiplicity histogram of p03 to p11 with different PSD cuts. Events classified as caused by a breaking PMT base are shown in (a) and (electronic) noise in plot (b). Non-physical noisy event PSD (c) is introduced in the processing chain. Plot (d) and (e) show events caused by flashing PMTs and events in the time-selection cut. After all PSD cuts (f) the muon branch is left over including events in the low-multiplicity bump.

6.4 Coincident event analysis

In order to investigate the correlation between muon-induced energy depositions in the HPGe detectors and their corresponding signatures within the muon veto system, a coincidence analysis

is performed. An event is considered to be coincident if a muon veto timestamp can be assigned to a matching HPGe event according to Section 6.1.2. Since the analysis of the HPGe events from p10 and p11 is not yet finalized at the time of writing of this work, only p03 to p09 are considered in the coincidence analysis. In total, 13823 coincident events between HPGe detectors and muon veto system were detected within that time interval, leading to a rate of $r_{\text{coincident}} \approx 0.62\,\text{mHz}$ as shown in Figure 6.22. Approximately 15.93 % of the events can be classified as valid HPGe events, meaning they pass the HPGe PSD criteria and have a HPGe multiplicity value of one HPGe detector (cf. Section 4.3.1), with a rate of $r_{\text{valid, coincident}} \approx 0.10\,\text{mHz}$.

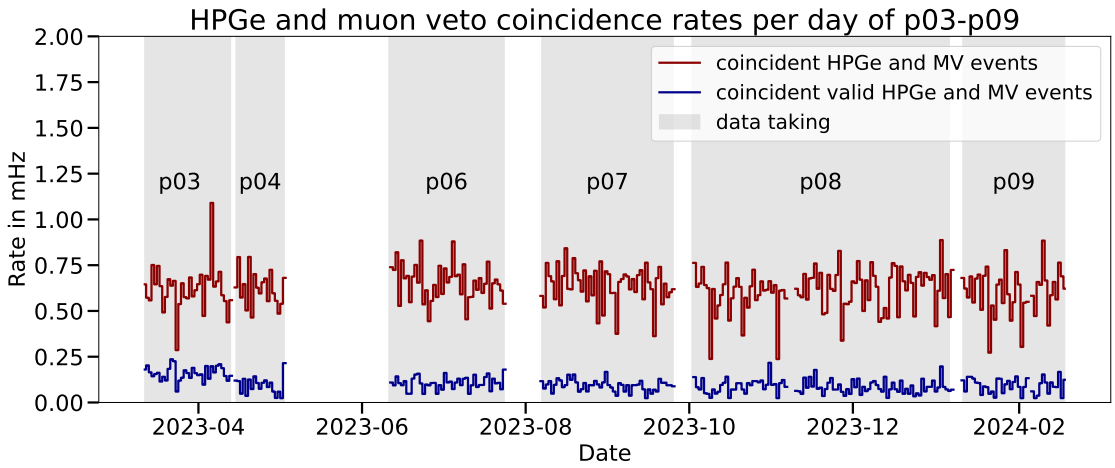

Figure 6.22.: Coincidence rate of HPGe events with muon veto events in red and valid HPGe events with muon veto in blue.

The rate of the random coincidences can be estimated using

$$r_{\text{random}} = t_{\text{HPGe}} \cdot t_{\mu} \cdot \Delta t\,, \tag{6.1}$$

where $t_{\text{HPGe}} \approx 350\,\text{mHz}$ (or $t_{\text{HPGe}} \approx 150\,\text{mHz}$ for valid HPGe events) corresponds to the HPGe rate, the muon rate is considered to be $t_{\mu} \approx 35\,\text{mHz}$ (cf. Section 6.1.1) and by a coincidence window of $\Delta t \approx 2.3841 \cdot 10^{-5}\,\text{s}$ (cf. Section 6.1.2). Using Equation 6.1 results in a random coincidence rate $r_{\text{random}} \approx 2.92 \cdot 10^{-4}\,\text{mHz}$ for all HPGe events and $r_{\text{random}} \approx 1.24 \cdot 10^{-4}\,\text{mHz}$ for valid HPGe events.

Separated into the PMT distribution areas of the muon veto system (cf. Section 5.2), Figure 6.23 shows the coincident events between HPGe detectors and muon veto system in terms of integral light in p.e. as a function of the PMT multiplicity histogram. The PMTs on the wall alone are capable of detecting 99.01 % of events coincident with the HPGe detectors, while the PMTs on the floor can detect 97.75 % and the pillbox 66.22 %. All events coincident between the HPGe detectors and the muon veto system fall within the muon branch outside the cuts and most of

them are around a multiplicity of 40 and an integral light of 60 p.e.. Accordingly, coincident HPGe detector and muon veto events are mainly bright events and are recorded across all PMT distribution areas of the muon veto.

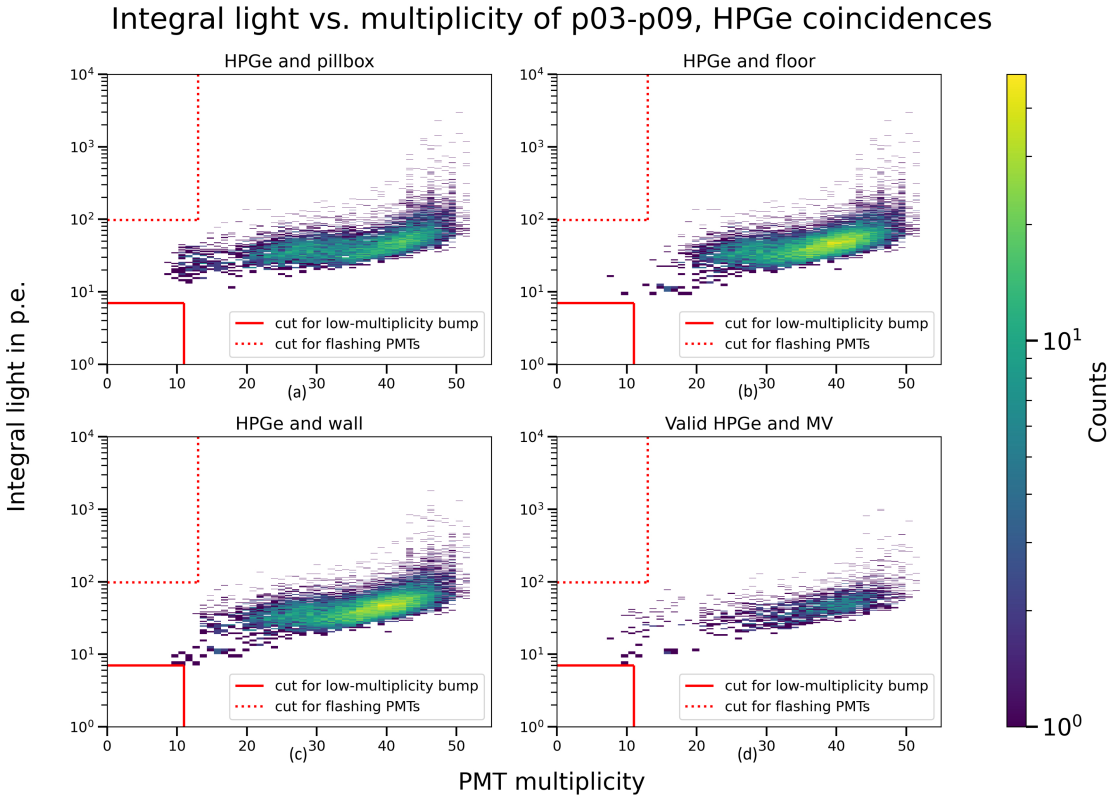

Figure 6.23.: Histogram of integral light in p.e. as a function of the PMT multiplicity for events coincident with (valid) HPGe events divided into different muon veto areas of p03 to p09. Plot (a) shows coincident events between HPGe detectors and events triggered in the pillbox. Correspondingly plot (b) represents coincident events between HPGe detectors and events triggered in the floor and (c) displays coincident events between HPGe detectors and events triggered in the wall. (a), (b) and (c) show both overlapping and distinct events, demonstrating the necessity of considering all PMT distribution areas. Events passing the PSD of the HPGe detector signals (cf. Section 4.3) are most important for the $0\nu\beta\beta$-decay analysis and referred to as valid HPGe events. Their coincidences with events triggered in the entire muon veto system are shown in plot (d).

However, combining events detected in the pillbox and wall area allows for the detection of 99.99 % of the coincident events. The pillbox and floor combination reaches 99.95 % and floor and wall 99.10 %, respectively. This highlights the key role of the pillbox in detecting muons entering through the cryostat neck.

6.4.1 Coincidence cut and muon-induced background index

All events triggering the muon veto and passing the cuts for the low-multiplicity bump, flashers, and the non-physical noisy PSD are considered as muons in the analysis chain and used for the anti-coincidence cut with the HPGe events. The resulting HPGe energy spectrum from p03 to p09 is shown in Figure 6.24 in counts per 10 keV as a function of the energy in keV. The gray line represents the unfiltered HPGe energy spectrum, including muon events and showing the $\beta\beta$-decay spectrum below 2000 keV of ^{76}Ge and the $0\nu\beta\beta$-decay analysis window (cf. Figure 4.2). The green line shows the coincident muon veto and HPGe events, while the red line illustrates the events that are coincident with the muon veto and valid HPGe events, which are the same events shown in Figure 6.23 lower right. Eight events below 1000 keV, shown in blue, are coincident between valid HPGe events and the muon veto, but not with the LAr instrumentation. Since the muon veto PSD cuts are not included in the data processing chain, as described above, these events still require a verification to ensure that they were not caused by PMT malfunctions.

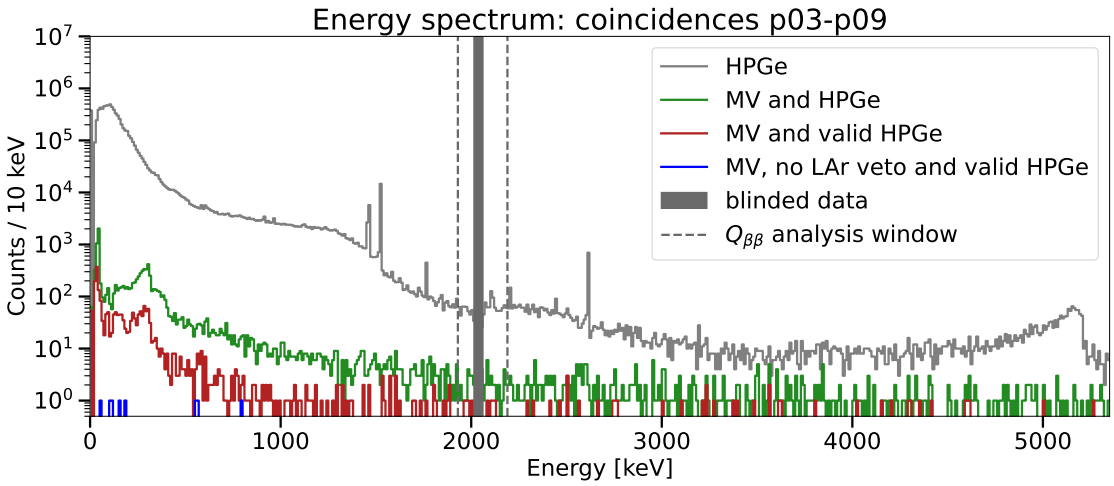

Figure 6.24.: HPGe energy spectrum in counts per 10 keV as a function of the energy in keV between p03 and p09. The pure HPGe data is shown with the gray line, the green line represents the data coincident with HPGe and muon veto (MV), valid HPGe and muon veto events are shown in red, and valid HPGe events coincident with the muon veto and not detected by the LAr instrumentation are illustrated in blue. The gray bar marks the blinded energies, while the gray dashed line refers to the $Q_{\beta\beta}$ analysis window.

Figure 6.25 shows the coincident events within the energy spectrum between valid HPGe events and the various muon veto cuts as well as the PSD. It indicates coincidences among events excluded by the flashing PMT or noisy PSD and time-selection criteria. In total 109 of 2202 coincident valid HPGe and muon veto events (approximately 4.95 %) can be found in the muon veto cuts. Two of these are among the coincident events between valid HPGe and muon veto events, which are not detected by the LAr instrumentation. One of them falls within both the noisy PSD

the time-selection cut, and the second one only within the time-selection cuts. Accordingly, these two events cannot be regarded as undetected by the LAr instrumentation, as they could have been caused by malfunctions of the PMTs.

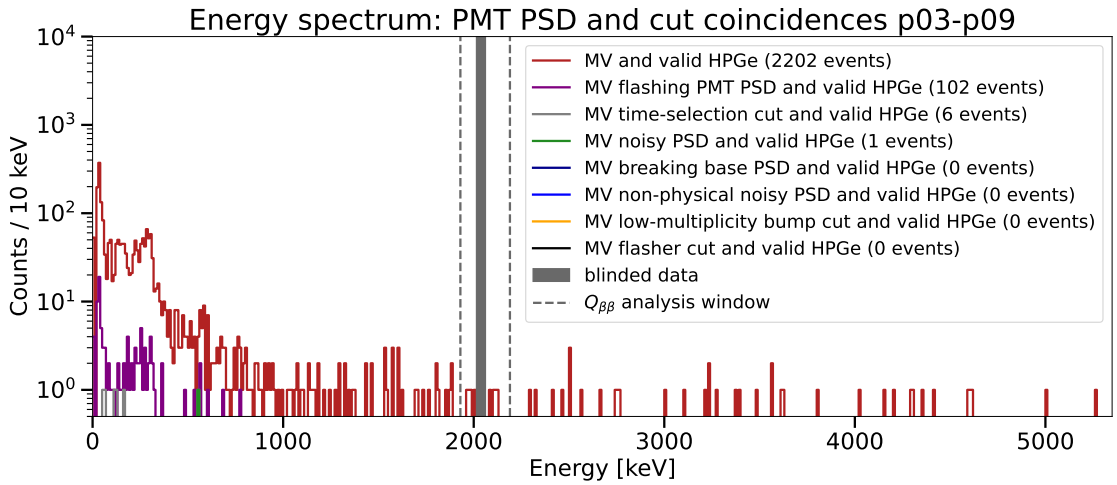

Figure 6.25.: HPGe energy spectrum in counts per 10 keV as a function of the energy in keV in between p03 and p09. The red line shows valid HPGe events coincident with the muon veto (MV). Coincident valid HPGe and flashing PMT PSD events are represented in purple, coincidences with the muon veto time-selection cut in gray and with noisy PMT PSD events in green. The remaining PSD and cuts have no coincident valid HPGe events. The gray bar marks the blinded energies, while the gray dashed line refers to the $Q_{\beta\beta}$ analysis window.

Assuming a flat spectrum, the six remaining events would lead, without the muon veto anti-coincidence cut, to a BI of

$$\frac{6}{5350\,\text{keV} \cdot 61\,\text{kg} \cdot \text{yr}} \approx 1.84 \cdot 10^{-5} \frac{\text{cts}}{(\text{keV} \cdot \text{kg} \cdot \text{yr})} \tag{6.2}$$

(cf. Section 4.3).

Figure 6.26 shows valid HPGe events induced by muons within the ROI of the energy spectrum. The ROI is defined as the energy range of 240 keV between 1930 keV and 2190 keV without the ±5 keV range around the ^{208}Tl γ-ray full energy peak (FEP) at 2104 keV and the ^{214}Bi γ-ray FEP at 2119 keV. Data in the energy range ±25 keV around $Q_{\beta\beta}$ is blinded for the analysis to prevent any biasing in the cuts. Within that energy range the muon veto system identifies two events as muons [83]. The muon-induced background would lead to an estimated BI of approximately $5.46 \cdot 10^{-4}$ cts/(keV · kg · yr) in the ROI, which is in good agreement to the measured muon-induced background in GERDA of $6.34 \cdot 10^{-4}$ cts/(keV · kg · yr) [1].

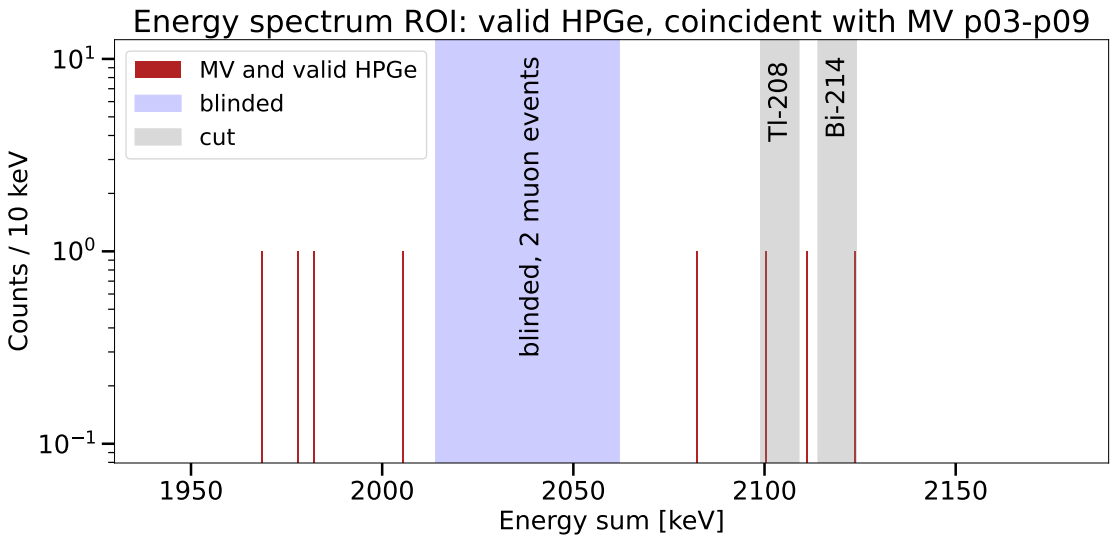

Figure 6.26.: Energy spectrum of muon events coincident with valid HPGe events in the ROI between 1930 keV and 2190 keV. The blue box marks the blinded window of an energy range ±25 keV around $Q_{\beta\beta}$, including two additional coincident muon events, and the gray boxes represent the cuts for the γ-ray FEPs of ^{208}Tl and ^{214}Bi.

Chapter 7

Monte Carlo simulation of the LEGEND-200 muon veto

"Damit das Mögliche entsteht, muss immer wieder das Unmögliche versucht werden."

— Hermann Hesse, Brief an Wilhelm Gundert

To gain deeper insight into the experimental data, detector performance and optimization potential, Monte Carlo simulations of LEGEND-200 are performed. The simulation toolkit Geometry and Tracking (Geant4) is used for this purpose and is further adapted to meet the specific requirements of the experiment. As part of this work, the simulation geometry of the muon veto was implemented and different simulations were performed.
The following chapter introduces the simulation framework, outlines the implemented simulation geometry of the muon veto, including the reflective foil VM2000 and the modeling of the PMTs, and concludes with a rough estimation of the muon veto efficiency.

7.1 Simulation framework

The current LEGEND-200 simulations are based on the Geant4 simulation toolkit developed at CERN. This object-oriented C++ software toolkit is implemented to perform Monte Carlo simulations of particles passing through matter. It enables the simulation of complex geometries and offers particle tracking, visualization, and event recording [84, 85, 86]. Additionally, Geant4 provides the possibility to be incorporated into other computational frameworks, which is done by the simulation framework "remage" [87]. This framework is specialized for Germanium experiments and collaborates with various related projects for simulations of the LEGEND experiment. In this work, remage was used in combination with the projects

- legend-pygeom-optics [88], which provides optical properties for the simulations,
- legend-pygeom-tools [89], which offers different implementation and visualization tools,
- and legend-pygeom-l200 [90], including the geometry of LEGEND-200.

To simulate muons with energy and angular distributions adapted to underground laboratory conditions, the MUon Simulations UNderground (MUSUN) generator was used. It samples a predefined number of muons within a user-defined rectangular volume around the experiment inside the laboratory, assuming a mean muon energy of approximately 270 GeV for the LNGS [91]. These muons are subsequently propagated through the LEGEND-200 geometry using remage, and the resulting events are stored in HDF5 format as the phy data (cf. Section 6.1). After post-processing (cf. Section 7.3), the data is analyzed similarly to the procedure described in Section 6.1. To provide the possibility of comparison with the real data, the amount of simulated muons is adapted to the amount of detected muon events in run p03 r002, which is used for the comparison as discussed in Section 8.1. Approximately 20,000 muons are detected within one run by the real system. Using the PDE maximum as an estimation of the muon detection efficiency of the muon veto system $\mathrm{PDE}_{\mathrm{max}} = \mathrm{QE}_{\mathrm{max}} \cdot \mathrm{CE}_{\mathrm{max}} = 30\,\% \cdot 85\,\% = 25.5\,\%$ (cf. Section 5.1.2), a muon detection efficiency of about 25 % of simulated muons is estimated. Therefore, to reproduce 20,000 detected muons, 80,000 muons are simulated to estimate one run.

7.2 Simulated muon veto geometry

As part of this work, the geometry of the water tank, including the muon veto instrumentation was added to legend-pygeom-l200, while the necessary optical components were implemented in legend-pygeom-optics. The water tank and its instrumentation are based on the geometry used in Majorana-Gerda (MaGe) [92], a simulation framework developed for MAJORANA, GERDA, and early LEGEND-200 simulations, but was significantly adapted, improved, and extended in this work. The geometry was implemented using the pyg4ometry package [93] for modeling simulation geometries with Python.

The water tank was implemented using the stainless steel predefined by Geant4, as the exact material composition of the stainless steel is unknown and the definition of the optical surface properties is independent of the underlying material. Inside, the tank is covered with VM2000 (see Section 7.2.1), which forms the relevant surface for optical simulations in the water tank. The tank was filled with water, which is sealed at the top by an air buffer (in the real muon veto system it is a nitrogen buffer, but that does not affect muon simulations). The absorption length of the simulated water is based on a study of Mason et al. [94]. It is defined for wavelengths between 100 nm and 600 nm (covering the PDE range of the PMTs as discussed in Section 5.1.2), beginning with 0.1 μm absorption length, increasing to 100 m between wavelengths of 350 nm and 450 nm and decreasing afterwards to 10 m (cf. Figure C.1). Wavelengths outside the defined range are set

to the next defined value. The implemented refractive index of water is set to $n_{\text{water}} = 1.33$. The cryostat containing the LAr volume, its instrumentation, and the HPGe strings is located within the water and air buffer. The pillbox volume is located directly below the cryostat, featuring two manholes, which connect the optical volumes of the water tank and pillbox. The inner and outer sides of the pillbox are covered with VM2000 as well as the outer side of the cryostat. The PMTs (see Section 7.2.2) are placed on the VM2000 along the inner walls of the water tank, the floor and on the inner side and floor of the pillbox. Figure 7.1 shows a visualization of the complete simulated LEGEND-200 geometry.

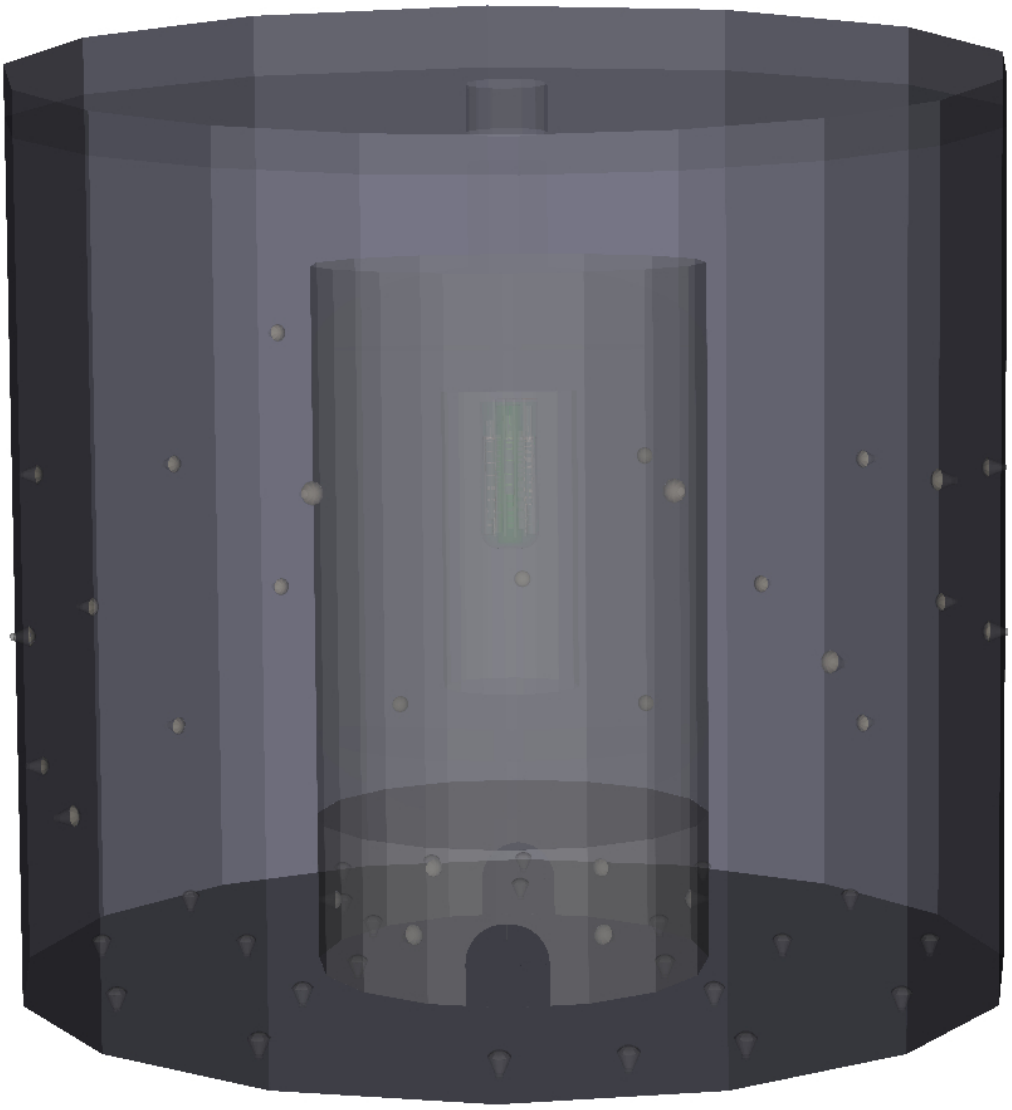

Figure 7.1.: Visualization of the LEGEND-200 simulation geometry. The water tank, including the muon veto instrumentation, surrounds the cryostat, which houses the LAr instrumentation and HPGe detector strings. The apparent protrusion of the PMT encapsulations from the tank wall is a visualization artifact. In the simulation, they are fully contained within the water volume.

7.2.1 Modeling of the reflective foil

As described in Section 5.1.1, the reflective foil VM2000 covering the inside of the LEGEND-200 water tank consists of PMMA and PEN layers. Since a precise implementation of these layers would increase the computational time of Geant4 simulations, the simulation geometry uses a simplification of the foil layers. To model the scintillation properties of the PEN layers, they are combined into a single PEN layer with a thickness of 40 μm in the simulation. The corresponding electron scintillation yield for PEN as a function of the wavelength is shown in Figure 7.2a. Its peak is located at a wavelength of 420 nm, matching approximately the maximum of the QE of the PMTs. Since only the electron scintillation is known experimentally [63], the scintillation yields for alpha particles, deuterons, ions, protons and tritons are not important for the simulation.
The WLS properties of the simulated VM2000 are presented in Figure 7.2b as two-dimensional histogram showing the emission wavelength as a function of the absorption wavelength. Only wavelengths below 380 nm are absorbed and re-emitted in the range between 400 nm and 600 nm with the maximum around 400 nm matching the PMT QE maximum.

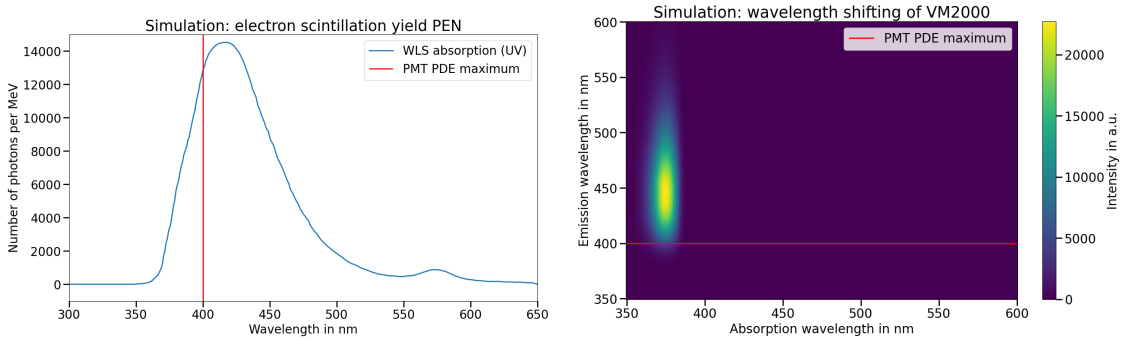

(a) (b)

Figure 7.2.: (a) Electron scintillation yield for PEN per MeV as a function of the wavelength in nm used for the VM2000 simulation. The peak is around a wavelength of 420 nm, which matches approximately the maximum of the QE of the PMTs shown by the red line. (b) Simulated VM2000 WLS properties as a two-dimensional histogram of the emission wavelength as a function of the absorption wavelength. Wavelengths below 380 nm are absorbed and shifted to a range between 400 nm and 600 nm with the maximum around 400 nm, which matches the PMT QE maximum (red line).

The simulated surface of the VM2000 exhibits a reflectivity of 95 % for visible light (above a wavelength of 370 nm) and 12 % for UV light (below a wavelength of 370 nm) according to the measurements of Geis et al. [61]. To ensure a conservative estimate, the lowest measured reflectivity values were applied in the simulation.

7.2.2 Photomultiplier tube configuration

The simulation geometry of the PMTs accounts for the optical properties of the acrylic cap, the intermediate air gap, the borosilicate glass, and the photocathode, while omitting the electronic components. Inside the simulated steel encapsulation, neither the dynode structure, the PMT base, nor the μ-metal shielding are implemented, as they are not relevant for the detection efficiency investigated in this work. The photon detection occurs entirely at the photocathode. Figure 7.3 shows a rendering of a visualized simulated PMT. The different layers at the cap represent the various materials used, considering the size and curvature of the photocathode given in the data sheet [64] (cf. Figure C.2). The steel encapsulation is approximated by a steel cone and cylinder to ensure the correct distance between the photocathode and the mounting surface and to prevent photons from reaching the photocathode from below.

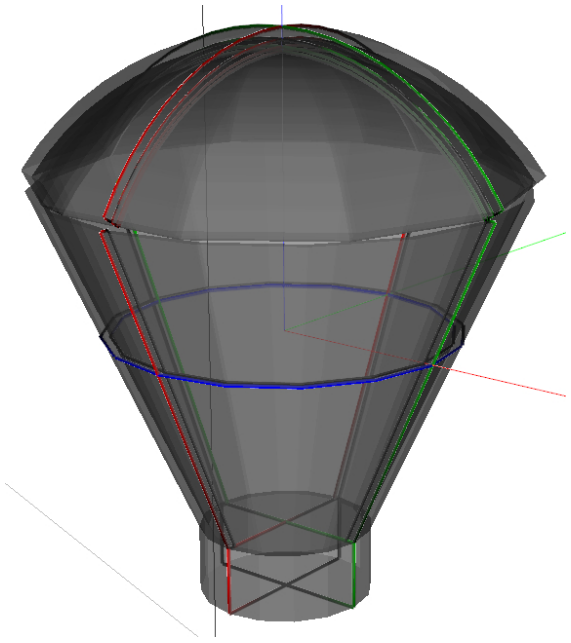

Figure 7.3.: Visualization of a PMT geometry simulated in legend-pygeom-l200, including the acrylic cap and air gap between the borosilicate glass of the PMT and steel encapsulation [90]. The small gap between cap and encapsulation of the PMT is a visualization artifact and not implemented in the simulation. The red, green and blue lines mark the zero of the x-, y- and z-axis of the geometry.

To enable an optical simulation of Geant4, the refractive index and absorption length of the materials used must be defined, which are summarized in Table 7.1.

Table 7.1.: Optical properties of the simulated acrylic cap, air gap and borosilicate glass. The absorption length of the materials is estimated and, for acrylic and borosilicate glass, given as a range over the photon energy between 1 and 6 eV.

Material	Refractive index	Absorption length [m]
acrylic	1.489	2.5-3.5
air	1.000	100.0
borosilicate glass	1.490	2.0-3.0

The photocathode is implemented as a detector surface and placed on the inner side of the borosilicate glass. If a simulated photon passes the acrylic cap, air gap and borosilicate glass of the PMT, it hits the photocathode. Here, it is absorbed and detected according to the wavelength, taking into account the PDE (cf. Section 5.1.2). The CE is estimated to 85 %, while the QE is provided by the data sheet [64] (cf. Figure 5.3). A detected photon is recorded as muon event once it meets the implemented trigger conditions described in the following section.

7.3 Event building and post-processing of simulated muons

As in the real system (cf. Section 5.2), trigger conditions must be met for an event to be recorded in the simulated muon veto. Since the simulated PMTs do not include an electronic simulation, the detection of a non-integer amount of photons is not possible. Therefore, the trigger threshold is set to one detected photon (corresponding to 1 p.e.) per PMT in the simulation. The multiplicity condition and trigger time window are identical to those of the real system. A simulated event is therefore recorded, if at least six PMTs in the pillbox or four on the floor or wall, each detect at least one photon within 60 ns.
If the trigger conditions are met, all photons subsequently detected by the PMTs are recorded. To approximate a realistic signal and account for additional PMT, DAQ, and ADC properties as well as processing chain parameters (cf. Section 6.1), each events is post-processed.

PMT properties The SPP is modeled using a normal distribution. Each detected photon is spread around a mean value of 1 with a standard deviation of 0.4 according to the fitted values of the SPP during a calibration (cf. Section 5.3). This transforms the integer p.e. counts of the simulation into a continuous distribution. The TTS is also modeled by a normal distribution, based on the value given in the data sheet of 2.7 ns at full width at half maximum (FWHM) [64]. The TTS is mainly relevant for the event clustering in the simulation, moreover for low-energy events, at the minimum of the trigger threshold. A slight variation in detection time can prevent the trigger conditions from being fulfilled. Both effects represent the variations of amplitude and

detection time of the p.e. signals, which are absent in the inherently discrete photon detections of the simulation. For simulations extending over several runs incorporating the real muon veto system status in each period by excluding signals from broken PMTs and adjusting the simulated SPP according to the PMT functionality relevant for that time (cf. Section 6.2.1).

DAQ properties To simulate a realistic muon event, the DAQ settings for digitizing muon veto events must be considered. A muon veto waveform lasts 880 ns, with approximately 320 ns reserved for the pre-signal baseline. Therefore, in the simulation the incoming photons are clustered according to their hit time at the photocathode in 560 ns windows, with each time window starting when all trigger conditions, including the model of the PMT properties, are met. All hits within the 560 ns window are assigned to one event. The next time the trigger conditions are met after a window, a new 560 ns window starts collecting the hits in between.

ADC properties Since the number of ADC channels limits the maximum possible signal amplitude, the simulation accounts for this by limiting the maximum number of detectable photons per sample (4 ns) within a 560 ns event window. For simulations of signals prior to the baseline shift in August 2023, a maximum of 126 p.e. is applied, which is reduced to 103 p.e. for simulations of data recorded thereafter.

Processing chain parameters To enable a comparison between simulated and real data (see Chapter 8), parameters analogous to those in the processing chain (cf. Section 6.1) are constructed. Accordingly, the event waveform is modeled by binning the data within a 560 ns window into 1 ns bins following linear upsampling of the original waveform (cf. Section 6.1). Afterwards, the maximum height (corresponding to the ADC limit) is then stored as the pulse height of the corresponding PMT.

7.4 Simulated muon veto efficiency

To obtain a rough estimate of the muon veto detection efficiency η, 80,000 muons (approximately one run) are simulated, with the cryostat also modeled with a "sensitive detector surface" featuring 100 % efficiency. This allows the efficiency of the muon veto to be determined by comparing it to muons passing through the cryostat. The simulated muon veto configuration corresponds to the start of phy data taking in March 2023, using 53 PMTs. However, it should be noted that this does not account for events that actually deposit energy in the HPGe detectors. All muons passing through the cryostat, even those only grazing its upper corners and therefore deposit no energy in the HPGe detectors, are included. The estimation therefore provides a conservative lower bound for the efficiency of the muon veto, which is calculated to be $\eta_{\text{sim}} \approx 99.18\,\%$.
The estimation provides a basis for predicting how the efficiency changes with modifications to the number and placement of PMTs, as discussed in Chapter 9.1.

Chapter 8

Comparison between simulation and data analysis

"All truths are easy to understand once they are discovered; the point is to discover them."

— Galileo Galilei

Comparing simulation (sim) and phy data provides valuable insights into the reliability of the simulation as well as into the interpretation of structures in the phy data.
This chapter discusses the quality of the simulation parameters based on muon simulations and their comparison with the phy muon data. The results serve as a basis for investigating further structures in the muon veto data. Specifically, the origin of the low-multiplicity bump is examined, the potential for classifying showering muons is considered, and finally an estimate of the detection capabilities of the muon veto for ^{77}Ge productions is presented.

8.1 A single run of events

In order to gain deeper insight into phy data and to validate the chosen simulation parameters, a single run of muon events was simulated and compared with a single run of measured data, as shown in Figure 8.1. During phy data taking, both the hardware configuration and the calibration remain unchanged (cf. Section 6.1). Therefore, selecting the duration of a single run ensures the comparability of the events. simulating only the muons from a single run, however, does not reproduce all data recorded by the muon veto during a run of phy data taking. The absence of the low-multiplicity bump in this simulation demonstrates that it cannot be attributed to muon events (cf. Section 8.1.1). Accordingly, the simulation of a single run is structured into two parts: the muon branch itself and a dedicated study of the origin of the low-multiplicity bump.

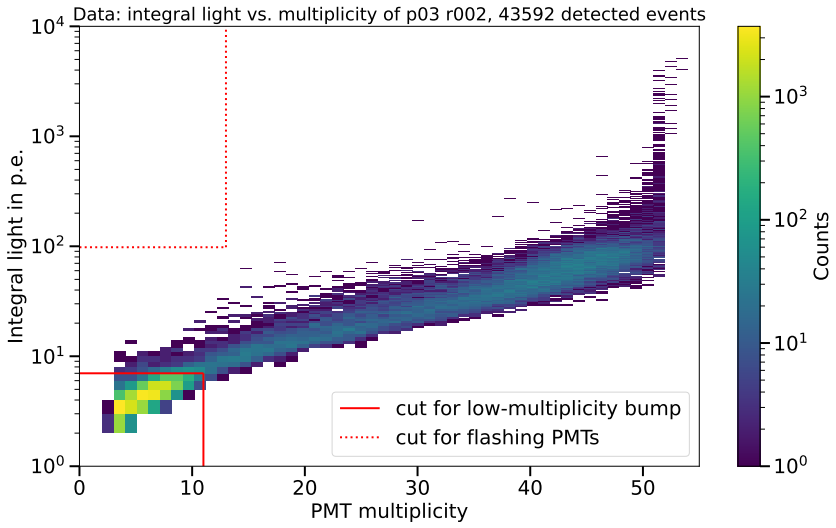

(a)

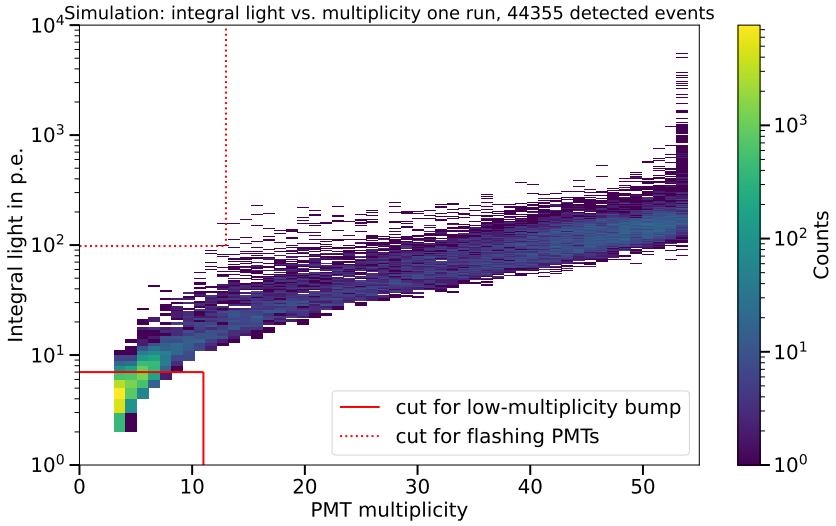

(b)

Figure 8.1.: Two-dimensional histogram of the integral light in p.e. as a function of the PMT multiplicity for a single run of muon veto events. (a) Shows phy muon veto data of p03 r002, as discussed in Section 8.1.1. (b) Represents the detection result of 80,000 muons and a specific ^{222}Rn activity of approximately 50 mBq/kg within the simulation, as shown in Section 8.1.2.

8.1.1 Muon branch evaluation

In the simulation of a single run of muons passing the muon veto of LEGEND-200, a total of 80,000 muons are generated with the MUSUN generator (cf. Section 7.1) and simulated using the geometry of legend-pygeom-l200 [90]. For comparison, recorded muon veto phy data of p03 r002 is used. This run is the first within phy data taking of LEGEND-200, lasting seven days

and featuring the highest number of operational PMTs before any malfunctioning or failure. The resulting integral light as a function of the PMT multiplicity histogram is presented in Figure 8.2. To improve the visualization of the amount of detected events, as indicated by the color bar, the phy data events of the low-multiplicity bump (cf. Section 6.1.1) are cut in Figure 8.2a.

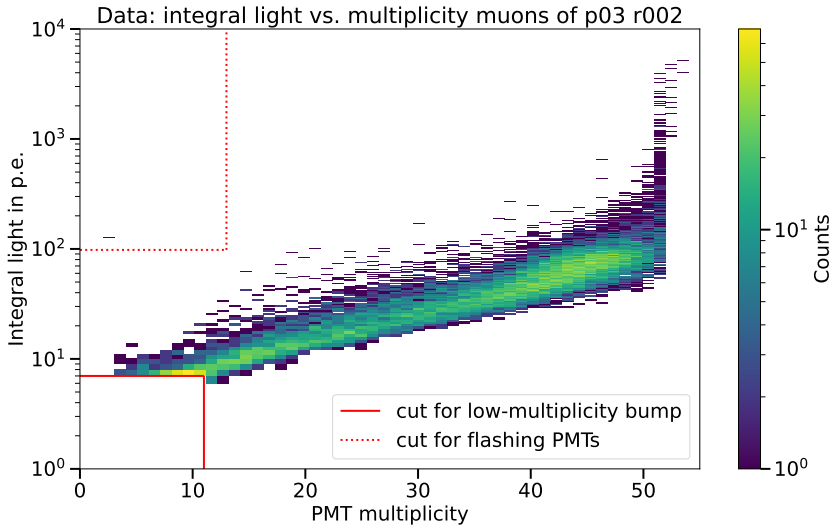

(a)

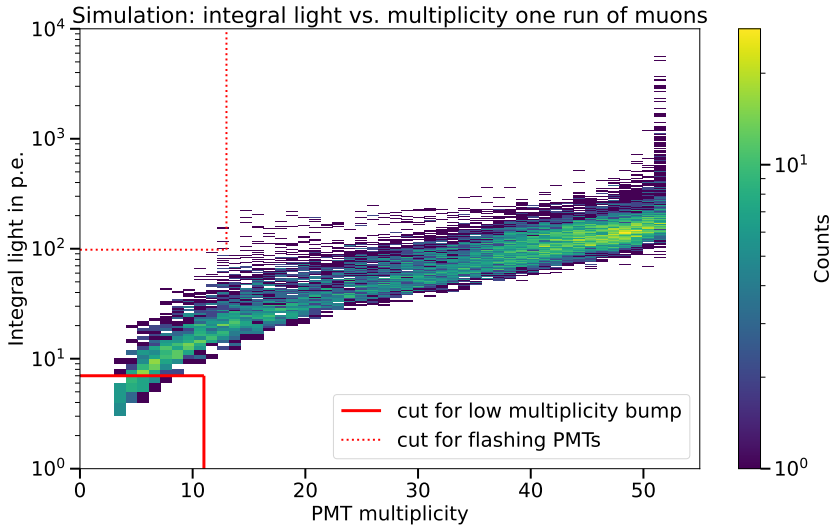

(b)

Figure 8.2.: Two-dimensional histograms of the integral light in p.e. as a function of the PMT multiplicity for a single run of muons. (a) Shows phy muon veto data of p03 r002 without the low-multiplicity bump to enable a better visualization of the pure muon amount due to the color bar. (b) Represents the detection result of 80,000 muons within the simulation.

The simulation detects 19875 muon events, while within the phy data taking 19988 muon events are detected. With a deviation of approximately 0.57 % of detected muons from sim to phy data, the total amount of detected muons is comparable. The basic structure of both muon branches is similar. Both start at the lower left of the plot and increases constantly with increasing multiplicity. The simulated muon branch overlaps with the cut for the low-multiplicity bump, indicating that low-energy muon events are also excluded by this cut. But, since the amount of muon events in the low-multiplicity bump (46 events) is several orders of magnitudes smaller than the low-multiplicity bump event in the phy data (24,208 events for p03 r002), muons can be excluded as a cause for these events. As a possible estimation of the light spread of the muon branch, the averaged coefficient of variation of the integral light of each PMT multiplicity value is calculated via

$$CV = \frac{\sigma}{\mu}, \tag{8.1}$$

where σ is the standard deviation and μ corresponds to the mean value. That results in a light spread of the simulated muon branch of $CV_{\text{sim, muon}} \approx 0.43$, which is approximately 26.47 % higher than the light spread of the phy data $CV_{\text{phy, muon}} \approx 0.34$. This difference can be caused by an overestimated PDE of the simulated PMTs, leading to an exaggerated light detection and, consequently, a higher light spread.

Comparing the maximum integral light of both muon branches, the maximum is approximately 5539.49 p.e. in the sim data, which is higher than the integral light maximum in the phy data of approximately 5133.49 p.e.. Furthermore, examining the shape of both muon branches reveals that the simulated muon branch is generally brighter, with an average integral light per muon event of approximately 130.93 p.e., compared to approximately 74.77 p.e. in the phy data. Thereby, the simulated muon events are approximately a factor of 1.75 brighter than the measured phy muon events.

This, together with the higher maximum of the integral light, indicates an overestimation of the light yield in the simulation, which may result from an overestimated water absorption length or an overestimated PMT detection efficiency. Applying a factor of 1.75 effectively adjusts the absorption length of the water, as this factor linearly scales the detected light across all PMTs.

Figure 8.3 shows the sim data divided by the factor of 1.75, leading to an averaged integral light of approximately 74.82 p.e.. An improved consistency with the sim data after applying that linear factor and the phy data, suggests an uniform effect to the entire muon system caused by the overestimation of simulated light detection.

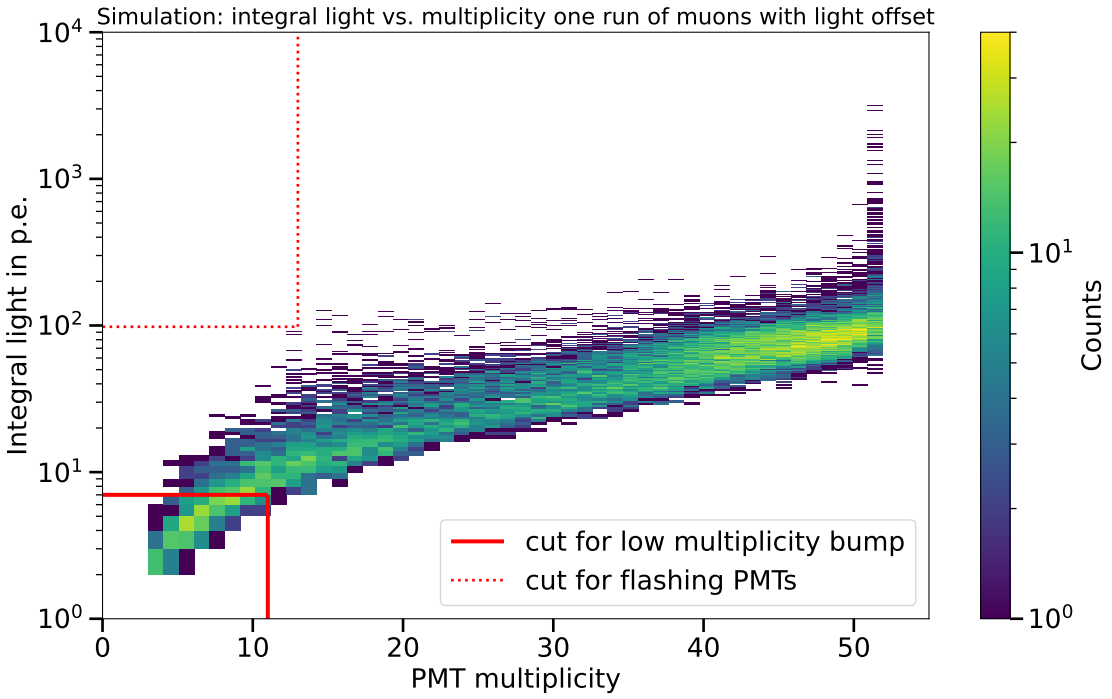

Figure 8.3.: Two-dimensional histogram of the integral light in p.e. as a function of the PMT multiplicity for a single run of simulated (80,000) muons. The simulated integral light was divided by a factor of 1.75 to adapt to the average detected amount of light to the phy data. The application of this factor corresponds to an adjustment to the simulated absorption length of the water or the PDE of the PMTs.

Examining the maximum integral light in the simulation after applying a factor, it is found to be approximately 3165.42 p.e., about 38.34 % lower than the maximum observed in the phy data. Together with the higher light spread of the sim data, which remains the same before and after the factor, a non-linear effect causing the overestimation of the detected light in the simulation can be concluded. Accordingly, for instance, the PDE of the PMTs, their functionality or the calculated gain (due to e.g., a damaged HV cable) is incorrectly assumed, possibly with an overestimated water absorption length in addition, in the simulation.
Nevertheless, the simulated event distribution and the basic structure of the muon branches matches the phy data. Thus, the simulation can be used for further analyses as an approximation of the real muon veto system.

8.1.2 Low-multiplicity bump investigation

Previous work on the GERDA muon veto examined the origin of the low-multiplicity bump [2, 3]. Random coincidences of the PMTs or coincidences with muons depositing energy in the HPGe detectors were excluded as possible reason. Instead, scintillation of the VM2000 was suggested

to be responsible for the low-multiplicity bump. The radioactive isotopes in the steel of the water tank and cryostat were investigated as potential sources of the scintillation. In measurements with a test setup, α- and β-sources illuminating a VM2000 sample placed in front of three PMTs, were investigated. As a result, the β decay of ^{60}Co in the stainless steel of the water tank was found to be the most likely source of the scintillation of the foil VM2000 [2].
To confirm this result, ^{60}Co was simulated in this work within the stainless steel of the LEGEND-200 geometry, using a realistic simulation setup that was not available in previous studies. Since 24,208 events were measured in the low-multiplicity bump in p03 r002, detecting approximately 24,000 events in the ^{60}Co simulation would confirm this assumption. ^{60}Co has a half-life of approximately 7.27 yr and decays with a probability of around 99.88 % into ^{60m2}Ni with the radiation of a single electron with an energy of $Q_{\beta,\,60\text{-Co}} \approx 310\,\text{keV}$ [95]. The average ^{60}Co activity in the steel of the water tank was measured to be approximately 19 mBq/kg [51]. For the ^{60}Co simulations of the stainless steel with a density of 7.9 g/cm^3, a corresponding number of ^{60}Co atoms is sampled in the water tank, pillbox and cryostat volumes as shown in Table 8.1.

Table 8.1.: Dimensions (diameter ∅, height h, thickness t, total volume V), mass m, activity A and corresponding number of samples S of the different stainless steel geometries considered in ^{60}Co simulations.

Geometry	∅ [cm]	h [cm]	t [cm]	V [cm^3]	m [kg]	A [Bq]	S [cts./run]
water tank	1000.0	888.6	0.70	2505280.07	19791.71	376.04	227430527
pillbox	400.0	130.0	0.12	19609.42	154.91	2.94	1780152
cryostat	400.0	708.0	0.12	90500.49	714.95	13.58	8215677

In the entire ^{60}Co simulation, three events are detected by the PMTs, which does not confirm the assumption that the β decay of ^{60}Co causes the low-multiplicity bump. However, it should be noted that the simulation may contain uncertainties that underestimate the detection of the scintillation photons from the VM2000 foil. For instance, deviations in the modeling of the photocathode curvature or borosilicate glass thickness of the PMTs could affect the result.
In this work, ^{222}Rn in the water of the muon veto system was simulated as another possible cause of the low-multiplicity bump. The possible contributing β decays are the β decays of ^{214}Pb ($Q_{\beta,\,214\text{-Pb}} \approx 1018\,\text{keV}$) and ^{214}Bi ($Q_{\beta,\,215\text{-Bi}} \approx 3269\,\text{keV}$) [95] as shown in the schematic representation of the ^{222}Rn decay chain in Figure 8.4. Since the half-life of ^{210}Pb is 22 yr and the muon veto water is continuously circulated in a water loop without the addition of new water, subsequent β decays are not considered.

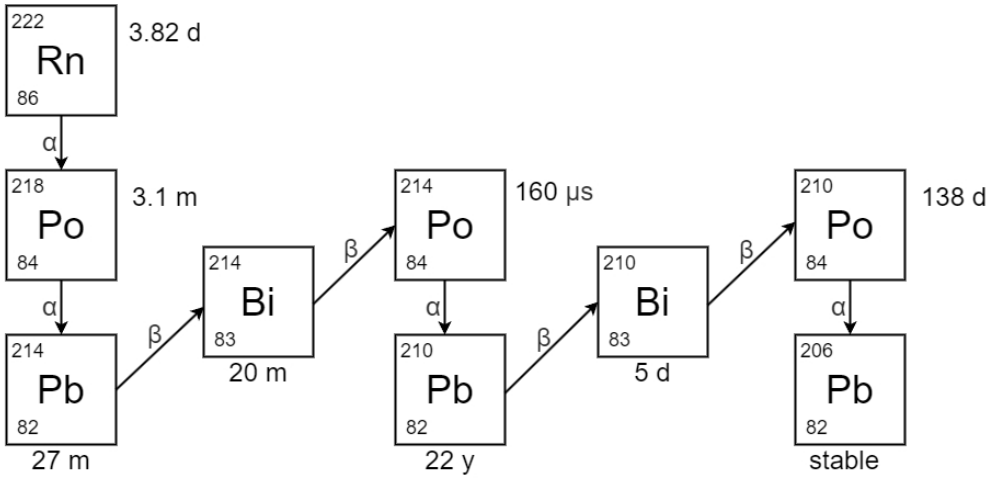

Figure 8.4.: Schematic illustration of the ^{222}Rn decay chain. The β decays of ^{214}Pb and ^{214}Bi could cause the low-multiplicity bump in the muon veto data.

Since the exact concentration of ^{222}Rn in water is unknown, an assumed concentration was used for the simulation. Due to the high memory requirements, the simulation was executed on the Perlmutter supercomputer at National Energy Research Scientific Computing Center (NERSC) [96], which imposes a maximum runtime limit of 48 h per job. This limit was reached after simulating 900,000,000 events, corresponding to the decay of the same number of ^{214}Pb and ^{214}Bi atoms in the water during a single run of phy data. The resulting activity is $A \approx 1488.1\,\mathrm{Bq}$ with a total water mass of $m \approx 590,000\,\mathrm{kg}$ (cf. Section 5.1). This corresponds to a specific activity of $a \approx 2.5\,\mathrm{mBq/kg}$ with

$$a = \frac{A}{m}\,. \tag{8.2}$$

With this specific activity, the simulated muon veto PMTs detect approximately 1200 events in the low-multiplicity bump region. In order to achieve the 24,000 measured events of the low-multiplicity bump, a specific ^{222}Rn activity of approximately 50 mBq/kg is therefore necessary. To visualize this specific activity, 20 cycles of post-processing (cf. Section 7.3) were used with the simulated data, adding the resulting integral light and PMT multiplicities for each post-processing cycle. Figure 8.5a shows the integral light as a function of the PMT multiplicity for the phy data of p03 r002, while Figure 8.5b represents the resulting data of the ^{222}Rn simulation. In total, 24,117 events are classified in the phy data, where approximately the same amount of events (24,321) are detected in the ^{222}Rn simulation. The overestimation of detected light in the simulation, as shown in Section 8.1.1, is also reflected in brighter low-multiplicity bump events. Correspondingly, the simulated events are recorded with higher integral light than the applied cut. Nevertheless, most events in the ^{222}Rn simulation are in the range of the low-multiplicity bump cut (cf. Section 6.1).

The occurrence maximum (represented by the color bar) of both, phy and sim data, is located at a multiplicity of four, which corresponds to the trigger conditions of floor and wall PMT distribution areas (cf. Section 5.2).

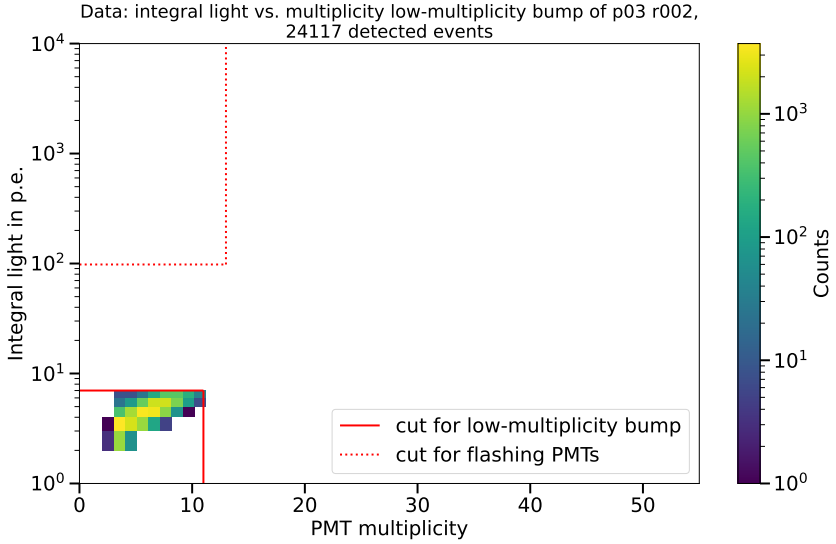

(a)

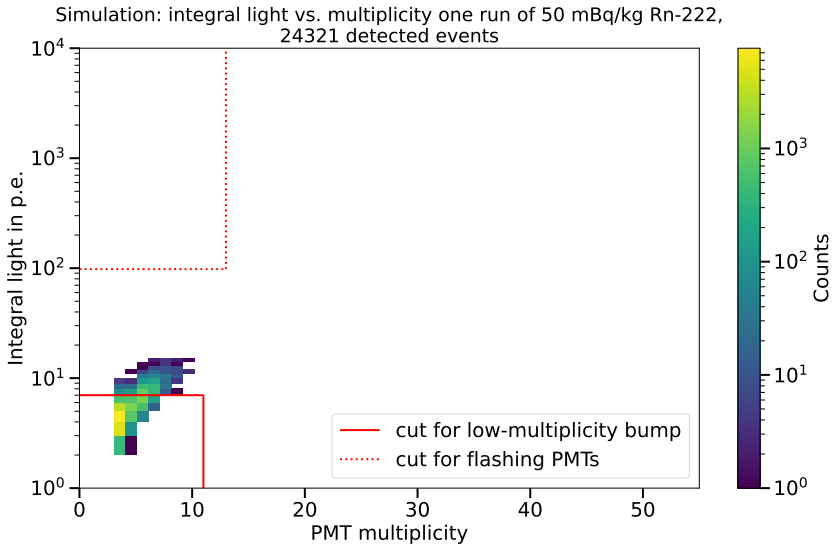

(b)

Figure 8.5.: Two-dimensional histogram of the integral light in p.e. as a function of the PMT multiplicity for a single run of low-multiplicity bump. (a) Shows phy muon veto data of p03 r002 of the low-multiplicity bump. (b) Represents the detection result of a specific ^{222}Rn activity of approximately 50 mBq/kg within the simulation.

The maximum occurrence of the sim data is about 7674.00 counts, which is approximately 206.34 % of the maximum occurrence of the phy data of approximately 3719.00 counts. However,

in the phy data there are three data points in the histogram with occurrences above 3000 counts, whereas the maximum occurrence of the sim data shows a single point above 7000 counts, resulting in a sharper maximum. If the trigger conditions in the muon veto are met, all PMTs are read out and their pulse heights are taken into account. In the simulation, PMTs with maximum pulse heights below the 0.5 p.e. threshold after post-processing are not considered in further analysis, even if the trigger conditions are met (cf. Section 5.2). This results in a wider distribution of the integral light of the phy data, which is not taken into account in the simulation and is particularly visible in the low p.e. range. This could be a possible explanation for the sharper maximum in the simulated low-multiplicity bump.
In total, the structure of the low-multiplicity bump can therefore be modeled using the ^{222}Rn simulation with a specific activity of 50 mBq/kg. This value exceeds the measured specific ^{222}Rn activity in the water, amounting to approximately 2.5 mBq/kg as measured by the XENONnT experiment [58], which uses the same water purification system that also supplies LEGEND-200. A possible explanation is the introduction of additional ^{222}Rn during water transport through the piping system to the LEGEND-200 experiment. To confirm this hypothesis and the simulation result, a water sample should be taken from the LEGEND-200 muon veto and the ^{222}Rn concentration analyzed. Since the low-multiplicity bump in the muon veto data can be removed by applying the corresponding cut, and the coincident events show a brighter integral light (cf. Section 6.4), it does not compromise the operation of the LEGEND-200 muon veto. However, for searches involving events with less light, such as in a neutron tagging system as planned for LEGEND-1000 (cf. Section 3.3.2), it is necessary to avoid contributions from the low-multiplicity bump.

8.2 Search for muon-induced ^{77}Ge production with the LEGEND-200 muon veto

Muons can induce electromagnetic showers in the water tank, hereafter referred to as ”showering muons”, which generate additional signals and secondary particles as described in Section 4.3.3. Among these secondary particles, neutrons can be produced through spallation or photo-nuclear reactions. These neutrons can be captured in a HPGe detector producing ^{77m}Ge, which has a half-life of approximately 53.7 s and subsequently decays to ^{77}Ge. During its decay, $^{77(m)}$Ge can produce $Q_{\beta\beta}$-like signals in the detector (cf. Section 4.1.1). To reduce this dangerous background, it is planned to apply a conservative dead time of 6 min, based on six times the half-life of ^{77m}Ge, in the LEGEND experiment following muon-induced ^{77}Ge triggers [97]. To identify such events, data from all subsystems, including HPGe detectors, LAr instrumentation, and the muon veto, will be used.
In this work, a criterion for muons producing ^{77}Ge is developed based solely on the muon veto data. This allows muons with potential neutron captures in the HPGe detectors to be distinguished

from other muons, using nearly a single year of data from the LEGEND-200 muon veto. For this purpose, the simulated signature in the muon veto of showering muons producing ^{77}Ge is first investigated to understand the relevant features, which are then used to develop distinguishing approaches presented in the following sections.

8.2.1 Simulation of muon-induced ^{77}Ge productions

Thus, to investigate neutron captures over nearly one year, 4,000,000 muons are simulated, storing only the events with $^{77(m)}$Ge production. In the simulation, six ^{77}Ge productions and, thus ^{77m}Ge decays, are generated, of which four are detected by the muon veto. The two events not detected by the muon veto likely passed vertically through the neck of the cryostat and therefore produce no signal in the muon veto. Figure 8.6 shows the corresponding integral light as a function of the multiplicity histogram. Different colors indicate the separate ^{77}Ge production events. Two detected events show multiple triggers in the muon veto due to signals fulfilling the trigger conditions (cf. Section 5.2) after the first trigger of an event. The number shown for each event in the figure indicates the order of muon veto triggers within that muon event. The first trigger of each event is registered at the highest possible multiplicity (called ”full multiplicity” in the following) of the muon veto. Two events show only one trigger with nearly the same integral light (cf. the green cross and the pink cross behind it in Figure 8.6). For events with multiple triggers, the first trigger in the sequence exhibits the highest integral light. Subsequent trigger signals of the multiple-trigger signals (labeled > 1 in Figure 8.6) exhibit lower multiplicity and integral light compared to the first trigger (labeled 1 in Figure 8.6). Since the simulation overestimates the detected light yield (cf. Section 8.1.1), the scaling factor of approximately 1.75 was applied to the events in Figure 8.6 as a verification check. This adjustment did not affect the number of detected events. Accordingly, the simulation results are used below as an approximation to the phy data.

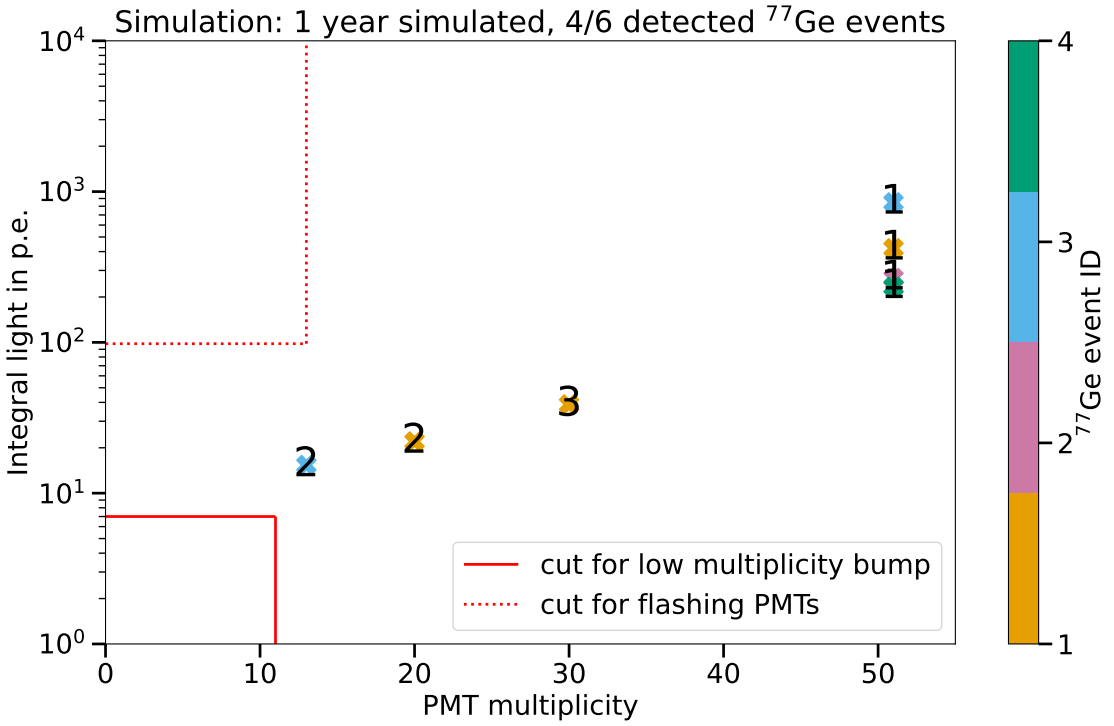

Figure 8.6.: Two-dimensional histogram of the integral light in p.e. as a function of the PMT multiplicity for a single year simulated muons producing ^{77}Ge. Out of six ^{77}Ge productions, four are detected by the muon veto system, which can be distinguished due to different colors. Two of the detected events cause multiple triggers. The events without a multiple trigger appear almost at the same position of the histogram (cf. green and pink cross). The number of count per ^{77}Ge production is indicated at the corresponding event.

All ^{77}Ge productions detected in the simulation by the muon veto show a trigger at full multiplicity. However, muons can also produce signals with full multiplicity of the muon veto via the Cherenkov effect (cf. Section 8.1.1). For this reason, showering muons are first classified, followed by two approaches:

- First (full multiplicity cut (FMC)) approach: Events are considered with full multiplicity, which corresponds to an identification of $4/6 \approx 66\,\%$ of muon-induced ^{77}Ge productions (cf. all events in Figure 8.6).
- Second (multiple trigger cut (MTC)) approach: Events are considered with maximum possible multiplicity and multiple triggers, which identifies of $2/6 \approx 33\,\%$ of muon-induced ^{77}Ge productions, but results in less overall dead time for the LEGEND experiment (cf. yellow and blue events in Figure 8.6).

For the MTC approach, the time differences between the multiple triggers are additionally investigated. Figure 8.7 shows this time differences in a histogram of the detection time. Colors indicate

the different ^{77}Ge production events. Events detected at a time difference of 0 μs correspond to the first trigger of each event. All multiple triggers are detected with a maximum time delay of approximately 1.18 μs to the first trigger (cf. Figure 8.7).

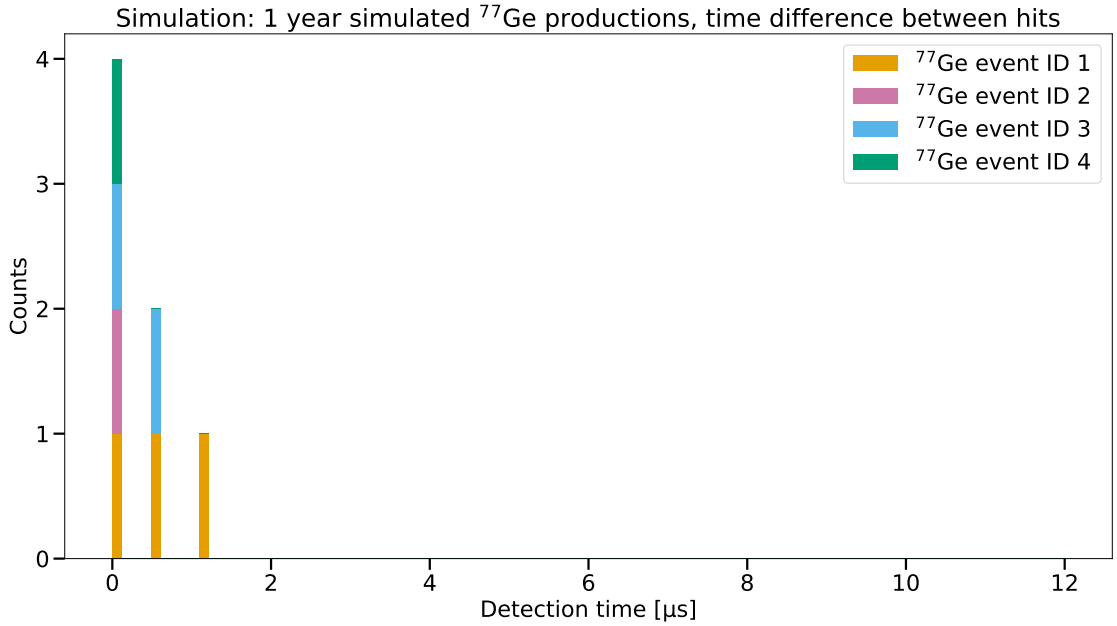

Figure 8.7.: Histogram of the detection time differences between multiple triggers in the muon veto originating from single ^{77}Ge production events. The different ^{77}Ge production events are distinguished by different colors.

In order to investigate both approaches in sim and phy data, the first step is to develop a criterion for classifying showering muons, to restrict the analysis to events that may involve neutron captures (cf. Section 8.2.2). Based on the MTC approach, an additional criterion is then derived to refine showering muon events into neutron-capture candidates via delayed coincidences (cf. Section 8.2.3). Finally, both approaches are applied to the sim and phy data, and their applicability to the LEGEND-200 analysis is assessed in Section 8.2.4.

8.2.2 Classification of showering muons

Since the PMT undershoot analysis in Section 6.3.2 did not provide a classification of showering muons, sim data, where the classification of showering and non showering muons is known, is used in the following to gain a more detailed understanding of the data.
The simulation provides the production process of a particle. In the muon simulation, muons are classified as showering when they produce secondary particles via ”hadron ionization” (the Geant4 process describing ionization by charged hadrons), ”muon ionization” (the Geant4 process describing ionization by muons), muon bremsstrahlung or muon pair production. This results in

approximately 11.02 % of showering muons, which are indicated by red crosses in Figure 8.8. Showering muon events are distributed across the entire muon branch in the histogram of integral light as a function of the multiplicity. Thus, it is not possible to classify showering muons in the phy data using only the light or multiplicity of the detected events.

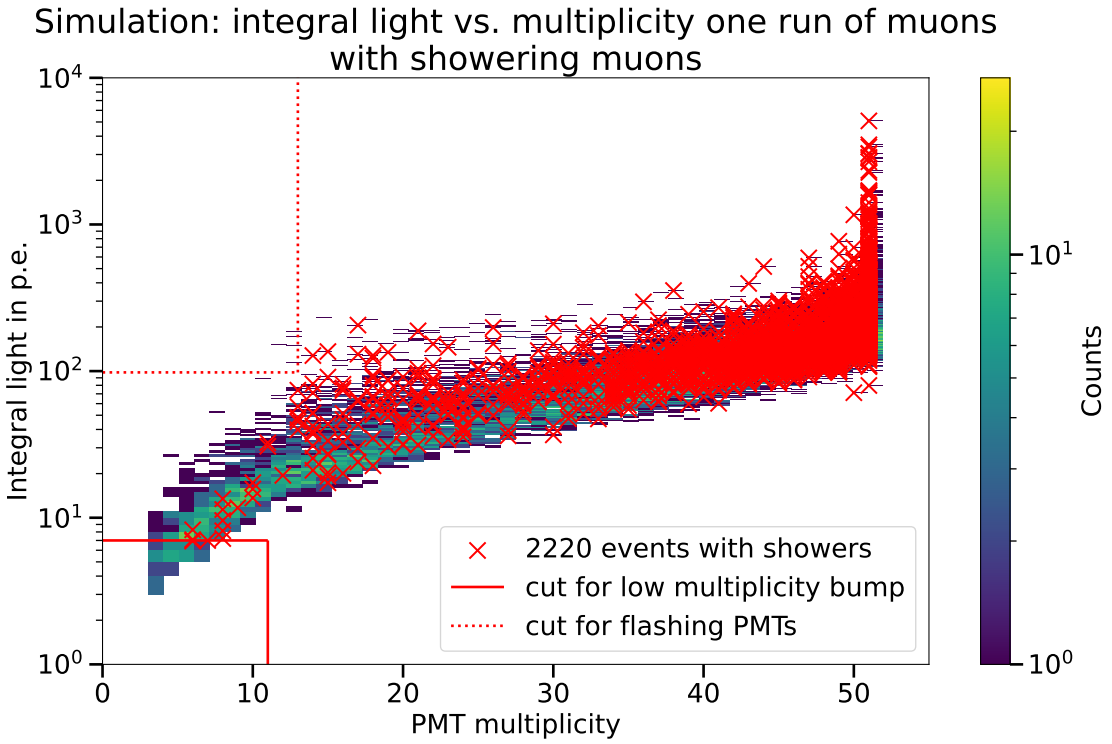

Figure 8.8.: Two-dimensional histogram of the integral light in p.e. as a function of the PMT multiplicity for a single run of simulated (80,000) muons. Muons creating particles via hadron ionization, muon ionization, bremsstrahlung or pair production are classified as showering and marked with red crosses.

The classification approach for showering muons developed in this work is based on the detection time of light across the pillbox and floor PMT distribution areas in the muon veto.
The underlying idea can be illustrated by considering the expected light distribution for showering and not showering muons: If a muon produces only Cherenkov light in the water tank, an even distribution of photons with the Cherenkov angle (cf. Section 4.1.1) is expected in the muon veto. As soon as the muon leaves the water tank, the light source is no longer present and only photons that have not yet been absorbed in the water can be detected by the PMTs. If a muon produces secondary particles (e.g., electrons or positrons) in the water tank, there are additional light sources in the muon veto that are not bound to the Cherenkov angle and thus the path of the muon. If these particles produce light in the pillbox, for example via bremsstrahlung or pair production, this can be observed as delayed light detections in the pillbox compared to the floor.

To verify this assumption, the time distribution of signals detected by the pillbox PMTs is compared to those detected by the floor PMTs. Since the absolute brightness of an event is not relevant for this approach, but the relative brightness and duration within each event are, the brightness of each signal is normalized to the maximum value of the respective event. Hereafter, in this Section, the term ”brightness” refers to its relative, normalized value. The resulting detection times are displayed as a function of the PMT channel in a two-dimensional histogram for a single run (80,000) of simulated muons (cf. Figure 8.9). The color bar of the histogram shows the normalized brightness of the measured events. The boundaries of the different PMT distribution ranges were marked with red lines (pillbox: channel 0-9, floor: channel 10-29 and wall: channel 30-52). The axis limits of the detection time are selected for the length of a waveform without the baseline lead time of approximately 320 ns. This histogram was created for the showering (cf. Figure 8.9a) and non-showering (cf. Figure 8.9b) muon events of the simulation. The pillbox channel of the showering muons shows brighter events up to a detection time of approximately 250 ns, while the floor and wall exhibit comparable brightnesses up to approximately 150 ns and 170 ns, respectively (cf. Figure 8.9a). For non-showering events, the overall signal duration of the events is shorter. The brightness decreases in the pillbox from approximately 160 ns, and in the floor and wall from approximately 130 ns and 150 ns, respectively. Overall, the pillbox is darker than the other areas (cf. Figure 8.9b).

Based on this result, a criterion can be built for the PSD filtered phy data, which can be used to classify between showering and non-showering muons. This criterion classifies muon veto events as showering if the average brightness of all pillbox PMTs with maxima above 2 p.e. is higher than the corresponding average brightness of all floor PMTs. The light limit of 2 p.e. is introduced to avoid the classification of low-multiplicity bump data. The criterion considers events between 80 (correspondingly 320 ns) and 180 samples (720 ns) in order to omit baseline and afterpulse events. With applying this criterion, the phy data is divided into showering (cf. Figure 8.9c) and non-showering (cf. Figure 8.9d) muons. The missing channels indicate broken PMTs from the start of data collection (channels 11, 37 and 45). The y-axis indicates the samples of the waveforms, so the first 80 samples (320 ns) are dark or contain no events because they represent the baseline. In addition, the phy data channels show events that are brighter than the previous samples at approximately 180 samples (720 ns), which are presumably caused by afterpulses of the PMTs or by saturation and recovery effects of the ADC. These events are mainly present in the data classified as showering, which are usually brighter according to Figure 8.8 and are therefore more likely to trigger afterpulses in the PMT. Overall, the brightness behavior of the phy data is comparable to that of the sim data. For showering muon events, the bright pillbox events last about 45 samples (180 ns), while they span over approximately 35 samples (140 ns) on the floor and 50 samples (200 ns) on the wall PMTs (cf. Figure 8.9c). For muon veto events classified as non-showering, the pillbox channels are darker than floor or wall channels. No distinctly brighter areas within the channels can be identified (cf. Figure 8.9d).

To illustrate the differences in brightness, the events classified as non-showering are subtracted from the showering events for both simulation (cf. Figure 8.9e) and phy data (cf. Figure 8.9f) and compared. In both plots, the higher and longer brightness of the pillbox is clearly visible. The simulation shows almost no data where the difference between showering and non-showering events on the floor and in the pillbox is greater than zero. The difference here is clearly in the brighter pillbox (cf. Figure 8.9e). Even in the phy data, the difference between pillbox events classified as showering and non-showering is approximately a factor of three brighter than the other areas (cf. Figure 8.9f). This allows the distinction between the brightness and exposure time of the pillbox and floor PMTs to be considered as an approximate classification of showering muons.

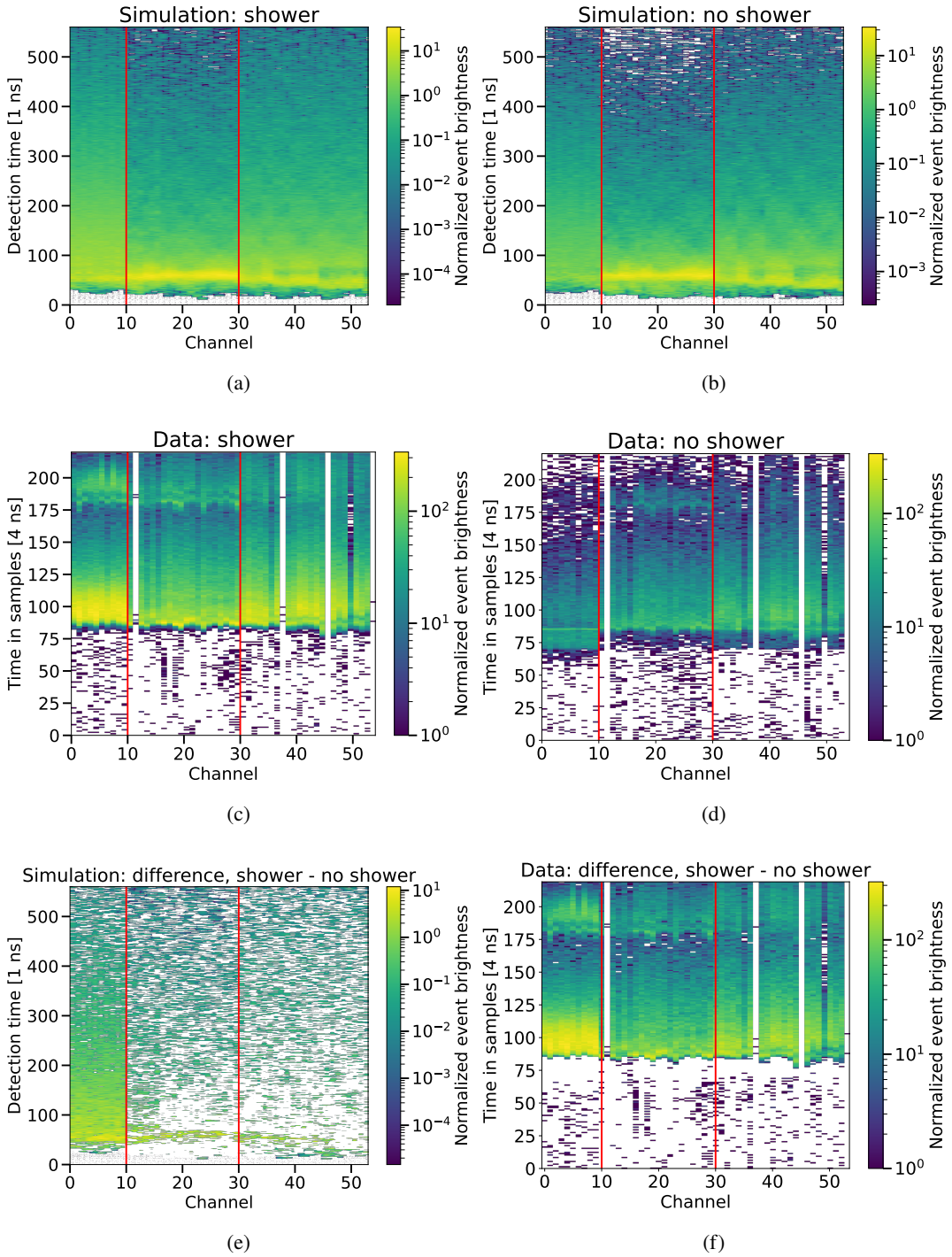

Figure 8.9.: Two-dimensional histogram of the detection time as a function of the PMT channel of a single run of events. (a) shows simulated data of showering and (b) of not showering muons. (c) shows phy data of p03 r002 of muon veto events classified as showering and (d) of not showering muons. Histogram (e) and (f) show the histogram difference of showering data subtracted by not showering data of the simulation (e) and phy data (f) of a single run. The red lines mark the transition between the PMT distribution areas (at 10 channels between Pillbox and floor and at 30 channels between floor and wall).

Figure 8.10 shows the integral light as a function of the PMT multiplicity histogram with events classified as showering marked with red crosses. 2046 of 19475 detected muon events (without the data of the low-multiplicity bump) and with that 10.51 % are classified as showering, which is in good agreement with the sim data (11.02 %). The small discrepancy could be due either to inaccuracies in the simulation itself or to the classification threshold of at least 2 p.e. per PMT, which excludes events with an integral light of less than 16 p.e. due to the multiplicity trigger threshold of six PMTs in the pillbox.

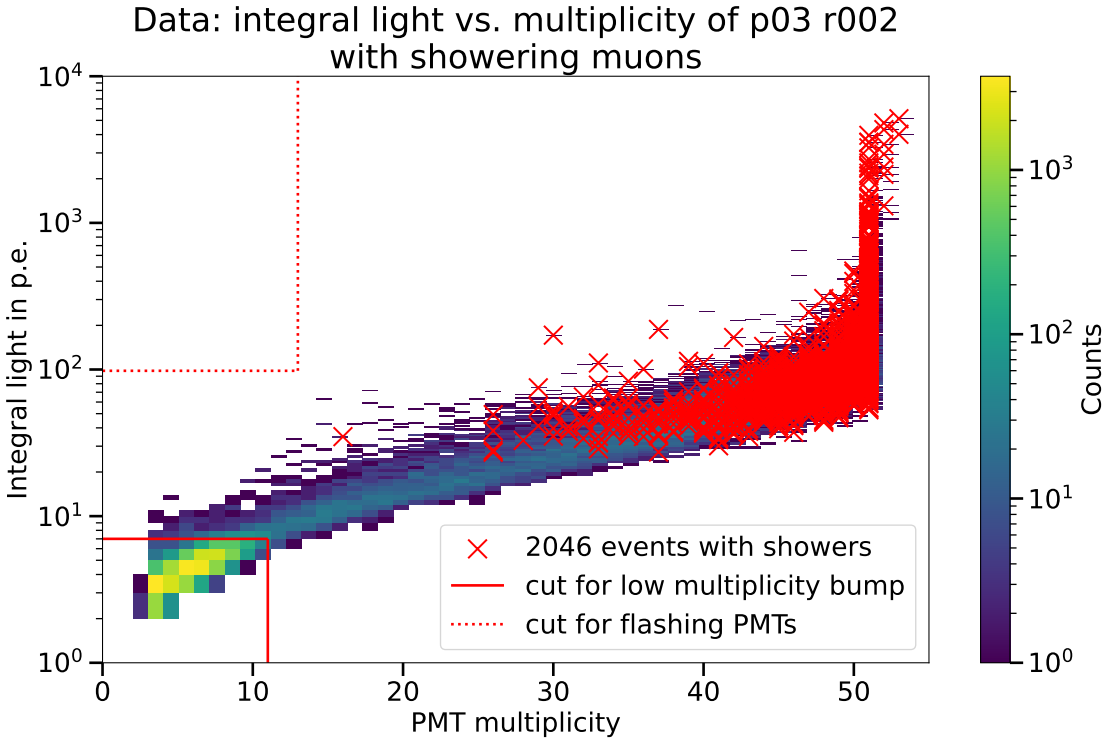

Figure 8.10.: Two-dimensional histogram of the integral light in p.e. as a function of the PMT multiplicity of p03 r002. Events classified as showering are marked with red crosses.

In order to visualize the counts of the showering and non-showering events of simulation and phy data, a histogram of the integral light with the shower classification is shown in Figure 8.11. Both histograms show the same behavior except for the absence of showering events below 16 p.e. in the phy data. Showering events exhibit a similar distribution to non-showering events, but with approximately an order of magnitude fewer counts. Nevertheless, with an integral light of above approximately 500 p.e., showering events are more numerous than non-showering ones. In the simulation the highest no-showering event is approximately at 1246.91 p.e. (cf. Figure 8.11a), while for the phy data it is at approximately 2209.57 p.e. (cf. Figure 8.11b). All data above this value are classified as showering. Thus, the probability of a showering muon increases with its energy.

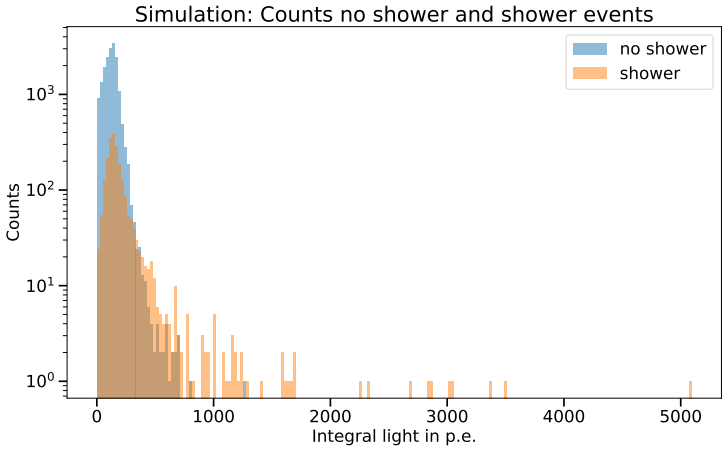

(a)

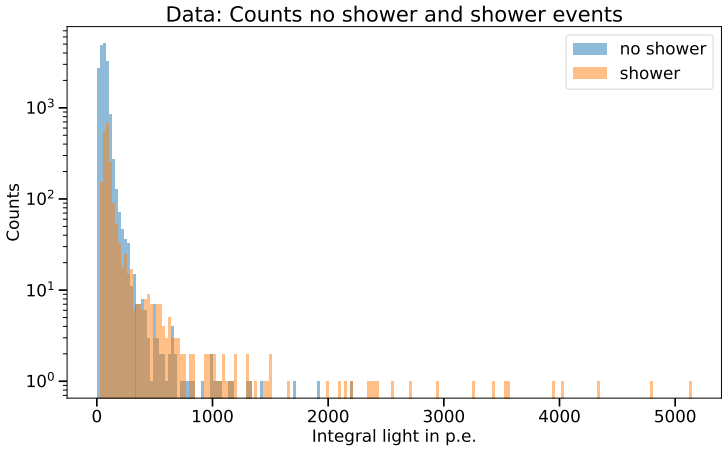

(b)

Figure 8.11.: Histogram of the integral light in p.e. of muon veto events classified as showering (orange) and non-showering (blue) of simulated (a) and phy (b) data.

In conclusion, a criterion for showering muons was derived from the sim data and applied to the phy data using the PMT waveforms. To further validate the transferred criterion, a comparison of the phy data results with a full waveform simulation, including the additional effects of the PMTs, and DAQ as well as ADC processes, would be required. Due to time constraints, this was not performed in this work, but could be implemented in future studies. For the following sections, the criterion for showering muons is assumed to be reliable when applied to the phy data.

8.2.3 Investigation of delayed coincidences

In order to examine delayed coincidences and potential differences of sim and phy data, events with multiple triggers are considered below, with the first trigger exhibiting full multiplicity. Events that

fulfill this delayed coincidence classification are shown in Figure 8.12 for nearly one year of data, both for sim and phy, as a two-dimensional histogram of the integral light in p.e. as a function of the PMT multiplicity. Figure 8.12a shows multiple trigger events from simulated muons for which ^{77}Ge production was not recorded. The amount of data corresponding to a single year of muon simulation is achieved through post-processing (cf. Section 7.3). The PMTs removed from the phy data acquisition between p03 and p11 are also taken into account (cf. Section 6.2), which reduces the full multiplicity according to the simulated runs. 2625 events can be classified as multiple trigger events, corresponding to 2625 ^{77}Ge production candidates in the muon simulation. Figure 8.12b represents the multiple triggers from p03 to p11 in the phy data. In total, 653 events fulfill the multiple trigger in approximately a single year of phy data. This corresponds to up to a factor of four fewer ^{77}Ge production candidates detected compared to the simulation. A possible reason for this discrepancy is that the reduced signal quality of malfunctioning PMTs affects the criterion for full multiplicity. In addition, as described in Section 8.1.1, the simulation overestimates the detected light of each PMT and thus the detection of multiple triggers with detected light near the trigger threshold.

To account for the overestimation of simulated light, different water absorption lengths, PDE maxima of the PMTs, and their combinations were investigated. However, no optimal configuration was found, since the overestimation is not linear (see Section 8.1.1). Consequently, for this criterion both the underestimation of delayed coincidence classification in phy data due to broken PMTs, and the overestimation in sim data must be noted.

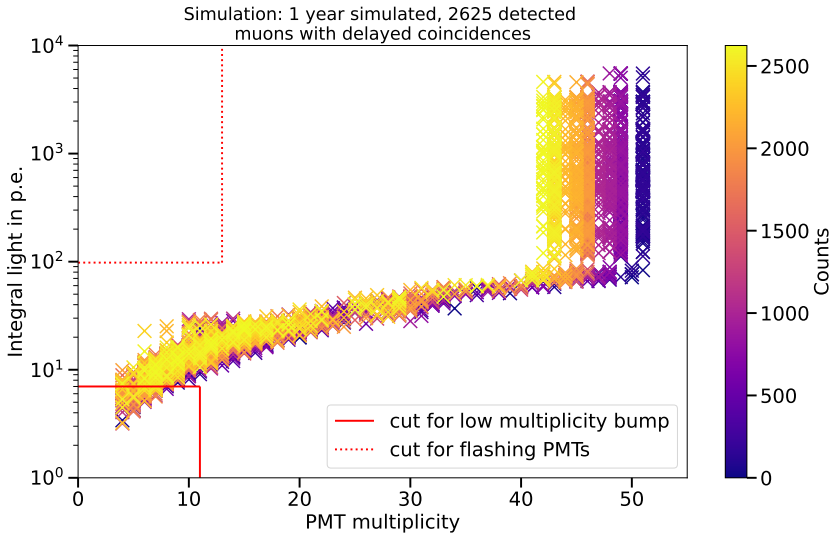

(a)

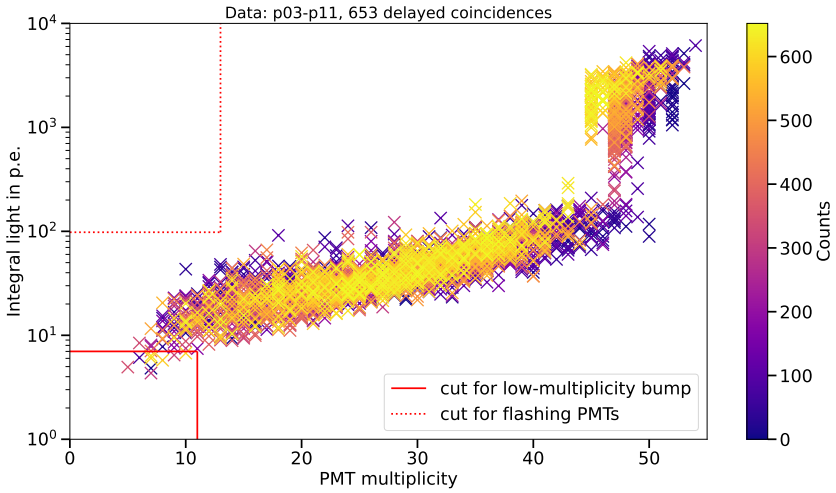

(b)

Figure 8.12.: Two-dimensional histogram of the integral light in p.e. as a function of the PMT multiplicity for approximately a single year of muon veto events. Only events with multiple triggers originating from single muon events are included, for both simulated (a) and phy (b) data. The first detected trigger shows the full multiplicity. The color bar indicates the total amount of detected muons with multiple muon veto triggers.

Additionally, the time differences of the multiple trigger events are examined. Figure 8.13 shows the corresponding time difference in a histogram of the detection time for sim (cf. Figure 8.13a) and phy (cf. Figure 8.13b) data. The bin width was set to 560 ns in order to cover a single muon veto trigger window (excluding the baseline). The second bin of the histogram shows a clear percentage difference compared to the first bin. In the simulation, the second bin includes approximately 99.30 % of the counts of the first bin, while in the phy data, the second bin

contains approximately 36.45 % of the counts of the first bin. Compared to Figure 8.7, the second bin recorded directly after the time window of a waveform, may also originate from a ^{77}Ge production. However, in the simulation, the overestimation of light can cause the signal to persist longer, which may immediately trigger what appears to be a second event following the first, although it does not correspond to a separate physical event.

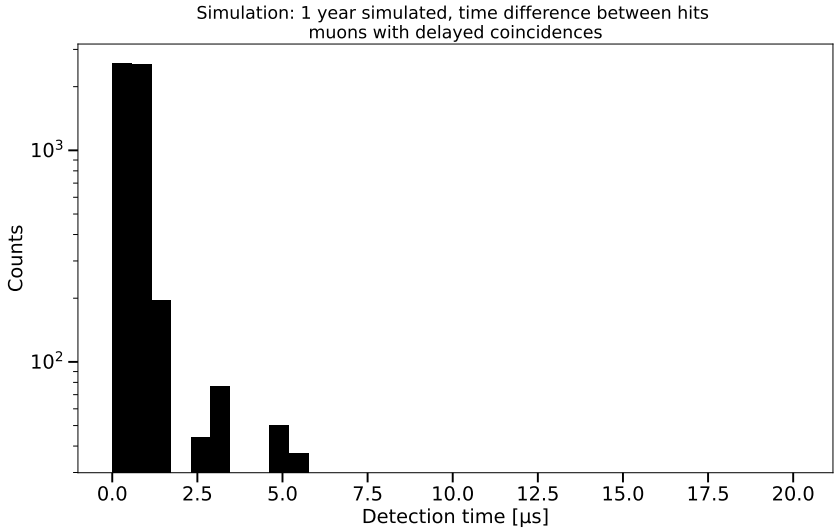

(a)

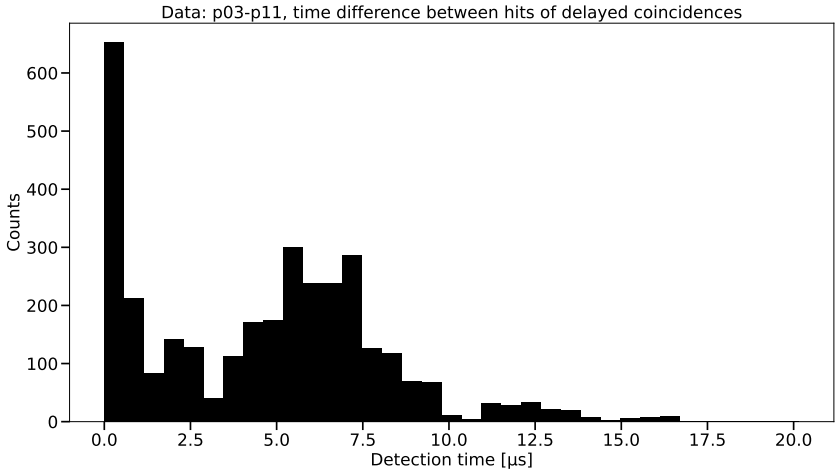

(b)

Figure 8.13.: Histogram of the detection time differences between multiple triggers in the muon veto originating from single muon events, with a bin width of 560 ns, for sim (a) (using a logarithmic y-axis for a better visualization) and phy (b) data.

In addition, the maximum detection time difference is given in the simulation by approximately 5.46 μs and in the phy data by approximately 17.17 μs. Nevertheless, in the sim data no peaks of

the detection time difference histogram can be distinguished and, in contrast, a second maximum (in addition to the first at 0 μs for the first trigger per event) at approximately 6 μs in the phy data. This second maximum could be caused by afterpulses from the PMTs, which trigger a second trigger after a detected event in several PMTs within the 60 ns trigger coincidence window (cf. Section 5.2). However, since the simulation also detects multiple triggers up to a time difference of 5.46 μs, afterpulses cannot be solely responsible for these triggers, as afterpulsing is not implemented in the simulated PMTs. Thus, the maximum could also originate from neutron thermalization, with an average thermalization time of approximately 4 μs (cf. Section 8.2.1).
In conclusion, while the criterion for multiple triggers using multiple triggers with full multiplicity of the first trigger can be applied to sim and phy data, it should be noted that it is overestimated in sim and underestimated in phy data.

8.2.4 Combined classification results for ^{77}Ge production

In order to verify the applicability of both approaches developed in Section 8.2.1, they are subsequently applied to the sim and phy muon veto data. Both approaches require a fulfilled muon shower criterion (cf. Section 8.2.2), since muon showers can produce neutrons which can be captured in the HPGe detectors and lead to ^{77}Ge production in the LEGEND experiment.

FMC approach The FMC approach considers showering muons seen by all operational PMTs of the muon veto. According to Section 8.2.1, this approach contains approximately 66 % of muon-induced ^{77}Ge productions. Figure 8.14 shows showering muon events for nearly one year of data according to the FMC approach for sim (cf. Figure 8.14a) and phy (cf. Figure 8.14b) data. The overestimation of integral light in the sim data and underestimation of multiplicity in the phy data, as discussed in Section 8.2.3, leads to approximately 3.15 times the amount of events in the sim data (7161 candidate events) compared to the phy data (2275 candidate events). Among the 7161 candidate events in the simulation, only four correspond to ^{77}Ge productions (cf. Section 8.2.1). This results in a substantial dead time of the experiment, as the 6 min dead-time window must be applied to all candidates (cf. Section 8.2 introduction). The percentage dead time τ_{dt} for the LEGEND experiment can be calculated by

$$\tau_{\mathrm{dt}} = \frac{T_{\frac{1}{2}} \cdot N_{\mathrm{events}}}{t_{\mathrm{measure}}}, \tag{8.3}$$

where $T_{\frac{1}{2}} \approx 6$ min corresponds to the half-life of $^{77\mathrm{m}}$Ge, N_{events} represents the number of detected events and $t_{\mathrm{measure}} \approx 525960$ min refers to the total measured time of nearly a single year. Using Equation 8.3, the sim data yield a percentage dead time of $\tau_{\mathrm{dt1,\,sim}} \approx 8.17$ % and the phy data to $\tau_{\mathrm{dt1,\,phy}} \approx 2.60$ % of the total measurement time using the FMC approach.

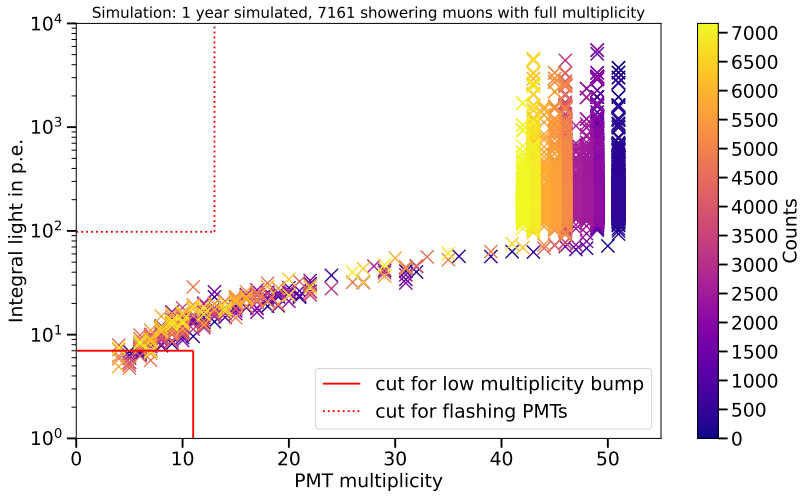

(a)

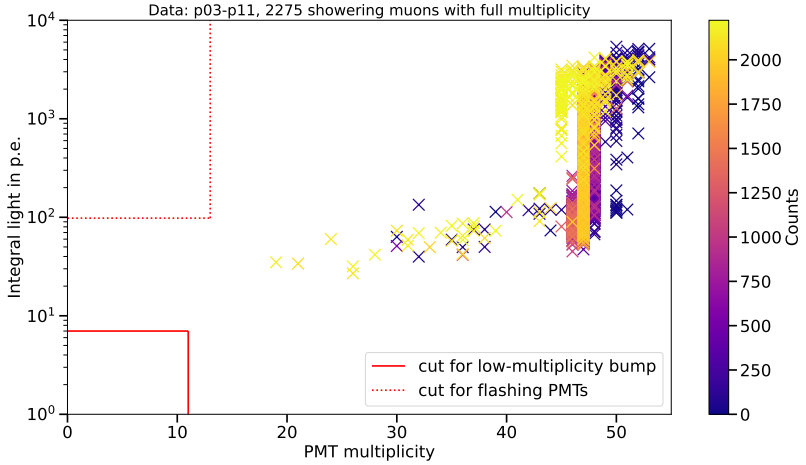

(b)

Figure 8.14.: Two-dimensional histogram of the integral light in p.e. as a function of the PMT multiplicity for approximately a single year of muon veto events. Only events classified as showering muons (cf. Section 8.2.2) and with full multiplicity of the muon veto, for both sim (a) and phy (b) data is displayed. The color bar indicates the total amount of detected muons.

MTC approach The MTC approach considers showering muons with full multiplicity and multiple triggers, according to the identification of approximately 33 % of muon-induced ^{77}Ge productions (cf. Section 8.2.1). Figure 8.15 shows showering muon events for nearly one year of data according to the MTC approach for sim (cf. Figure 8.15a) and phy (cf. Figure 8.15b) data. In the sim data 303 events fulfill the criteria for the MTC approach. This represents approximately 11.54 % of the simulated events with multiple triggers without the showering muon criterion (2625 events, cf. Section 8.2.3) and are thus in good agreement with the proportion of showering muons in the simulation of approximately 11.02 % (cf. Section 8.2.2).

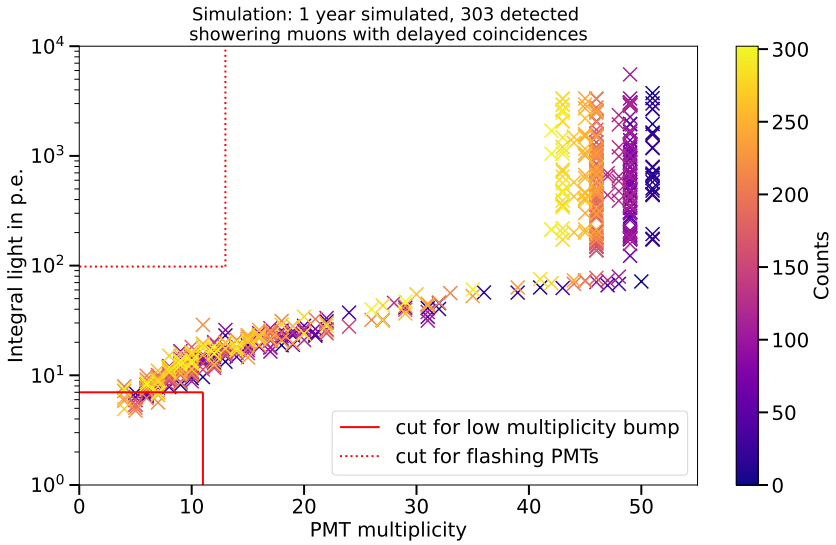

(a)

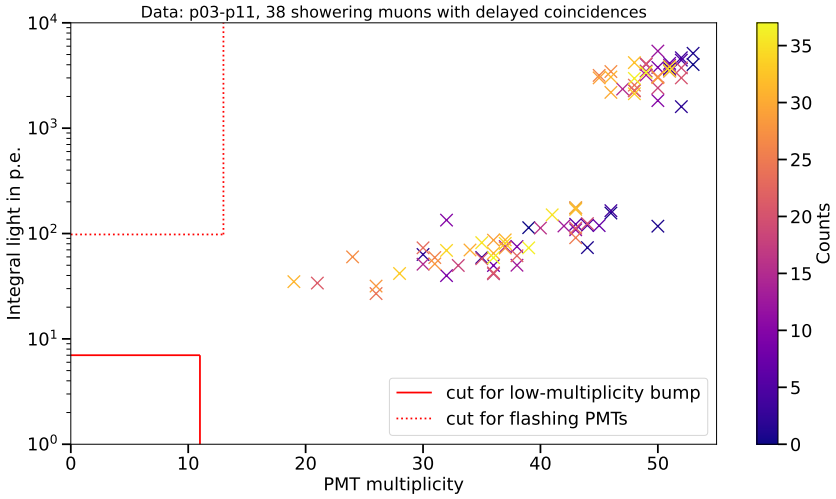

(b)

Figure 8.15.: Two-dimensional histogram of the integral light in p.e. as a function of the PMT multiplicity for approximately a single year of muon veto events. Only events classified as showering muons (cf. Section 8.2.2) and fulfilling the multiple trigger criterion defined in Section 8.2.3 are included, for both sim (a) and phy (b) data. The color bar indicates the total amount of detected muons.

In the phy data, only 38 events are identified using the MTC approach, corresponding to approximately 5.82 % of the multiple triggers without showering muon classification. The criterion for showering muons led to approximately 10.51 % showering muons in the phy data (cf. Section 8.2.2), which is almost twice the showering and multiple trigger phy data. This effect may arise due to PMT afterpulsing (cf. peak around approximately 6 μs in Figure 8.13b). Afterpulsing

events are not related to showering muons. This interpretation is supported by an examination of the time difference histogram of showering muons according to the MTC approach in Figure 8.16. The second bin of the simulated histogram (cf. Figure 8.16a) shows the light overestimation of the simulation, as described in Section 8.2.3.

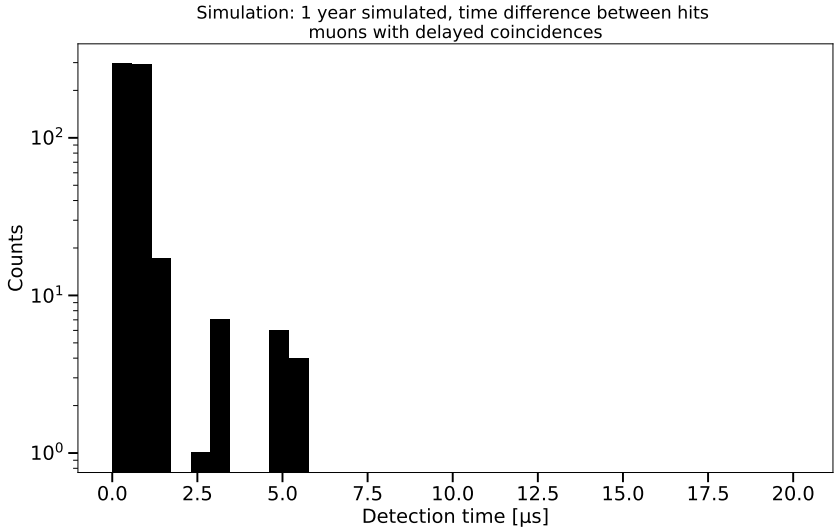

(a)

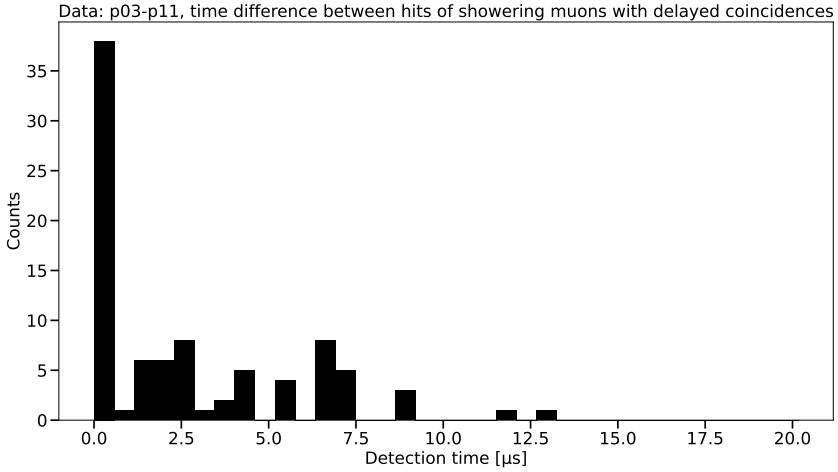

(b)

Figure 8.16.: Histogram, with a bin width of 560 ns, of the detection time differences between showering muon events fulfilling the multiple trigger criterion defined in Section 8.2.3, for both sim (a) (using a logarithmic y-axis for a better visualization) and phy (b) data.

The remaining bins with detection times greater than 0 μs in the sim and phy data (cf. Figure 8.16b) mainly exhibit a flat distribution, except for a small peak around approximately 6 μs in the phy histogram. This indicates that the classification is consistent across sim and phy data.

In total, considering the uncertainties of the full multiplicity identification in the phy data, the number of showering muon events classified via multiple triggers is reduced to about one tenth of that in the sim data. Accordingly, the MTC approach leads to a percentage dead time of $\tau_{\text{dt2, sim}} \approx 0.35\,\%$ for sim and $\tau_{\text{dt2, phy}} \approx 0.04\,\%$ for phy data.

Since the sim data can be directly compared, they are used below to evaluate the applicability of the approaches. The FMC approach results in the detection of 66 % of muon-induced ^{77}Ge productions, with a percentage dead time of $\tau_{\text{dt1, sim}} \approx 8.17\,\%$. In contrast, the MTC approach identifies about 33 %, but achieves an approximately 23-fold lower percentage dead time of $\tau_{\text{dt2, sim}} \approx 0.35\,\%$ by using only the muon veto system.
If both approaches perform reliably, the FMC approach could be applied in the LEGEND experiment. Given the current uncertainties in the simulation, the PMTs breaks in the real muon veto system, and the limited statistics of the ^{77}Ge production simulation (cf. Section 8.2.1), the MTC approach is preferred for LEGEND-200 at the time of writing. In future work, refining the simulation parameters, for example by determining the water absorption length and measuring the individual PMT PDEs, as well as replacing the broken PMTs (cf. Chapter 9), could reduce the uncertainties associated with the approaches. Furthermore, coincidence analyses involving the LAr instrumentation and events in the HPGe detectors could further improve the approaches and enable the detection of ^{77}Ge production in LEGEND-200.

Chapter 9

Preparation of the LEGEND-200 muon veto PMT update

"One must imagine Sisyphus happy."

— Albert Camus, The Myth of Sisyphus

PMT failures in the muon veto reduce the detection efficiency of the muon veto system of LEGEND-200. This affects the muon-induced background and thus also on the remaining runtime of the muon veto. Accordingly, the efficiency of the muon veto must be maintained, which requires the replacement and addition of functional PMTs. Hamamatsu R1408 PMTs are characterized in a test stand and prepared for operation in the muon veto system.
This chapter provides an overview of the efficiency development of the muon veto with the status of operational PMTs and corresponding remaining runtime of the muon veto system. An update plan is presented, followed by a description of the preparation and characterization of the PMTs on a test stand, concluding with the status of the muon veto update at the time of writing of this work.

9.1 Muon veto performance with the PMT update

With an increasing number of PMT failures, as described in Section 6.2, the detection efficiency of the muon veto decreases. Figure 9.1 illustrates the impact of PMT breaks on the muon veto detection efficiency. The term "relative muon veto efficiency" refers to the efficiency normalized to the initial efficiency of the muon veto at the beginning of phy data taking in mid-March 2023, prior to the first PMT failure in p03 r003. At the time of writing of this work, in total 27 PMTs broke. Consequently, the order of failure is known for these PMTs. For future possible failures, a Monte Carlo approach was used: PMTs designated to fail were assigned in a randomized order, and

the corresponding relative efficiency was calculated. This procedure was repeated several times and the results averaged to obtain the final relative efficiency for the estimation. Additionally, the multiplicity trigger was considered and therefore the muon veto efficiency drops to zero as soon as three or less PMTs are remaining. The colored lines in Figure 9.1 represent the relative efficiency in the data acquisition at the beginning of the corresponding periods. To estimate the limit for the relative efficiency at which the muon veto can be operated, the eight muon background events in the ROI (cf. Section 6.4.1) are assumed to be distributed linearly with the mean relative efficiency between p03 and p11. Based on this assumption, at a relative efficiency of approximately 86.7 % at least one background event would remain undetected, which is therefore defined as operational limit (see the black horizontal line in Figure 9.1). In total, up to 36 PMTs may break before the muon veto reaches its operational limit.

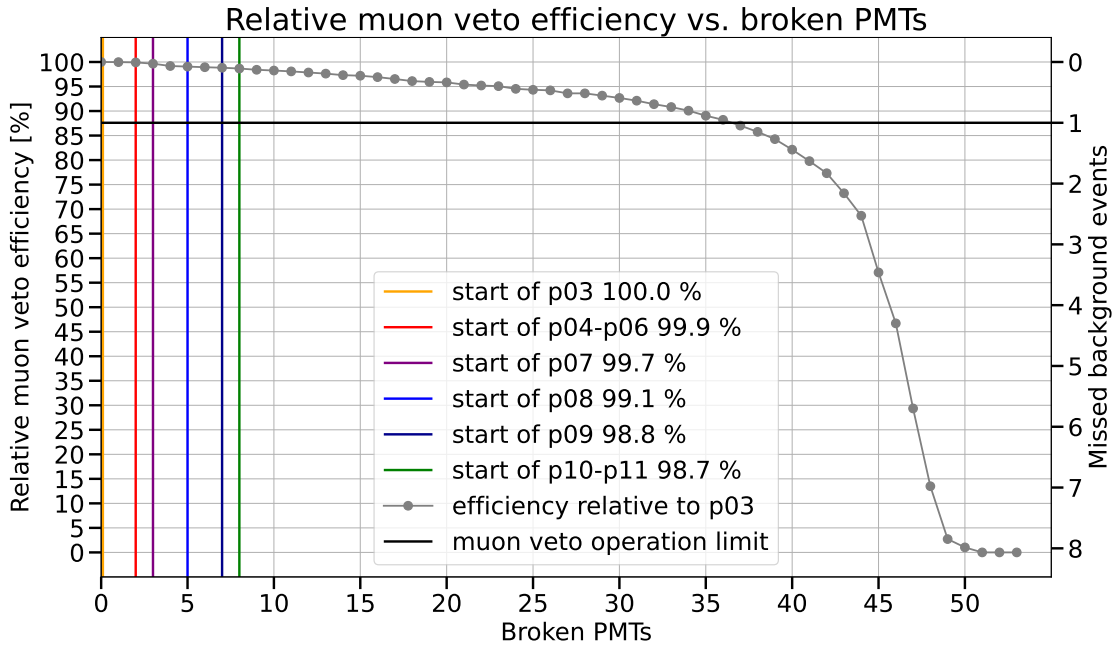

Figure 9.1.: Muon veto efficiency relative the beginning of p03 for different numbers of working PMTs. The colored lines mark the status at the beginning of the corresponding period. Eight detected background events in the ROI are distributed linearly over the mean relative efficiency between p03 and p11 at the right y-axis. The black horizontal line corresponds to at least 1 missed background event in the ROI and is therefore defined as the operational limit of the muon veto.

Figure 9.2 shows the muon-induced background index with increasing number of PMT failures. The black horizontal line shows the operational limit of the muon veto, while the red horizontal line represents the total background goal of the LEGEND-200 experiment of $2 \cdot 10^{-4}$ cts/(keV $\cdot$ kg $\cdot$ yr) (cf. Section 3.3.1). Thus, 36 broken PMTs correspond to a muon-induced background index of almost half the background goal of LEGEND-200. Accordingly, it is necessary to maintain the muon veto efficiency.

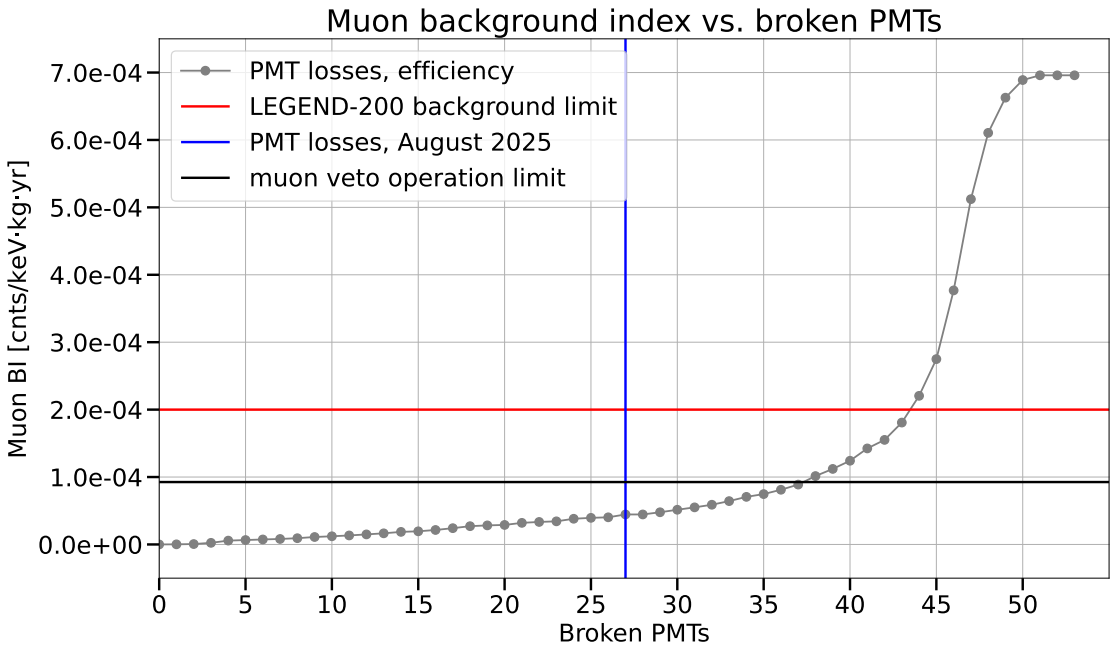

Figure 9.2.: Muon-induced background index based on events detected by the muon veto as a function of broken PMTs. The red line marks the total background goal of LEGEND-200 (cf. Section 3.3.1), while the black line shows the operational limit of the muon veto. The vertical blue line indicates the situation at the time of writing in August 2025.

In order to prevent the muon veto from exceeding its operational limit and to achieve the goal the muon-induced background index, its efficiency must be maintained. For this purpose, 19 broken PMTs will be replaced and 9 PMTs added to available positions in the muon veto in a planned update (cf. Section 9.4). Figure 9.3 shows the PMT distribution across the muon veto in August 2025 with functioning PMTs in yellow and those to be exchanged or added in gray. Compared to the PMTs present at the beginning of LEGEND-200 data taking (cf. Figure 5.1b), the PMTs at position 08, 09, 18-21 and 24-26 will be added to the muon veto (see Figure 9.3). PMT 508 remains as a gap between PMT 26 and 28, since it broke in April 2025 and thus after the preparation of the update plan. Broken PMTs at the wall above a height of 3.5 m remain unchanged, in order to avoid the delay due to the construction of a scaffolding within the muon veto. In total 54 PMTs are operational in the muon veto after the exchange and addition of 28 PMTs.

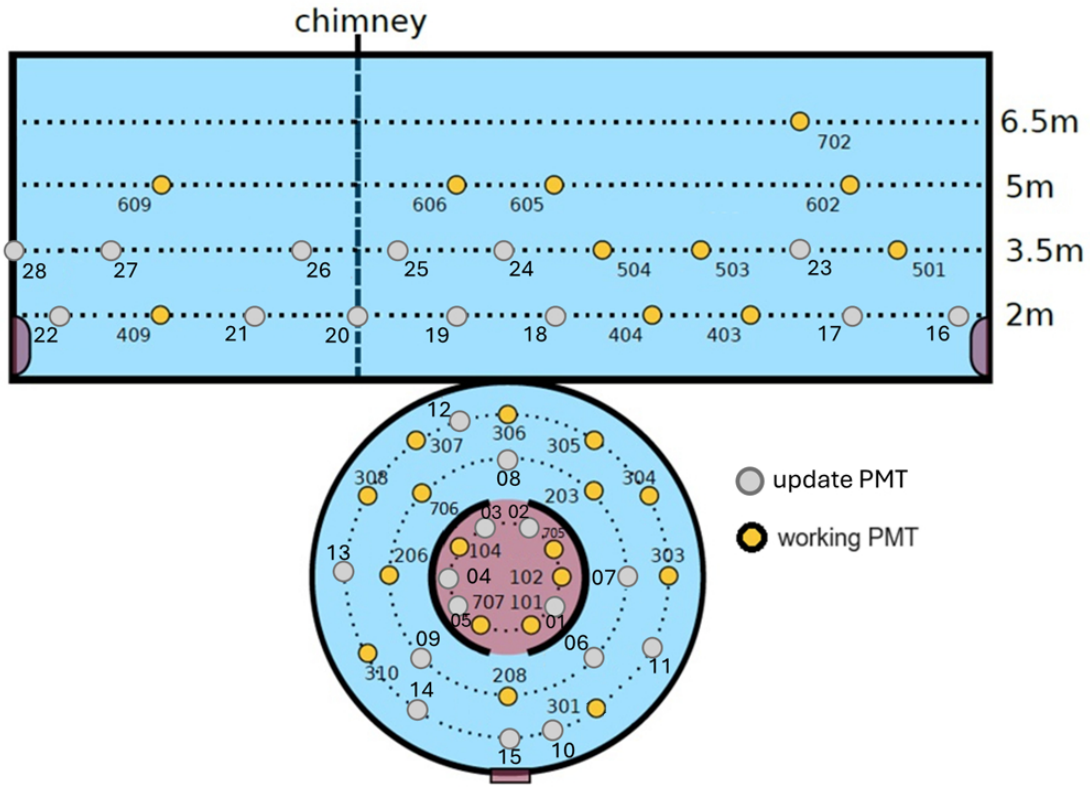

Figure 9.3.: PMT distribution across the muon veto system with operational PMTs (yellow) and PMTs to be added or exchanged during the muon veto update (gray). PMT 508, the gap between PMT 26 and 28, is not exchanged, since it broke in April 2025 and thus, after the preparation of the update PMTs. Adapted from [2].

Figure 9.4 shows the relative efficiency of the muon veto as a function of runtime beginning at the situation in August 2025 with (gray) and without (blue) a PMT update. Including the commissioning time of LEGEND-200 in 2022 [59], 27 PMTs broke in about three years. Accordingly, the loss rate is assumed to be $r_{\text{loss, working}} \approx 9$ PMTs/yr without an update. Thus, the operational limit is expected to be reached after almost 1 yr (i.e. around August 2026) without the PMT update. PMTs used in the outer veto of the Double Chooz experiment [98], which had a loss rate of 0 PMTs/yr during operation [99], are to be used for the update. To take a conservative approach, the loss rate of the update PMTs is estimated to $r_{\text{loss, update}} \approx 1.5$ PMTs/yr. The total loss rate of the updated muon veto system $r_{\text{loss, total}}$ can be calculated via

$$r_{\text{loss, total}} = \frac{N_{\text{working}}}{N_{\text{total}}} \cdot r_{\text{loss, working}} + \frac{N_{\text{update}}}{N_{\text{total}}} \cdot r_{\text{loss, update}} \tag{9.1}$$

where $N_{\text{working}} = 26$ is the number of still working PMTs in the muon veto, $N_{\text{total}} = 54$ the total number of muon veto PMTs after the update and $N_{\text{update}} = 28$ the corresponding number of the

PMTs used for the update. This results in a total loss rate of $r_{\text{loss, total}} \approx 5.11$ PMTs/yr after the PMT update, leading to a remaining runtime of about 7.3 yr. Thus, updating the PMTs in the muon veto is necessary to ensure its operability for the live time goal of the LEGEND-200 experiment of 5 yr in total (cf. Section 3.3.1).

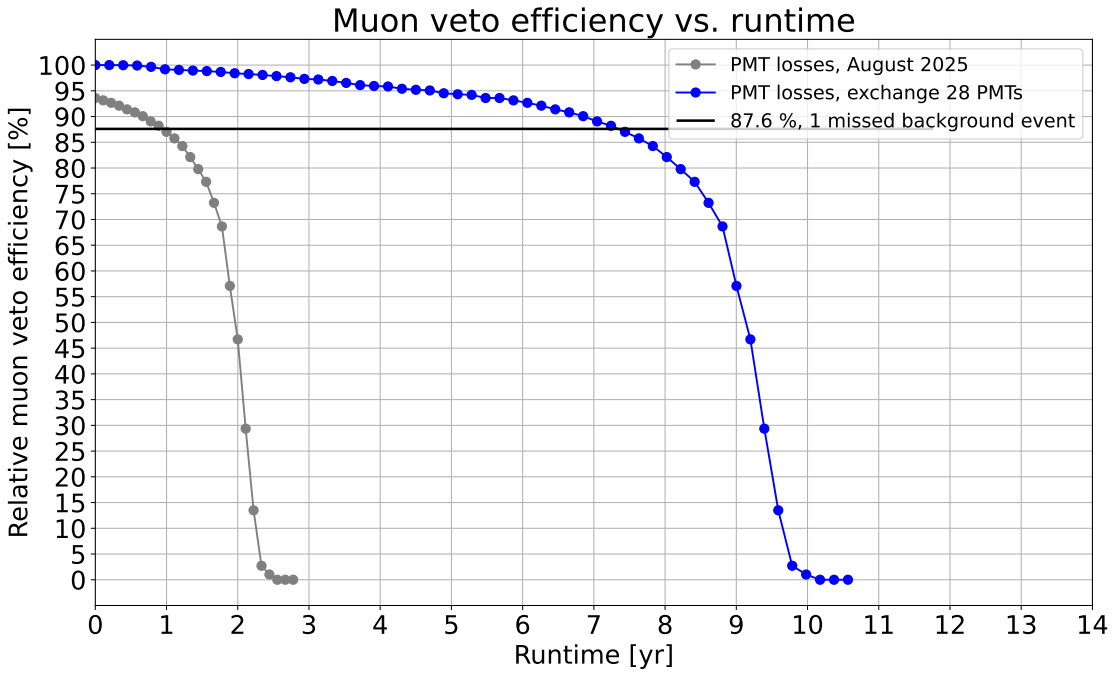

Figure 9.4.: Relative muon veto efficiency as a function of the runtime beginning at the situation in August 2025. The gray dots mark the situation without an PMT update, while the blue dots show the situation with 28 update PMTs. The black line shows the operational limit of the muon veto.

9.2 PMT test stand

In order to verify the functionality of the PMTs required for the update of the LEGEND-200 muon veto, a test stand was set up. Figure 9.5 shows a schematic representation of the DAQ chain of the test stand (a picture of the DAQ electronics can be found in Figure D.1) in the Appendix. A frequency generator triggers both an ADC and a pulser connected to a LED. The used LED is supplied with up to 12 V. Pulser, LED, and PMT (cf. Section 9.2.1) are mounted inside a dark box located in a dark room to prevent the detection of external light and to protect the PMTs from damage due to potential light exposure. The LED faces the PMT, which detects the light and sends the signal to a splitter box (cf. Figure A.1), which separates the supplied HV from the signal. The signal can be sent to an oscilloscope for measuring dark counts or directly to the ADC, specifically a V1740D ADC with a 12-bit resolution and a sampling rate of 62.5 MHz [100]. It is connected to a PC, which manages the DAQ and stores the data for analysis. Measurements at

different PMT and LED voltages are performed to characterize the PMTs (cf. Section 9.3), with each measurement containing 600,000 triggers, resulting in the same number of stored entries.

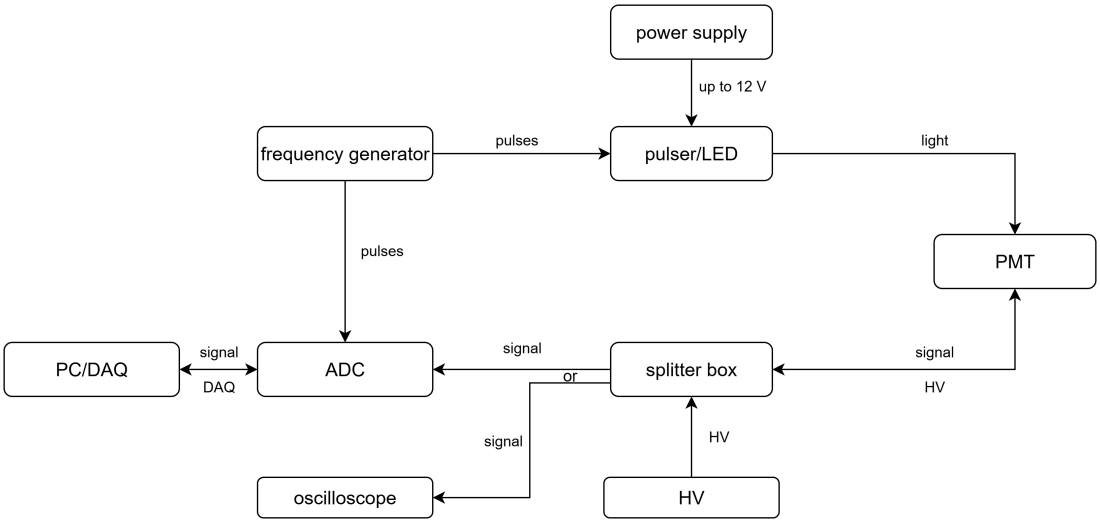

Figure 9.5.: Schematic representation of the DAQ chain of the PMT test stand. A frequency generator pulses an ADC and a pulser connected with a LED. The LED light is measured by the PMT, which is placed in a dark box. The PMT signal is separated from the HV by a splitter box and forwarded to the ADC or an oscilloscope. The ADC forwards signals to an PC with the DAQ. Here the data is stored and analyzed.

9.2.1 PMTs for the muon veto update

The PMTs intended for the LEGEND-200 muon veto update are 8" Hamamatsu R1408 PMTs [101]. The dynode structure of these PMTs differs from the linear-focused type of the ETL 9350KB and 9354KB PMTs previously used in the muon veto of LEGEND-200. Hamamatsu PMTs of type R1408 feature a "venetian blind" dynode structure with 13 dynode stages. Figure 9.6 shows a schematic representation of a PMT with such a dynode structure, where the dynodes are arranged in layers, each tilted in alternating directions. Photoelectrons released from the photocathode upon photon excitation trigger secondary electrons in the dynode structure. However, these electrons can follow different paths through the dynode structure, which prevents a clear single photon resolution [102]. Thus, the gain of the R1408 PMTs cannot be calculated via the single p.e. peak (cf. Section 5.3), as described in more detail in Section 9.3.

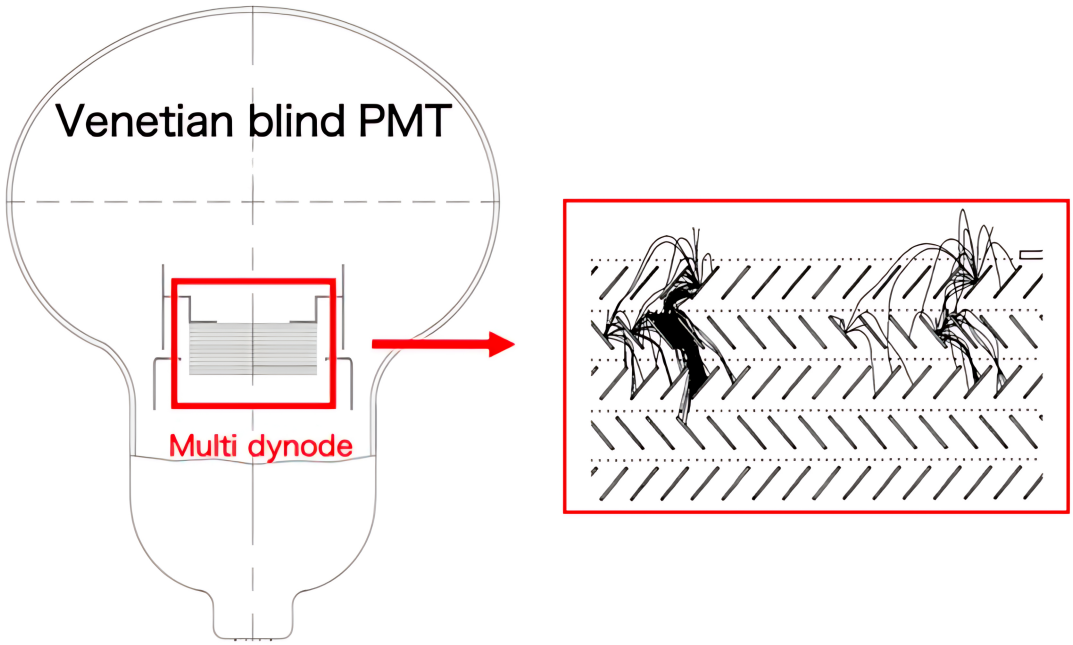

Figure 9.6.: Schematic representation of a PMT with venetian blind dynode structure highlighted in the red box. The inset schematically illustrates the initial stages of two electron avalanches occurring between the dynodes. Adapted from [103].

The QE and the cathode radiant sensitivity, describing the sensitivity of the cathode as a function of the wavelength, of the Hamamatsu R1408 PMTs are shown in Figure 9.7. The QE spans over a wavelength range of approximately 280 nm – 720 nm with a maximum at approximately 400 nm, which is comparable to the ETL PMTs in the muon veto (cf. Figure 5.3). However, the maximum QE of the Hamamatsu PMTs is about 25 %, which is 5 % lower than the maximum of the ETL PMTs. Additionally, the CE of venetian blind dynodes is typically lower compared to the linear-focused type, as secondary electrons can follow multiple paths [66].

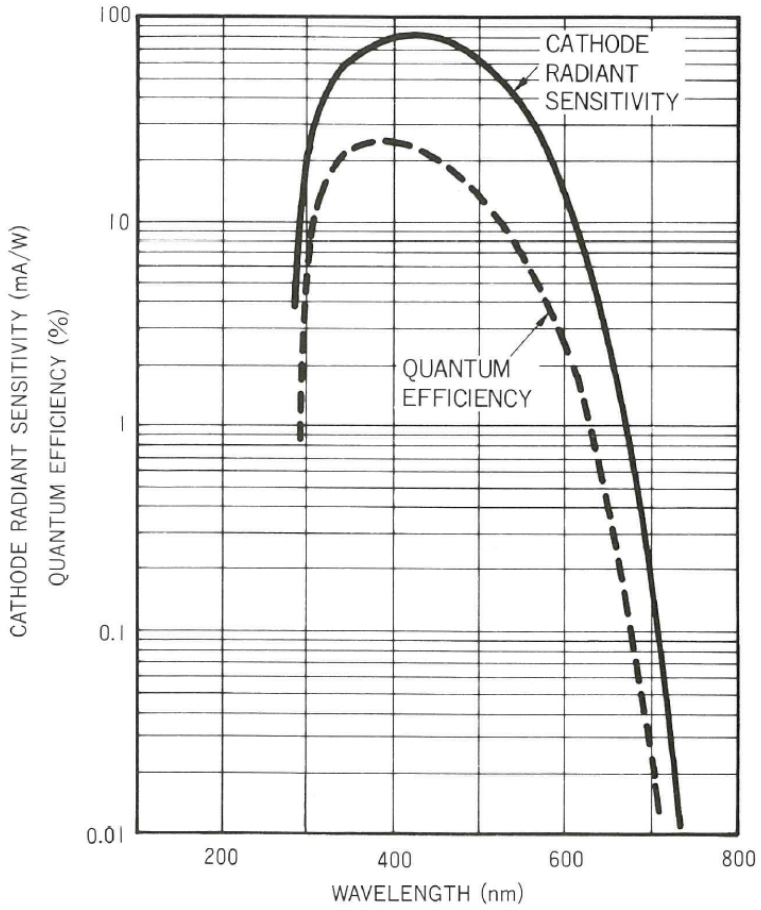

Figure 9.7.: Exemplary response curve of a Hamamatsu R1408 PMT showing the QE and radiant sensitivity of the cathode as a function of the wavelength. Taken from [101].

Consequently, the overall PDE of the Hamamatsu PMTs is lower. To compensate the reduced PDE, the PMT distribution density on the floor of the muon veto is increased with the update (see Figure 9.3) compared to the beginning of the LEGEND-200 data collection (see Figure 5.1b). Despite their lower PDE compared to the ETL PMTs, the Hamamatsu R1408 PMTs were chosen for the update because of their availability, operational stability, and compatibility with the LEGEND-200 muon veto.

9.3 PMT characterization

Unlike linear-focused PMTs, venetian blind PMTs must be calibrated using a different method based on multiple p.e. events, as described in [102, 104]. The method defines the probability $P_1(q)$ of measuring a specific charge q during a single photon event via

$$P_1(q)dq = \frac{1}{q_0}\exp\left(-\frac{q}{q_0}\right)\Theta(q)dq\,, \tag{9.2}$$

where $\Theta(q)$ is the Heaviside function for the corresponding charge q and $q_0 = E_{P_1}$ denotes the charge expectation value. The variance V_{P_1} can be derived accordingly via $V_{P_1} = q_0^2$. To describe multiple photon events $P_n(q)$ that represent the superposition of single photon events, the function $P_1(q)$ in Equation 9.2 is convolved with itself:

$$P_n(q)dq = \frac{q^{n-1}}{(n-1)!q_0^n}\exp\left(-\frac{q}{q_0}\right)\,. \tag{9.3}$$

With a constant number of incoming photons through the LED, the probability of generating m p.e.s can be described using a Poisson distribution depending on the mean number of photons μ_γ via

$$P(m,\mu_\gamma) = \frac{\mu_\gamma^m}{m!}\exp(-\mu_\gamma)\,. \tag{9.4}$$

The combination of Equation 9.3 and Equation 9.4 results in the probability $P(q,\mu_\gamma)$ to observe a charge q at a mean number of photons μ_γ described with

$$P(q,\mu_\gamma) = \sum_{m=1}^{\infty}\left(\frac{\mu_\gamma^m\exp(-\mu_\gamma)}{m!}\right)\frac{q^{m-1}}{(m-1)!q_0^m}\exp\left(-\frac{q}{q_0}\right)\,. \tag{9.5}$$

This yields, for a mean number of photons μ_γ, an expectation value of $E(q,\mu_\gamma) = \mu_\gamma q_0$ with a variance of $V(q,\mu_\gamma) = 2\mu_\gamma q_0^2$. Using Equation 5.2, the relation between expectation value and variance is given by

$$V(q) = 2gq_0E(q)\,. \tag{9.6}$$

From Equation 9.6, the gain g can be determined via the slope of variance V and expectation value E according to

$$\frac{\partial V}{\partial E} = 2gq\,, \tag{9.7}$$

where q is assumed to be the elementary charge $q \approx 1.602\cdot 10^{-19}$ C. Accordingly, the gain g can be derived from measurements at different LED intensities with the same supplied voltage of the PMT.

Subsequently, for calibrating the PMTs to the desired gain, the measurements at varying LED

intensities must be repeated for different supplied PMT voltages. Using Equation 5.3, where $n = 13$ for the Hamamatsu R1408 PMTs, the target voltage V_{target} corresponding to the desired gain g_{target} can then be determined by fitting the measured gain-voltage relation of the PMT.

9.3.1 Characterization results

In total, 51 Hamamatsu R1408 PMTs were characterized by the test stand (cf. Section 9.2) using the method described in Section 9.3. The code used during the measurements was adapted from gain determination measurements of Hamamatsu R1408 PMTs performed in [105]. To obtain the variance and expectation value as described in Equation 9.6, multiple p.e. peaks of the PMTs were recorded for six different LED voltages. For the determination of the PMT gain, 30 measurements per PMT were performed. For five PMT voltages (with steps of 50 V), the charge is measured for six different LED voltages in steps of 0.1 V. In order to measure multiple p.e. spectra, the minimum LED was set to 8.5 V, increased to 9.0 V.
The corresponding charge histograms for an example PMT are shown in Figure 9.8. With increasing PMT and LED voltage, the mean μ and standard deviation σ of the charge spectra increase, reflecting the higher gain and brighter light. The charge distributions can be approximated by a Gaussian distribution, originating from statistical variations in the secondary photon generation, and are thus fitted with a Gaussian function [105]. Here, the variance $V(q)$ corresponds to the square of the standard deviation σ^2 and the expectation value $E(q)$ to the mean value μ of the Gaussian fit.
Figure 9.9 shows the corresponding values of the variance $V(q)$ as a function of the expectation values $E(q)$ for different PMT voltages. Using a linear fit (cf. red line in Figure 9.9a to 9.9e), the corresponding PMT gain is determined via Equation 9.7. The error bars represent the related uncertainties of the fit.
Using Equation 5.3 the gain-voltage relation can be fitted, as represented with the red line in Figure 9.10. The displayed error bars correspond to the uncertainties of the gain fit (cf. Figure 9.9). In order to compare the PMTs with each other, the supplied voltage is set to a corresponding gain of $g_{\text{target}} = 10^7$, which is marked with the black cross in Figure 9.10. The target gain was set to 10^7, representing an upper limit, to test whether the corresponding supply voltage and current remain within the operational ranges of the SlowControl of the muon veto system, which are $0 - 1000\,\mu$A for the current and $0 - 4000$ V for the voltage.

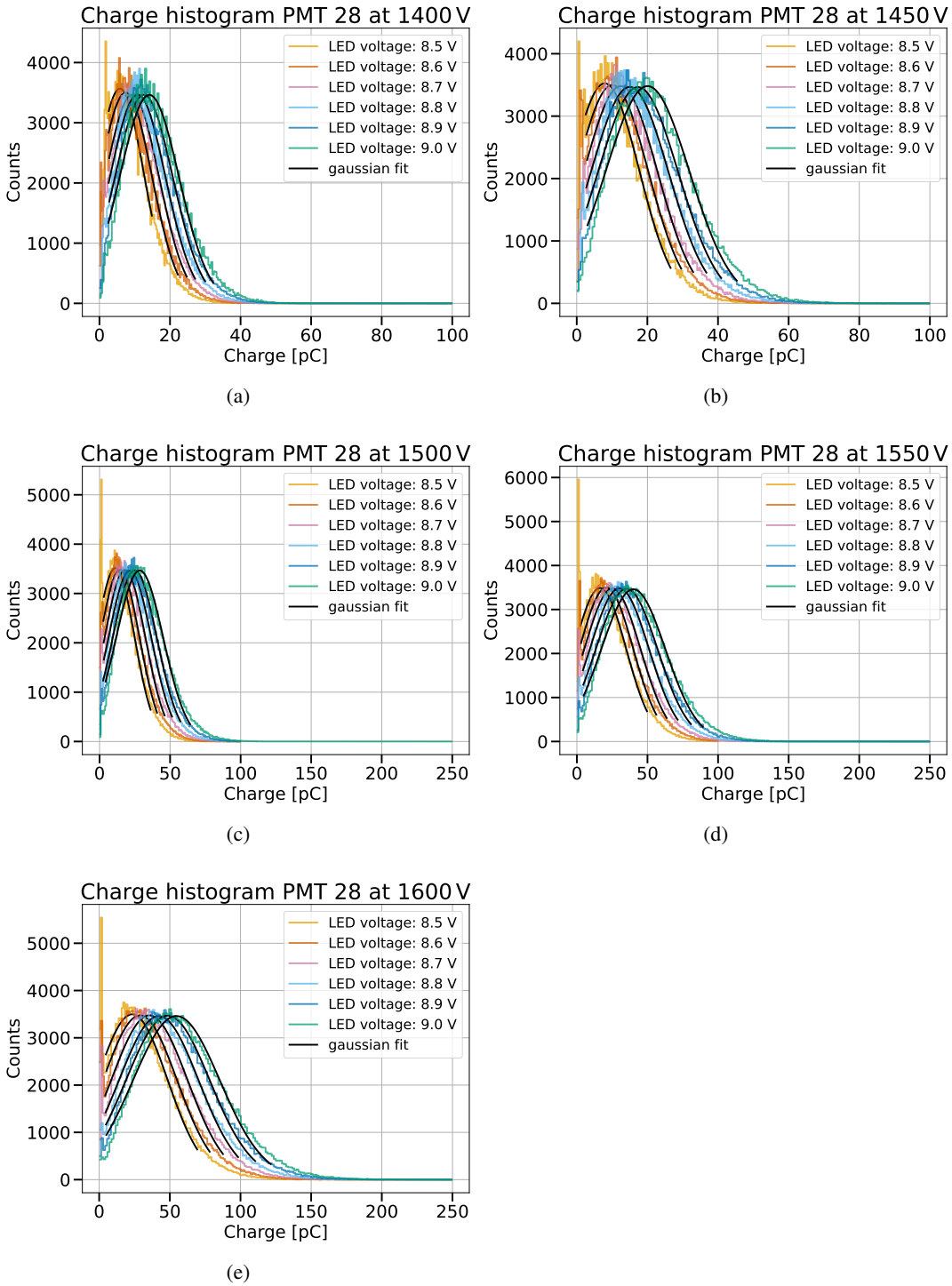

Figure 9.8.: Charge histogram of multiple p.e. events with six different LED voltages in between 8.5 V and 9.0 V (represented with different colors) with corresponding Gaussian fits (black lines) for an example Hamamatsu R1408 PMT. Different PMT voltages are supplied: (a) 1400 V, (b) 1450 V, (c) 1500 V, (d) 1550 V and (e) 1600 V.

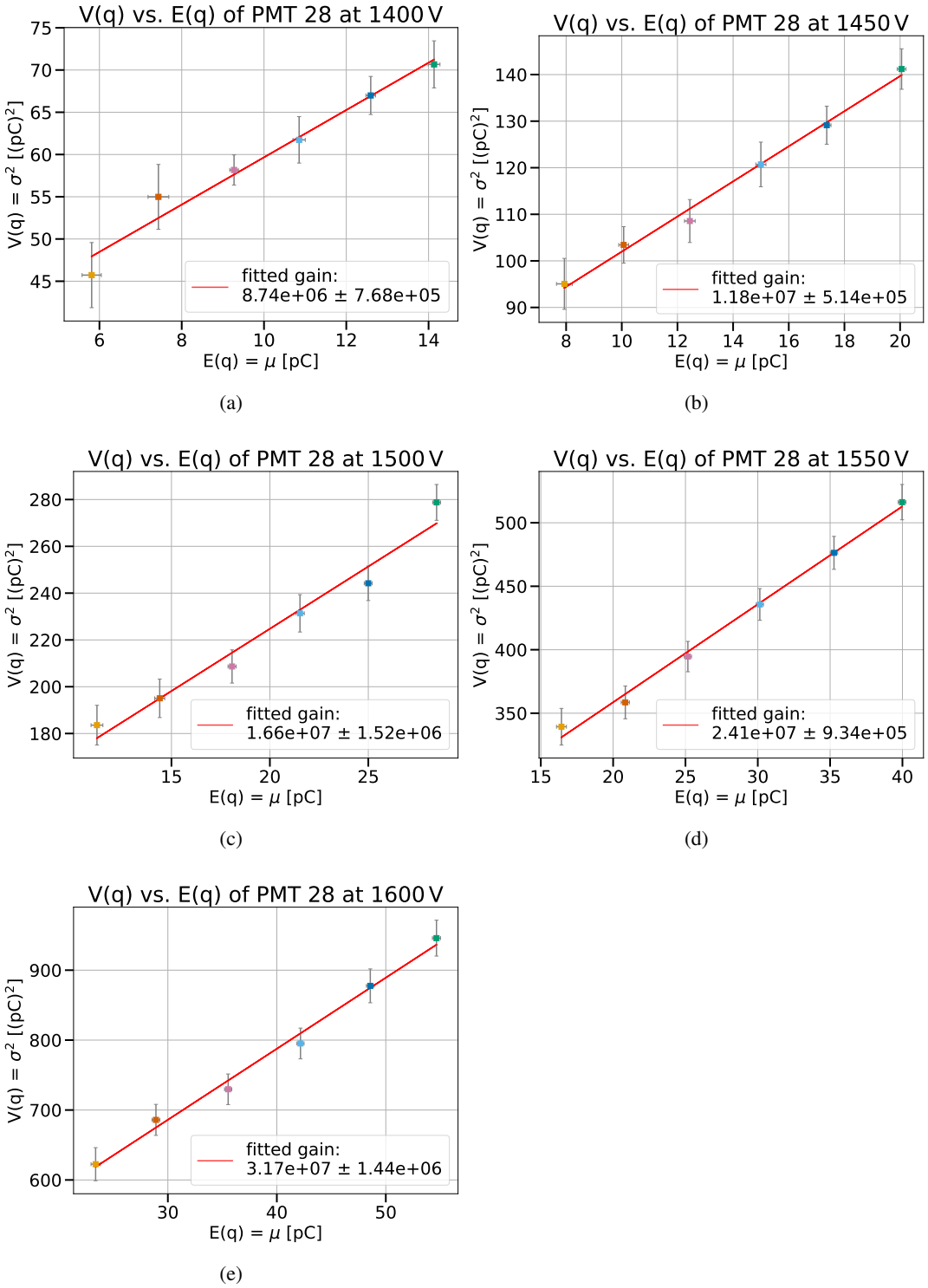

Figure 9.9.: Variance (corresponding to the squared standard deviation σ^2 of the gaussian fits of Figure 9.8) as a function of the expectation value (corresponding to the mean μ of the gaussian fits of Figure 9.8) for an example Hamamatsu R1408 PMT. The red lines represent the fit of the gain via Equation 9.7. Different PMT voltages are supplied: (a) 1400 V, (b) 1450 V, (c) 1500 V, (d) 1550 V and (e) 1600 V.

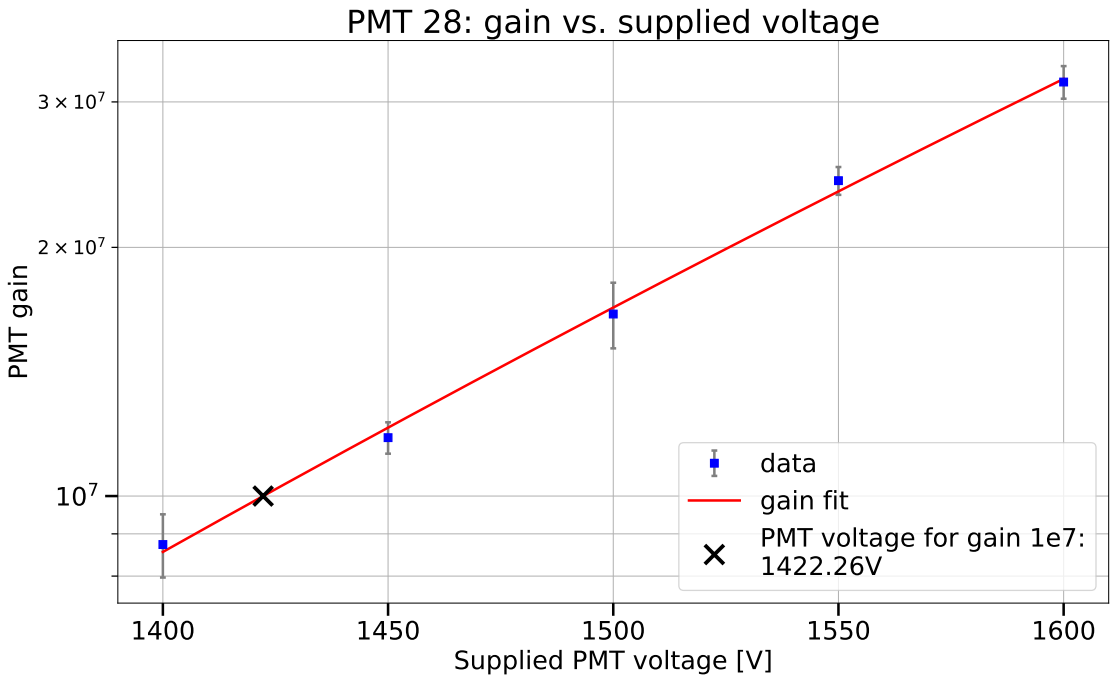

Figure 9.10.: PMT gain as a function of the supplied voltage for an example Hamamatsu R1408 PMT. The relation between gain and supplied voltage is fitted using Equation 5.3 and displayed as the red line. The black cross marks the voltage used for a reference gain of 10^7 in order to compare different PMTs responses with the same gain.

Table 9.1 shows the results of the PMT characterization measurements. The supplied PMT voltage is related to a gain of $g_{\text{target}} = 10^7$ for the corresponding PMT. In total 28 PMTs were prepared for the muon veto update. PMT 4 and PMT 20 showed overcurrent respectively a high dark count rate and were therefore excluded from the update plan. PMT 15 could not be included in the update, as its encapsulation was damaged during the preparations.

Since the PMTs had previously been used in the Double Chooz experiment, they were enclosed in a capsule filled with spectroscopy oil [102]. To test their functionality, six PMTs were first tested with the spectroscopy oil. For environmental reasons [59], however, no PMT encapsulations including spectroscopy oil may be used in the LEGEND-200 muon veto. After six PMTs had been successfully characterized with spectroscopy oil, it was removed and the PMTs and encapsulations were cleaned with acetone and petroleum ether [106] and the PMTs were re-characterized. The resulting supplied voltages differ with a standard deviation of approximately 38.49 V between measurements with and without spectroscopy oil, corresponding to a deviation of approximately 2.68 %, with a mean voltage of 1435.67 V without the oil, likely due to the different refraction indices of air $n_{\text{air}} \approx 1$ and typical spectroscopy oils $n_{\text{oil}} \approx 1.5$ [107]. Since the deviation is small and fluctuates between positive and negative voltage changes (cf. line one to twelve Table 9.1), the following PMTs were immediately emptied and measured without oil.

Table 9.1.: Prepared Hamamatsu R1408 PMTs measurements with corresponding filling status of spectroscopy oil in the encapsulation, supplied voltage, current and dark count rate at a gain of $g_{\text{target}} = 10^7$.

PMT	Oil	Voltage [V]	Current [µA]	Dark count rate [Hz]
1	yes	1538	141.000	865.16
1	no	1553	142.404	1420.00
2	yes	1299	119.018	614.04
2	no	1368	125.470	1149.60
3	yes	1546	141.752	1076.00
3	no	1552	142.316	3074.00
5	yes	1397	127.864	3871.67
5	no	1361	124.686	4601.40
6	yes	1359	124.714	1137.07
6	no	1403	128.760	2804.30
7	yes	1475	135.182	929.10
7	no	1550	142.086	9867.70
8	no	1526	139.792	7869.60
9	no	1450	132.982	6446.70
10	no	1284	117.726	1052.90
11	no	1377	126.230	5953.50
12	no	1463	134.106	2599.40
13	no	1453	133.322	4619.30
14	no	1341	126.342	5302.50
16	no	1341	122.818	4390.90
17	no	1373	125.754	1317.40
18	no	1458	133.658	1500.80
19	no	1407	129.044	7344.00
21	no	1522	139.470	966.53
22	no	1284	117.760	3719.00
23	no	1375	125.880	3448.50
24	no	1437	131.698	1613.80
25	no	1404	128.668	5015.00
26	no	1227	112.424	1421.90
27	no	1329	121.796	1514.10
28	no	1422	134.112	1501.30
29	no	1302	119.360	1736.50
30	no	1493	136.744	1475.70
31	no	1429	131.036	1376.50

As Table 9.1 shows, the supplied PMT current at a gain of $g_{\text{target}} = 10^7$ varies between approximately 117 μA and approximately 142 μA, well below the overcurrent threshold of 600 μA set in the muon veto SlowControl (cf. Section 6.2.1). The PMT voltages differ between 1227 V and 1553 V, similar to the ETL PMTs with a maximum supplied voltage of approximately 1800 V. Thus, the Hamamatsu R1408 PMTs can be operated within the LEGEND-200 muon veto SlowControl system.
The last column of Table 9.1 represents the dark current rate of the PMTs at a gain of $g_{\text{target}} = 10^7$. For these measurements, the output signal was forwarded to the oscilloscope (cf. Figure 9.5). Without an external light source, measurements were performed for 100 s and PMT signals were counted via the counter of the oscilloscope. Since the data sheet of the Hamamatsu R1408 PMTs refers to a dark count rate of (10000 – 30000) Hz at a gain of 10^8 [101], the measured dark count rate at a gain of $g_{\text{target}} = 10^7$ is expected to be smaller. Accordingly, a dark count rate above 10000 Hz at $g_{\text{target}} = 10^7$ was considered as too high, and the corresponding PMT was excluded from the muon veto update.

9.4 Status of the PMT update

At the time of writing, 28 PMTs have been characterized using the test stand (cf. Section 9.2) and encapsulated. They will be delivered to LNGS in September 2025 and are expected to be installed in the muon veto of LEGEND-200 at the end of 2025. This will require a new calibration procedure that combines the previous calibration of the ETL 9350KB and 9354KB PMTs with that required for the Hamamatsu R1408 PMTs. Therefore, it is recommended to first perform calibration in the single p.e. range of the ETL PMTs, as described in Section 5.3, in order to prevent afterpulsing caused by prior exposure to higher light levels. Then, the voltage of the pulsed LEDs should be increased to the multiple p.e. region and a gain scan according to Section 9.3.1 should be carried out for the Hamamatsu PMTs. Here, the gain of both PMT types should be set to $g_{\text{target}} = 2.9 \cdot 10^6$ in order to enable measurements of up to 100 p.e. for each PMT (cf. Section 5.3).
Afterwards, the light intensity trigger threshold should be compared using the pulsed LEDs for both PMT types. Since the Hamamatsu PMTs exhibit a lower PDE than the ETL PMTs (cf. Section 9.2.1), the same light intensity produces weaker signals in the Hamamatsu PMTs. Therefore, a lower light intensity trigger threshold or higher gain could be necessary for the Hamamatsu PMTs in order to ensure a comparable response of both PMT types for the same light intensity. One possible approach would be to operate the pulsed LEDs in the single p.e. range of the PMTs. By analyzing the waveforms, the level of the single p.e. signals of the PMTs can be compared. If these differ, the light intensity trigger threshold should be scaled accordingly.
After the calibration and verification of the trigger threshold for both PMT types, the muon veto can be operated as before, but with a restored efficiency and extended runtime.

Chapter 10

Conclusion and outlook

"The important thing is not to stop questioning. Curiosity has its own reason for existing."

— Albert Einstein

The Large Enriched Germanium Experiment for Neutrinoless $\beta\beta$ Decay (LEGEND) research program is dedicated to the search for $0\nu\beta\beta$-decay in enriched ^{76}Ge in order to investigate the Majorana nature of neutrinos and thereby explain their small mass beyond the SM. The current phase, LEGEND-200, serves as a demonstrator for the ton-scale LEGEND-1000 and aims for a half-life sensitivity of more than $T^{0\nu}_{1/2} = 10^{27}$ yr, corresponding to a BI below $2 \cdot 10^{-4}$ cts/(keV $\cdot$ kg $\cdot$ yr) in the ROI. Achieving such a low background requires both passive and active background rejection strategies. In LEGEND-200, the LAr instrumentation provides an active shielding mainly against radiogenic background sources near the HPGe detectors and a water Cherenkov veto operates as an active muon veto system. The muon veto uses PMTs to detect Cherenkov light produced by muons traversing the water tank, while a reflective foil, covering the inner surfaces of the water tank, increases the light yield.

In this work, the LEGEND-200 muon veto was analyzed, muon event structures were studied through Monte Carlo simulations, and additional PMTs were prepared for an update to maintain its detection efficiency.
To ensure stable signal performance, the calibration method of the muon veto system was further developed in this work, and the PMTs were calibrated once or twice per month. In this way, the single p.e. response of each PMT was adjusted to approximately 30 ADC channels, allowing a measurable range of at least 100 p.e.
The analysis presented in this work covers nearly one year of data from the muon veto system, from mid-March 2023 (p03) to early May 2024 (p11). Detected events include muons, persistent low-multiplicity signals (the low-multiplicity bump), and spontaneous signals caused by broken PMTs. To remove most of these non-muon contributions, two cuts were applied in the data. The

first excludes the low-multiplicity bump (multiplicity ≤ 11 and p.e. ≤ 7), while the second suppresses flashing PMT signals (multiplicity ≤ 13 and p.e. ≥ 98). After these cuts, the resulting muon rate is $r_{\text{muon}} \approx 35\,\text{mHz}$, which is in good agreement with the value determined from commissioning data in [59] and from the GERDA muon veto [2].

Muon events were matched with the HPGe DAQ. This enabled an assignment of muon events to the corresponding HPGe events in the LEGEND-200 processing chain. Additionally, overview plots were generated to monitor PMT stability using cal and phy data. These plots were included in the LEGEND-200 dashboard monitoring. Between p03 and p11, several PMTs breaks were observed, which were classified into three types: aging, flashing, and spontaneous breaks. Waveform analysis allowed the definition of different waveform classes. An analysis of the undershoots did not reveal any new structures in the muon veto events. However, by combining the monitoring systems with waveform analysis, criteria could be identified to predict PMT breaks in advance. A waveform criterion regarding non-physical noisy events could be included in the LEGEND-200 data processing.

PSD of the muon veto events, combined with the cuts for flashing PMTs and the low-multiplicity bump, enabled a clear separation of the muon events. These events were then analyzed in coincidence with the HPGe detectors and LAr instrumentation. The coincidence rate between muon veto and HPGe events was found to be $r_{\text{coincident}} \approx 0.62\,\text{mHz}$, while the rate for valid HPGe, after the application of their quality criteria, was $r_{\text{valid, coincident}} \approx 0.10\,\text{mHz}$. In total, six muon events were detected by the muon veto but not by the LAr instrumentation, corresponding to an additional muon-induced background of approximately $1.84 \cdot 10^{-5}$ cts/(keV · kg · yr), assuming a flat spectrum. The total muon-induced background in the ROI would lead to a BI of approximately $5.46 \cdot 10^{-4}$ cts/(keV · kg · yr) without an active muon suppression. This agrees with the measured muon-induced background in GERDA of $6.34 \cdot 10^{-4}$ cts/(keV · kg · yr) [1].

In order to gain a deeper insight into the phy data, a simulation geometry of the muon veto was implemented in the scope of this work in the LEGEND-200 simulation framework. Additionally, an event building and post-processing procedure was used to model the data of the real system. Using Geant4 Monte Carlo simulations, a lower limit of the muon veto detection efficiency was determined to be $\eta_{\text{sim}} \approx 99.18\,\%$.

In this work, the comparison between sim and phy data serves as a validation of the simulation parameters and enables further investigation of structures in the phy muon veto data. By comparing one week of data, a non-linear overestimation of the simulated light yield was found. However, the structure of the muon events is comparable between sim and phy data, and thus the simulation can be employed for further analyses.

An investigation of the origin of the low-multiplicity bump did not confirm the assumption made in [2, 3] that ^{60}Co β decays induce scintillation in the reflective foil and thus explain the low-multiplicity bump. Instead, as part of the ^{222}Rn decay chain, ^{214}Pb and ^{214}Bi β decays could account for the low-multiplicity bump, corresponding to a specific ^{222}Rn activity of approximately

50 mBq/kg.

Since showering muons in the water tank can produce neutrons, which may be captured in a HPGe detector and mimic a $0\nu\beta\beta$-like signal through ^{77}Ge productions, this process was further investigated. For this purpose, showering muons were first classified. The information on particle production processes provided by the simulation allows the classification of showering muon events that generate secondary particles in the water tank. A classification criterion applicable to both sim and phy data was established by comparing the light intensities of different PMT distribution areas in the muon veto. This criterion enabled the identification of 11.02 % showering muons in the sim and 10.51 % in the phy data.

By simulating one year of muons, six neutron captures in HPGe detectors were observed, four of which were also detected by the muon veto. Two of these detected events showed multiple triggers in the muon veto, with the first trigger at full multiplicity. Using these features, two approaches for the classification of muon-induced neutron captures in HPGe detectors were developed for sim and phy data. The first approach detects approximately 66 % of muon-induced ^{77}Ge productions, with a percentage dead time of $\tau_{\mathrm{dt1,\,sim}} \approx 8.17\,\%$ for the experiment, while the second detects about 33 % with an approximately 23-fold lower percentage dead time of $\tau_{\mathrm{dt2,\,sim}} \approx 0.35\,\%$ using only the muon veto. However, both approaches exhibit large uncertainties, due to breaking PMTs or potentially incorrect simulation parameters.

The failure of several PMTs between p03 and p11 also affects the detection efficiency as well as the muon-induced background and the remaining runtime of the LEGEND-200 muon veto. In this work, an examination of detection efficiency with an increasing number of PMT failures sets the operational limit of the muon veto at 36 broken PMTs. This corresponds to a remaining runtime of almost 1 yr starting from August 2025. Beyond this limit, at least one background event would no longer be vetoed by the muon veto after passing this operational limit.

To avoid this, 28 PMTs from the Double Chooz experiment [98] were characterized in a test stand and prepared for installation in the LEGEND-200 muon veto. By the end of 2025, the prepared PMTs will be installed in the LEGEND-200 muon veto to restore its efficiency and extend its runtime to approximately 7.3 yr thereby ensuring that the live time goal of LEGEND-200 of 5 yr can be achieved.

For future improvements of the simulation parameters, a water sample from the LEGEND-200 muon veto could be analyzed for its absorption length and the ^{222}Rn content could be measured to test its contribution to the low-multiplicity bump. With appropriately adjusted simulation parameters, further studies could include muon track reconstruction using both sim and phy data. The approaches for the classification of muon-induced neutron captures in HPGe detectors could be verified and refined. Combining these data with the muon veto results from the GERDA experiment [35] would refine the statistics for rare neutron captures. Optimizing the simulation parameters would enhance the reliability of the sim and phy criteria. Furthermore, adding or replacing PMTs in the LEGEND-200 muon veto would ensure stable detection efficiency and

enable a more precise multiplicity criterion for neutron capture analysis.
In the future LEGEND-1000 phase, an additional neutron tagging system in the water tank will measure muon-induced neutron captures in HPGe detectors. The low-multiplicity bump could be mitigated in both the neutron tagger and the muon veto by using a different reflective foil in the water tank. Moreover, the stability criteria and monitoring methods developed in this analysis could be scaled to the LEGEND-1000 muon veto, supporting the achievement of the LEGEND background goals and enhancing the potential to detect $0\nu\beta\beta$-decay.

Appendix A

PMT hardware and DAQ configurations

This appendix presents the wiring diagram of the splitter boxes used to separate the PMT voltage and signal in the LEGEND-200 muon veto (cf. Figure A.1) and a PMT channel mapping for the DAQ (cf. Table A.1) and SlowControl system (cf. Table A.2). Additionally, Table A.3 provides an overview of the data taking periods and PMT stability.

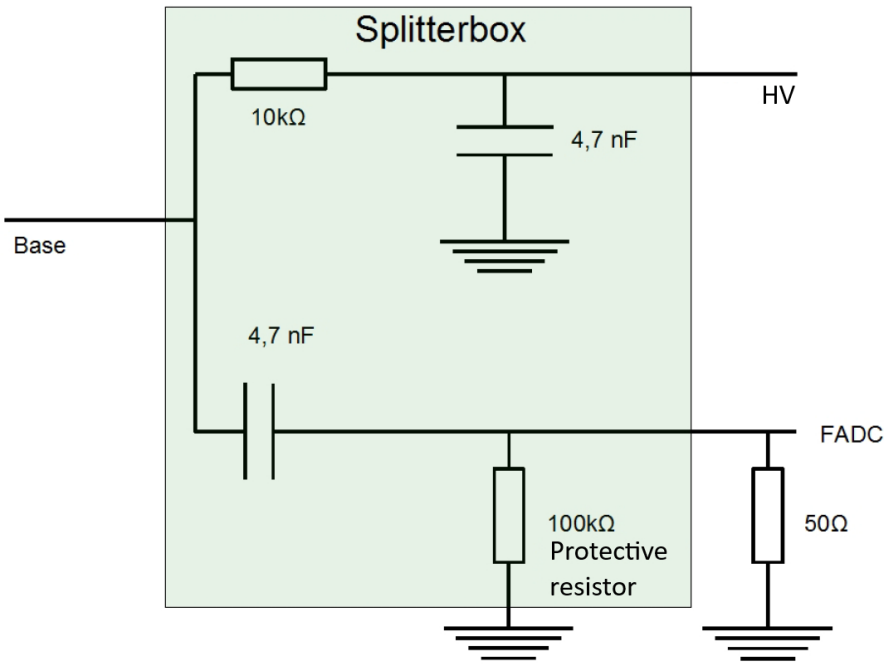

Figure A.1.: Wiring diagram of a splitter box for the PMTs of the LEGEND-200 muon veto. Adapted from [1].

Table A.1.: Assignment of channel and board number used from ORCA and corresponding PMT ID.

Ch./Brd. ORCA	0 Pillbox	1 Floor	2 Wall
0	Pulser	201	401
1	101	202	402
2	704	203	403
3	102	706	404
4	705	206	409
5	708	208	410
6	104	701	501
7	709	703	502
8	105	301	503
9	710	302	504
10	707	303	507
11		304	508
12		305	509
13		306	510
14		307	602
15		308	603
16		309	605
17		310	606
18		311	607
19		312	608
20			609
21			610
22			702
23			-

Table A.2.: Assignment of PMT channel and corresponding PMT ID.

PMT Channel	PMT ID	PMT Channel	PMT ID	PMT Channel	PMT ID
0	101	18	301	36	501
1	704	19	302	37	502
2	102	20	303	38	503
3	705	21	304	39	504
4	708	22	305	40	507
5	104	23	306	41	508
6	709	24	307	42	509
7	105	25	308	43	510
8	710	26	309	44	602
9	707	27	310	45	603
10	201	28	311	46	605
11	202	29	312	47	606
12	203	30	401	48	607
13	706	31	402	49	608
14	206	32	403	50	609
15	208	33	404	51	610
16	701	34	409	52	702
17	703	35	410	53	-

Table A.3.: Overview of data LEGEND-200 taking periods analyzed in this work.

Period	Run	Date	PMT break date	Comments
3	0	12-17.03.2023		
	1	18.-24.03.2023		
	2	24.-31.03.2023		
	3	01.-06.04.2023	402 (04.04.2023), 704 (05.04.2023)	
	4	06.-12.04.2023		
	5	12.-13.04.2023		
4	0	15.-21.04.2023		
	1	21.-24.04.2023		
	2	24.04.-01.05.2023		
	3	01-03.05.2023		
	4	03.05.2023		only calibration
	5	04.05.2023		test run
	6	09.-12.05.2023		excluded
	7	14.05.2023		test run
5	0	-		deleted
	1	18.-22.05.2023		excluded

Period	Run	Date	PMT break date	Comments
5	2	22.-27.05.2023		excluded
	3	27.05.2023		excluded
	4	01.-07.06.2023		excluded
	5	07.-10.06.2023		test run
6	0	11.-19.06.2023		
	1	19.-26.06.2023		
	2	26.06.-03.07.2023		
	3	03.-10.07.2023		
	4	10.-17.07.2023	703 (13.07.2023)	
	5	17.-24.07.2023		
	6	24.-25.07.2023		test run
	7	25.-28.07.2023		test run
	8	25.-28.07.2023		test run
7	0	31.07.-07.08.2023		excluded
	1	07.-14.08.2023	311 (09.08.2023)	
	2	14.-21.08.2023	309 (21.08.2023)	
	3	21.-28.08.2023		
	4	28.08.-04.09.2023		
	5	04.-11.09.2023		
	6	11.-18.09.2023		
	7	18.-25.09.2023		
	8	25.09.2023		only calibration
	9	25.09.-01.10.2023		test run
8	0	02.-09.10.2023		
	1	09.-16.10.2023		
	2	16.-23.10.2023		
	3	23.-30.10.2023		
	4	30.10.-06.11.2023		
	5	06.-09.11.2023		excluded
	6	10.-13.11.2023		
	7	14.-20.11.2023		
	8	20.-27.11.2023		
	9	27.11-04.12.2023		
	10	05.-10.12.2023		
	11	11.-17.12.2023	509 (11.12.2023)	
	12	18.-24.12.2023		
	13	25.12.2023-01.01.2024		
	14	01.-06.01.2024	507 (03.01.2024)	
	15	08.-09.01.2024		only calibration
9	0	11.-17.01.2024	701 (11.01.2024) (during cal)	
	1	17.-24.01.2024		
	2	26.-31.01.2024		

Period	Run	Date	PMT break date	Comments
9	3	01.-08.02.2024		
	4	09.-11.02.2024		
	5	12.-18.02.2024		
	6	18.-24.02.2024		only calibration
10	0	26.02.-03.03.2024		
	1	04.-10.03.2024		
	2	11.-12.03.2024		
	3	12.-18.03.2024		
	4	19.-25.03.2024		
	5	26.03.-02.04.2024		
	6	02.04.-05.04.2024		
	7	06.04.-09.04.2024		
11	0	12.04.-13.04.2024		
	1	16.04.-18.04.2024		
	2	21.04.-22.04.2024		
	3	23.04.-29.04.2024		
	4	29.04.-05.05.2024	610 (02.05.2024)	

Appendix B

LEGEND-200 monitoring dashboard - muon veto

In this chapter, the calibration (cf. figs. B.1, B.2, B.3) and data taking monitoring plots (cf. figs. B.4, B.5, B.6) implemented in the LEGEND-200 muon veto are presented.

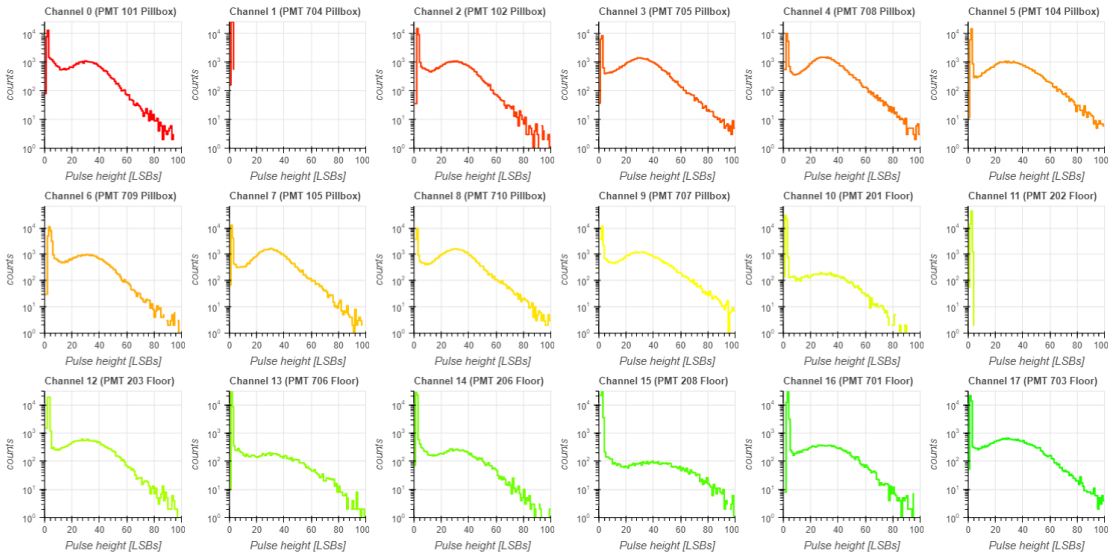

Figure B.1.: Representative muon veto calibration single photoelectron (SPE) spectra for PMTs 101 to 703 as shown in the LEGEND-200 monitoring dashboard.

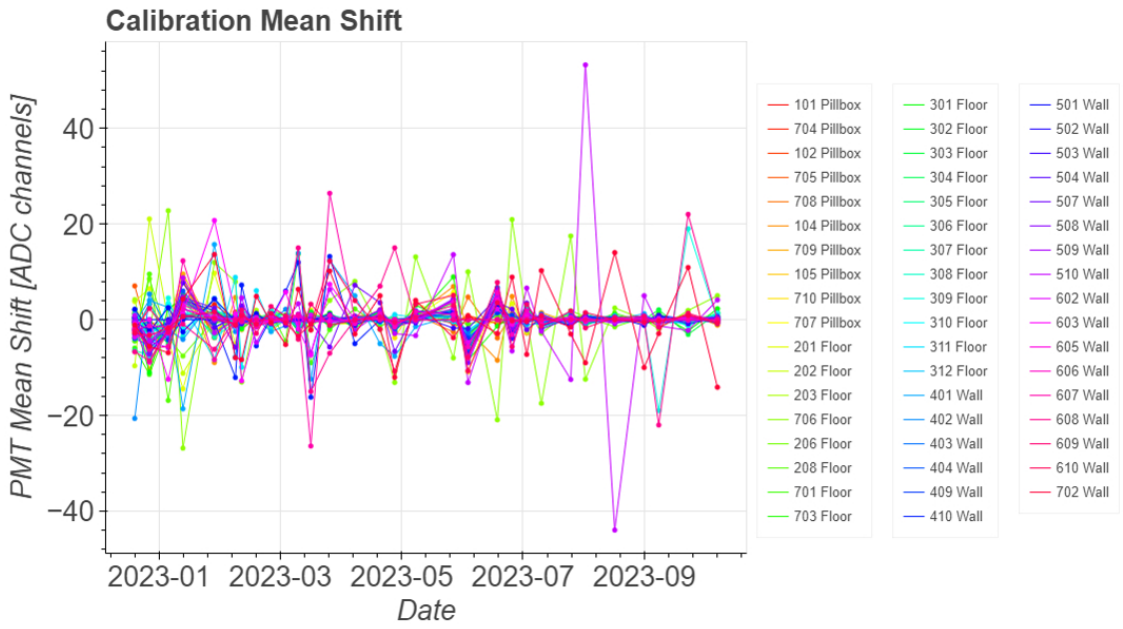

Figure B.2.: Representative shift of the fitted SPP mean between muon veto calibrations from January to October 2023 as shown in the LEGEND-200 monitoring dashboard.

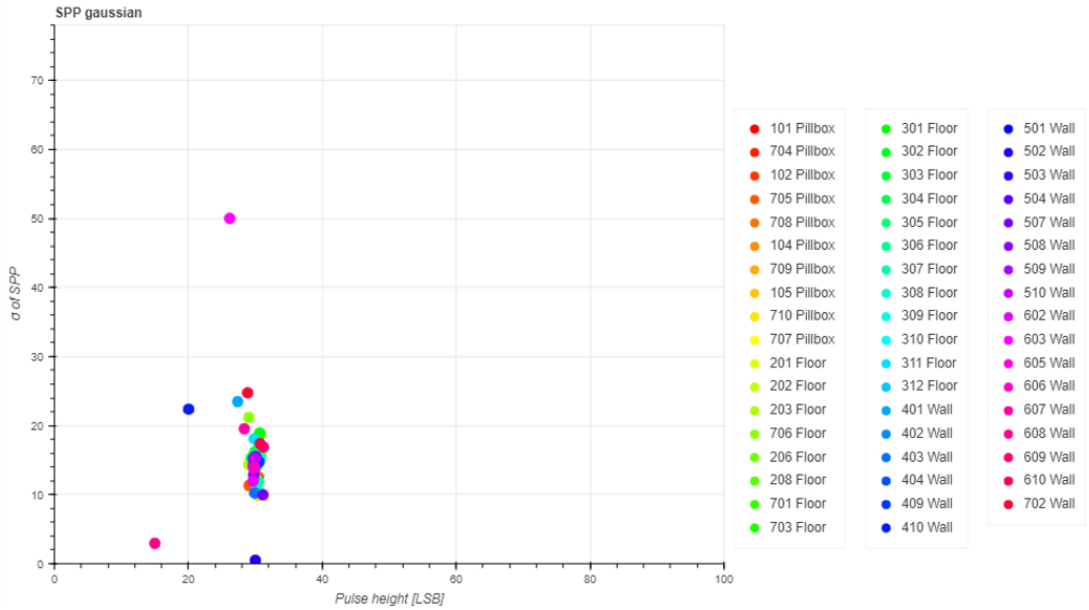

Figure B.3.: Representative standard deviation distribution as function of corresponding SPE spectra taken during a muon veto calibration as shown in the LEGEND-200 monitoring dashboard.

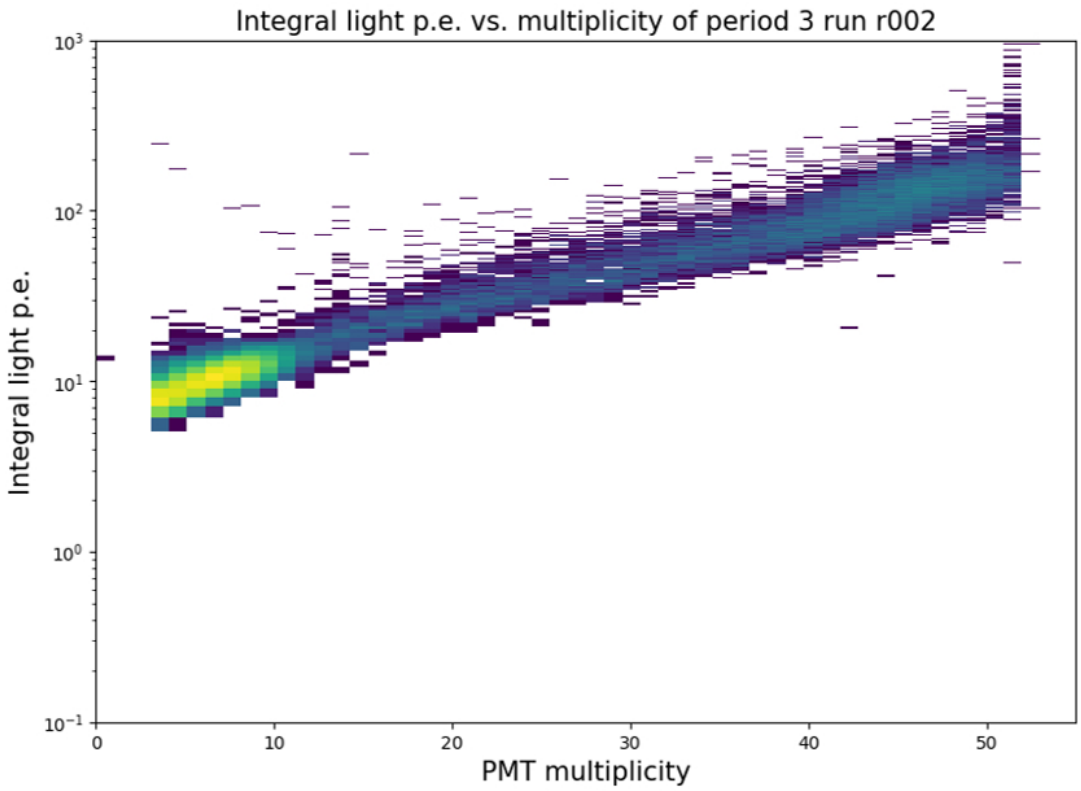

Figure B.4.: Representative integral light in p.e. as function of the PMT multiplicity of one run as shown in the LEGEND-200 monitoring dashboard.

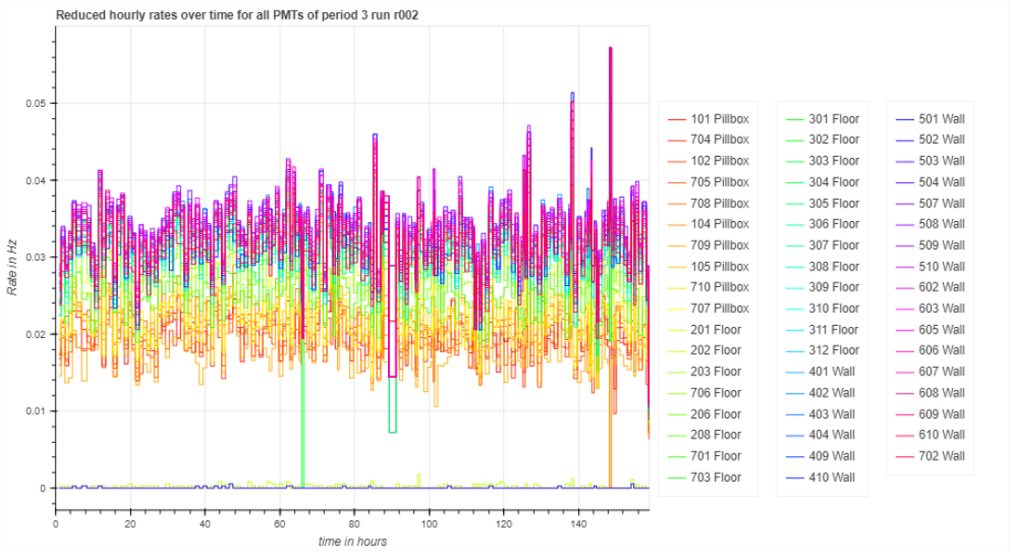

Figure B.5.: Representative reduced hourly PMT rate as shown in the LEGEND-200 monitoring dashboard. Reduced refers to the applied cut for the low-multiplicity bump.

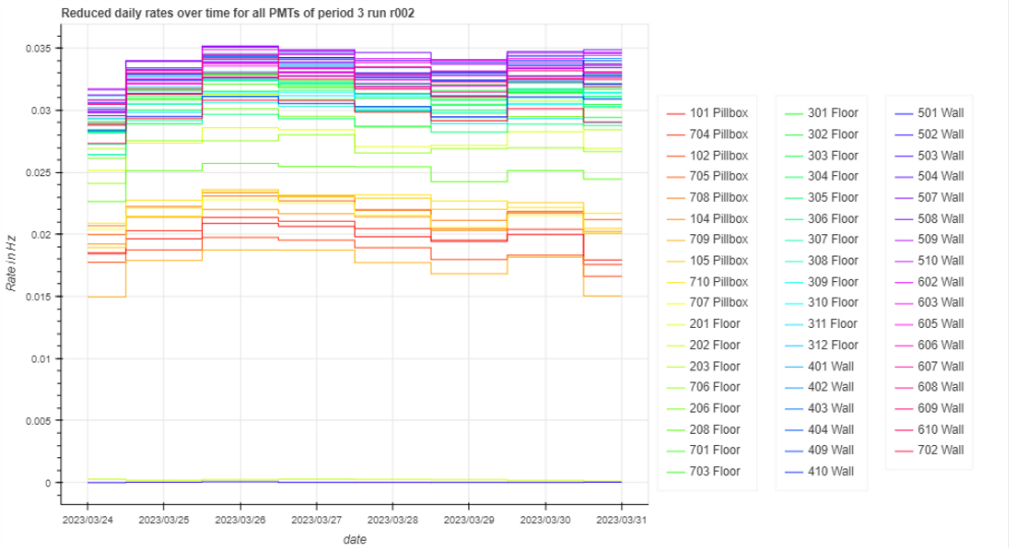

Figure B.6.: Representative reduced daily PMT rate as shown in the LEGEND-200 monitoring dashboard. Reduced refers to the applied cut for the low-multiplicity bump.

Appendix C

Simulation geometry

This appendix provides additional material used in the implementation of the LEGEND-200 simulation geometry. It includes the implemented water absorption length as a function of photon energy in Figure C.1 and the geometrical PMT specifications provided by the manufacturer [64] (cf. Figure C.2).

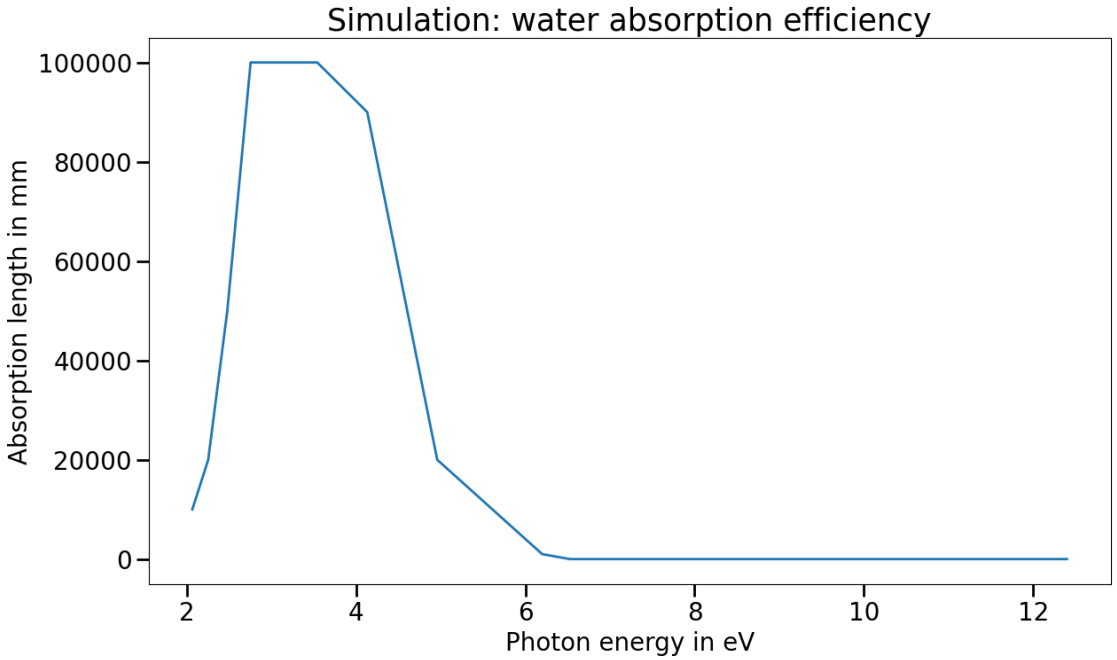

Figure C.1.: Implemented absorption length as a function of the photon energy in eV of the simulated water inside the LEGEND-200 water tank.

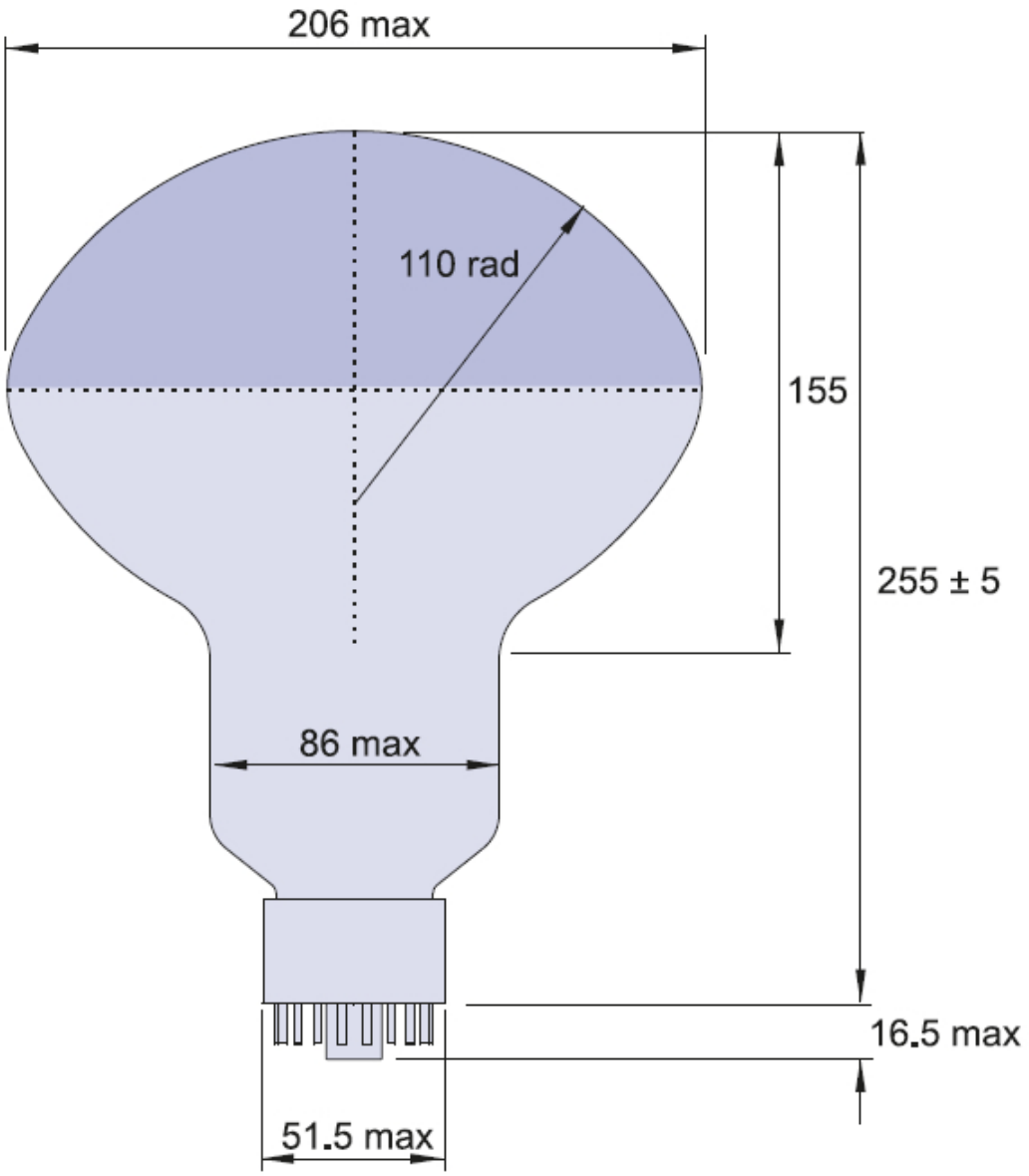

Figure C.2.: Dimensions of 9354KB PMTs used in the muon veto of LEGEND-200 and manufactured by ETL [64].

Appendix D

PMT test stand DAQ

In this appendix a picture of the PMT test stand DAQ components is presented (cf. Figure D.1).

Figure D.1.: Picture of the PMT test stand DAQ electronics. The rack houses the power supplies for the LED, the tested PMT, and the ADC. On the table, the DAQ PC is positioned next to the oscilloscope and frequency generator. A second PC controls the voltages of the PMT power supply, since the operating system of the DAQ PC does not support the power supply software.

Appendix E

My contribution and collaborative work

The following appendix summarizes my contribution and the collaborative work in this thesis. This work was developed as part of the LEGEND experiment, primarily using data from LEGEND-200. In addition, data processing, analysis and simulation frameworks as well as monitoring platforms developed by collaboration members were utilized. Hardware maintenance on the LEGEND-200 setup (LNGS, Italy) was also performed by the LEGEND collaboration.
Table E.1 presents a breakdown of the contributions by chapter in this work. Since Chapters 1-5.2 and Chapter 10 mainly comprise literature search or summary text, they are not explicitly listed.

Table E.1.: Overview of collaborative and my contributions of this work.

Chapter	Work Performed	Collaborative Contribution	My Contribution
5.3	Calibration, data processing, and analysis	• DAQ operation for calibration release (LEGEND collaboration, mostly Dr. Brady Bos) • Development of data processing and analysis frameworks and muon veto calibration procedure (LEGEND collaboration)	• Further development of the muon veto calibration procedure • Muon veto calibration • Data analysis • Further development of the data processing framework • My total contribution: ~ 70%

Chapter	Work Performed	Collaborative Contribution	My Contribution
6	Data processing and analysis	• Development of data processing and analysis frameworks (LEGEND collaboration) • Development of monitoring platforms (LEGEND collaboration)	• Data analysis • Further development of the data processing framework • Development of muon veto plots for the dashboard monitoring system • My total contribution: ~ 90%
7	Simulations	• Development of simulation frameworks used (LEGEND collaboration)	• Simulations • Further development of the simulation framework • My total contribution: ~ 95%
8	Simulations, data processing and analysis	• Development of simulation frameworks used (LEGEND collaboration) • Development of data processing and analysis frameworks (LEGEND collaboration)	• Simulations • Further development of simulation framework • Data analysis • Further development of data processing framework • My total contribution: > 99%
9	Data processing and analysis, PMT characterization	• Development of data processing and analysis frameworks (LEGEND collaboration) • Analysis code for this PMT type: Ivana Nikolac • Testing of PMTs: – Jibin Thomas – Marius Schweizer – Michelle Stumpf	• Data analysis • Further development of data processing framework • Adaptation and further development of analysis code • Setup, maintenance, and first characterization of the PMT test stand • Supervision of PMT testers • My total contribution: ~ 70%

Acronyms

0$\nu\beta\beta$ neutrinoless double-beta. 1–3, 11, 13, 14, 17, 18, 22, 23, 25, 30–32, 43, 44, 68, 69, 123, 125, 126, 147, 148, 152

ADC analog-to-digital converter. 37–41, 44, 45, 57–62, 65, 78, 79, 94, 98, 111, 112, 139, 149, 151, 156, 157

BEGe Broad Energy Germanium. 21, 22, 147

BI background index. 1, 18, 22, 23, 25, 32, 43, 70, 123, 124, 147

cal calibration. 43, 44, 51, 124

CE collection efficiency. 36, 37, 74, 78, 113

CKM Cabibbo-Kobayashi-Maskawa. 5, 7

CL confidence level. 18, 46–48, 62, 147, 149, 150

Coax semi-coaxial. 21, 22, 31, 147

DAQ data acquisition. 38, 44, 49, 50, 52–56, 78, 79, 98, 111, 112, 124, 127, 139, 141, 149–151, 156, 157

DONUT Direct Observation of the NU Tau. 6

DS discovery sensitivity. 18, 147

dsp digital signal processing. 44, 45, 149

ETL ET Enterprises Limited. 35–37, 112–114, 121, 138, 148, 157

evt event. 44, 45, 50, 149

FEP full energy peak. 70, 71, 153

FMC full multiplicity cut. 91, 102, 106

FPGA Field Programmable Gate Array. 37

FWHM full width at half maximum. 78

Geant4 Geometry and Tracking. 73, 74, 76, 77, 92, 124

GERDA GERmanium Detector Array. 17, 21–23, 28, 33, 34, 37, 48, 70, 74, 85, 124, 125

GPS Global Positioning System. 49

GUT Grand Unified Theory. 10

HDF5 Hierarchical Data Format 5. 44, 74

HPGe high-purity Germanium. 1, 2, 17, 19–24, 28–32, 34, 43, 44, 48–50, 66–71, 75, 79, 85, 89, 102, 106, 123–126, 147, 148, 150, 152, 153

HV high voltage. 36–38, 85, 111, 112, 149, 156

ICPC Inverted Coaxial Point Contact. 21–23, 147

ID identification. 37, 45, 128, 129, 149, 159

IO Inverted Ordering. 8, 18, 147

JUNO Jiangmen Underground Neutrino Observatory. 9

LAr liquid argon. 1, 19, 23, 24, 29–32, 43, 69, 70, 75, 89, 106, 123, 124, 147, 148, 153

LED light-emitting diode. 38–40, 111, 112, 115–117, 121, 139, 156, 157

LEGEND Large Enriched Germanium Experiment for Neutrinoless $\beta\beta$ Decay. i–iv, 1, 2, 15, 17–19, 21–25, 27–39, 41, 43, 44, 50–53, 73–76, 82, 86, 89–92, 102, 106–112, 114, 119, 121, 123–127, 133–138, 141, 142, 147–149, 153, 156, 157

LH5 LEGEND HDF5. 44

LNGS Laboratori Nazionali del Gran Sasso. 1, 17, 19, 23, 27, 29, 33, 51, 74, 121, 141

LQ late-charge. 31

m.w.e. water equivalent. 19, 29

MaGe Majorana-Gerda. 74

MSE multiple-site event. 30, 31, 148

MTC multiple trigger cut. 91, 92, 103–106

MUSUN MUon Simulations UNderground. 74, 82

NERSC National Energy Research Scientific Computing Center. 87

NO Normal Ordering. 8

ORCA Object-orientated Real time Control and Acquisition. 37, 44, 50, 54, 128, 151, 159

p.e. photoelectrons. 32, 38–41, 45–48, 54–56, 59–68, 78, 79, 82–85, 88, 89, 91, 93, 94, 97–100, 103, 104, 112, 114–117, 121, 123, 124, 135, 149–152, 154–157

PC Personal Computer. 38, 111, 112, 139, 149, 156, 157

PDE photon detection efficiency. 36, 74, 78, 84, 85, 99, 106, 114, 121, 154

PEN polyethylene naphthalate. 35, 76, 153

PET polyethylene terephthalate. 37

phy physics. 43, 44, 51, 57, 74, 79, 81–85, 87–90, 92–107, 124, 125, 154, 155

PMMA poly(methyl methacrylate). 23, 24, 35, 76, 148

PMNS Pontecorvo-Maki-Nakagawa-Sakata. 7, 8, 14

PMT photomultiplier tube. i, iii, 2, 19, 24, 32–41, 43–70, 73–79, 82–89, 91–100, 102–104, 106–121, 123–125, 127–129, 133, 135–139, 142, 148–157, 159

PPC p-type point contact. 21, 22, 147

PSD pulse shape discrimination. 30, 31, 46–48, 58, 62–70, 94, 124, 148–150, 152, 153

QE quantum efficiency. 36, 74, 76, 78, 113, 114, 148, 153, 156

QED quantum electrodynamics. 5

ROI region of interest. i, iii, 1, 18, 28, 29, 32, 43, 70, 71, 108, 123, 124, 153, 156

sim simulation. 81, 84, 85, 88, 89, 92, 94, 97–106, 124, 125, 155

SiPM Silicon Photomultiplier. 19, 23, 32

skm skimmed. 44, 48, 149

SM Standard Model of particle physics. 1, 3–5, 7, 9, 10, 13, 14, 123

SPE single photoelectron. 133, 134, 157

SPP single photoelectron peak. 40, 41, 51, 78, 79, 134, 149, 157

SSE single-site event. 30, 31, 148

TT transit time. 37

TTS transit time spread. 37, 78

UGLAr underground liquid argon. 23

UV ultra-violet. 34, 36, 38, 39, 76

WLS wavelength shifting. 19, 32, 34, 76, 147, 153

YAML yet another markup language. 44

List of Figures

List of Tables

Bibliography

[1] M. A. Knapp. “Design, Simulation und Aufbau des GERDA-Myonvetos”. PhD thesis. Eberhard Karls Universität Tübingen, 2009.

[2] K. L. Freund. “Muonic Background in the GERDA $0\nu\beta\beta$ Experiment”. PhD thesis. Eberhard Karls Universität Tübingen, 2014.

[3] F. Ritter. “Analysis of the GERDA Muon Veto - First Light”. PhD thesis. Eberhard Karls Universität Tübingen, 2011.

[4] Y. Fukuda et al. “Evidence for Oscillation of Atmospheric Neutrinos”. In: *Phys. Rev. Lett.* 81 (8 Aug. 1998), pp. 1562–1567. DOI: 10.1103/PhysRevLett.81.1562. URL: https://link.aps.org/doi/10.1103/PhysRevLett.81.1562.

[5] Q. R. Ahmad et al. “Measurement of the Rate of $\nu_e + d \rightarrow p + p + e^-$ Interactions Produced by ^8B Solar Neutrinos at the Sudbury Neutrino Observatory”. In: *Phys. Rev. Lett.* 87 (7 July 2001), p. 071301. DOI: 10.1103/PhysRevLett.87.071301. URL: https://link.aps.org/doi/10.1103/PhysRevLett.87.071301.

[6] Q. R. Ahmad et al. “Direct Evidence for Neutrino Flavor Transformation from Neutral-Current Interactions in the Sudbury Neutrino Observatory”. In: *Phys. Rev. Lett.* 89 (1 June 2002), p. 011301. DOI: 10.1103/PhysRevLett.89.011301. URL: https://link.aps.org/doi/10.1103/PhysRevLett.89.011301.

[7] LEGEND Collaboration. *LEGEND-1000 Preconceptual Design Report*. 2021. arXiv: 2107.11462 [physics.ins-det]. URL: https://arxiv.org/abs/2107.11462.

[8] D. Griffiths. *Introduction to Elementary Particles*. 2nd ed. Weinheim, Germany: WILEY-VCH, 2008. ISBN: 978-3-527-40601-2.

[9] L. Oberauer and J. Oberauer. *Neutrinophysik*. Heidelberg, Germany: Springer Spektrum, 2019. ISBN: 978-3-662-59334-9.

[10] B. Povh et al. *Teilchen und Kerne*. Heidelberg, Germany: Springer Spektrum, 2014. ISBN: 978-3-642-37821-8.

[11] C. Amsler. *Nuclear and Particle Physics*. 2053-2563. Bristol, UK: IOP Publishing, 2015. ISBN: 978-0-7503-1140-3. DOI: 10.1088/978-0-7503-1140-3. URL: https://dx.doi.org/10.1088/978-0-7503-1140-3.

[12] W. Demtröder. *Experimentalphysik 4: Kern-, Teilchen- und Astrophysik*. Heidelberg, Germany: Springer Spektrum, 2017. ISBN: 978-3-662-52883-9.

[13] K. Zuber. *Neutrino Physics*. 3rd ed. Boca Raton, Florida: CRC Press, 2020. ISBN: 9781315195612. DOI: 10.1201/9781315195612.

[14] Particle Data Group and R.L. Workman et al. "Higgs Boson". In: *Prog. Theor. Exp. Phys.* 2022.8 (2022). Particle Data Group, Review of Particle Physics (2022), p. 083C01. DOI: 10.1093/ptep/ptac097. URL: https://pdg.lbl.gov/2023/reviews/rpp2022-rev-higgs-boson.pdf.

[15] W. Pauli. *Letter to the Physical Society of Tübingen*. Unpublished letter. 1930.

[16] C. L. Cowan et al. "Detection of the Free Neutrino: a Confirmation". In: *Science* 124.3212 (1956), pp. 103–104. DOI: 10.1126/science.124.3212.103. eprint: https://www.science.org/doi/pdf/10.1126/science.124.3212.103. URL: https://www.science.org/doi/abs/10.1126/science.124.3212.103.

[17] G. Danby et al. "Observation of High-Energy Neutrino Reactions and the Existence of Two Kinds of Neutrinos". In: *Phys. Rev. Lett.* 9 (1 July 1962), pp. 36–44. DOI: 10.1103/PhysRevLett.9.36. URL: https://link.aps.org/doi/10.1103/PhysRevLett.9.36.

[18] K. Kodama et al. "Observation of tau neutrino interactions". In: *Physics Letters B* 504.3 (Apr. 2001), pp. 218–224. ISSN: 0370-2693. DOI: 10.1016/s0370-2693(01)00307-0. URL: http://dx.doi.org/10.1016/S0370-2693(01)00307-0.

[19] C. S. Wu et al. "Experimental Test of Parity Conservation in Beta Decay". In: *Phys. Rev.* 105 (4 Feb. 1957), pp. 1413–1415. DOI: 10.1103/PhysRev.105.1413. URL: https://link.aps.org/doi/10.1103/PhysRev.105.1413.

[20] M. Goldhaber, L. Grodzins, and A. W. Sunyar. "Helicity of Neutrinos". In: *Phys. Rev.* 109 (3 Feb. 1958), pp. 1015–1017. DOI: 10.1103/PhysRev.109.1015. URL: https://link.aps.org/doi/10.1103/PhysRev.109.1015.

[21] J. H. Christenson et al. "Evidence for the 2π Decay of the K_2^0 Meson". In: *Phys. Rev. Lett.* 13 (4 July 1964), pp. 138–140. DOI: 10.1103/PhysRevLett.13.138. URL: https://link.aps.org/doi/10.1103/PhysRevLett.13.138.

[22] R. Davis, D. S. Harmer, and K. C. Hoffman. "Search for Neutrinos from the Sun". In: *Phys. Rev. Lett.* 20 (21 May 1968), pp. 1205–1209. DOI: 10.1103/PhysRevLett.20.1205. URL: https://link.aps.org/doi/10.1103/PhysRevLett.20.1205.

[23] B. Pontecorvo. "Neutrino Experiments and the Problem of Conservation of Leptonic Charge". In: *Zh. Eksp. Teor. Fiz.* 53 (1967), pp. 1717–1725.

[24] I. Esteban et al. "The fate of hints: updated global analysis of three-flavor neutrino oscillations". In: *Journal of High Energy Physics* 2020.9 (Sept. 2020). ISSN: 1029-8479. DOI: 10.1007/jhep09(2020)178. URL: http://dx.doi.org/10.1007/JHEP09(2020)178.

[25] A. de Gouvêa, J. Jenkins, and B. Kayser. "Neutrino mass hierarchy, vacuum oscillations, and vanishing $|U_{e3}|$". In: *Phys. Rev. D* 71 (11 June 2005), p. 113009. DOI: 10.1103/PhysRevD.71.113009. URL: https://link.aps.org/doi/10.1103/PhysRevD.71.113009.

[26] F. An et al. "Neutrino physics with JUNO". In: *Journal of Physics G: Nuclear and Particle Physics* 43.3 (Feb. 2016), p. 030401. DOI: 10.1088/0954-3899/43/3/030401. URL: https://dx.doi.org/10.1088/0954-3899/43/3/030401.

[27] Hyper-Kamiokande Proto-Collaboration. *Hyper-Kamiokande Design Report*. 2018. arXiv: 1805.04163 [physics.ins-det]. URL: https://arxiv.org/abs/1805.04163.

[28] E. Rutherford. "VIII. Uranium radiation and the electrical conduction produced by it". In: *The London, Edinburgh, and Dublin Philosophical Magazine and Journal of Science* 47.284 (1899), pp. 109–163. DOI: 10.1080/14786449908621245. eprint: https://doi.org/10.1080/14786449908621245. URL: https://doi.org/10.1080/14786449908621245.

[29] M. F. L'Annunziata, ed. *Handbook of Radioactivity Analysis*. 3rd ed. Academic Press, 2012. DOI: 10.1016/C2009-0-64538-3.

[30] C. B. Paul. *Controversy and Consensus: Nuclear Beta Decay 1911–1934*. Springer, 2000. DOI: 10.1007/978-94-011-4026-5.

[31] M. G. Inghram and J. H. Reynolds. "Double Beta-Decay of Te^{130}". In: *Phys. Rev.* 78 (6 June 1950), pp. 822–823. DOI: 10.1103/PhysRev.78.822.2. URL: https://link.aps.org/doi/10.1103/PhysRev.78.822.2.

[32] C. F. v. Weizsäcker. "Zur Theorie der Kernmassen". In: *Zeitschrift für Physik* 96.7 (1935), pp. 431–458. DOI: 10.1007/BF01337700. URL: https://doi.org/10.1007/BF01337700.

[33] A. Bohr and B. R. Mottelson. *Nuclear Structure*. Vol. 2. Reading, Massachusetts, London: W. A. Benjamin, Inc., Advanced Book Program, 1975.

[34] S. M. Bilenky and C. Giunti. "Neutrinoless double-beta decay: A probe of physics beyond the Standard Model". In: *International Journal of Modern Physics A* 30.04n05 (Feb. 2015), p. 1530001. ISSN: 1793-656X. DOI: 10.1142/s0217751x1530001x. URL: http://dx.doi.org/10.1142/S0217751X1530001X.

[35] M. Agostini et al. "Background-free search for neutrinoless double-β decay of ^{76}Ge with GERDA". In: *Nature* 544.7648 (Apr. 2017), pp. 47–52. ISSN: 1476-4687. DOI: 10.1038/nature21717. URL: https://doi.org/10.1038/nature21717.

[36] W. R. Leo. *Techniques for Nuclear and Particle Physics Experiments: A How-to Approach*. 2nd ed. Berlin: Springer, 1994. DOI: 10.1007/978-3-642-57920-2. URL: https://cds.cern.ch/record/302344.

[37] G. F. Knoll. *Radiation Detection and Measurement*. 4th ed. Hoboken, NJ: John Wiley & Sons, 2010. ISBN: 978-0-470-13148-0. URL: https://www.wiley.com/en-us/Radiation+Detection+and+Measurement%2C+4th+Edition-p-9780470131480.

[38] M. Agostini et al. "The background in the 0nubb experiment Gerda". In: *European Physical Journal C* 74 (Apr. 2014), p. 2764.

[39] D. Palioselitis on behalf of the GERDA collaboration. "Experience from operating germanium detectors in GERDA". In: *Journal of Physics: Conference Series* 606.1 (Apr. 2015), p. 012007. DOI: 10.1088/1742-6596/606/1/012007. URL: https://dx.doi.org/10.1088/1742-6596/606/1/012007.

[40] M. Agostini et al. "Characterization of 30 ^{76}Ge enriched Broad Energy Ge detectors for GERDA Phase II". In: *The European Physical Journal C* 79.11 (Nov. 2019). ISSN: 1434-6052. DOI: 10.1140/epjc/s10052-019-7353-8. URL: http://dx.doi.org/10.1140/epjc/s10052-019-7353-8.

[41] E. Aguayo et al. "Characteristics of signals originating near the lithium-diffused N+ contact of high purity germanium p-type point contact detectors". In: *Nuclear Instruments and Methods in Physics Research Section A: Accelerators, Spectrometers, Detectors and Associated Equipment* 701 (2013), pp. 176–185. ISSN: 0168-9002. DOI: https://doi.org/10.1016/j.nima.2012.11.004. URL: https://www.sciencedirect.com/science/article/pii/S0168900212012752.

[42] R. Cooper et al. "A novel HPGe detector for gamma-ray tracking and imaging". In: *Nuclear Instruments and Methods in Physics Research Section A: Accelerators, Spectrometers, Detectors and Associated Equipment* 665 (2011), pp. 25–32. ISSN: 0168-9002. DOI: https://doi.org/10.1016/j.nima.2011.10.008. URL: https://www.sciencedirect.com/science/article/pii/S0168900211018985.

[43] M. Neuberger et al. "The cosmic muon-induced background for the LEGEND-1000 alternative site at LNGS". In: *Journal of Physics: Conference Series* 2156.1 (Dec. 2021), p. 012216. DOI: 10.1088/1742-6596/2156/1/012216. URL: https://dx.doi.org/10.1088/1742-6596/2156/1/012216.

[44] T. K. Gaisser. *Cosmic Rays and Particle Physics*. Cambridge University Press, 1990. ISBN: 9780521339315.

[45] S. Navas et al. "Review of particle physics". In: *Phys. Rev. D* 110.3 (2024), p. 030001. DOI: 10.1103/PhysRevD.110.030001.

[46] J. Beringer et al. "Review of Particle Physics". In: *Phys. Rev. D* 86 (1 July 2012), p. 010001. DOI: 10.1103/PhysRevD.86.010001. URL: https://link.aps.org/doi/10.1103/PhysRevD.86.010001.

[47] F. E. Close. *The Particle Odyssey: A Journey to the Heart of the Matter*. New ed. Oxford; New York: Oxford University Press, 2002.

[48] L. Pandola et al. “Monte Carlo evaluation of the muon-induced background in the GERDA double beta decay experiment”. In: *Nuclear Instruments and Methods in Physics Research Section A: Accelerators, Spectrometers, Detectors and Associated Equipment* 570.1 (2007), pp. 149–158. ISSN: 0168-9002. DOI: https://doi.org/10.1016/j.nima.2006.10.103. URL: https://www.sciencedirect.com/science/article/pii/S0168900206018031.

[49] C. Wiesinger, L. Pandola, and S. Schönert. “Virtual depth by active background suppression: revisiting the cosmic muon induced background of Gerda Phase II”. In: *The European Physical Journal C* 78.7 (2018), p. 597. ISSN: 1434-6052. DOI: 10.1140/epjc/s10052-018-6079-3. URL: https://doi.org/10.1140/epjc/s10052-018-6079-3.

[50] H. Acharya et al. *First Results on the Search for Lepton Number Violating Neutrinoless Double Beta Decay with the LEGEND-200 Experiment*. 2025. arXiv: 2505.10440 [hep-ex]. URL: https://arxiv.org/abs/2505.10440.

[51] W. Maneschg et al. “Measurements of extremely low radioactivity levels in stainless steel for GERDA”. In: *Nuclear Instruments and Methods in Physics Research Section A: Accelerators, Spectrometers, Detectors and Associated Equipment* 593.3 (2008), pp. 448–453. ISSN: 0168-9002. DOI: https://doi.org/10.1016/j.nima.2008.05.036. URL: https://www.sciencedirect.com/science/article/pii/S0168900208007833.

[52] S. Westerdale and P. Meyers. “Radiogenic neutron yield calculations for low-background experiments”. In: *Nuclear Instruments and Methods in Physics Research Section A: Accelerators, Spectrometers, Detectors and Associated Equipment* 875 (Dec. 2017), pp. 57–64. ISSN: 0168-9002. DOI: 10.1016/j.nima.2017.09.007. URL: http://dx.doi.org/10.1016/j.nima.2017.09.007.

[53] K. Freund et al. “The performance of the Muon Veto of the Gerda experiment”. In: *The European Physical Journal C* 76.5 (May 2016). ISSN: 1434-6052. DOI: 10.1140/epjc/s10052-016-4140-7. URL: http://dx.doi.org/10.1140/epjc/s10052-016-4140-7.

[54] M. Agostini et al. “Pulse shape analysis in GERDA Phase II”. In: *The European Physical Journal C* 82.4 (2022), p. 284. ISSN: 1434-6052. DOI: 10.1140/epjc/s10052-022-10163-w. URL: https://doi.org/10.1140/epjc/s10052-022-10163-w.

[55] I. J. Arnquist et al. “Final Result of the Majorana Demonstrator’s Search for Neutrinoless Double-β Decay in ^{76}Ge”. In: *Phys. Rev. Lett.* 130 (6 Feb. 2023), p. 062501. DOI: 10.1103/PhysRevLett.130.062501. URL: https://link.aps.org/doi/10.1103/PhysRevLett.130.062501.

[56] P. Krause. “Shining light on background - An advaced Liquid argon scintillation light detector for boosting background suppression in LEGEND’s neutrinoless double beta decay search”. PhD thesis. Technische Universität München, 2023.

[57] N. Burlac. “Optimizing the Search for Neutrinoless Double Beta Decay - Liquid Argon Instrumentation for Background Suppression in LEGEND-200 Experiment”. PhD thesis. Università degli Studi Roma Tre, 2024.

[58] XENON Collaboration. *The XENONnT Dark Matter Experiment*. 2024. arXiv: 2402.10446 [physics.ins-det]. URL: https://arxiv.org/abs/2402.10446.

[59] K. Habib. “Muonic Background Analysis in GERDA Phase II (II+) and in LEGEND-200 Commissioning Data”. PhD thesis. Eberhard Karls Universität Tübingen, 2023.

[60] 3M Company. *3M^{TM} Specular Film DF2000MA Technical Data Sheet*. https://multimedia.3m.com/mws/media/9824490/3mtm-specular-film-df2000ma-technical-data-sheet.pdf. Accessed: 2025-05-30. 2017.

[61] C. Geis et al. “Optical response of highly reflective film used in the water Cherenkov muon veto of the XENON1T dark matter experiment”. In: *Journal of Instrumentation* 12.06 (June 2017), P06017–P06017. ISSN: 1748-0221. DOI: 10.1088/1748-0221/12/06/p06017. URL: http://dx.doi.org/10.1088/1748-0221/12/06/P06017.

[62] T. J. Nevittand, R. T. Fabick, and L. R. Gilbert. “Polymeric Multilayer Optical Film”. US11009638B2. https://patents.google.com/patent/US11009638B2. May 2021.

[63] L. Manzanillas et al. “Optical properties of low background PEN structural components for the Legend-200 experiment”. In: *Journal of Instrumentation* 17.09 (Sept. 2022), P09007. ISSN: 1748-0221. DOI: 10.1088/1748-0221/17/09/p09007. URL: http://dx.doi.org/10.1088/1748-0221/17/09/P09007.

[64] ET Enterprises Ltd. *200 mm (8”) photomultiplier*. https://lampes-et-tubes.info/pm/9354KB.pdf. Accessed: 2025-05-30. 2010.

[65] M. A. U. Elorietta. “Studies on dark rates induced by radioactive decays of the multi-PMT digital optical module for future IceCube extensions”. Master’s thesis. Westfälische Wilhelms-Universität Münster, Dec. 2017. URL: https://www.uni-muenster.de/imperia/md/content/physik_kp/agkappes/abschlussarbeiten/masterarbeiten/1712-ma_munland.pdf.

[66] Hamamatsu Photonics. *Photomultiplier Tubes: Basics and Applications*. Fourth Edition, Version 4E. Accessed: 2025-05-30. Hamamatsu Photonics K.K., 2017. URL: https://www.hamamatsu.com/content/dam/hamamatsu-photonics/sites/documents/99_SALES_LIBRARY/etd/PMT_handbook_v4E.pdf.

[67] L. U. Rauscher. “Setup and proof-of-concept of a test stand for High Purity Germanium spectoscropy detectors”. PhD thesis. Eberhard Karls Universität Tübingen, 2023.

[68] A. Gadola et al. “FlashCam: a novel Cherenkov telescope camera with continuous signal digitization”. In: *Journal of Instrumentation* 10.01 (Jan. 2015), p. C01014. DOI: 10.1088/1748-0221/10/01/C01014. URL: https://dx.doi.org/10.1088/1748-0221/10/01/C01014.

[69] Analog Devices. *AD9634: 12-Bit, 170/210/250 MSPS Analog-to-Digital Converter*. Rev. 0. 2014. URL: https://www.analog.com/media/en/technical-documentation/data-sheets/AD9634.pdf.

[70] J. Chase and I. Baldin. *A Retrospective on ORCA: Open Resource Control Architecture*. Tech. rep. CS-2014-XXX. Accessed: 2025-06-10. Department of Computer Science, Duke University, Dec. 2014. URL: https://renci.org/wp-content/uploads/2010/03/orca-retro.pdf.

[71] G. Grünauer. “Muon Veto of the LEGEND Experiment”. In: *PoS* TAUP2023 (2024), p. 261. DOI: 10.22323/1.441.0261.

[72] M. Menzel. *Methodenvergleich zur Ladungsberechnung von PMT-Signalen des LEGEND-200 Myonvetos*. Bachelor’s thesis. Mar. 2024.

[73] M. Menzel. *Development of an alternative event processing for the LEGEND-200 muon veto with Julia*. 2025.

[74] Grafana Labs. *Grafana*. https://grafana.com/. Version 12.0.2. 2025.

[75] A. Tridgell. *rsync*. https://rsync.samba.org/. Accessed: 2025-06-16.

[76] B. Leskovar. *Photomultiplier characteristics considerations for the deep underwater muon and neutrino detection system*. California Univ., Berkeley (USA). Lawrence Berkeley Lab., Feb. 1980. URL: https://www.osti.gov/biblio/5240241.

[77] S. Aiello et al. “Aging characterization on large area photo-multipliers”. In: *Nuclear Instruments and Methods in Physics Research Section A: Accelerators, Spectrometers, Detectors and Associated Equipment* 725 (2013). VLVνT 11, Erlangen, Germany, 12 - 14 October, 2011, pp. 151–154. ISSN: 0168-9002. DOI: https://doi.org/10.1016/j.nima.2012.11.130. URL: https://www.sciencedirect.com/science/article/pii/S0168900212014775.

[78] F. Scuri. “Long term aging test of the new PMTs for the HL-LHC ATLAS hadron calorimeter upgrade”. In: *Nuclear Instruments and Methods in Physics Research Section A: Accelerators, Spectrometers, Detectors and Associated Equipment* 1045 (2023), p. 167660. ISSN: 0168-9002. DOI: https://doi.org/10.1016/j.nima.2022.167660. URL: https://www.sciencedirect.com/science/article/pii/S0168900222009524.

[79] G. Alimonti et al. “The Borexino detector at the Laboratori Nazionali del Gran Sasso”. In: *Nuclear Instruments and Methods in Physics Research Section A: Accelerators, Spectrometers, Detectors and Associated Equipment* 600.3 (Mar. 2009), pp. 568–593. ISSN: 0168-9002. DOI: 10.1016/j.nima.2008.11.076. URL: http://dx.doi.org/10.1016/j.nima.2008.11.076.

[80] Y. Abe et al. “Characterization of the spontaneous light emission of the PMTs used in the Double Chooz experiment”. In: *Journal of Instrumentation* 11.08 (Aug. 2016), P08001–P08001. ISSN: 1748-0221. DOI: 10.1088/1748-0221/11/08/p08001. URL: http://dx.doi.org/10.1088/1748-0221/11/08/P08001.

[81] S. Qian et al. “The study on the 20 inch PMT flasher signal”. In: *Journal of Instrumentation* 15.06 (June 2020), T06008. DOI: 10.1088/1748-0221/15/06/T06008. URL: https://dx.doi.org/10.1088/1748-0221/15/06/T06008.

[82] University of Liverpool, Nuclear Instrumentation Group. *Pulse Processing: Pulse Shaping*. Nuclear Instrumentation: Lecture 2, University of Liverpool. Accessed: 2025-07-29. about 10 years ago. URL: https://ns.ph.liv.ac.uk/~ajb/ukgs_nis/pre-course-material/lec2-03.pdf.

[83] L. Pertoldi. *The first year of LEGEND-200 physics data in the quest for 0νββ decay*. Conference presentation, XXXI International Conference on Neutrino Physics and Astrophysics. Accessed: 2025-07-22. Milano, Italy, June 2024. URL: https://agenda.infn.it/event/37867/contributions/233912/.

[84] S. Agostinelli et al. “Geant4—a simulation toolkit”. In: *Nuclear Instruments and Methods in Physics Research Section A: Accelerators, Spectrometers, Detectors and Associated Equipment* 506.3 (2003), pp. 250–303. ISSN: 0168-9002. DOI: https://doi.org/10.1016/S0168-9002(03)01368-8. URL: https://www.sciencedirect.com/science/article/pii/S0168900203013688.

[85] J. Allison et al. “Geant4 developments and applications”. In: *IEEE Transactions on Nuclear Science* 53.1 (2006), pp. 270–278. DOI: 10.1109/TNS.2006.869826.

[86] J. Allison et al. “Recent developments in Geant4”. In: *Nuclear Instruments and Methods in Physics Research Section A: Accelerators, Spectrometers, Detectors and Associated Equipment* 835 (2016), pp. 186–225. ISSN: 0168-9002. DOI: https://doi.org/10.1016/j.nima.2016.06.125. URL: https://www.sciencedirect.com/science/article/pii/S0168900216306957.

[87] L. Pertoldi et al. *remage*. Version v0.12.1. July 2025. DOI: 10.5281/zenodo.16049299. URL: https://doi.org/10.5281/zenodo.16049299.

[88] L. Pertoldi et al. *legend-pygeom-optics*. May 2024. DOI: 10.5281/zenodo.11115646.

[89] L. Pertoldi. *legend-pygeom-tools*. June 2024. DOI: FILLME.

[90] LEGEND Collaboration. *legend-pygeom-l200*. https://github.com/legend-exp/legend-pygeom-l200. Accessed: 2025-07-24. 2023.

[91] V. Kudryavtsev. “Muon simulation codes MUSIC and MUSUN for underground physics”. In: *Computer Physics Communications* 180.3 (2009), pp. 339–346. ISSN: 0010-4655. DOI: https://doi.org/10.1016/j.cpc.2008.10.013. URL: https://www.sciencedirect.com/science/article/pii/S0010465508003640.

[92] Y.-D. Chan et al. *MaGe - a Geant4-based Monte Carlo framework for low-background experiments*. 2008. arXiv: 0802.0860 [nucl-ex]. URL: https://arxiv.org/abs/0802.0860.

[93] S. Boogert et al. "Pyg4ometry: A Python library for the creation of Monte Carlo radiation transport physical geometries". In: *Comput. Phys. Commun.* 272 (2022). DOI: 10.1016/j.cpc.2021.108228.

[94] J. D. Mason, M. T. Cone, and E. S. Fry. "Ultraviolet (250–550 nm) absorption spectrum of pure water". In: *Appl. Opt.* 55.25 (Sept. 2016), pp. 7163–7172. DOI: 10.1364/AO.55.007163. URL: https://opg.optica.org/ao/abstract.cfm?URI=ao-55-25-7163.

[95] National Nuclear Data Center (NNDC). *NuDat 3.0 Database*. https://www.nndc.bnl.gov/nudat3/. Accessed: 2025-08-08. 2025.

[96] National Energy Research Scientific Computing Center. *NERSC: National Energy Research Scientific Computing Center*. https://www.nersc.gov. Accessed: 2025-08-12. Berkeley, CA, USA, 2025. URL: https://www.nersc.gov.

[97] E. Esch. Personal communication, 2025.

[98] Y. Abe et al. "Indication for the disappearance of reactor electron antineutrinos in the Double Chooz experiment". In: *Physical Review Letters* 108.13 (Mar. 2012). ISSN: 1079-7114. DOI: 10.1103/physrevlett.108.131801. URL: http://dx.doi.org/10.1103/PhysRevLett.108.131801.

[99] T. Lachenmaier. Personal communication, 2023.

[100] CAEN S.p.A. *740 Digitizer Family, 64/32 Ch. 12-bit 62.5 MS/s Digitizer*. https://www.caen.it/products/v1740d.

[101] Hamamatsu Photonics K.K. *8 inch Hemispherical Photomultiplier Tube R1408, Technical Data Sheet*. Manufacturer's data sheet, internal copy. Printed in Japan, Cr-2000. Oct. 1985.

[102] D. B. Greiner. "Design und Aufbau des Double Choot Myon-Vetos". PhD thesis. Eberhard Karls Universität Tübingen, 2013.

[103] M. Smy. "Hyper-Kamiokande". In: Aug. 2023, p. 41. DOI: 10.3390/psf2023008041.

[104] K. Zbiri. *Simplified PMT Model*. https://arxiv.org/pdf/0809.4210. Version 1, 24 September 2008. 2008.

[105] I. Nikolac. "Set Up and Run of A Cherenkov Test Detector". MA thesis. Eberhard Karls Universität Tübingen, 2023.

[106] Kremer Pigmente GmbH & Co. KG. *Siedegrenzbenzin 60/95 Petrolether*. https://www.kremer-pigmente.com/elements/resources/products/files/70394_SHD.pdf. Accessed: 2025-08-26.

[107] Sigma-Aldrich. *Specification 1.04699.0000 Immersion oil for microscopy*. https://www.sigmaaldrich.com/DE/de/specification-sheet/SPEC/MDA/CHEM/1.04699/1046999023. Accessed: 2025-09-08.

Danksagung

An dieser Stelle möchte ich mich bei allen bedanken, die mich während der Entstehung dieser Arbeit unterstützt, begleitet und motiviert haben.

Zunächst möchte ich einen besonderen Dank Prof. Dr. Josef Jochum widmen, für die Betreuung und Möglichkeit diese Arbeit erstellen zu dürfen. Insbesondere für die Unterstützung in schwierigen Phasen, viel Verständnis, die Förderung meiner wissenschaftlichen Arbeit sowie die Freiheit, deren Schwerpunkte festzulegen, möchte ich aufrichtig danken.

Vielen Dank an Prof. Dr. Tobias Lachenmaier für die Zweitbetreuung meiner Arbeit sowie die interessanten Diskussionen, neue Blickwinkel und die Unterstützung in schwierigen Situationen.

Ich möchte Gaby Behring, Gabriele Enßlin-Richter und Dr. Günter Lang für die Organisation und Verwaltung in der Gruppe ganz herzlich danken. Außerdem gilt ein Dank den Mitgliedern der Arbeitsgruppen Jochum und Lachenmaier für die gemeinsame Zeit und Zusammenarbeit.

Ganz herzlich möchte ich mich bei meinem Vater Bernd Grünauer dafür bedanken, sich immer um meine Sicherheit und mein Wohlergehen zu kümmern, wie auch für viele absurde und schöne Gespräche, gute Ratschläge und ausgiebige Wanderungen und Skifahrten. Danke für alles.

Bei meiner Mutter Christine Grünauer möchte ich mich sehr dafür bedanken, immer ihr Bestes gegeben zu haben, mich zu beschützen, ihre Erfahrungen zu teilen und immer ein offenes Ohr für mich zu haben. Danke für alles.

Ich möchte mich ganz herzlich bei meiner Großeltern Rosemarie und Bernhard Grünauer bedanken für unzählige Binokel-Abende, tiefgründige Gespräche und jede Unterstützung.

Ein Dank gilt, in liebevoller Erinnerung, meinen Großeltern Konrad und Thea Haufe, die mich immer ermutigt haben, mich ernstzunehmen und mich so angenommen haben, wie ich bin.

Ein liebevoller Dank gilt Dr. Lukas Rauscher für die gemeinsame Zeit und die Erkenntnis, dass ein Zuhause eine Person sein kann. Danke für all die Akzeptanz, Bedingungslosigkeit, Unterstützung, Ehrlichkeit, Authentizität und Sicherheit, die mich während meiner Promotion begleitet haben.

Ein besonderer Dank gilt den ”Gentlemen”: Marc Breisch, Dr. Tobias, Sterr, Jessica Eck, Dr. Tobias Heinz, Dr. Katja Wurster, Dr. Katharina Kilgus, Colin Heckmeyer, Lukas Woltz und Dr. Ann-Katrin Schütz für viele inspirierende Gespräche, immer wieder neue Motivation und unfassbaren Support und Zusammenhalt in jeder Situation. Herzlichen Dank an Jessi, für alle stärkenden Gespräche, eine tolle Büroathmosphäre, inklusive spannender Geräusche, viel Inspiration und die herzliche Aufnahme in die Gruppe. Vielen Dank an Marc, für gemeinsame Demotivation und Gespräche. Danke auch an Tobi H. für alle Gespräche und unvergessliche Ausflüge nach Chooz. Herzlichen Dank an Colin und Katha für das Korrekturlesen einzelner Kapitel meiner Arbeit. Vielen lieben Dank an meinen Postdoc Tobi S. fürs ausführliche Korrekturlesen meiner Arbeit, viele interessante Gespräche und ein offenes Ohr zu jeder Zeit.

Ganz herzlichen Dank an Ulrich Pfister für eine tolle, fast lebenslange Freundschaft. Danke für gute Gespräche, gemeinsame Hundeausflüge, unzählige Trampolinnachmittage, die gemeinsame Leidenschaft für verschiedenste Konsolen, Spiele und auch für die Physik, einen komplett bekloppten Humor, die Erweiterung meines musikalischen Horizontes und dafür, dass du der Bruder bist, den ich nie hatte.

Ein besonders liebevoller Dank gilt Jona Siedle für eine langjährige, schöne Freundschaft voller Akzeptanz, Mitgefühl, Sicherheit und gemeinsamem Anderssein. Ich weiß nicht, wie ich die Schulzeit ohne dich überstanden hätte.

Meiner Cousine Alina Summers möchte ich sehr für unfassbar lange Telefonate, ein offenes Ohr zu jeder Zeit, jährliche gemeinsame Wochenenden und eine aufrichtige Freundschaft danken.

Herzlichen Dank auch an Terence Kumordzie für eine tolle Freundschaft, Verlässlichkeit in jeder Situation und unzählbare Stunden, in denen wir uns online über Mitspieler aufgeregt haben.

Ich möchte mich von Herzen bei Hannah Amann für eine tiefgründige Freundschaft, gute Gespräche und gemeinsame Filmeabende bedanken. Danke, dass du mich immer siehst.

Bei Sandra Glocker, Sofia Morelli, Jakob Sappler möchte ich mich sehr für das gemeinsame Lernen im Studium und eine tolle Freundschaft zwischen Kultur und Absurdität bedanken.

Danke an Sina Ruis, Gloria Kessler und Karina Karg für den Zusammenhalt während der Schulzeit und darüber hinaus.

Dankeschön für individuelle Freundschaften und gute Gespräche auch an Lydia Vaas, Nicolas Albenge, Florian Babisch, Lana Dambacher, Dominik Bammert, Oliver Schüle, Patrick Kern, Ines Kunze, Sabrina Bebon und Dr. Vanessa Altdörfer.

Um niemanden zu vergessen und da, ich nicht alle namentlich aufzählen kann, möchte ich meinen Dank allen widmen, die die Realisierung dieser Arbeit in irgendeiner Form ermöglicht haben. Danke euch allen!